

Mechanisms determining structural
changes during the extratropical transition
of Typhoon Sinlaku (2008):
a modelling study

Zur Erlangung des akademischen Grades eines
DOKTORS DER NATURWISSENSCHAFTEN
der Fakultät für Physik des
Karlsruher Instituts für Technologie (KIT)

genehmigte

DISSERTATION

von

M.Sc. Hilke Simone Lentink
aus Vriezenveen, die Niederlande

Datum der mündlichen Prüfung: 19.05.2017
Referent: Prof. Dr. Sarah C. Jones
Korreferent: Prof. Dr. Corinna Hoose

*"In considering the study of physical phenomena, [...],
we find its noblest and most important result
to be a knowledge of the chain of connection,
by which all natural forces are linked together,
and made mutually dependent upon each other; and
it is the perception of these relations
that exalts our views and ennobles our enjoyments."*

ALEXANDER VON HUMBOLDT

COSMOS: A SKETCH OF THE PHYSICAL DESCRIPTION
OF THE UNIVERSE, VOL. 1

Abstract

The extratropical transition (ET) of a tropical cyclone (TC) is the transformation of an axi-symmetric to an asymmetric cyclone structure in a baroclinic environment. ET is often associated with high impact weather. At the same time, the complexity of the structural changes makes it difficult for models to adequately forecast the development. The combination of high impact weather and low predictability forms a risk for society. Therefore it is necessary to improve the dynamical understanding of ET, as well as the understanding of the challenges involved in modelling such events. An excellent case study for this goal is the ET of Typhoon Sinlaku in 2008. Sinlaku was one of the cyclones that was investigated during the T-PARC field campaign (2008) which provided a unique measurement dataset for structural changes during Sinlaku's ET.

This research is divided into two parts. In the first part, the objective is to analyse the sensitivity of the model in simulating the cyclone structure during ET. Furthermore it is aimed to model the ET of Sinlaku with sufficient quality to be able to use the simulation to investigate the physical processes involved. In the second part, the objective is to obtain a better understanding of the mechanisms that determine the structural changes during ET. In order to reach the objectives, first the observational data is used to verify the quality of the model's initial data. The environment in which Sinlaku is embedded is represented relatively well in the initial data, but the cyclone structure is too weak and often located too close to Japan. The model is then initialised with different setups, using the standard initial data. Subsequently, Sinlaku's vortex in the initial data is replaced by a more realistic version of the storm by the use of observational data and the piecewise PV inversion technique. The storm can then be moved horizontally with respect to its original location near Japan.

In this case study the initialisation of the model played a key role in obtaining an adequate simulation. Simulations of Sinlaku benefited from the use of a higher horizontal resolution which resulted in a more realistic development of the cyclone. The improved cyclone structure in the initial data and the additional relocation away from land, resulted in a reliable simulation. Two high-resolution simulations are selected in which the structural changes agree well with the observations. These two simulations are used for the analysis of structural changes during Sinlaku's tropical re-intensification period and ET period, respectively. Both simulations are analysed with a range of diagnostic tools (trajectory analysis, vorticity budget analysis, quasi-geostrophic omega forcing, 2-D frontogenesis). By using high resolution simulations meso-scale features can be identified that have not been described in previous studies.

Sinlaku had a rather unusual ET development, in which the cyclone first re-intensified

tropically, although transformation into an extratropical cyclone was expected. During this period, Sinlaku was located south of Japan and the orography played a key role in blocking the inflow of midlatitude air. Sinlaku therefore remained in a warm and moist environment, with the potential for re-intensification. Convergence between the outer and inner cyclonic circulation caused a band of convection with associated diabatic PV modification. Low-level high PV air from the rain band is advected towards the center and causes Sinlaku to intensify.

The actual ET period of Sinlaku was postponed by orographic blocking of low-level midlatitude air. Once Sinlaku moved over the open ocean again, away from Japan, cold dry air was free to move equatorwards and Sinlaku interacted with the baroclinic zone. The evolving frontal structure of Sinlaku resembled a Shapiro-Keyser-like cyclone development. Related to this development, the low-level wind field included features that were relatively similar to a warm jet, cold jet and sting jet. Additional remarkable changes in the structure are the development of a stable area south of Sinlaku by sinking air that created a warm anomaly. The sinking air is caused by three mechanisms: evaporative cooling, frontolysis and a vertical-wind-shear-related dipole in vertical motion. All three mechanisms are co-located and create a tower of descent, which lies over the area of strongest wind speeds.

Below the warm anomaly, a low-level positive PV anomaly is observed with a broadening low-level wind field around it. Air with high PV and high relative vorticity is advected from along the warm front towards the center, and causes a slower decay of the cyclone. Over time, however, the interaction with the baroclinic zone causes advection of dry air towards the warm front. A decrease in moisture supply and an increase in vertical wind shear weakened Sinlaku's intensity and eventually the cyclone decays.

Contents

1. Introduction	1
2. Background information	5
2.1. Extratropical transition of tropical cyclones	5
2.1.1. Tropical and extratropical cyclones from a PV perspective . . .	5
2.1.2. The concept of ET	12
2.2. Relevant mechanisms causing structural changes and TC motion . . .	19
2.2.1. Vertical wind shear	19
2.2.2. Baroclinic zone related changes	22
2.2.3. Topographic influences	27
2.3. Challenges in modelling ET	30
2.3.1. Initialization of the model	30
2.3.2. Multi-scale interactions	33
2.4. The ET of Typhoon Sinlaku (2008)	36
3. Data and methods	41
3.1. Observational data	41
3.1.1. Aircraft data	41
3.1.2. Satellite data	43
3.2. The COSMO model	44
3.2.1. Model description	45
3.2.2. Initializing the model	47
3.3. Diagnostic tools	49
3.3.1. Potential vorticity inversion	50
3.3.2. Relative vorticity budget	52
3.3.3. Quasi-geostrophic forcing of vertical motion	56
3.3.4. Frontogenesis function	58
3.3.5. Trajectory calculations	59
3.3.6. Additional post-processing tools	60
4. Challenges in modelling the ET of TY Sinlaku	63
4.1. Sinlaku’s development according to observations and analysis data . .	63
4.1.1. General development	64
4.1.2. Storm development during the tropical re-intensification period	68
4.1.3. Storm development during the extratropical transition period	74
4.1.4. Discussion	77
4.2. Challenges in modelling with standard COSMO simulations	79
4.2.1. General development	80

4.2.2.	Storm structure during the tropical re-intensification period	83
4.2.3.	Discussion	87
4.3.	Modifying the initial data for COSMO simulations	88
4.3.1.	SAMURAI as initial data	88
4.3.2.	General development	90
4.3.3.	Storm structure during the ET period	92
4.3.4.	Discussion	96
4.4.	Conclusions	97
5.	Structural changes during the ET of TY Sinlaku	99
5.1.	The re-intensification as a tropical cyclone	99
5.1.1.	Overview	99
5.1.2.	Mechanisms behind tropical re-intensification	103
5.1.3.	Mechanisms behind tropical decay	112
5.1.4.	Additional influences of topography	116
5.1.5.	Discussion	117
5.2.	The development during extratropical transition	118
5.2.1.	Overview	118
5.2.2.	Distribution of midlatitude and subtropical air masses	125
5.2.3.	Mechanisms behind structural changes during ET	138
5.2.4.	Development of extratropical cyclone characteristics	150
5.2.5.	Discussion	163
5.3.	Conclusions	165
6.	Summary and outlook	169
	Appendices	175
A.	Verification of the Best Track data	175
B.	Details to Sinlaku's evolution in CTT data	178
C.	Details to Sinlaku's evolution in standard COSMO simulations	179
D.	Characteristics of the low level wind field at 19/18	183
	List of abbreviations	185
	Bibliography	187
	Acknowledgements	201

1. Introduction

Sinlaku is the legendary goddess of the island Kosrae. She is goddess of the heavens and breadfruit, and queen of nature. Sinlaku is able to make typhoons, and so she does. Deadly storms are named after her. In 2002, Typhoon Sinlaku had destructive wind speeds for over seven days, before making landfall in China. In 2008, Sinlaku caused a lot of damage to life and property twice, first during its landfall in Taiwan, and afterwards during its extratropical transition near the coast of Japan. Most recently, Sinlaku was a tropical storm in 2014 that moved over the Philippines. This thesis will be about the extratropical transition of Typhoon Sinlaku in 2008.

Tropical cyclones (TCs) are one of the most hazardous natural phenomena on earth. They develop over the warm ocean surface of the subtropics in nearly all ocean basins. When TCs move close to land, they get special attention from the media because their destructive wind speeds and excessive rainfall have a high impact on human activity in the densely populated coastal areas. When TCs move poleward over the ocean, they often weaken as a tropical system and get less attention. Nevertheless, these poleward moving cyclones should not be underestimated because they can still be the source for high impact weather. When a TC moves poleward it experiences a decrease in sea surface temperature, an increase in vertical wind shear and it impinges on a horizontal temperature gradient, called the midlatitude baroclinic zone. Due to these environmental changes, the axi-symmetric structure of the TC, which is dominated by deep convection, changes into an asymmetric frontal structure, characteristic for an extratropical cyclone. This transformation is called the extratropical transition (ET) of a TC (Jones et al., 2003).

ET is associated with high impact weather, both locally and downstream. The local direct impact is related to the wind and precipitation field. Extreme wind gusts belong either to the TC remnants or to a subsequent developing extratropical cyclone, and severe precipitation develops along a warm frontal zone. This leads to, amongst other things, large surface waves over the ocean and flooding in the surrounding of the TC (Jones et al., 2003). The upper level outflow of the transitioning cyclone also influences the orientation of the upper level jet stream, and by the formation of a wave pattern it indirectly modifies the weather downstream, with the possibility for high impact weather over the adjacent continent. Simultaneously, the forecast skill is relatively low during ET (e.g. Aiyyer, 2015; Harr et al., 2008; Anwender et al., 2008; Grams et al., 2015; Quinting and Jones, 2016). The combination of high impact weather and low predictability forms a risk for society and

threatens life and property. Despite ongoing research, the processes that occur during ET are not fully understood yet. Furthermore, a numerical weather prediction model is prone to small errors that evolve during the complex interaction between a poleward moving TC and its environment, and the errors grow during the ET and associated downstream development. So there is a need to improve the dynamical understanding, as well as the understanding of sensitivities in modelling ET.

Many previous studies focused on the larger scale direct and downstream impact of ET, and base their results on analysis data or model simulations with a relatively low horizontal resolution that does not capture the smaller scale structural changes well. Yet, these structural changes can be a source of model errors, and they have not been extensively investigated before. Therefore, this study focuses on structural changes during ET based on high resolution modelling. The first objective is to analyse the sensitivity of the model in simulating the cyclone structure during ET. The second objective is to obtain a better understanding of mechanisms that determine the structural changes during ET. An excellent case study for this goal is the ET of Typhoon Sinlaku in 2008. Sinlaku was a relatively weak system that moved close to Japan during the investigated period of 18 to 20 September. It is an interesting case for this study because (1) it had an unexpected tropical re-intensification when ET was expected and (2) its development during ET was uncertain in deterministic forecasts and even an extratropical re-intensification was predicted. Furthermore, (3) a unique measurement dataset is available for Sinlaku's ET which is an eminent basis for the investigation of structural changes during cyclone transformation.

In the following chapters of this thesis, first a review of relevant literature is given. Background information, as well as existing gaps in the current knowledge will be made clear, on which the research questions are based (Chapter 2). In order to answer research questions model simulations are performed, that are verified by observational data, and analysed by the use of diagnostics tools (Chapter 3). Since the aforementioned objectives are twofold, also the results of this study are divided in two parts. The first part deals with the modelling of Typhoon Sinlaku (Chapter 4) and addresses the following research questions:

- How well does the analysis data represent Sinlaku's development?
- How well can Sinlaku be simulated with standard initial data?
- What is the influence of different initialization times on the simulation of Sinlaku?
- Can the piecewise PV inversion method be used to improve the initial data and thereby the simulation?
- What is the influence of orography on a proper simulation of Sinlaku, from a technical perspective?
- Is a computationally expensive high horizontal resolution needed to properly simulate Sinlaku during its ET?
- Are any of the simulations sufficiently close to the observed evolution of Sinlaku to justify them being used to investigate mechanisms that determine the structural evolution during an ET event?

The second part continues with the dynamical understanding of structural changes during Sinlaku's ET (Chapter 5). It addresses the following questions:

- What mechanisms contributed to the tropical re-intensification and decay of Sinlaku?
- How did the structure of Sinlaku change during its ET?
- What mechanisms govern the structural changes during the ET of Sinlaku?
- What influence does orography have on the track and structural changes of Sinlaku?

These research questions will be answered at the end of both chapters, and at the end of this thesis a summary and outlook is given (Chapter 6).

This dissertation is integrated in phase 2 of the research project PANDOWAE (Predictability ANd Dynamics Of Weather systems in the Atlantic-European sector - Forschergruppe FOR896), funded by the German Research Foundation (Deutsche Forschungsgemeinschaft, DFG). It contributes to the sub-project TROP which focuses on the impact of tropical-extratropical interactions on downstream predictability.

2. Background information

In this chapter, the current understanding of ET is reviewed (section 2.1). Mechanisms that play a role in the structural change of a transitioning cyclone are described in more detail (section 2.2). The structural changes are not always well captured in numerical weather prediction models and challenges in modelling are therefore common (section 2.3). This chapter ends with an overview of the evolution of Typhoon Sinlaku (section 2.4).

2.1. Extratropical transition of tropical cyclones

Extratropical transition is the transition from a cyclone with a tropical structure into a cyclone with an extratropical structure. Therefore, a basic overview of tropical and extratropical cyclones is given, before continuing with the transition between both. In this section the potential vorticity (PV) perspective is introduced as well, which will turn out to be a useful tool later in this research.

2.1.1. Tropical and extratropical cyclones from a PV perspective

Tropical cyclones

Tropical cyclones (TCs) are low pressure systems in the tropics that have an axisymmetric structure with a radius on the order of 100-1000 km and often a cloud-free eye in the middle (Figure 2.1). They are associated with strong winds (> 33 m/s) and heavy precipitation and are destructive weather phenomena accounting for many deaths and large damages every year. The wind damage is largest near the radius of maximum winds (RMW) at about 10-100 km from the center. TCs occur in most ocean basins around the world, where they have different names. In the western North Pacific a TC is also called typhoon (TY).

Above the boundary layer, a TC is close to gradient wind balance, and the horizontal wind follows a cyclonically closed circulation. This is the primary circulation. Transverse to the primary circulation, the secondary circulation consists of radial inflow in the boundary layer, maximum ascent in the eyewall, a thin radial outflow layer at the top and subsiding air far away from the center. This circulation is thermally

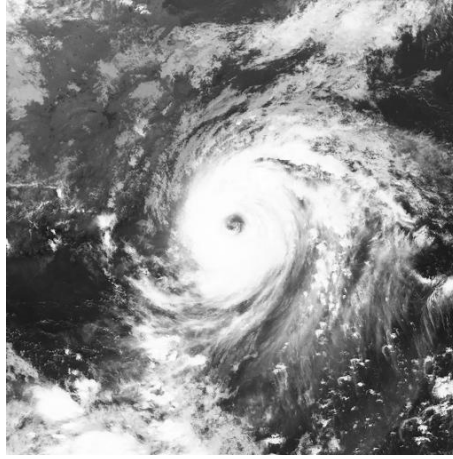


Figure 2.1. – Multifunctional Transport Satellite (MTSAT) infrared (IR) channel 4 (3.5 - 4.0 μm) imagery of TY Sinlaku at 12 UTC at 12 September 2008 (obtained from <http://agora.ex.nii.ac.jp/digital-typhoon/summary/wnp/i/200813.html.en>).

direct, meaning that air rises where it is relatively warm compared to its surroundings and sinks as soon as the air parcel becomes cooler than its surrounding. From a vertical perspective, the strongest horizontal cyclonic winds occur near the surface and they decrease upward, with a reversed direction (anticyclonic flow) at about 15 km height (Emanuel, 1991, 2003). The eyewall slopes outward with height, 5 to 100 km from the center (Emanuel, 1991, 2003). The eyewall is characterized by a ring of deep convective clouds, whereas the eye is often characterized by forced subsidence (thermally indirect circulation) and therefore relatively warm and dry and often free of clouds. In the lower troposphere, a tropical cyclone is relatively warm compared to its environment and therefore also called a warm-core cyclone. Due to the forced sinking air, the center is even warmer than the surrounding warm-core area (Palmén, 1948; Shea and Gray, 1973). The vertical profile in Fig. 2.2 shows the temperature distribution in a TC with the warm core (in the figure up to about 500 km from the center), the even warmer eye and sloping eyewall. Outside the eyewall, clouds and precipitation exist in one or more spiral bands.

TCs develop over tropical oceans and need an initial disturbance to form. General criteria for TC development are a sea surface temperature (SST) of more than 26° C throughout a depth of at least 50 m, moisture availability in the lower and mid-troposphere for the continued development of deep convection, a weak vertical wind shear, an initial disturbance containing positive vorticity (for example a meso-scale convective system) and a distance of at least 5° from the equator since for tropical cyclogenesis a certain value of planetary vorticity is required (e.g. Gray, 1968). A mature TC gains its energy from heat transfer from the ocean and can be compared with a Carnot heat engine (Emanuel, 1986). A higher rate of heat transfer causes higher wind speeds which in turn causes a higher uptake of heat by friction. This positive feedback causes a self-maintaining system. A TC loses its intensity only when the heat source is gone, for example over lower sea surface temperature or over land, or when external phenomena (e.g. environmental vertical wind shear or

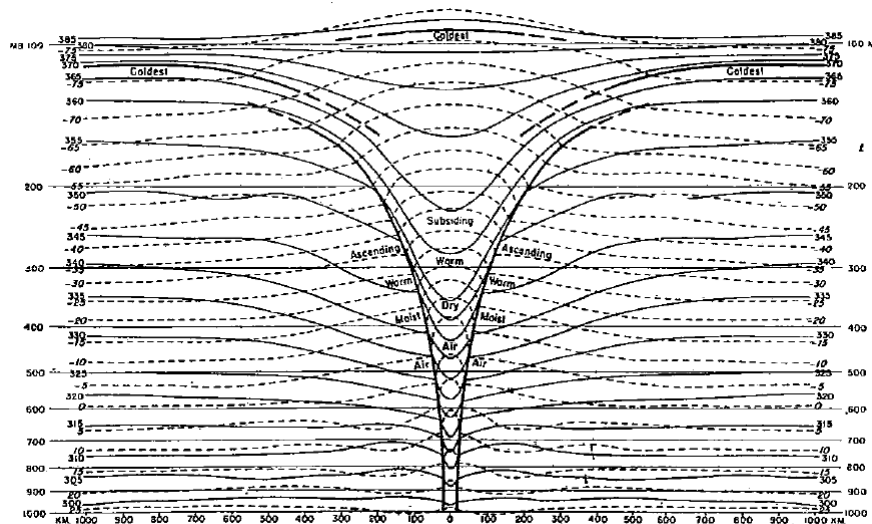


Figure 2.2. – Cross section through a hurricane from 17-20 September 1947. Thin dashed lines indicated temperature, thin solid lines potential temperature, thick solid or dashed lines either the eyewall boundary or the tropopause surface. Reprinted from Palmén (1948) © Geophysical Society of Finland. Used with permission.

orography) disturb the primary and secondary circulation of the closed system. The focus of this thesis lies on the structural changes of a TC during ET rather than on TC development. More information about the development of tropical cyclones and their dynamics can be found in e.g. Chan and Kepert (2010).

Extratropical cyclones

In contrast to TCs, an extratropical cyclone is a cold-core cyclone at the surface, meaning that it has a cold center relative to its environment. Maximum winds and a warm center relative to its surroundings are found at the upper troposphere. The cyclone develops in a baroclinic environment, where cold (warm) air is advected southward (northward) and forms an asymmetric frontal structure. Where a TC gains its intensity by conversion from potential energy into kinetic energy via ocean heat transfer, an extratropical cyclone develops its circular motion field by energy conversion along the pressure and temperature gradients of the baroclinic zone. An upper-level disturbance that causes a cyclonic motion can therefore not maintain itself. For intensification it needs an interaction with the lower-level baroclinic zone. This will be explained in more detail in the next subsection based on PV.

Cyclones from a PV perspective

Cyclones can be viewed from a perspective of standard meteorological quantities, but also from a PV perspective. PV is a meteorological quantity with dynamic

and thermodynamic properties. Ertel's definition of PV (Ertel, 1942) in pressure coordinates (Eq. 13 in Hoskins et al. (1985)) is

$$PV = -g(f\hat{\mathbf{k}} + \nabla_p \times \vec{V}_h) \cdot \nabla_p \theta \quad (2.1)$$

where g is the acceleration due to gravity, f the Coriolis parameter, $\hat{\mathbf{k}}$ the unit vector in the vertical direction, ∇_p the 3D gradient operator in pressure coordinates, \vec{V}_h the horizontal velocity vector and θ the potential temperature (K)

$$\theta = T \left(\frac{1000}{p} \right)^{R_d/c_p} \quad (2.2)$$

with T the air temperature (K), p the pressure (hPa), R_d the gas constant for dry air (287.053 J kg⁻¹ K⁻¹) and c_p the specific heat capacity at constant pressure for dry air (1005.7 J kg⁻¹ K⁻¹). After scale analysis, the dynamically most relevant term of PV in tropical and extratropical cyclones is the vertical component

$$PV = -g(f + \zeta) \frac{\partial \theta}{\partial p} \quad (2.3)$$

where $\zeta = \hat{\mathbf{k}}(\frac{\partial v}{\partial x} - \frac{\partial u}{\partial y})$ is the vertical component of relative vorticity (hereafter called relative vorticity), $\eta = f + \zeta$ is the vertical component of absolute vorticity, u and v are the horizontal velocity components in the x and y direction respectively and p the pressure. PV is often expressed in potential vorticity units (1 PVU = 10⁻⁶ m² s⁻¹ K kg⁻¹).

PV is a powerful quantity for two reasons: the 'conservation principle' and the 'invertibility principle'. The conservation principle can be expressed as

$$\frac{dPV}{dt} = -g\vec{\eta} \cdot \nabla_p \dot{\theta} - g(\nabla_p \times \vec{F}) \cdot \nabla_p \theta \quad (2.4)$$

with $\vec{\eta}$ the absolute vorticity vector, \vec{F} the frictional force and $\dot{\theta} = \frac{d\theta}{dt}$ the diabatic heating. From Eq. 2.4 it is seen that PV is conserved in absence of diabatic heating or frictional sources. So, for an adiabatic frictionless flow PV is conserved. The name *potential* vorticity comes from the potential for creating *relative* vorticity in adiabatic flow. This can occur when an air parcel (1) changes its latitude (f) or (2) changes its static stability ($-\partial\theta/\partial p$) (Martin, 2006). A parcel will retain its characteristic PV value and can be traced by it in space and time. Isentropic weather maps are an example of how PV features in an adiabatic flow can be represented and traced. In nature, however, PV is not always conserved. Above the boundary layer frictional processes can be neglected, so, on an isentropic surface, changes in PV are an indication of diabatic heating (e.g. Stoelinga, 1996).

The invertibility principle of PV lies in the fact that characteristics of the atmospheric structure can be determined from the PV field. From the vorticity field, information about the horizontal wind components u and v can be obtained. From the static stability, information about the vertical distribution of potential temperature can be retrieved. To recover the information that is contained in PV, it should

be inverted. Details about the method of inversion are given in section 3.3.1. Piecewise inversion of PV is often used to elucidate the influence of a specific part of a PV disturbance on the tropospheric flow (Davis and Emanuel, 1991; Davis, 1992).

PV is not evenly distributed in the atmosphere and local deviations from the long-term large-scale mean state are most interesting because they can be associated with specific circulation features. In case of a positive (negative) PV anomaly, a cyclonic (anti-cyclonic) circulation is expected. Weather phenomena can therefore be viewed from a PV perspective. This is called 'PV thinking' (Hoskins et al., 1985). We now consider typical PV signatures of tropical and extratropical cyclones. When looking at the modification of PV by diabatic heating (Eq. 2.4), it can be seen from Fig. 2.3a that instantaneous diabatic heating alters the local vertical structure of the isentropic layers in such a way that they are closer to each other below the diabatic heat source and stretched above it. The static stability below the heating is higher than the environmental mean, and therefore a positive PV anomaly is present. Above the heating source, a negative anomaly is found. When the diabatic heating continues long enough, a situation of 'steady diabatic heating' is established and the anomalies in potential temperature and PV are transported vertically (Fig. 2.3b). A TC can be compared to a case of steady diabatic heating. A positive PV anomaly, denoted as "PV tower", is generated throughout the troposphere with a shallow broad layer of anomalously low PV near the tropopause, indicative of the anticyclonic outflow (Fig. 2.4).

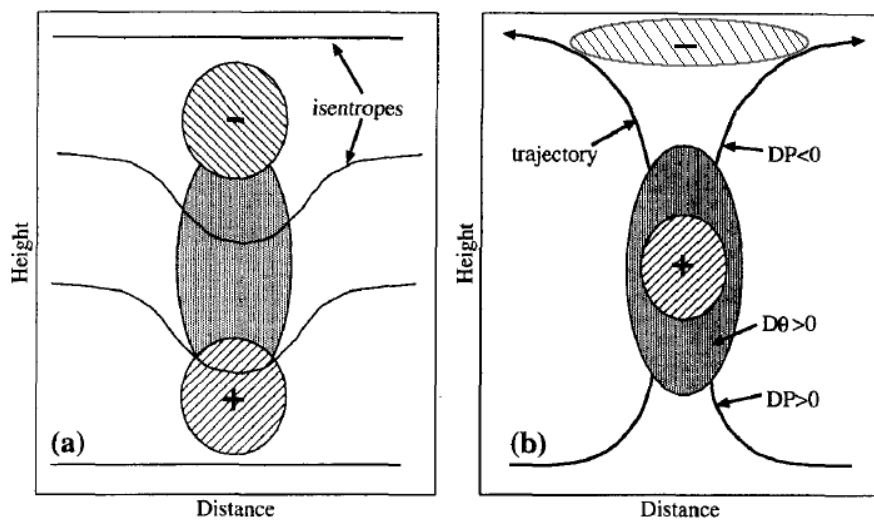


Figure 2.3. – Schematic vertical cross-sections showing diabatically produced positive (+) or negative (-) PV anomalies (cross hatched regions) for the idealized cases of (a) 'impulsive diabatic heating', and b) 'steady condensation' in a frontal zone. Solid shading indicates the region of diabatic heating. In (a) the solid lines are isentropes and in (b) the bold lines with arrows refer to air-parcel trajectories. $D\theta$ and DP denote material tendencies of potential temperature and potential vorticity, respectively. Reprinted from Wernli and Davies (1997) © Royal Meteorological Society. Used with permission from John Wiley & Sons, Inc.

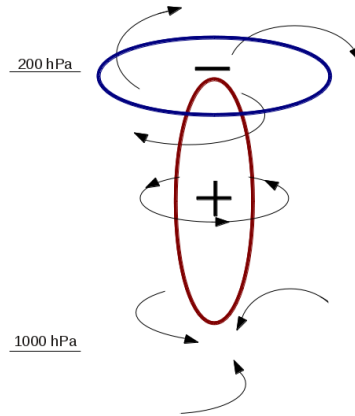


Figure 2.4. – Schematic representation of a tropical cyclone from a PV perspective. The red contour represents the positive PV "tower" with cyclonic motion and cyclonic inflow in the boundary layer shown by the black arrows. The blue contour represents the negative PV anomaly with anticyclonic outflow.

The development of an extratropical cyclone from a PV perspective is different. Here an interaction of the upper and lower troposphere occurs. A disturbance in the upper tropospheric temperature field gives a positive PV anomaly due to the high stratification of the stratospheric air (Fig 2.5a). The PV anomaly induces a modification of the wind field which is strongest in the upper troposphere near the PV anomaly but also present on a much larger scale than the anomaly itself. The wind speed decreases towards the surface. According to the thermal wind balance a cold core is expected below the PV anomaly, which is seen near the surface in Figure 2.5a. Now, consider a low-level warm anomaly as shown in Fig. 2.5b. If the isentropes were artificially connected below the surface, a maximum in static stability would be found near the surface, which causes a positive PV anomaly (Bretherton, 1966). A low-level warm anomaly can therefore be related to a low-level positive PV anomaly. This anomaly can be associated with cyclonic motion that, again, is present at a larger horizontal and vertical scale than the PV anomaly itself. An induced wind and thermal field can therefore influence the atmosphere at a distance from the PV anomaly.

The upper and lower troposphere cases of Figures 2.5a and 2.5b can be combined in a dynamic interaction, as is schematically shown in Figure 2.6. In the first place, the upper-level cyclonic motion penetrates through the troposphere to modify the low-level temperature field east of the upper-level anomaly (Fig. 2.6a). The induced warm anomaly (and therefore positive PV anomaly) has its strongest cyclonic motion at lower levels and penetrates through the atmosphere as well. It amplifies the upper-level PV anomaly to its west. The upper and lower-level PV anomalies are in phase and there is a mutual amplification. As long as the anomalies are in phase (the upper anomaly should be west of the lower anomaly), the extratropical cyclone can intensify and when the phasing is disrupted the cyclone consequently starts to decay.

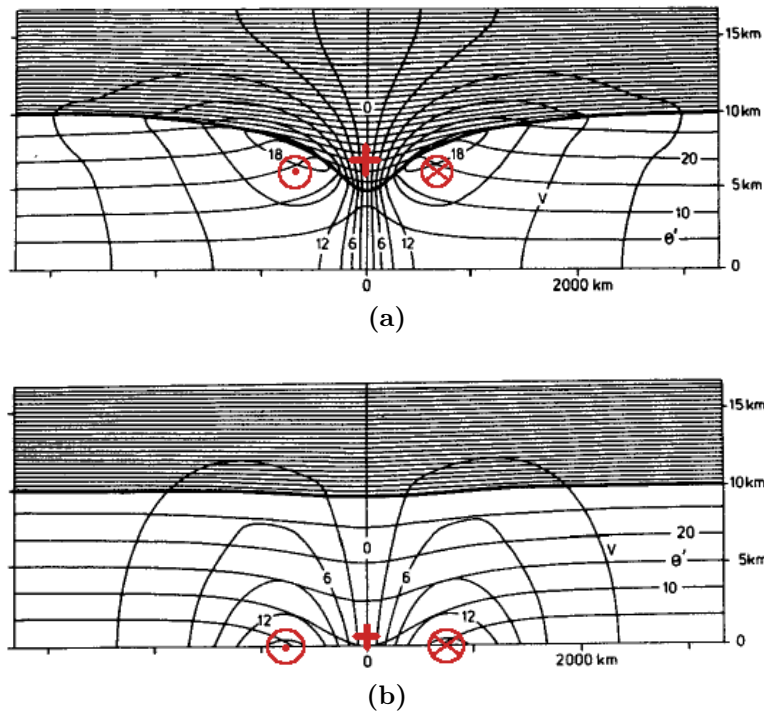


Figure 2.5. – A cold core upper cyclone (a) and warm core lower cyclone (b). The semi-horizontal lines represent isentropes (every 5 K), the semi-vertical lines the cyclonic wind speed across the section (every 3 m/s, red dot: out of the cross section, red cross: into the cross section). The thick black line indicates the tropopause and the red plus indicates a positive PV anomaly. Reprinted and adapted from Thorpe (1986) © American Meteorological Society. Used and adapted with permission.

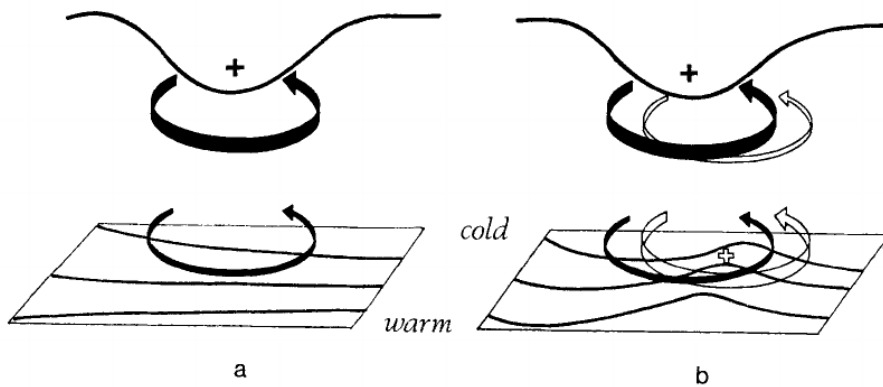


Figure 2.6. – Schematic representation of cyclogenesis (a) by an upper-level positive PV anomaly (black arrows and + sign) over a baroclinic zone (black contours of potential temperature at the surface). (b) The upper air cyclonic PV anomaly leads to advection of warm air and induces a warm anomaly ahead of the upper-level PV anomaly. The warm anomaly induces cyclonic circulation (white arrows and + sign). Reprinted from Hoskins et al. (1985) © Royal Meteorological Society. Used with permission from John Wiley & Sons, Inc.

2.1.2. The concept of ET

The transition from a tropical system into an extratropical system occurs over almost all the ocean basins in which TCs are found. Most ET events take place in the western North Pacific, while the North Atlantic experiences the highest percentage of TCs undergoing ET. In general, the amount of ET events is related to the total number of TCs in that basin (Jones et al., 2003). The percentage of ET events is season dependent and has for example a peak in August and September in the western North Pacific (Jones et al., 2003; Klein et al., 2000). For extended climatologies the reader is referred to Klein et al. (2000) (western North Pacific), Wood and Ritchie (2014) (eastern North Pacific), Sinclair (2002) (western South Pacific), Hart and Evans (2001) (North Atlantic) and Griffin and Bosart (2014) (Indian Ocean).

During the transition period, many processes take place due to which the cyclone structure changes. The axi-symmetric TC structure first transforms into a so-called hybrid cyclone with a warm core and frontal structure (Evans and Hart, 2003) before a cold-core frontal EC structure develops. After the transformation, the cyclone can re-intensify as a strong extratropical cyclone. ET can therefore be divided into a transformation stage and an extratropical re-intensification stage (Klein et al., 2000). These two stages are introduced now, before continuing with a PV perspective on ET and modification of the midlatitude flow.

Transformation stage

Many similarities in the satellite imagery and analysis data of 30 cases of ET in the western North Pacific (Klein et al., 2000) gave the impression that processes during the transformation stage of ET are essentially the same for all recurving TCs. This brought Klein et al. (2000) to develop a conceptual model of the transformation stage of ET, which is shown in Fig. 2.7. The transformation stage is divided into three steps. First, the TC moves poleward over a lower SST. A decrease in the amount of warm moist air from the ocean decreases the available potential energy for the cyclone and therefore its intensity. Meanwhile, the TC approaches the baroclinic zone. Relatively cold dry air flows into the lower-level outer circulation to the west of the system. Deep convection is inhibited, which is seen by a cloudless area (Fig. 2.7, step 1). At the east side of the TC outer circulation, tropical air is advected poleward. This warm moist air ascends over the tilted isentropic surfaces of the baroclinic zone, maintaining deep convection.

Secondly, while these processes continue, the storm moves closer to the jet stream. Vertical wind shear (VWS) tilts the TC structure at the top (Fig. 2.7). In the lower troposphere a dipole exists of cold air advection to the west and warm air advection to the east of the core. From the ascending parcels in the northeastern quadrant, some turn cyclonically towards the western quadrant where they descend, whereas other parcels are advected anti-cyclonically to the northeast by the influence of the jet stream. Confluence of outflowing TC air and the jet can be seen in satellite

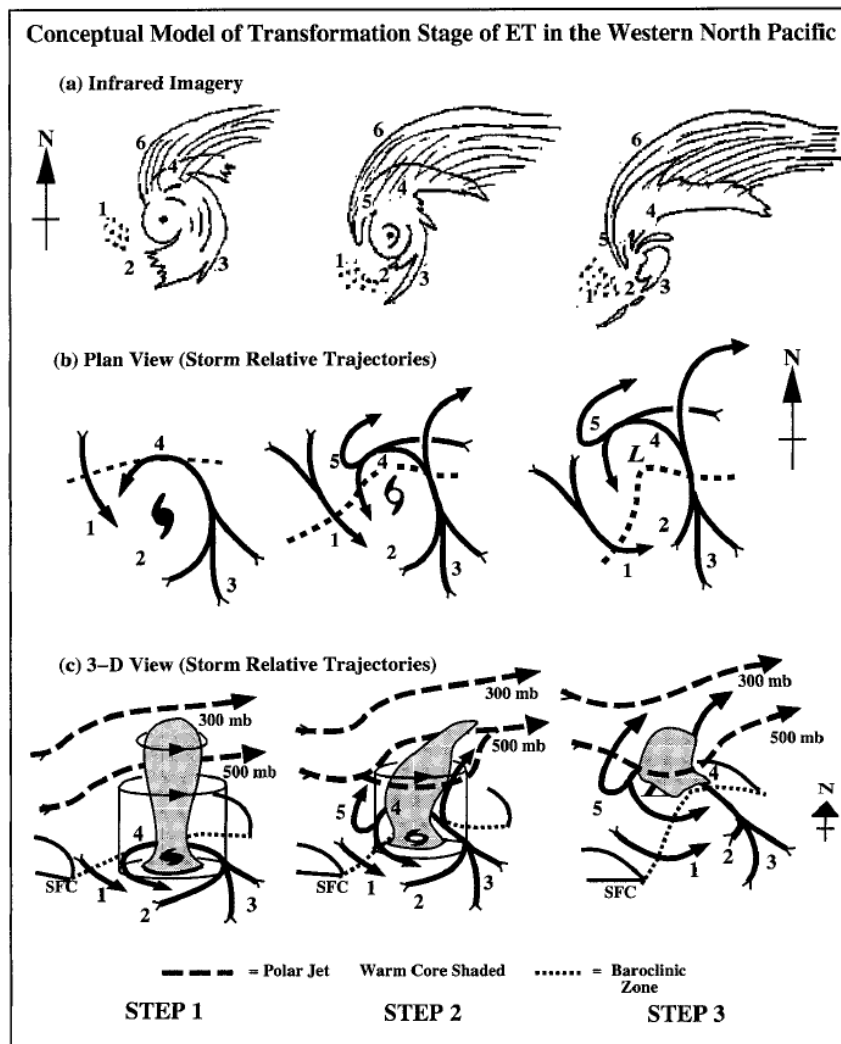


Figure 2.7. – Conceptual model of the transformation stage of extratropical transition. Labelled areas: 1) environmental equatorward flow of cooler, drier air, 2) decreased tropical cyclone convection in the western and southern quadrants, 3) environmental poleward flow of warm, moist air is ingested into tropical cyclone circulation, 4) ascent of warm, moist inflow over tilted isentropic surfaces associated with baroclinic zone (dashed line in middle and lower panels), 5) ascent (undercut by dry-adiabatic descent) that produces cloud bands wrapping westward and equatorward around the storm center, 6) cirrus shield with a sharp cloud edge if confluent with polar jet. Reprinted from Klein et al. (2000) © American Meteorological Society. Used with permission.

imagery by the sharp edge of the cirrus shield. Although the cyclone has weakened, the inner core still exhibits deep convection.

During the third step in Fig. 2.7, the storm is embedded in the baroclinic zone and also the inner core is affected. The eyewall is eroded by dry-adiabatic descent of midlatitude air to the west, further weakening the convection on this side. Vertical wind shear increases and advects the top of the upper-tropospheric core downstream.

A warm conveyor-belt-like warm front and cirrus shield can be seen to the northeast. A weak cold front at the southeast is visible by a small cloud band.

Ritchie and Elsberry (2001) performed idealized experiments for the 3 steps of the conceptual model. They used a higher horizontal resolution than Klein et al. (2000) (15 km instead of 1° (~ 100 km)), which gave the ability to reveal the evolution of structural changes in more detail. In general, Ritchie and Elsberry (2001) confirm the findings of Klein et al. (2000). One significant difference is that suppression of convection in the eyewall to the southwest of the cyclone center occurred due to dry-adiabatic warming by isentropic subsidence, rather than by intrusion of cold air advection from the north. Although ET is a gradual developing process, Ritchie and Elsberry (2001) furthermore define that the main environmental influences during step one, two and three are SST, VWS and the baroclinic zone, respectively.

Re-intensification stage

All recurring TCs behave in a similar manner during the transformation stage, but large differences are observed during the re-intensification stage. After transforming from a tropical into an extratropical structure, some systems deepen as an extratropical cyclone and others decay. This process is independent of the initial structure of the cyclone. Whether a TC re-intensifies or not depends on the large scale environment. In the northwest Pacific, the upper-level synoptic scale configuration can be divided into a north-east pattern and a north-west pattern (Harr et al., 2000) (Figure 2.8). The pattern is named after the location of a pre-existing trough (upper-level PV anomaly, like in Fig. 2.5a) with respect to the location of the northward moving TC. A downstream (north-east) trough blocks the re-development, while an upstream (north-west) trough has a high potential for strong re-intensification (Harr et al., 2000). Klein et al. (2002) compared the re-intensification with type-B cyclogenesis (Petterssen and Smebye, 1971) in which positive PV advection ahead

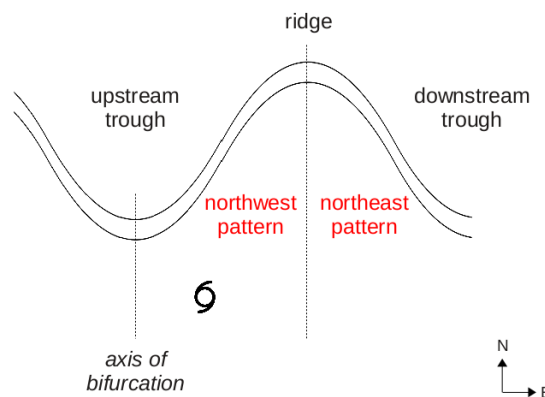


Figure 2.8. – Schematic representation of the northwest and northeast patterns of Harr and Elsberry (2000). The curved line represents the jet stream or another upper-level border between the subtropics and the midlatitudes like a gradient in PV.

of a pre-existing upper-level trough vertically aligned with low-level warm advection, like in Fig. 2.6. In the case of ET, the warm advection is supported by the interaction between the cyclonic motion and the baroclinic zone.

The magnitude of extratropical re-intensification depends on the phasing between the TC and the upper-level flow. When the TC phases with an upper-level trough, strong re-intensification occurs. Without proper phasing, only moderate or little re-intensification occurs (Klein et al., 2002). Several studies investigated the influence of the initial position of the TC on re-intensification (e.g. Ritchie and Elsberry, 2007; Riemer and Jones, 2014; Scheck et al., 2011b). The initial location strongly influences the phasing with the midlatitude trough and thereby has an impact on the peak intensity of the final extratropical cyclone (Ritchie and Elsberry, 2007). A bifurcation point (Figure 2.8) has been identified and lies on the trough axis at a location where the zonal translation speed of the cyclone equals the phase speed of the upper-level wave pattern (Scheck et al., 2011b). The relative position to the bifurcation point determines whether a TC re-intensifies or decays. Small displacements can already be decisive. TY Jangmi (2008), for example, either decayed or re-intensified when it was displaced by less than 1.25° (~ 130 km) in the initial conditions (Grams et al., 2013a). Riemer and Jones (2014) continued with the determination of three regimes: no-ET and ET in a northwest pattern and ET in a northeast pattern. The bifurcation point on the trough-axis separates the no-ET and ET regimes. When a cyclone is just west of the trough axis, it misses the influence of the midlatitude steering flow and stays relatively south as a TC. A stagnation point on the downstream ridge axis determines whether the TC is in a northwest or northeast pattern (Riemer and Jones, 2014). The phasing between a TC and the midlatitude flow is therefore a critical factor for the re-intensification as an extratropical cyclone.

ET from a PV perspective

ET is a dynamical process in which both the midlatitude circulation and the TC have their contribution to the interaction (Klein et al., 2002). To elucidate the coupling between upper and lower-level phenomena, it is useful to view ET from a PV perspective. A schematic representation of ET in terms of PV is given by Agustí-Panareda et al. (2004) and shown in Fig. 2.9. A tropical cyclone can be identified by a positive PV tower (4) and the shallow outflow area (5), similar to Fig. 2.4. The cyclonic motion of the TC (4) induces a northward low-level warm advection (1). Warm air ascends over the baroclinic zone, where clouds form and local positive PV anomalies are created by diabatic heating (2). The upper-level trough (3) may be in phase with the surface warm anomaly (1).

The transitioning cyclone can enhance the low-level warm anomaly and thereby promote cyclogenesis (Fig. 2.6). When either the TC or the induced surface warm anomaly is in phase with the upper-level trough, they subsequently re-intensify. The coupling between a PV tower and a trough is shown from a PV perspective in Fig. 2.10. In the first place, an upper-level trough with associated positive PV anomaly approaches the PV tower of the TC (Figs. 2.10a,b). When both

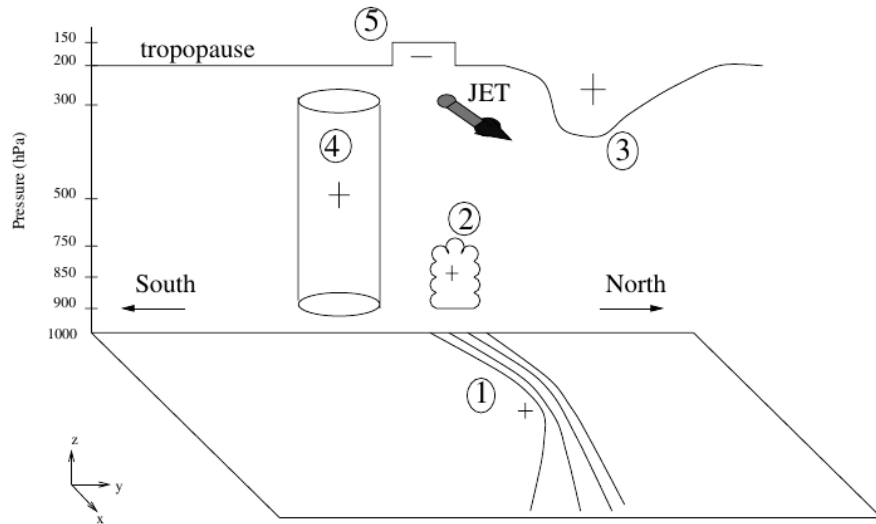


Figure 2.9. – Schematic representation of ET. + and - signs represent positive and negative PV anomalies respectively. The meaning of the numbers is explained in the text. Reprinted from Agustí-Panareda et al. (2004) © Royal Meteorological Society. Used with permission from John Wiley & Sons, Inc.

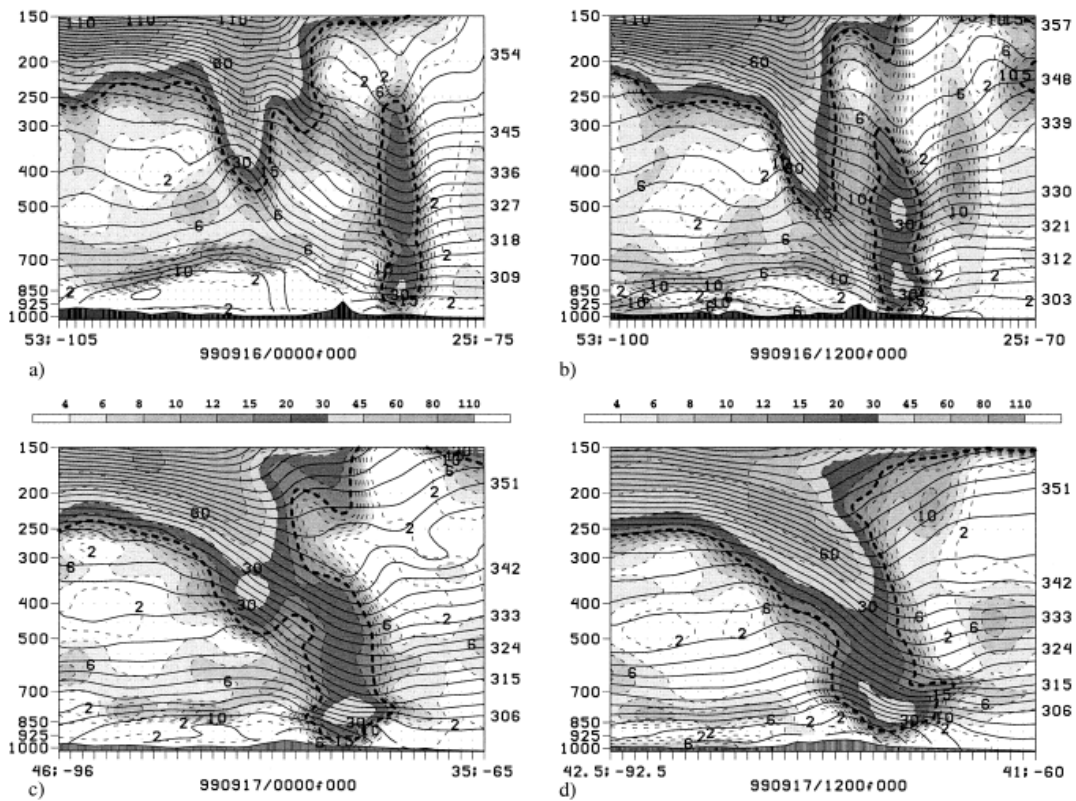


Figure 2.10. – Cross sections of PV (shaded, in PVU) and potential temperature (solid black lines, every 3 K) at (a) 16 Sep. 00UTC, (b) 16 Sep. 12UTC, (c) 17 Sep. 00UTC and (d) 17 Sep. 12 UTC, 1999, of Hurricane Floyd. Reprinted from Atallah and Bosart (2003) © American Meteorological Society. Used with permission.

disturbances approach each other they merge with a westward tilt, as is favourable for intensification (Fig. 2.6), and the coupled system intensifies as an extratropical cyclone (Fig. 2.10c,d). The cold core below the trough and warm core within the TC can be identified from the isentropes in the initial stage. During the re-intensification, cold (warm) air can be identified at the west (east) side of the low-level PV anomaly, indicating a frontal structure.

Modification of the midlatitude flow

A tropical cyclone near the baroclinic zone influences the lower levels by advecting subtropical air northwards and midlatitude air southwards at the east and west side respectively. This is similar to what would happen if a cyclonic circulation was superimposed on a temperature gradient (Fig. 2.11). At upper levels, a similar process takes place, but now the role of PV becomes more dominant. First, a cyclonic circulation just south of the jet stream creates a ridge downstream of its location, and a trough upstream (e.g. Scheck et al., 2011a; Riemer et al., 2008). Second, the divergent outflow of the cyclone advects a negative PV anomaly which amplifies the ridge building (e.g. Grams et al., 2013b; Archambault et al., 2013; Riemer et al., 2008) (Fig. 2.12). The negative PV anomaly develops from diabatically reduced low PV. It is partly created by deep convection within the TC, and partly by the advection of warm moist air northward. The air is forced to ascend when impinging on the baroclinic zone and forms a warm conveyor belt (WCB) like structure (Grams et al., 2013b), where large amounts of latent heat are released over a broader area than the TC itself, producing PV at lower levels and destroying PV above it. Once the low-PV air is established, it is again advected adiabatically along the isentropes. With a higher moisture flux along the warm front, more precipitation and a stronger ridge amplification is found (Torn, 2010). Subsequently, the presence of low PV air increases the horizontal PV gradient and therefore intensifies the wind speed

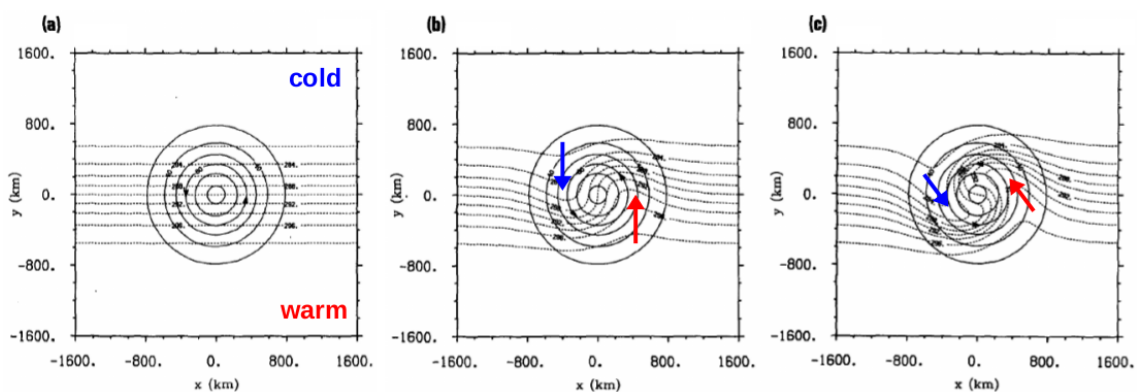


Figure 2.11. – Evolution of potential temperature (dashed lines) when a cyclonic motion (represented by the circles) is placed on a temperature gradient at $t=0$ (a), $t=1$ (b) and $t=2$ (c). Reprinted and adapted from Keyser et al. (1988) © American Meteorological Society. Used and adapted with permission.

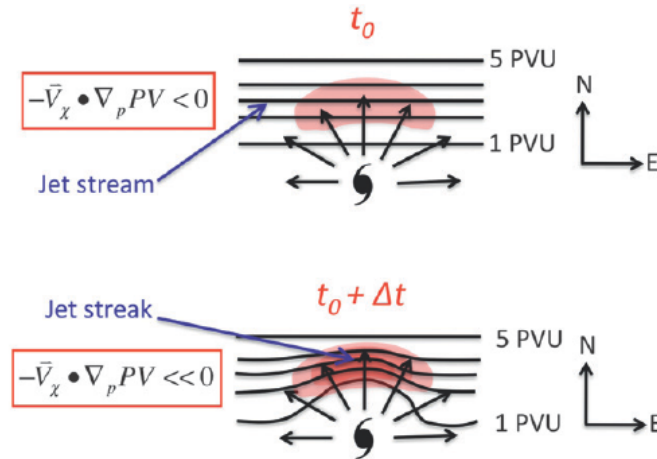


Figure 2.12. – Schematic representation of the jet stream as PV gradient (black lines). Ridge amplification and jet streak intensification is associated with the divergent outflow (vectors) and advection of low or negative PV air (shaded) from a TC impinging upon the upper tropospheric jet stream. Reprinted from Archambault et al. (2013) © American Meteorological Society. Used with permission.

within the jet stream, creating a jet streak (e.g. Grams, 2011; Grams et al., 2013b; Archambault et al., 2013).

The formation of a trough-ridge couplet and the intensification of the jet stream are a *direct impact* of the cyclone on the midlatitude flow. The direct impact is important because it can affect a positive phasing between an upper-level trough and a low-level PV anomaly, favourable for extratropical re-intensification. Furthermore, a trough-ridge couplet, or also called Rossby wave packet, in general moves eastward with the jet stream. The outflow anomaly can reduce the eastward motion of the trough-ridge couplet and thereby promotes a phase-lock between the TC and the midlatitude trough (Riemer et al., 2008). The development of a trough upstream of the cyclone also leads to an overall northward environmental flow, and consequently a northward steering of the cyclone (Scheck et al., 2011a). Other direct impacts of ET are related to the lower-level wind field and precipitation, causing damage at the surface.

The *downstream impact* of the TC on the midlatitude flow is characterized by the development of multiple downstream trough-ridge couplets, also called a Rossby wave train, or the amplification of a pre-existing Rossby wave train. The downstream response can exist for days to a week, and the midlatitude circulation may be related to high-impact weather far downstream, indirectly forced by ET (Harr and Dea, 2009), like for example severe thunderstorms in Europe that were influenced by the the ET of Hurricane Katia (2011) over the Atlantic basin (Grams and Blumer, 2015). Rossby waves occur without ET as well, but the Rossby wave packets that are associated with ET are stronger and with a higher amplitude than generally observed in the midlatitudes (Quinting and Jones, 2016).

2.2. Relevant mechanisms causing structural changes and TC motion

During ET, changes in the structure of the initially axi-symmetric cyclone are dominated by the SST, VWS and the baroclinic zone. The influence of SST lies in the transport of potential energy via surface moisture fluxes. Over a cooler ocean, less moisture is evaporated, and consequently less latent heat is set free during condensation. This causes a decrease in storm intensity. The mechanisms that govern the cyclone changes due to VWS and the baroclinic zone are more complex. They will be described in more detail in this section. Next to characteristic ET changes, also the influence of land on tropical cyclones will be reviewed. This is of interest because TY Sinlaku moved close to Japan.

2.2.1. Vertical wind shear

Environmental VWS influences both the kinematic and thermodynamic structures of a TC and in doing so, also the intensity. It has therefore an important influence on structural changes during ET. Most information about the role of VWS on TCs is gained by analysis of mature hurricanes and idealized experiments with TC-like vortices. The goal of these experiments was most often to find the influence of VWS on the intensity change of developing TCs. Nevertheless, during ET a TC also experiences wind shear by the interaction with the jet stream. In previous studies, dry experiments, in which the atmosphere is artificially free of moisture, are carried out to reveal the influence of adiabatic and kinematic mechanisms (e.g. Jones, 1995). Moist experiments show additional diabatic and thermodynamic processes (e.g. Wang and Holland, 1996; Frank and Ritchie, 1999, 2001; Riemer et al., 2010, 2013). Results show that VWS causes an asymmetry in vertical motion, temperature and precipitation distribution, with the highest temperature and maximum convection in the downshear left quadrant, and maximum precipitation left of the shear vector. The physical processes behind the structural changes of first the dry experiments (mainly based on Jones (1995)), second the moist experiments (mainly based on Wang and Holland (1996)) and third, new insights of more recent studies are reviewed.

In the following example, it is for simplicity assumed that the environmental wind shear is only present in the longitudinal direction, and increases with height. In the example of Fig. 2.13 the wind shear is towards the east and the east (west) side is therefore called the downshear (upshear) side. In general, the modification of a cyclonic vortex in VWS shear starts with tilting of the vortex by differential advection (Fig. 2.13a). Due to the tilt, an internal vertical shear within the vortex develops, which is shown by the profiles A, B and C. Along the profiles, only meridional wind is assumed. Now, consider the meridional component of the thermal wind balance

$$\frac{\partial v_g}{\partial p} = -\frac{R}{f p} \frac{\partial T}{\partial x} = -\frac{1}{f \rho \theta} \frac{\partial \theta}{\partial x} \quad (2.5)$$

with v_g the meridional component of the geostrophic wind, R the ideal gas constant and ρ the air density. Although this relation holds for geostrophic wind, it approximately applies here as well. From Eq. 2.5 it is seen that in order to maintain balance within the vortex, a positive θ -gradient in zonal direction is required in profiles A and C, and a negative θ -gradient in profile B (Fig. 2.13a). The new balanced situation is shown in Fig. 2.13b, where a cold anomaly is present at the downshear side and a warm anomaly at the upshear side. To achieve this state, vertical advection of air is needed with upward motion at the downshear side and downward motion at the upshear side. But a cyclonic vortex is not as simple as this 2D concept (Fig. 2.13b), and the balance does not hold. Cyclonic motion of the vortex move along the isentropes due to the adiabatic dry experiment. The elevated (sunken) isentrope at the downshear (upshear) side cause a dominant upward (downward) motion at the right (left) side of the shear vector (Fig. 2.13c). Cyclonic rotation of the anomalies finally gives a situation with maximum upward (downward) motion at the downshear right (upshear left) side (Fig. 2.13d) in dry experiments.

In reality, moist processes, in particular latent heat release, plays an important role in TCs. When moisture was added in VWS experiments, it was found that at the downshear right side, where maximum ascent and convection is present, latent heat is released. This heat destroys the initial downshear cold anomaly of the dry run, and therefore the isentropic uplifting mechanism of Fig. 2.13c (Frank and Ritchie, 1999). But another mechanism establishes. During latent heating, diabatic PV is created in the downshear right quadrant. It is transported cyclonically upward and destroyed in the downshear left quadrant (Fig. 2.13e). When projected on a horizontal plane, the asymmetric PV anomalies create large-scale counter rotating gyres of divergent flow (Fig. 2.13f), that oppose the non-divergent flow of the TC. The gyres initiate convergence (divergence) at the downshear (upshear) side and thereby enhance (suppress) convection downshear (upshear) (Wang and Holland, 1996). Over time, the asymmetries rotate cyclonically and reach a quasi-steady configuration with maximum convection in the downshear left quadrant (Fig. 2.13g) (Wang and Holland, 1996). Ascending air now tends to be co-located with the warmest temperatures (Frank and Ritchie, 1999). Rain droplets are advected cyclonically and therefore maximum precipitation is found on the left side when looking down the shear vector.

The intensity of a TC is usually reduced under VWS, compared to its potential intensity. Riemer et al. (2010, 2013) explained the intensity reduction from a thermodynamic point of view, in which the TC is represented by a Carnot cycle. They found that the asymmetric precipitation, as described above, causes evaporative cooling of the unsaturated air below, outside of the eyewall. Downdrafts develop, and transport air with low equivalent potential temperature (θ_e) into the boundary layer. The low- θ_e air in the boundary layer cannot recover sufficiently by fluxes of warm moist (high- θ_e) air from ocean surface, and therefore low- θ_e air flows into the eyewall. This decreases the energy cycle of the TC, where the cool dry air serves as a negative fuel for the Carnot-engine.

The sensitivity of TCs to VWS depends on multiple factors like the magnitude

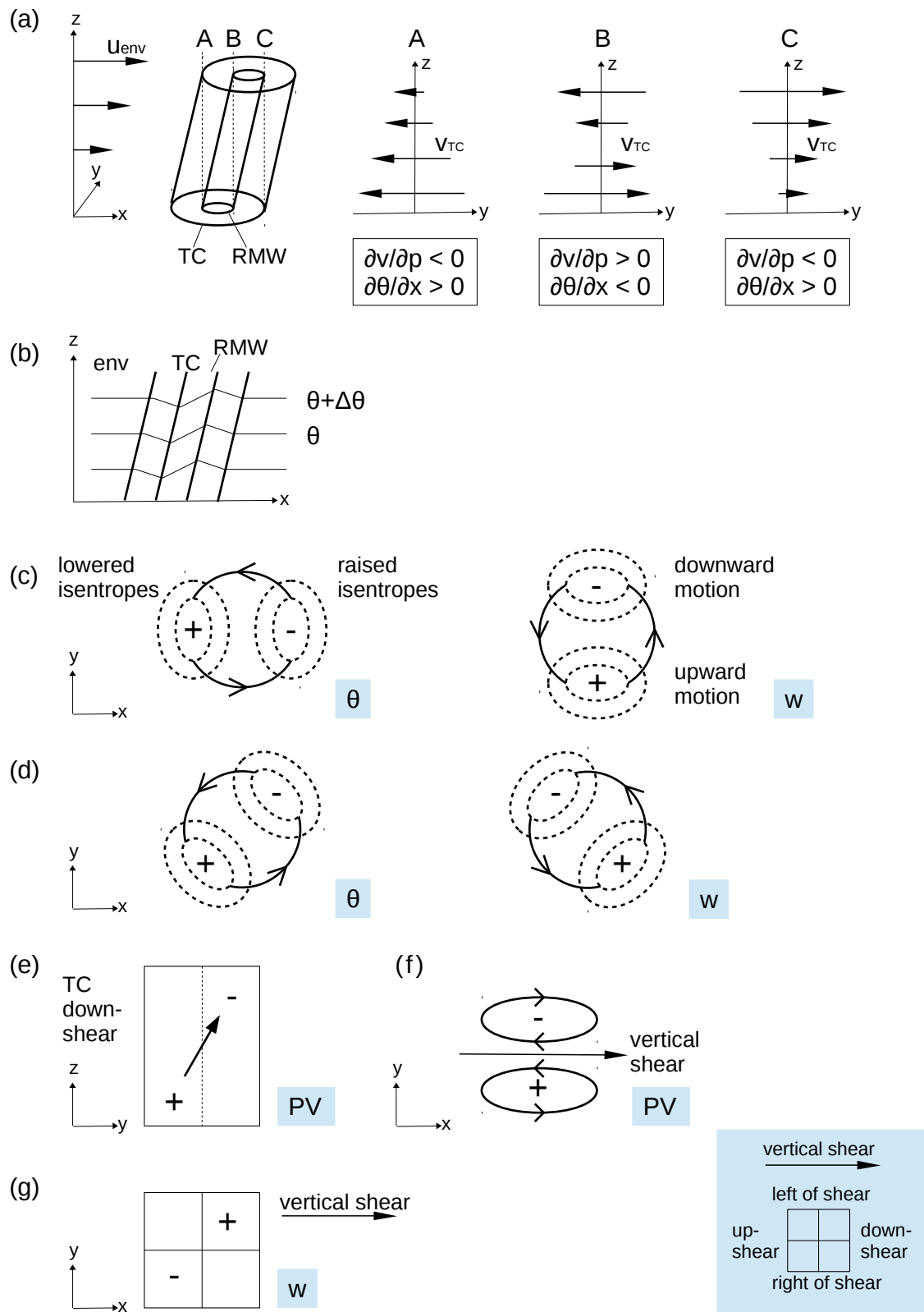


Figure 2.13. – Schematic representation of the structural change of a cyclonic vortex in environmental vertical wind shear (u_{env}). Modification of the cyclonic motion (v_{TC}) results in positive (+) and negative (-) anomalies of θ , w and PV in case of (a,b,c,d) dry dynamics (based on Jones (1995), Fig. 4) and (e,f,g) moist dynamics (based on Wang and Holland (1996), Fig. 9).

and depth of the shear and characteristics of the vortex. The tilt increases with increasing shear, and if the shear is less than about 20-25 m/s the vertical mass flux is proportional to the magnitude of the shear (Davis et al., 2008). Values of 15-20 m/s are typical for ET and therefore the vertical mass flux is enhanced, which influences the development and predictability of ET. When shear reaches values above about 20 m/s, the vortex is no longer resilient and the circulation decreases.

2.2.2. Baroclinic zone related changes

During the transformation from a tropical to an extratropical cyclone, a major part of the structural changes occurs during the interaction with the baroclinic zone. Cyclones that develop in the midlatitudes also develop along the baroclinic zone. For comparison first the development of an extratropical cyclone will be reviewed, before an overview is given about baroclinic zone related changes during ET.

Structural changes during extratropical cyclone development

The frontal evolution during the life cycle of most extratropical cyclones can be described by either the Norwegian cyclone model (Bjerknes and Solberg, 1922) or the Shapiro-Keyser cyclone model (Shapiro and Keyser, 1990). In this thesis, the Shapiro-Keyser model is most relevant and will be explained in more detail based on Fig. 2.14. (I) An initial sharp temperature gradient represents the polar front, which is a baroclinic zone. An initial disturbance caused the warm air to move northwards and cold air to move southwards, but the gradient exists still along one consecutive line. In this step the Norwegian and Shapiro-Keyser cyclone model are still similar. (II) As the fronts advance north- and southwards, the consecutive line of high temperature gradient breaks, which is called a frontal fracture (in the Norwegian model this fracture is not observed). At the same time the temperature gradients contract, producing stronger fronts. The cold front is now situated south of the cyclone and not in the vicinity of the center any more. The warm front is located to the north and east, still close to the center. (III) The warm front develops cyclonically around the center and forms a so-called bent-back front at the western side of the center. The cold front is oriented perpendicular to the warm front and forms a T-structure, called the T-bone. (IV) When the bent-back warm front advances, it wraps around the center and forms a seclusion of warm air that is warmer than the cold surrounding air. The warm seclusion is not a remnant of the warm sector but develops within the baroclinicity of the polar air and may be cooler than the warm sector. In the mean time, the cold front exists to the east of the cyclone center. The exact course of development is very cyclone dependent and takes roughly 1 to 7 days. Most often, a rapid deepening occurs after the frontal fracture, between step II and III, and the cyclone has its maximum intensity either at step IV or between step III and IV.

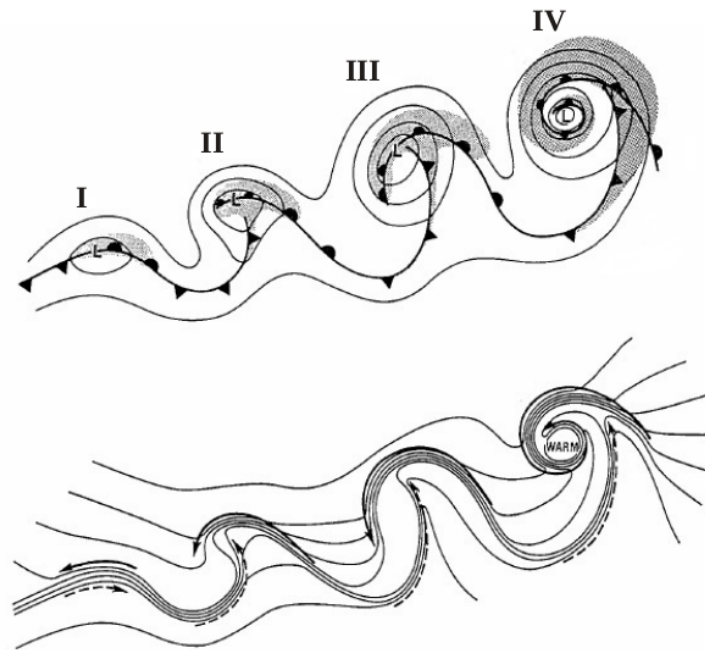


Figure 2.14. – Schematic representation of the frontal evolution of a marine extratropical cyclone. Upper: sea-level pressure (solid lines), fronts (bold lines) and cloud signature (shaded). Lower: temperature (solid lines) and cold and warm air currents (solid and dashed arrows respectively). (I) incipient frontal cyclone, (II) frontal fracture, (III) bent-back warm front and frontal T-bone, (IV) warm-core frontal seclusion. Reprinted from Shapiro and Keyser (1990) © American Meteorological Society. Used with permission.

Within a classical extratropical cyclone, multiple synoptic- and meso-scale air flows can be distinguished accompanied by ascending and descending motion. On the synoptic scale, equatorward moving descending air is found west of the cyclone and poleward ascending air is found to the east. Both air flows split into an anti-cyclonic and cyclonic branch (Thorncroft et al., 1993). The descending air is relatively dry and forms a so-called dry slot or dry intrusion (DI in Fig. 2.15). The ascending air is present in the warm sector ahead of the cold front and transports warm moist air from the boundary layer over the baroclinic zone of the warm front towards the upper troposphere. It is also called a warm conveyor belt (WCB). Clouds are formed during the ascent where the cyclonic branch wraps around the cyclone and forms a cloud head over the bent-back warm front (Fig. 2.15). In the conveyor belt model of Carlson (1980) a third airflow is present, called the cold conveyor belt (CCB). The CCB starts in the cold sector along the warm front. It also consists of two branches (Schultz, 2001). One branch originates in the mid-troposphere, ascends to jet level and turns anti-cyclonically. The other branch originates and remains in the lower troposphere, turning cyclonically around the low pressure center.

The focus here lies on the cyclonic branches that wrap around the cyclone center, as given in Fig. 2.15. The CCB and DI both originate in the midlatitude air. The DI is, however, descending and present on a higher isentropic surface, while the

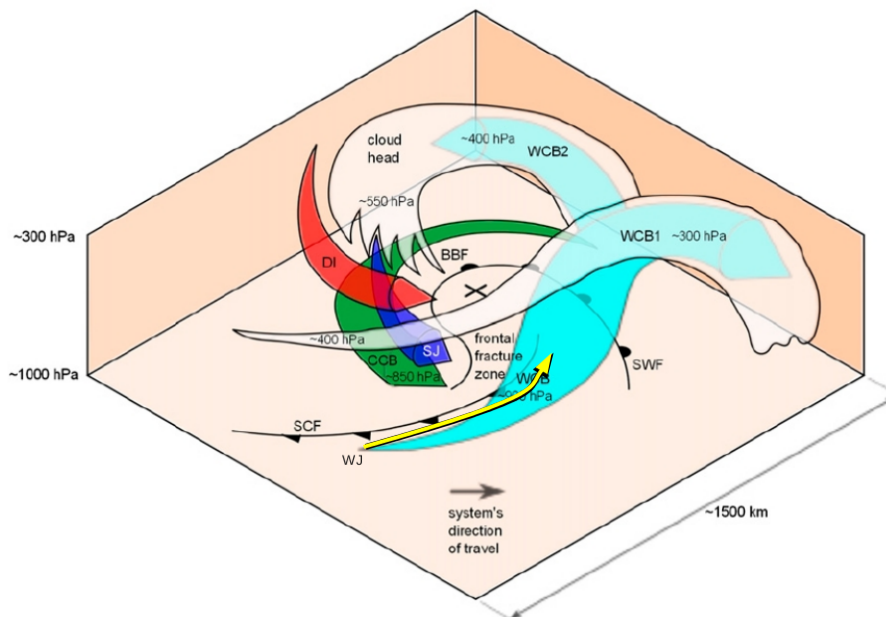


Figure 2.15. – Schematic representation of a Northern Hemisphere Shapiro-Keyser cyclone at stage III, with its surface center marked by X. The following features can be identified: a surface cold front (SCF), surface warm front (SWF), bent-back front (BBF), cold conveyor belt (CCB), sting jet (SJ), dry intrusion (DI), WCB anticyclonic branch (WCB1), WCB cyclonic branch (WCB2) and a warm jet (WJ). Clouds are represented by the white shading. Reprinted and adapted from Martínez-Alvarado et al. (2014) © American Meteorological Society. Used and adapted with permission.

CCB is either moving horizontally or slightly ascending and present at a lower isentropic surface that can possibly intersect the ground in the warm sector (Martínez-Alvarado et al., 2014). On the meso-scale, frontal structures give rise to a horizontal along-frontal flow and vertical motion across the front. In case of frontogenesis, the gradient in temperature increases over time. According to semi-geostrophic theory a direct vertical circulation can be expected with rising air at the warm side of the front and sinking air at the cold side. During frontolysis (negative frontogenesis), the temperature gradient decreases and a thermally indirect circulation is observed. Warm air sinks and cold air rises.

Within a Shapiro-Keyser cyclone there are two regions of lower tropospheric wind maxima and three mechanisms that are responsible for the high wind speeds. The first region is the warm conveyor belt jet (WJ), in the warm sector along the cold front (yellow in Fig. 2.15). Hewson and Neu (2015) mentioned two mechanisms for the elevated wind speeds in the warm sector. In the first place the isobars are relatively straight, due to which the wind speed can come close to the geostrophic wind. Secondly, the horizontal thermal gradients (south of the front) are relatively small. Therefore, only little vertical shear is expected according to thermal wind balance. This implies that if the upper-level jet is strong, the lower-level jet can be strong as well. This occurs often during step I-III in the Shapiro-Keyser cyclone model, when the extratropical cyclone has its largest translation speed.

The second region of strong low-level winds is found in the cold sector along the warm front and bent back front. The highest baroclinicity is found in the bent-back front, which slopes radially outward with height. The highest wind speeds are found below the bent back front. Two different air streams can be identified that both end at the same region: the cold conveyor belt jet (CJ) and the sting jet (SJ). The CJ follows the CCB (green in Fig. 2.15) and has its maximum wind speeds in the order of 40 - 50 m/s just above the boundary layer (e.g. Martínez-Alvarado et al., 2014). When the cyclone evolution continues, the cyclone widens and horizontal thermal gradients decrease. The CJ therefore becomes wider as well and it decreases in strength. The CJ is characterized by saturated air (e.g. Martínez-Alvarado et al., 2014; Smart and Browning, 2014) that slowly ascends from the boundary layer (e.g. Martínez-Alvarado et al., 2014).

The SJ is an exceptionally strong wind that develops suddenly (within a few hours) and occurs for only a short period (few hours) over a relatively small horizontal distance (~ 20 -200 km) (e.g. Browning, 2004; Clark et al., 2005; Hewson and Neu, 2015). The SJ develops between the bent back front and the cold front, often around the period of maximum deepening in step III of the Shapiro-Keyser model. Two characteristics of the SJ air in comparison to the CJ are the subsaturated air that descends from the cloud head at the end of the bent back front towards lower altitudes. The descending air brings high-momentum air from the upper troposphere towards the lower troposphere. As a mechanism for the descent, Schultz and Sienkiewicz (2013) hypothesized the indirect vertical circulation of frontolysis at the end of the bent back front. Frontolysis would at the same time explain the ascending motion of the CJ in the cold sector. The SJ is present at the leading edge of the CJ and often above the undercutting CJ (blue in Fig. 2.15). Although it is possible to see all three low-level jets within one cyclone, they are not necessarily all present. During many wind storms over land, the damage can often be linked to only one of the three jets (Hewson and Neu, 2015). The CJ is the most common of the three, the WJ is fairly unusual and the SJ is rare.

Structural changes observed during ET

When a tropical cyclone vortex impinges on a baroclinic zone, the most remarkable structural change is the development of a frontal structure, similar to Fig. 2.11. The frontal structure is accompanied by an asymmetric field of vertical motion, temperature, moisture and precipitation. The warm frontal region is especially well pronounced during ET, due to the horizontal deformation of the temperature field by the movement of the TC (Harr and Elsberry, 2000). In the cold sector, the deformation field and sinking motion contribute to frontolysis and thereby suppress the cold front (Harr and Elsberry, 2000). The frontal evolution can develop in several ways. Kitabatake (2008) distinguished three types of frontal development: seclusion-occlusion (35%), open wave (52%), and cold advection (13%). During the cold-advection-type development, a TC moves towards a pre-existing front and relatively straight upper-level jet stream. The TC rapidly loses its tropical characteristics due

to cold air advection. The structural development of an seclusion-occlusion-type is similar to a Shapiro-Keyser cyclone. Cyclones of this type are often more intense and move relatively northward. The open-wave-type is most common (12 of 23 TCs) and shows characteristics of both the seclusion-occlusion-type and cold-advection-type (Kitabatake, 2008).

ET systems of the seclusion-occlusion-type retain part of their tropical characteristics and contain a warm core seclusion. Hart et al. (2006) also found a warm core seclusion in 30% of their examined ET cases (6 of 21) with the use of the cyclone phase space. The cyclones did not necessarily re-intensify, but could also weaken during warm core seclusion. A difference of the ET warm core seclusion is that where the Shapiro-Keyser warm core seclusion developed within the baroclinic polar air, the seclusions of, for example, Hurricanes Lili (1996) and Sandy (2012) developed by encircling cold air around a steady pre-existing warm inner core (Browning et al., 1998; Galarneau-Jr. et al., 2013). The cold air increased the potential temperature gradient and caused frontogenesis. Subsequently the tangential wind speeds increased (Galarneau-Jr. et al., 2013). The seclusion of Hurricane Iris (1995) showed a warm core throughout the troposphere, with an overlapping profile of relatively high and well mixed equivalent potential temperature, representing deep convection (Thorncroft and Jones, 2000). The deep convection maintained the warm core in a similar way as a tropical cyclone does. Enhanced convection can also be found in the form of convective bursts along the baroclinic zone due to rising motion in a potentially unstable environment (see Fig. 2.9). It is argued that these burst are important in the maintaining of the diabatically produced PV tower (Agustí-Panareda et al., 2004).

During the interaction with the baroclinic zone the wind field expands. This occurs at the same time as cooling inside the RMW is observed, and is similar but opposite to the effect of contracting eyewalls in intensifying TCs (Evans and Hart, 2008). Typically, the strongest winds are found right of the track during ET. Nevertheless, near Japan, a "U"-shaped pattern of strongest winds is sometimes found, with maxima to the left-of-track as well (Fujibe and Kitabatake, 2007; Kitabatake and Fujibe, 2009; Loridan et al., 2014). The increased left-of-track wind can, for example, be a result of VWS dynamics (Uhlhorn et al., 2014) or channelling between the cyclone and orography (Mashiko, 2008). Considering the vertical wind field, subsidence is enhanced at the upshear side of the cyclone and adiabatic sinking produces a second warm anomaly at this side. The area of sinking might even extend as a column through the entire troposphere when convergence between the environmental flow and the cyclone circulation mechanically force subsidence (Ritchie and Elsberry, 2001, their Figs. 14d and 17c). The structural changes of both the horizontal and vertical wind fields are not fully understood yet, and will be analysed in more detail in this thesis.

2.2.3. Topographic influences

ET often occurs over an ocean where SST, VWS and the baroclinic zone are dominant factors that influence structural changes. TY Sinlaku, however, moves close to Japan. Therefore mechanisms related to topography will play a role as well. Most topography-related research is based on landfalling TCs, and therefore first a review of TC-related studies is given. Topography, which can be distinguished in an effect by the land-sea contrast and orography, has an influence on both the TC structure and the TC motion. Over the ocean, the primary mechanism for TC motion is the advection of the TC's relative vorticity by the environmental horizontal flow (Chan and Kepert, 2010, and references therein), referred to as 'steering'. Nevertheless, all tracks deviate poleward compared to the direction of the steering flow. This effect is caused by the advection of relatively high planetary vorticity on the poleward-west side by the TC circulation (Chan and Kepert, 2010, and references therein), called the beta-effect. Additionally, the effect of diabatic PV creation in deep convection has to be added to the effect of advection of relative and planetary vorticity, in order to get a good approximation of the TC motion Wu and Wang (2000). Irregularities in the convection pattern in a TC, for example due to a small VWS by the steering flow, lead to variations in the location of maximum PV, and may explain irregular track changes, especially for slower moving cyclones (Chan et al., 2002). The effect of diabatic heating is of great importance for landfalling cyclones also, as explained next.

Land-sea contrast influencing the TC structure

When a TC vortex impinges on land, it experiences two things in particular: a higher roughness and a lower moisture supply. Moisture serves as a transporter of potential energy, the fuel of the TC engine. So a reduction of moisture supply in the first place affects the cyclone intensity. Even small areas like a river delta can have a positive effect on the moisture supply and TC intensity (e.g. Au-Yeung and Chan, 2010). Second, if a cyclone approaches land, dry air from land is transported offshore by the vortex circulation and advected upwards (Chan and Liang, 2003). When dry air moves over moist air, this reduces the moist static stability on the offshore side and convection and cloud activity is expected. Precipitation was indeed found downstream of the reduced stability. So, a change in moisture fluxes near land influences the asymmetric vertical motion pattern (Chan and Liang, 2003).

If a TC is partly over land and partly over the ocean, the difference in surface roughness has a dominant effect on vertical motion asymmetries, compared to moisture supply Wong and Chan (2006). The mechanism behind it exists of four steps (Wong and Chan, 2006). (1) Due to friction, wind velocity over land is reduced compared to over sea. This induces convergence in the boundary layer at the onshore side, and divergence on the offshore side, with accompanying rising and sinking motion, respectively. (2) Above the boundary layer, in the upper and lower troposphere,

an opposite response pattern is found with divergence (convergence) and an anti-cyclonic (cyclonic) gyre at the onshore (offshore) side, that steer the cyclone. The orientation of the large-scale gyres, and therefore the steering flow in the absence of environmental flow, depends on the orientation of the coastline (Szeto and Chan, 2010). (3) The signal of the large-scale relative vorticity asymmetry due to divergence is similar in the lower and upper troposphere, but different in magnitude, which causes vertical wind shear. (4) The vertical wind shear finally induces an asymmetric pattern of vertical motion, with convection at the landward side, which can also be related to the location of maximum rainfall (Li et al., 2014). Additionally, the asymmetry in vertical motion induces differential diabatic heating, with a maximum PV production at the landward side. Similar to TC motion over the ocean, a motion vector is present in the direction of the maximum PV over land (Wong and Chan, 2006). So, differential friction causes asymmetries in the cyclone structure and cause the TC to move towards land in the absence of environmental flow (Wong and Chan, 2006; Szeto and Chan, 2010).

A combination of the moisture and roughness effects was found by Li et al. (2015) in their high resolution idealized experiments. In the outer core region (~ 100 -300 km from the center) rainfall over the ocean is induced by the dry air flow from land, while rainfall over land develops by differential friction. The inner core (within ~ 100 km from the center) has an asymmetric rainfall pattern with stronger rainfall over land, developing only when the core experiences the rough surface (Li et al., 2015).

In the previous discussion, no environmental flow was present. When a weak environmental wind shear is added to a landfalling cyclone experiment, this strongly influences the inner core. The storm-scale vertical wind shear changes continuously due to changes in the wind field by asymmetric diabatic heating. Inner core rainfall follows the VWS on the downshear-left side (Li et al., 2015), as was found in the VWS experiments discussed in Section 2.2.1. In the presence of environmental VWS, differences in roughness are of less importance to the inner core structure. The outer core, however, is strongly influenced by the surface roughness, and affected by VWS first after landfall (Li et al., 2015). For ET, when a strong environmental background flow is present and the TC circulation is broadening, the effect of land has not yet been investigated.

Orographic influences on the TC structure

Orography can be regarded as barrier that blocks the lower-level air flow. Air parcels of a TC or a larger scale air mass either need to flow over the barrier or around it. As a consequence, the orography influences both the track (e.g. Chang, 1982) and structural changes of a TC. The magnitude of orographic blocking depends among others on the type of barrier and the velocity and stability of the atmospheric flow. For a TC near the Taiwan mountain range, strong orographic flow blocking gives a southward deflection, while a weak blocking gives a northward deflection (Lin et al., 2005). In addition, steep mountains give a stronger blocking and subsequently a

discontinuous track (Lin et al., 2005; Wu et al., 2015). Next to topography characteristics, also the structure, size, intensity and translation speed of a TC can influence the interaction of the cyclone with the blocking orography (Yeh and Elsberry, 1993; Jian and Wu, 2008). Rapid moving storms experience in general less track deflection, because the time during which the mountains exerts an impact on the cyclone is reduced (Yeh and Elsberry, 1993).

When a TC approaches an orographic barrier, several changes in the structure occur. Apart from orographic lifting, Tang and Chan (2014) distinguished three other mechanisms concerning asymmetric vertical motion, divergence and diabatic heating. A fourth mechanism occurs when the cyclone is about to make landfall and especially influences the horizontal wind field. (1) When a TC is about 2-3° removed from the barrier, dry air from the land is advected from the outer circulation cyclonically inward, until it reaches the inner core at the onshore side. This drier side experiences a reduced amount of latent heat release and can therefore not sustain its strong vertical motion in comparison to the still moist offshore side of the inner core. An asymmetric vertical motion pattern develops and subsequently an asymmetric divergence pattern in the boundary layer. (2) Moving closer to land, the TC's wind field between the orography and the core (about 1.5-1.0° distance between them) is forced to flow parallel to the orographic barrier. At the same time, the larger scale outer circulation flows cyclonically over the mountains. When it arrives at the offshore side, positive PV is induced by stretching of the air column, which causes a cyclonic deflection of the outer flow towards the core. The two flows enhance convergence at the offshore side, affecting the asymmetric vertical motion and diabatic heating pattern. (3) Close to orography, just before landfall (<0.5°), the mechanism is relatively similar to (2) but at a smaller scale and closer to the core. Downslope winds at the offshore side turn cyclonically due to stretching and converge with the orography-parallel flow at the landward side. The convergence now moves cyclonically inwards and is present in the core. (4) When the cyclone is about to make landfall, the flow parallel to the orography has accelerated, and the strongest winds are found at the landward side. This is also called channelling.

ET-related orographic influences

ET most often occurs over the ocean. Nevertheless, the transition can also take place near land and orography, like Japan, New Zealand and the United States east coast. For storms over the Atlantic, Hart and Evans (2001) found enhanced precipitation rates due to upslope winds at the eastern side of the Appalachians, when recurving TCs move along the eastern side. The heavy precipitation, related to Cyclone Bola (1988) in New Zealand, was enhanced by orographic lifting of warm moist air (Sinclair, 1993). Orography however, does not always play a key role in heavy precipitation development. The large-scale atmospheric circulation and frontogenesis are of importance as well. In the case of Hurricane Floyd (1999), for example, the Appalachian mountains had only a minor effect on the heavy precipitation in the coastal areas (Colle, 2003). Also during the ET of TY Peter (1997), that

moved parallel to the mountains on the Japan main island Honshu, the precipitation was dominated by the interaction with the midlatitude environment (Ritchie and Elsberry, 2001).

In midlatitude areas, mountain barriers can also have an influence on the distribution and blocking of colder and warmer air masses. For example cold-air damming (Lackmann, 2011, Chapter 8) east of the Appalachians can enhance precipitation during ET as well (Jones et al., 2003). Tropical Storm Agnes (1972) is a well described example of high precipitation rates along the eastern Appalachians (DiMego and Bosart, 1982a,b). This precipitation was enhanced by cold-air damming (Bosart and Dean, 1991). A similar situation occurred for Tropical Storm Marco (1990) and Hurricane Floyd (1999) (Srock and Bosart, 2009; Atallah and Bosart, 2003, resp.). Nevertheless, documented case studies of ET near land mainly mention enhanced precipitation due to forced ascent along an orographic barrier. Not much is known about the effect of orography on structural changes of the transitioning cyclone.

2.3. Challenges in modelling ET

In the previous two sections it is seen that the processes that take place during ET are complex and that interactions of processes take place on different horizontal scales. In this section the focus lies on the simulation of these processes in a numerical weather prediction (NWP) model. It is important to model ET well in order to properly forecast the associated high impact weather. Still, ET is related to large forecast errors. This is due to multi-scale flow interactions and non-linear error growth. Small errors in the initial conditions or parametrisation can rapidly develop to large errors and consequently make the forecast unreliable. Many cases of ET with a low forecast skill have been studied by the use of hindcasts and ensembles, and the reason for the bad predictability has been documented. Most authors focus on only one or a few elements that are important for the predictability. A conceptual overview diagram is developed here (Figure 2.16) to summarize the challenges from a model perspective. The diagram shows the relations between model properties during initialization (blue area) and relevant dynamic couplings at large- (green area) and meso- to small-scales (yellow area). The arrows symbolize the direction of error-propagation within the model and are discussed in more detail below.

2.3.1. Initialization of the model

Two types of NWP models can be distinguished: global models and limited-area models. Despite ongoing technical progress, operational global models still have resolutions that are too coarse for a proper representation of the tropical cyclone. So there are severe limitations on the ability of a global model to produce a proper interaction between different horizontal scales. The limited-area model can be used at a higher resolution and has the possibility to represent smaller scale processes

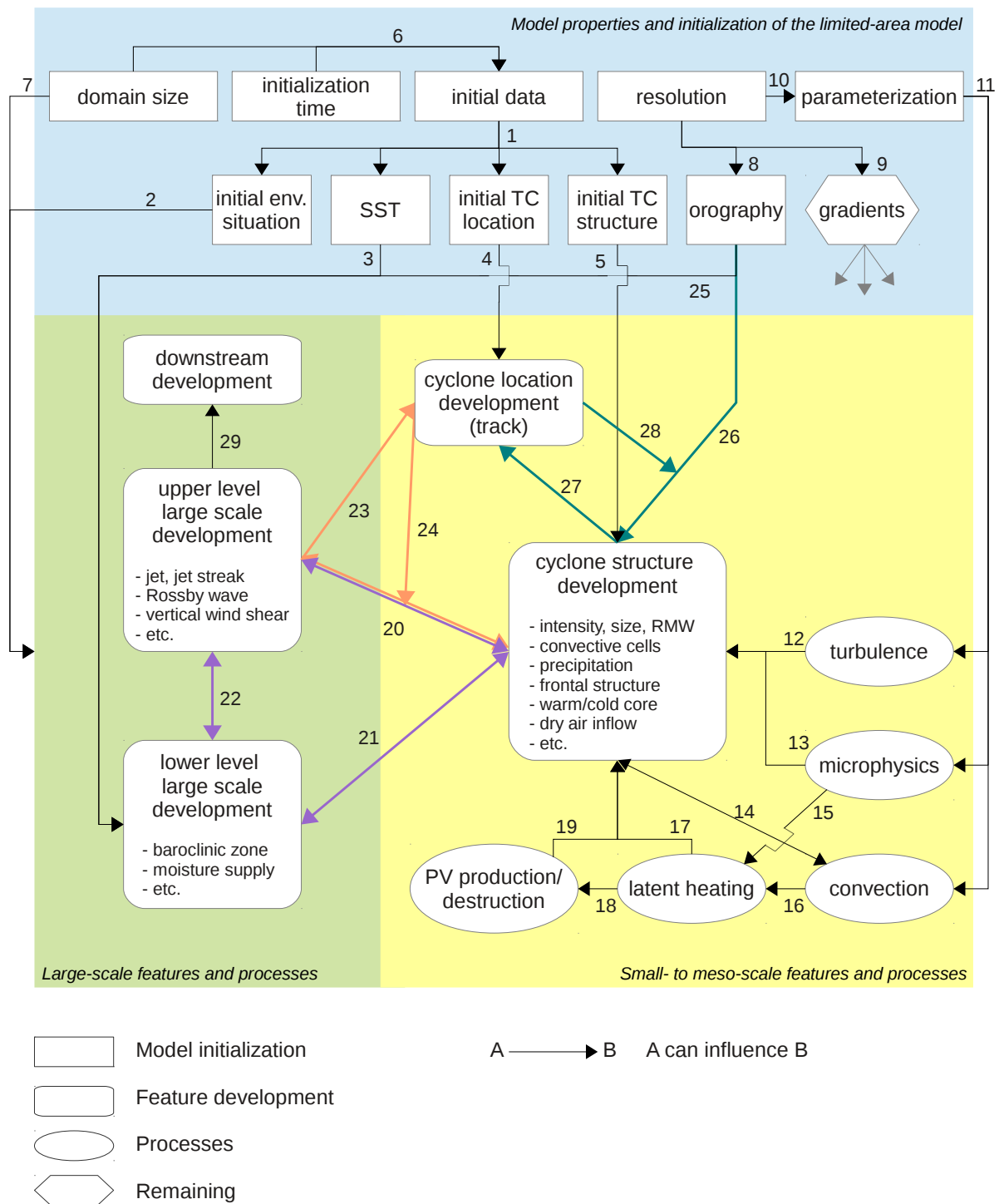


Figure 2.16. – Schematic overview of model error propagation during ET, between the model properties and initialization (blue area), large- (green area) and meso- to small-scale (yellow area) features and processes. The arrows represent the coupling between two objects (model initialization, feature, process or remaining objects) and the direction of error propagation. The arrows are discussed in the text and referred to by the associated numbers. Coloured arrows form a feedback process (explained in the text) and the grey arrows that emerge from the 'gradients'-object apply on the representation of all features in the model.

relatively well. The conceptual diagram (Fig. 2.16) therefore focuses on a limited-area model. The disadvantage, however, is the need for initial and boundary data, which still comes from a global model. This gives a first uncertainty (arrow 1). If the TC structure and location, the environmental situation and other initial fields like the SST are misrepresented in the initial data, these errors will propagate and grow, thus influencing various processes throughout the model (arrows 2, 3, 4, 5).

The representation of atmospheric phenomena, like a jet stream, in the global model output or analysis data is dependent on the availability of assimilated observational data. In data-sparse areas, the representation can be unrealistic or an intense meso-scale feature, like a TC, cannot be captured well. When the TC or a jet streak moves closer to a point of observation, the quality of the global model data may increase also. Because this data is used as initial and boundary data in the limited-area model, the initialization time and domain size can, among others, influence the quality of the initial data (arrow 6). Besides, when a model is initialized close to an ET event, errors have less time to develop. This is shown by Anwender et al. (2008), who found a higher predictability when initialization time was closer to the ET event, independent of forecast lead time. An initialization time closer to the ET event also increases the possibility of a good representation of the SST. The SST field is in reality modified by the cyclone that moves over it, but, depending on the model, often not updated during a model simulation. An anomalous SST, and subsequent boundary layer fluxes, can contribute largely to the intensity and wind speed of the cyclone during an ET event (e.g. Fogarty et al., 2006; Magnusson et al., 2014) (arrow 3).

The domain size defines the midlatitude circulation that is present at the borders of the domain (arrow 2). The quality of the upstream midlatitude analysis can be of importance for the skill of the forecast (Ma et al., 2003). A larger domain can for example include an observation that is crucial for a better predictability. On the other hand a larger domain does not necessarily improve a simulation, when erroneous features at the edge of the initial domain propagate through the entire domain over time (Fogarty et al., 2007). The domain size is also important in determining the boundary conditions (arrow 7). A simulation is partly interpolated at the borders of the domain to fit with the prescribed boundary conditions. On a small domain, the midlatitude circulation is therefore determined by the prescribed flow at the borders. On a larger domain, there is more freedom for large-scale features (e.g. Rossby waves) to develop according to the model's physics.

Initial data can be improved in several ways. Data assimilation gives a good representation of the current atmospheric state. However, there is a lack of (multilevel) data over the ocean (Jones et al., 2003) and a single observation in a data-sparse area can have a large impact on the predictability (Torn and Hakim, 2009). The low resolution initial data in general does not represent a cyclone structure well. A way to improve initial data is the insertion of a synthetic vortex, also called 'bogus vortex'. This is an idealized representation of a TC in gradient wind balance, which is inserted in order to improve the initial cyclone structure. This is often applied in

forecasting TC tracks but still discussed for its usage during ET events. Because the bogus structure represents a TC and not a transitioning cyclone it may delay the onset of ET (Jones et al., 2003; Evans et al., 2006). Nevertheless, McTaggart-Cowan et al. (2006); Fogarty et al. (2006, 2007) did find a positive influence of the synthetic vortex insertion on the forecast skill of ET. Also piecewise PV inversion (Section 3.3.1) can modify the initial conditions. To the author's knowledge this tool is up to now only used for sensitivity analyses (e.g. Grams, 2011; Grams et al., 2013b,a; Agustí-Panareda et al., 2004, 2005; Agustí-Panareda, 2008; McTaggart-Cowan et al., 2001, 2004) and not for the purpose of improving initial data for forecasting.

Next to the initial data, domain size and initialization time, one can choose the horizontal resolution of a model. A higher resolution comes with the possibility for stronger gradients of state variables, which influences all dynamic developments in the model (arrow 9). For example, Gray et al. (2014) found a weaker PV gradient for lower horizontal resolutions, with a subsequent weaker Rossby wave development. The chosen resolution also influences constant fields with high horizontal variability, like orography (arrow 8), which is more realistically represented at higher resolution (see also Fig. 3.3). The higher the resolution, the more processes become grid-scale processes and do not need to be parametrized (arrows 10, 11). This is especially relevant for convection, which can be resolved at a horizontal resolutions of a few kilometers. However, high resolutions do not necessarily improve all features of a forecast. For the ET of Hurricane Floyd (1999), a higher resolution overpredicted the amounts of moderate precipitation (Colle, 2003) and although hurricane-force winds were predicted better at high resolution, gale-force winds were predicted better at coarser resolution (Davis et al., 2010). Even at higher resolution, there are still sub-grid scale processes that need to be parameterized like the microphysics and the turbulent transfer of moisture and energy (arrow 11). Nevertheless, in general, a higher resolution is associated with a better representation of the evolution of the atmosphere. An experimental high-resolution version of the ECMWF global model, for example, greatly improved the cyclone intensity forecast during Hurricane Sandy's (2012) ET (Magnusson et al., 2014). Although higher resolution simulations perform better, its usage is limited by the computational capacity. Since during ET small-scale processes interact with larger scale processes a large domain on high resolution would be favourable. This has, however, a high computational cost which is on the limit of present day computational sources. Only a few recent ET studies use a high horizontal resolution ($< 5\text{km}$) with resolved convection. Mostly this is a small ($< 1500\text{ km}$) nested domain enclosing the storm (e.g. Galarneau-Jr. et al., 2013; Fogarty et al., 2006). Only Pantillon et al. (2013) used a large domain ($\sim 12000\text{ km}$ in width) on 4-km resolution, including the large-scale downstream development.

2.3.2. Multi-scale interactions

After initializing the model, it is assumed that some uncertainties in the representation of features like the jet stream and the TC are present. Errors that do not dissipate during the first hours of model simulations have the possibility to grow.

Due to the interactions between several horizontal scales, growing errors are able to propagate between small- to meso-scale features and processes, including the cyclone itself (200-1000 km diameter) and larger scale features (> 2000 km diameter). The green and yellow areas in Fig. 2.16 show possible interactions along which errors in the model can propagate and grow. The three main dynamic interactions are between the large-scale lower and upper troposphere and the structure of the cyclone (purple arrows). For example ageostrophic outflow of the storm influences the jet stream (arrow 20), the jet influences the VWS which changes the storm structure (arrow 20), the boundary layer serves as a supplier for warm moist air (arrow 21), the cyclonic movement disturbs the configuration of the baroclinic zone (arrow 21) and the lower and upper troposphere can interact according to the thermal wind balance or influence each other during cyclogenesis (arrow 22).

For convenience, internal processes that can alter the structure are not considered in Figure 2.16, except for processes that are parametrized (dependent on resolution) and for the production and destruction of PV by latent heat release (arrow 18). The latter influences the divergent outflow of low-PV air and alters the midlatitude circulation (Section 2.1.2) (arrows 19, 20)¹. This is of special interest because here sub-grid scale processes influence the large-scale flow and potentially the downstream development (arrow 29). Errors in the diabatic processes of the model can alter the Rossby wave structure and propagate downstream (Gray et al., 2014) with the group-speed of the Rossby wave train (Pantillon et al., 2013) (arrow 29). Not only the (either parametrized or resolved) convection (arrow 16) is of importance for the location and quantity of latent heating, also the parameterized microphysics (arrow 15) plays a role in this process (e.g. Joos and Wernli, 2012; Pantillon et al., 2013). Microphysical processes (e.g. condensation, evaporation of rain, sublimation or depositional growth of snow), latent heating and turbulent interactions also alter the cyclone's temperature, moisture and precipitation field and determine the formation of clouds (arrows 12, 13, 17). Convection, furthermore, modifies the kinematic cyclone structure by updrafts and downdrafts (arrow 14). The cyclone structure on its turn determines areas with vertical instability and a potential for convection (arrow 14).

The cyclone track as a source of error growth

The track of a cyclone is, next to intensity, the main focus in TC forecasting because it states where severe weather warnings should be given. However, the cyclone location is a point in space and time and can not interact with other objects. Nevertheless, the track is important because it influences the interactions between two objects, and in return is influenced by objects. The most well-known example is what in literature is often called the TC-jet interaction or phasing with the jet (orange arrows). It determines whether the cyclone re-intensifies or decays (section

¹Although most literature directly refers to the link between low-PV outflow that influences the upper-level large-scale development, the low-PV air is here regarded as part of the tropical cyclone (arrow 19) that subsequently influences the large-scale flow (arrow 20)

2.1.2). The location of the storm relative to the jet influences the way the storm and jet interact (arrows 24, 20). The jet is on its turn considered as the dominant factor in the steering flow that transports the cyclone (arrow 23). This feedback mechanism together with the presence of a bifurcation point (section 2.1.2) makes the TC-jet interaction sensitive to errors in the track. The initial position of the storm (arrow 4) can already be crucial for the development of both the cyclone and the large-scale flow (e.g. Grams et al., 2013a, 2015).

The influence of complex terrain on model performance is taken into account in Figure 2.16 as well, although not much is known about the actual influence of orography on ET. Most knowledge is gained from the interaction of TCs with orography. Next to the flow blocking of low-level air masses (arrow 25), orography also modifies the cyclone structure (arrow 26) and the modified storm can alter the track (arrow 27) (section 2.2.3). Although changes in the track due to orographic interactions are assumed to be small in comparison to the steering by the jet stream, it may cause a difference that is sufficient to move the storm to the other side of the bifurcation point. The location of the cyclone relative to the orography influences the effect that the orography has on the storm (arrow 28). In literature this is often called the typhoon-topography interaction (turquoise arrows). A change in the initial TC structure (size, strength, arrow 5) influences the typhoon-topography interaction and can therefore cause a different track (Wu, 2001; Wu and Wang, 2001). At higher resolutions the typhoon-topography interaction and simulation of the track deflection is improved due to a better representation of terrain height (Huang et al., 2011).

Examples of complex model error propagation

It will now be shown how an initial error can propagate through the conceptual diagram to cause an unrealistic simulation. To do this, a few studies are chosen as an example and relevant arrow numbers in these studies are listed in Table 2.1. Pantillon et al. (2013) found that due to a wrong initialization of the storm and

Paper	Consecutive arrows of error propagation
Pantillon et al. (2013)	2 + 5 + 10, 11, 15, 16, 18, 19 → (20, 23, 24, 20) → 29
Torn et al. (2015)	5 → (14, 16, 17, 14) + 18, 19 → (20, 23, 24, 20)
Prater and Evans (2002)	11 → 14, 20, 23
Torn and Hakim (2009)	2 → (20, 23, 24, 20) 2, 22, 21
Huang et al. (2011)	8 → (26, 27, 28, 26)

Table 2.1. – Examples of model error propagation. The numbers refer to the arrows in Figure 2.16. A + adds errors, a comma gives consecutive errors and numbers in brackets are a positive feedback of errors. The black arrows in this table divide cause and result, as stated in the literature at the left side.

its environment, and due to resolution and parameterizations, the PV production was altered and the TC-jet interaction was modified. Consequently the downstream development was not predicted well. Torn et al. (2015) added the influence of a decreased vertical motion and latent heating due to initial conditions, which in return weakened the vertical motion. Prater and Evans (2002) investigated the role of convection parameterization that influenced the vertical structure in the storm and thereby the TC-jet interaction and track. The predictability of the phasing between the TC and the jet is hypothesized to be dependent on the speed of the westerly flow (Torn and Hakim, 2009). In faster flow, small initial errors in the TC-jet orientation grow faster than in slow flow. Besides, an ET forecast is also sensitive to the the initial phasing between a 500-hPa trough and a downstream surface cyclone that modifies the low-level temperature field in the ET region and consequently alters the cyclone intensity (Torn and Hakim, 2009). Concerning topography, Huang et al. (2011) experienced a more realistic track deflection when using a higher resolution. The structural changes near complex terrain were represented better and therefore also the typhoon-topography interaction and track.

From Figure 2.16 it can be seen that many processes interact on different scales and these interactions and feedbacks give rise to error growth during the forecast. Not only the TC itself is compromised, but also the environment around the cyclone and downstream of it. Thereby the forecast skill across an entire ocean basin decreases (Jones et al., 2004). The use of ensembles gives a partial solution by generating multiple scenarios (Keller et al., 2011). Another aspect of properly modelling ET which is mainly neglected in the flow diagram is the presence of internal processes. Forecasters often focus on track and intensity changes, but even when the track is good, the structure of the cyclone can be unreliable, including the location of extreme winds and precipitation (Evans et al., 2006). Even with different initial conditions, a similar track with different cyclone structure can be obtained (Fogarty et al., 2006). So, it is still very difficult to properly simulate, and also forecast, ET and additional studies are needed to both model sensitivity and the dynamic understanding of interactions.

2.4. The ET of Typhoon Sinlaku (2008)

This thesis presents a case study of the ET of TY Sinlaku (2008). The focus lies on the structural changes and direct impact during the transformation stage of ET. In this section, an overview of the development of TY Sinlaku is given. Sinlaku was one of the Typhoons that was investigated during THE Observing system Research and Predictability EXperiment (THORPEX) Pacific Asian Regional Campaign (T-PARC) and Tropical Cyclone Structure 2008 (TCS08) field campaigns. One of the objectives of T-PARC was to extend the knowledge about the interaction between TCs and the midlatitude flow and processes that account for structural changes during ET. Measurements from four aircrafts during 28 flights during the entire lifetime of Sinlaku provide a unique dataset for detailed analysis of structural development.

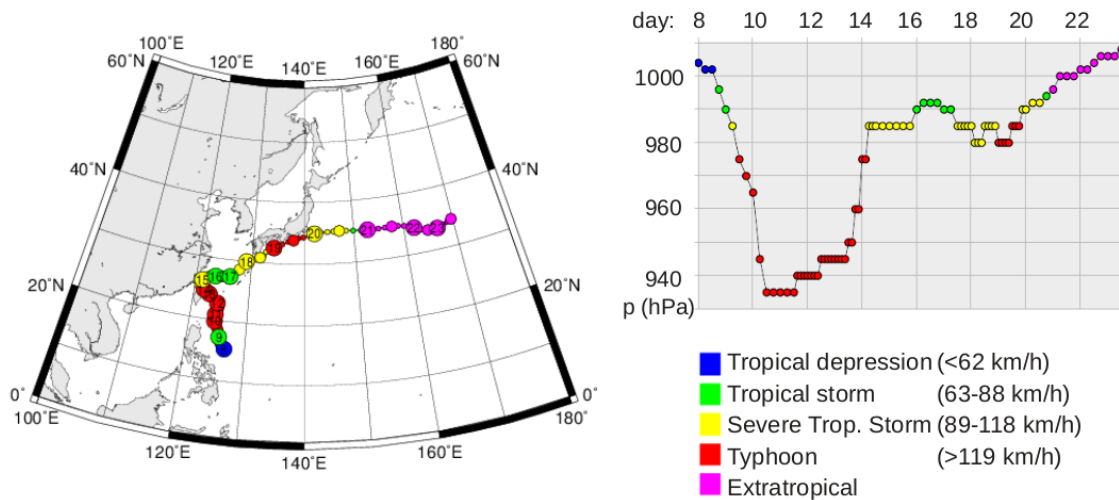


Figure 2.17. – The location (left) and mean sea level core pressure (right) development of TY Sinlaku, from 8 to 23 September 2008. Obtained from <http://agora.ex.nii.ac.jp/digital-typhoon/summary/wnp/s/200813.html.en>.

Sinlaku developed over the western North Pacific and was named by the Japan Meteorological Agency (JMA) on 8 September when the storm was east of the Philippines (Fig. 2.17). The storm rapidly intensified from a tropical depression to typhoon intensity. A pressure fall over 60 hPa occurred within 42 hours and the maximum (10-min mean) wind velocity increased from 35 knots to 100 knots (~ 65 km/h to ~ 185 km/h). The rapid intensification at this time was favoured by a low vertical wind shear, enhanced outflow and a large ocean heat content (Leroux et al., 2013). Details about the structural organisation of convection and the eyewall formation of Sinlaku can be found in Leroux et al. (2013), Huang et al. (2012) and Wu et al. (2012b). The typhoon was advected northwestward, primarily by a subtropical high east of the storm (Wu et al., 2012a), and made landfall at the northern part of Taiwan on 14 September. Most of the northern part of the island experienced over 500 mm of rain within 3 days, with locally more than 1000 mm in the mountains (Wu et al., 2013, their Fig. 4a). During landfall Sinlaku weakened rapidly to severe tropical storm intensity.

After landfall, Sinlaku recurved on 15 September as a tropical storm (Fig. 2.17). The path of recurvature was highly sensitive to the intensity of remote midlatitude short-wave troughs (Komaromi et al., 2011). Between 16 and 17 September a weak Rossby wave was located at the same longitudinal range as Sinlaku, but north of 45°N (Quinting, 2015). Sinlaku was still south of 30°N and had a smaller translation speed than the phase velocity of the Rossby wave. They therefore did not interact at this time and no downstream development occurred (Quinting, 2015). The midlatitude influence was, however, present in the form of strong vertical wind shear that reduced convective activity and contributed to a highly asymmetric structure (Harr et al., 2010). Recurvature, asymmetries and increased vertical wind shear are indications for the transformation stage of ET. Nevertheless, a clear ET was not observed yet and Sinlaku re-intensified instead of completing the transformation stage.

Sanabia (2010) investigated the period directly after recurvature (15-17 September)². The large-scale monsoon flow transported tropical air from the southwest towards the intensifying TC and favoured the development of convection. Observations showed that a re-intensification after landfall was initiated by an interaction of the TC remnants with three meso-scale vortices. Multiple convective bursts arose and rotated cyclonically inward, consistent with axi-symmetrization and thereby tropical intensification. The re-intensification also modified the structure and thereby reduced the predictability of Sinlaku's impact on the midlatitude circulation downstream (Harr et al., 2010). Both the track and structure characteristics contributed to a 'false-alarm' forecast of a significant downstream development (Harr et al., 2010).

Sinlaku continued intensifying on 18 September (Kuo et al., 2012) and reached a secondary peak intensity on early 19 September. With maximum wind speeds of over 65 kt (~ 130 km/h) Sinlaku was classified as a typhoon again. On 19 September between 0000 UTC and 0600 UTC (time is hereafter indicated as dd/hh: 19/00 and 19/06 respectively, in September 2008, where hh is in UTC. In case of measurement data that is not present at the full UTC hour, the format dd/hh:mm will be used.) the research aircrafts Naval Research Laboratory P-3 and the U.S. Air Force WC-130 flew through the core region to obtain measurements of the eyewall. A partial eyewall was present with individual convective cells that formed in the east (downshear region), reached maximum ascent in the northeast (downshear left) and decayed as they travelled cyclonically downstream, with descending motion primarily in the west (upshear region) (Foerster et al., 2014). This pattern represents the impact of VWS on the TC. The environmental flow was southwesterly and increased with height, with a deep layer VWS (850-200 hPa) of 13.4 m/s (Foerster et al., 2014). The primary impact by VWS suggests that Sinlaku was at step 2 of the transformation stage of ET at this time. Satellite imagery is also consistent with step 2 of the conceptual model of ET on 19/00 (Fig 2.18). The cloud structure is asymmetric with an extended cloud region to the northeast.

Sinlaku continued to move close to the southern coast of Japan (Fig. 2.17). On 20 September, Sinlaku started to interact with the midlatitude baroclinic zone (step 3 of the transformation stage). On the satellite image this is seen by the WCB-like structure in the northeast and almost cloudless air at the west side which cyclonically wraps around the center (Fig. 2.18). The eyewall structure is not present anymore. Aircraft measurements were conducted 6 hours later on 20/06, both near the TC core remnants and in the midlatitude outflow region northeast of the storm. At this time a convective burst developed. Quinting et al. (2014) analysed this unique set of observations. Major changes in the structure on 20/06 are dominated by the inflowing midlatitude cold dry air. This air is advected from the north and rapidly descends from 400-600 hPa to about 800 hPa. The descent occurs almost adiabatically and subsequently the midlatitude sinking air becomes warm and dry. This dry

²Note that Sanabia (2010) referred to this period as the re-intensification period. In later sections the term "re-intensification" is explicitly used for the end of 18 September and early 19 September, when Sinlaku reached typhoon intensity again.

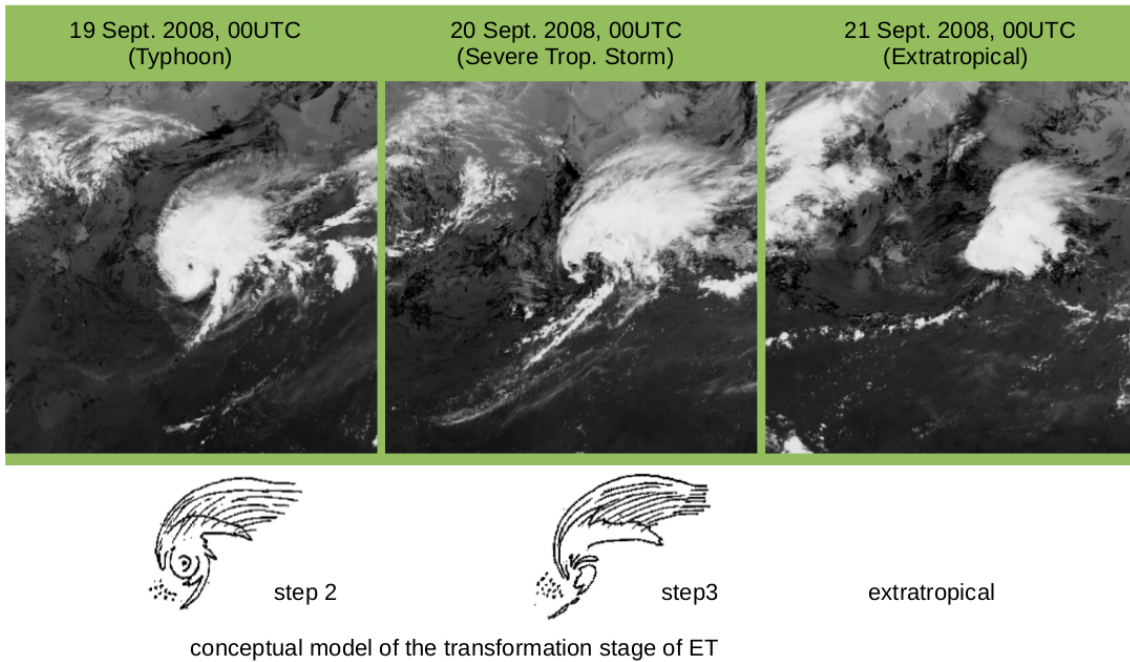


Figure 2.18. – Multifunctional Transport Satellite (MTSAT) infrared channel 4 ($3.5 - 4.0 \mu\text{m}$) imagery at 00UTC at 19, 20 and 21 September 2008 (obtained from <http://agora.ex.nii.ac.jp/digital-typhoon/summary/wnp/i/200813.html.en>). At 19 and 20 September the satellite images are compared to relevant images in the conceptual model of ET from Klein et al. (2000) (see Fig. 2.7).

intrusion ($\theta_e < 330 \text{ K}$) wraps around the center with a leading edge present east of the center. Meanwhile, warm moist air ($\theta_e > 340 \text{ K}$) is transported northwards by the large-scale high pressure system to the south of Sinlaku, and arrives at the eastside of the storm at about 900 hPa. Warm moist air (high- θ_e) is now situated below the dry sinking air (low- θ_e) which gives potential instability in the vertical profile. Quinting et al. (2014) hypothesized that within this potentially unstable environment, the forced ascent over the baroclinic zone triggered the convective burst. At the end of ET, on 21/00, Sinlaku's cloud structure does not exhibit a classical extratropical structure (Fig. 2.18). Sinlaku was rather a cyclonic circulation in the presence of a convective burst.

On the larger scale, the jet stream was split into two branches. Sinlaku was located south of the southern branch that was nearly zonal (Fig. 2.19). To the northwest of Sinlaku, a weak trough is present in the upper troposphere (130°E , 48°N). Analysis of the quasigeostrophic forcing of vertical motion, associated with the trough, showed that they did not produce a favourable environment for re-intensification of Sinlaku (Quinting et al., 2014). To the northeast, a low-level low pressure system and upper-level trough ($\sim 160^\circ\text{E}$) can be identified. This pattern is comparable to the northeast pattern of Harr et al. (2000), which is unfavourable for extratropical re-intensification. Consequently, Sinlaku did not re-intensify as an extratropical cyclone. After several days of continued convective activity Sinlaku finally decayed over the Pacific.

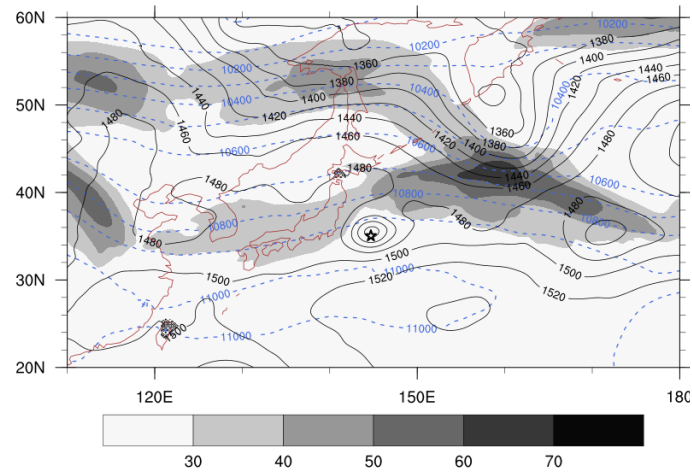


Figure 2.19. – Wind speed at 250 hPa (shaded) and geopotential height at 250 hPa (dashed blue contours) and 850 hPa (black contours) at 20/06. Sinlaku’s location at sea level is marked by a star.

The last part of the transformation stage of Sinlaku (18-21 September) is special because of the unexpected tropical re-intensification and a relatively slow extratropical decay. In addition, Sinlaku moved close to Japan’s orography, without making landfall. The availability of a unique observational dataset makes it an important case study for the analysis of the structural development during the transformation stage of ET.

3. Data and methods

In this chapter the data and methods are described that are used to answer the research questions. First, measurement data from the T-PARC field campaign is described. Most data is publicly available in the T-PARC data archive¹. Secondly, the COSMO model is described, with which all simulations in this study are performed. Thirdly, diagnostic tools are described that will be applied to the simulated data, in order to gain insight in the dynamics of the atmosphere.

3.1. Observational data

3.1.1. Aircraft data

During the T-PARC field campaign three aircrafts were operational and flew in or nearby Sinlaku. These are the United States Air Force Weather C-130J (USAF WC-130J, hereafter called C130), the Naval Research Laboratory P-3 (NRL P-3, hereafter called P3) and the German Aerospace Center Falcon 20E D-CMET (DLR Falcon 20E D-CMET, hereafter called Falcon). During two intensive observation periods, at the beginning of 19 and 20 September, respectively, the aircrafts conducted observations during Sinlaku's ET (Fig. 3.1). At 19 September, the P3 and C130 aircrafts flew near Sinlaku at 3 km and 9 km height respectively (Fig. 3.1), and released GPS dropsondes² that measured standard meteorological quantities like pressure, temperature, humidity and wind speed and direction (Hock and Franklin, 1999). Furthermore, the P3 was equipped with an Electra Doppler Radar (ELDORA, Hildebrand et al., 1996) which provided a high resolution image of the the 3-D wind field. At 19 September around 4 UTC, the P3 flew inside the eyewall of Sinlaku which resulted in a detailed depiction of the structure of Sinlaku's wind field shortly after its tropical re-intensification (Foerster et al., 2014). At this time, the Falcon aircraft was operational in the environment of Sinlaku in order to measure the interaction between the TC and the midlatitudes (Fig. 3.1). The Falcon flew at 11 km height and was equipped with a Doppler Wind Lidar³ (DWL, e.g. Weissmann et al., 2005) and Differential Absorption Lidar⁴ (DIAL, e.g. Harnisch et al., 2011) which

¹<http://data.eol.ucar.edu/>, maintained by the National Center for Atmospheric Research (NCAR) Earth Observing Laboratory (EOL) under sponsorship of the National Science Foundation

²Retrieved from <https://doi.org/10.5065/D6NG4NTS> and <https://doi.org/10.5065/D6HQ3X4X> at 9 April 2013

³Retrieved from <http://data.eol.ucar.edu/dataset/110.083> at 26 September 2013

⁴Retrieved from <http://data.eol.ucar.edu/dataset/110.081> at 26 September 2013

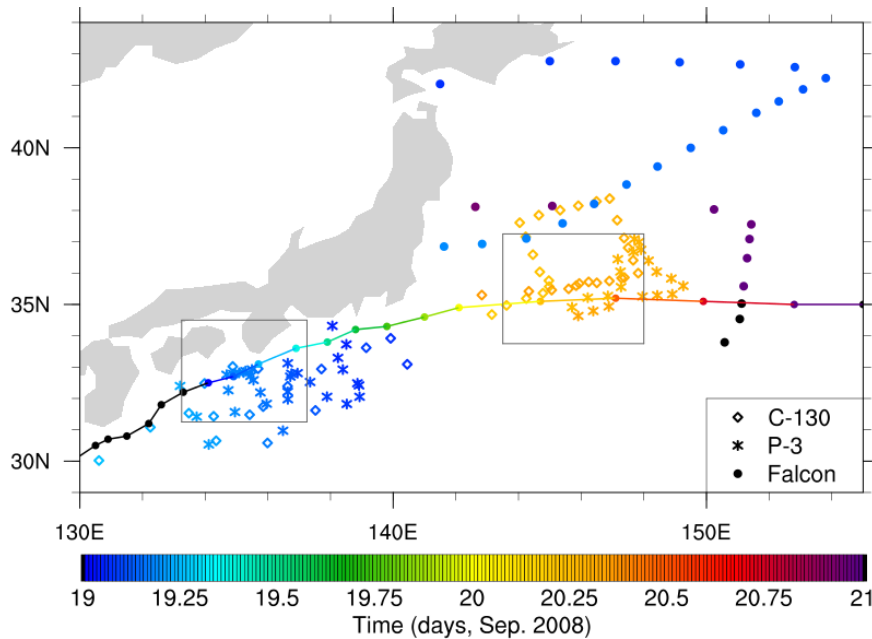


Figure 3.1. – Location of dropsonde release of the C130, P3 and Falcon research aircraft. The C130 and P3 flight tracks had a zig-zag pattern, flying from east to west at 19 September, and a closed quasi-circular pattern at 20 September. The Falcon flew along 2 straight legs at 19 September and around 21/00, starting in the north. The line represents the Best Track of Sinlaku. The colors indicate the time of the dropsonde release, and the time of Sinlaku’s location along the Best Track. The black boxes are the locations of the available SAMURAI data at 19 and 20 September.

provided a vertical profile of wind and water vapour along the flight track below the aircraft. Additionally, also GPS dropsondes⁵ were released. One day later, at 20/00, both the P3 and C130 flew near Sinlaku at 3.5 km and 3 km height respectively (Fig. 3.1). Now, observations were obtained during the interaction of Sinlaku with midlatitude air (Quinting et al., 2014) and again a high resolution image of the wind field was provided by the airborne ELDORA radar. At the end of 20 September and the beginning of 21 September, Sinlaku moved with a high translation away from Japan over the ocean and the Falcon aircraft only reached the western outer circulation (Fig. 3.1).

The observational data is brought to a gridded data set by the use of the Spline Analysis at Mesoscale Utilizing Radar and Aircraft Instrumentation (SAMURAI) software (Bell et al., 2012). This software tool aims to assimilate different sources of airborne and satellite measurement data in order to obtain a best estimate of the kinematic and thermodynamic structure of the atmosphere. P3 radar wind observations, dropsonde wind, pressure, temperature and humidity from the P3 and C130 and atmospheric motion vectors (explained in the next subsection) were assimilated on a background of analysis data, using a cubic B-spline approach. In the end product, the detailed information of the radar-derived wind field is dominant over the

⁵Retrieved from <https://doi.org/10.5065/D6D21VSC> at 9 April 2013

point-information of pressure, temperature and humidity from the dropsondes.

For Sinlaku, the SAMURAI data was available around the two time intervals of intensive observation at 19 and 20 September, as used by Foerster et al. (2014) and Quinting et al. (2014), respectively (Fig. 3.1). In both cases, all aircraft observations within the observation period have a time and space correction to Sinlaku's position. At 19 September, the observations are corrected to Sinlaku's position on 19/04, when the P3 flew in Sinlaku's center. Foerster et al. (2014) chose the 6-hourly analysis data of 19/00 as background, because the specific structure of the storm in the analysis data better resembled the observed structure at that time. But from the SAMURAI end product, they only used the gridpoints where observational data was actually available. For the purpose here, a continuous grid is needed and the location of Sinlaku in the analysis data on both 19/00 and 19/06 did not fit with the location of the observed cyclone at 19/04. Instead, the analysis data closest to the observation time was chosen as background. Additionally, a space correction ($\Delta x = 0.3207^\circ$, $\Delta y = -0.49611^\circ$) was applied to the analysis data, based on the vorticity center at 2 km height. The new SAMURAI data was kindly produced and provided by Annette Foerster and Michael Bell and was available at a horizontal resolution of 5 km and vertical levels every 0.5 km from 0 - 14 km height. At 20 September, the SAMURAI data as in Quinting et al. (2014) was used, with a horizontal resolution of 4 km and vertical levels every 0.25 km from 0 to 15 km. The observations here, were space- and time-corrected to Sinlaku's location at 20/06.

Foerster et al. (2014) and Quinting et al. (2014) used the SAMURAI data to analyse Sinlaku's structure at two specific time steps. Quinting et al. (2014) also highlighted a few differences between the SAMURAI data and the analysis data. In this thesis, the observational based gridded SAMURAI data is used to further verify the analysis data and to verify model simulations. Furthermore, it will be used to improve the data with which the COSMO model will be initialized. Additional details of the SAMURAI technique or the specific SAMURAI data used here, can be found in Bell et al. (2012), Foerster et al. (2014) and Quinting et al. (2014).

3.1.2. Satellite data

Remote sensing via satellites is a globally frequently used technique for a wide range of applications, among which are meteorological products. In this thesis four satellite products are used.

Atmospheric motion vectors (AMVs, e.g. Velden et al., 1997, 2005) are satellite-derived wind data based on upper-level water vapour and infrared imagery. For each type of image, three sequential figures are used. On the second figure, targets are defined, which can be for example a cirrus cloud edge, small cumulus cloud or gradient in water vapour. Based on the location of these targets in the first and third image, two displacement vectors are obtained, which are averaged to give the atmospheric motion vector. AMVs are therefore only available at the height of targets, which is dominated during ET by the edge of the cirrus shield from the

outflowing air. Here, the hourly cloud drift wind data is obtained from the geostationary Multifunctional Transport Satellite (MTSAT) at different wave lengths⁶. The MTSAT is operated by the Japan Meteorological Agency (JMA) and the AMV end product is provided by the Cooperative Institute for Meteorological Satellite Studies (CIMSS).

Surface winds are measured by the SeaWind scatterometer onboard the Quick Scatterometer satellite (QuikSCAT, Ebuchi et al., 2002). The SeaWind instrument transmits microwave pulses (13.4 GHz) to the earth surface and measures the backscattered power. The returned signal has a high correlation with the surface roughness, which over the ocean surface is related to the near-surface wind speed and direction. The radar signal therefore provides information about the cyclone center at the surface, under all weather conditions, at a location where other observations are sparse. The QuikSCAT/SeaWind data (hereafter called Quikscat data) measures over a width of 1800 km, with a horizontal resolution of 25 km. It was available for Sinlaku every 12 hours (at 9 UTC and 21 UTC)⁷ and covers at least part of Sinlaku's circulation at every time step.

The cloud top temperature (CTT) is derived from the MTSAT infrared channel 1 (10.3 - 11-3 μm). Brightness temperature of clouds gives an indication of the cloud top height; the colder the top, the higher the cloud. During ET this is useful in order to identify the location and spatial development of deep convective clouds. The CTT data was available every half an hour at .15 and .45 UTC⁷.

The so-called Best Track of a TC is a product that gives an indication of the location and minimum central pressure of cyclone. It contains all available measurement data, but in the absence of surface and aircraft observations it is based on satellite data. It is an often used source for the analysis of cyclone tracks, and is very useful for estimation of cyclone intensity in a data-sparse region. However, the estimated pressure at mean sea level, which is mainly determined by the Dvorak technique (Dvorak, 1975; Velden et al., 2006), can have a significant bias (Kossin and Velden, 2004). Especially during ET the intensity information is not always reliable. The Best Track of Sinlaku⁸ was complemented with T-PARC observations and is therefore more reliable. Nevertheless, the Best Track data was verified in detail (Appendix A) and it is found to be suitable as reference data for Sinlaku's track and pressure development.

3.2. The COSMO model

In this study the COSMO model is used to simulate extratropical transition. COSMO (CONsortium for Small-scale MOdeling) is a non-hydrostatic limited-area numerical weather prediction model, originally developed at the German Weather Service

⁶Retrieved from <http://data.eol.ucar.edu/dataset/110.028> at 15 July 2015.

⁷The Quikscat and CTT data were kindly provided by the JMA at 18 June 2015.

⁸Retrieved from <http://agora.ex.nii.ac.jp/digital-typhoon/summary/wnp/1/200813.html.en>

("Deutscher Wetterdienst", DWD). It has been used operationally at the DWD since 1999, initially under the name "Lokal-Modell" (LM). Over time, the model was further developed by members of the consortium for small-scale modelling and conform this the name changed to COSMO. More information about COSMO can be found at <http://www.cosmo-model.org>. In this study COSMO version 4.21 is used. First the model structure will briefly be described and afterwards the specific initialisation as used in this study will be explained.

3.2.1. Model description

Basic equations

The COSMO model is based on the primitive hydro-thermodynamical equations which consists of a combination of prognostic and diagnostic equations. This forms a closed set of equations with which the future state of the moist atmosphere can be predicted, based on an initial reference state of wind velocity $\vec{V} = (u, v, w)$, pressure p , temperature T , mass fractions of the different constituents of atmospheric water q_x with $x = d$ (dry air), v (water vapour), l (liquid water), f (frozen water), and density ρ . An overview of the equations, as found in Steppeler et al. (2003), is given here:

Prognostic equations:

$$\text{Equation of motion} \quad \rho \frac{d\vec{V}}{dt} = -\nabla p + \rho \vec{g} - 2\vec{\Omega} \times (\rho \vec{V}) - \nabla \cdot \vec{\tau} \quad (3.1)$$

$$\text{Temperature tendency equation} \quad \rho C_p \frac{dT}{dt} = \frac{dp}{dt} + Q_h \quad (3.2)$$

$$\text{Pressure tendency equation} \quad \frac{dp}{dt} = -\frac{C_p}{C_v} p \nabla \cdot \vec{V} + \left(\frac{C_p}{C_v} - 1\right) Q_h \quad (3.3)$$

$$\text{Humidity tendency equation} \quad \rho \frac{dq_x}{dt} = -\nabla \cdot \vec{J}_x + I_x \quad (3.4)$$

Diagnostic equation:

$$\text{Equation of state} \quad \rho = \frac{p}{R_d \left(1 + \left(\frac{R_v}{R_d} - 1\right) q_v - q_l - q_f\right) T} \quad (3.5)$$

with

$\frac{d}{dt} = \frac{\partial}{\partial t} + \vec{V} \cdot \nabla$	total (Lagrangian) time derivative
$\frac{\partial}{\partial t}$	local (Eulerian) time derivative
$\nabla = \hat{\mathbf{i}} \frac{\partial}{\partial x} + \hat{\mathbf{j}} \frac{\partial}{\partial y} + \hat{\mathbf{k}} \frac{\partial}{\partial z}$	gradient operator
\vec{g}	gravitational acceleration
$\vec{\Omega}$	earth rotation vector
$\vec{\tau}$	stress tensor
C_p	heat capacity for constant pressure
C_v	heat capacity for constant volume
Q_h	diabatic heating
\vec{J}_x	diffusion flux of atmospheric water constituent x
I_x	sources of x
R_v	gas constant for water vapor
R_d	gas constant for dry air

Numerical solution

The partial differential equations 3.1-3.4 can be solved numerically. Therefore the equations are first re-written in horizontal geographical coordinates, and a vertical time-independent terrain-following coordinate. The continuous prognostic equations are then spatially discretized using the Arakawa-C/Lorenz staggering grid (Fig. 3.2). T , p and q_x are defined in the center of a grid box with side lengths $\Delta\lambda$ (longitude), $\Delta\varphi$ (latitude), $\Delta\zeta$ (vertical) and center coordinates i , j , k . The wind vectors are defined on the box sides. The grid forms a rigid lid on the boundaries and propagating wave disturbances are damped near the boundaries, so that they are not reflected back.

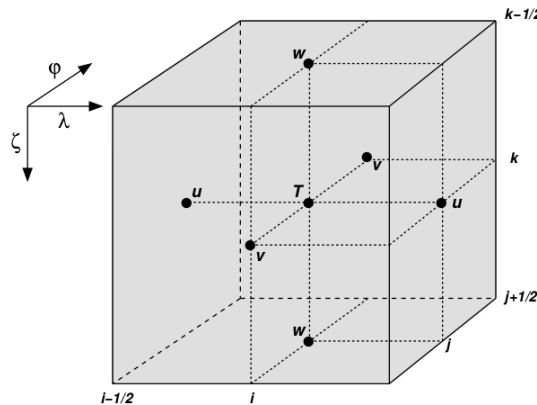


Figure 3.2. – A grid box volume $\Delta V = \Delta\lambda\Delta\varphi\Delta\zeta$ showing the Arakawa-C/Lorenz staggering of the dependent model variables. From Schättler et al. (2011).

The prognostic equations are integrated forward in time using the leapfrog method with a fixed timestep Δt . The magnitude of Δt is dependent on the horizontal resolution and related to the density. Since ρ is not a constant, the model equations describe a compressible atmosphere. This has the advantage of being valid for weather systems on different scales, but a disadvantage is that sound waves (compressible waves) are part of the solution. Sound waves are meteorologically unimportant, but they are very fast. When the sound wave moves across a discrete spatial grid, the amplitude of the wave needs to be computed at a single grid point at every time step. Otherwise, it is possible that more mass than available is advected away from a grid point, which would violate the conservation of mass. The duration of a timestep must therefore be less than the time the wave needs to travel to an adjacent grid point. The relation between grid spatial resolution and time steps is found in the Courant-Friedrich-Lewy (CFL) condition $U\Delta t/\Delta x < 1$, where U is the propagation speed of the sound waves and Δx the horizontal grid scale. The CFL-criterion needs to be fulfilled in order to have numeric stability. This also states that for a higher horizontal resolution (smaller grid cells), a smaller time step is required for a stable integration of the basic equations, and this demands a higher computational cost. To reduce this cost, but to keep numerical accuracy, a time-splitting scheme is introduced (Klemp and Wilhelmson, 1978). The time step Δt is split into a number of small time steps and also the prognostic equations are separated into fast terms (directly linked to sound waves) and slow modes of motion. The fast terms are computed for every small time step, while slow terms are computed for the normal time steps only.

On a spatial scale, a single grid box has a size in the order of kilometers. Some processes take place on a scale that is smaller than the size of a grid box, like turbulence or cloud droplet formation. These processes are therefore approximated by the use of parameterization schemes. Moist convection is the only sub-grid scale process that is of interest in this study. It is parameterized using the Tiedtke mass-flux scheme (Tiedtke, 1989) in which all the clouds within one grid cell are treated as one big cloud (bulk cloud) and the resulting mass flux is the sum of the updrafts and downdrafts of the ensemble of single clouds. Three types of clouds are distinguished: penetrative convection, mid-level convection and shallow convection. Only one type of convection can be present in a grid cell at a time. At low horizontal resolution, all types are parameterized, while at high resolution (0.025°) only shallow convection is parameterized, and the others are explicitly computed. For all parameterized processes the default parametrization scheme of COSMO is used, which is described in detail in Doms et al. (2011).

3.2.2. Initializing the model

Input data

A limited-area model needs both initial and boundary data from a global model in order to perform dynamical downscaling. The analysis data of the deterministic

global Integrated Forecast System (IFS) model of the European Center for Medium-range Weather Forecast (ECMWF) are used to initialize COSMO with. These data include assimilated global measurement data like radiosondes and satellite products. In this study, however, data from a research analysis is used in preference to the operational analysis. Due to the T-PARC field campaign, additional measurement data was available and Weissmann et al. (2011), Weissmann et al. (2012) and Harnisch et al. (2011) performed data assimilation experiments with dropsonde data from multiple aircrafts and DWL and DIAL lidar data from the Falcon aircraft. In this study, the interest lies in a good representation of smaller scale structures near the cyclone center. ECMWF analysis data with either additional assimilated dropsondes, DWL observations or DIAL observations⁹ are compared to SAMURAI data. The best representation of key elements, like the location of wind maxima and the inflow of midlatitude air, is found when dropsondes are assimilated (not shown). Therefore the research ECMWF analysis data with assimilated T-PARC dropsondes is used as initial and boundary data for COSMO (from now on called "analysis data"). This analysis data was provided every six hours on a 0.25° horizontal grid. It was interpolated to the COSMO grid by the pre-processing program INT2LM Version 1.18. Note that aircraft data from T-PARC was only available during certain observation periods. Therefore not all data will be improved near the core region of the cyclone.

Surface properties (e.g. surface height, vegetation, albedo, land use) are provided by an external data set and are constant during the simulations. For TC modelling, the SST is of particular interest. It is available every 24 hours and kept constant during a simulation, although this is not entirely realistic, since a cyclone strongly influences the upper layers of the ocean. The SST data near Japan has only minor differences between 18 and 19 September, so all simulations are started with about the same SST data. Since Sinlaku moves near Japan, the terrain height is of importance also. Large differences in terrain representation exist between high and low resolution simulations (Fig. 3.3), which will influence the typhoon-terrain interaction. Finally, the COSMO output data is given at model levels, and interpolated to pressure levels with a vertical separation of 25 hPa.

Model setup

Now, a suitable setup for modelling ET should be found. The operationally used setup of the DWD for Europe (0.0625° horizontal resolution and 40 vertical levels) and Germany (0.025° horizontal resolution and 50 vertical levels) is not appropriate for this study. The 'top of the atmosphere' is determined at about 22 km height, and a Rayleigh damping layer starts at 11 km. For extratropical phenomena these values are adequate, but tropical cyclones usually penetrate to higher levels than 11 km. Therefore, a tropical setup is used here (Ulrich Blahak (DWD), personal communication). The tropical setup has 57 vertical levels and the top of the model is located at 30 km, with a damping layer starting at 18 km. The vertical distribution

⁹This data was kindly provided by M. Weissmann

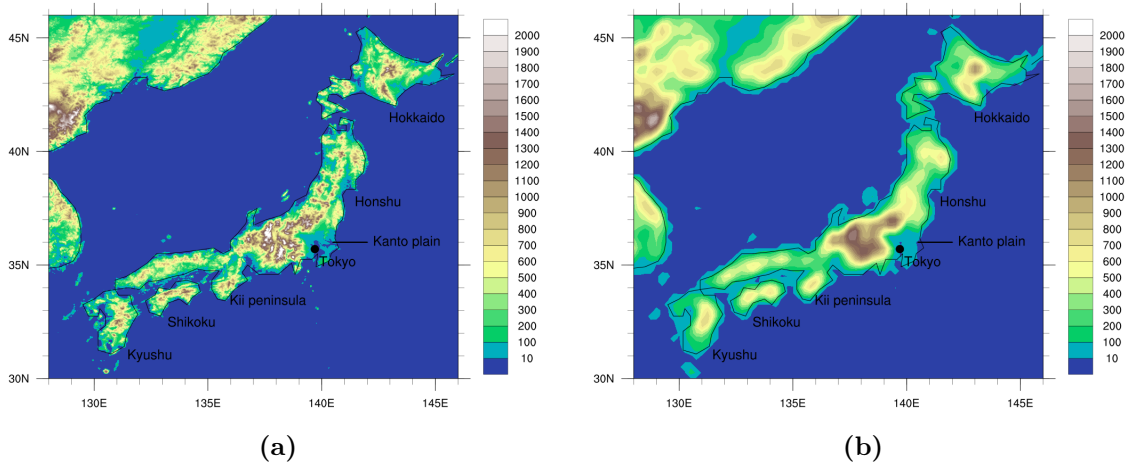


Figure 3.3. – Geometric height (m) as initial condition in the COSMO model, including geographically relevant locations, for (a) 0.025° resolution (~ 2.8 km) and (b) 0.25° resolution (~ 28 km).

of levels is similar to the operational setup for Germany, with most levels in the planetary boundary layer and 7 additional levels above 22 km height. Furthermore, the tropical setup differs from the operational setup by its reference atmosphere, which has a warmer reference temperature at sea level (300 K instead of 288.15 K).

COSMO is built in order to predict midlatitude weather. Nevertheless, COSMO is also able to simulate a TC structure realistically (e.g. Frisius, 2004; Frisius et al., 2006; Frisius and Hasselbeck, 2009). Furthermore, it has been used to successfully simulate ET (e.g. Grams et al., 2013b,a). Therefore there is confidence in the COSMO model to adequately simulate structural changes during ET.

3.3. Diagnostic tools

The structural changes during ET are diagnosed based on the COSMO model output, but the piecewise PV inversion method was also used to modify the data with which COSMO was initialized. The relative vorticity budget, quasi-geostrophic forcing, frontogenesis function, trajectory analysis and additional tools were all applied to the COSMO output data. Where COSMO uses a full set of equations in a non-hydrostatic atmosphere, all tools describe a simplified version of the atmospheric development. Thereby the tools can be used to disentangle single mechanisms within the complex evolution of the simulation. The momentum equation (Eq. 3.1) is used as a basis for most diagnostic tools, and from here on assumption and modifications are made in order to obtain the governing equations of a specific tool. Assuming hydrostatic balance ($\frac{\partial \phi}{\partial p} = -\frac{R_d T}{p}$, in isobaric coordinates) the horizontal part of the

momentum equations is used here, and written in isobaric coordinates:

$$\frac{\partial \vec{V}_h}{\partial t} + \vec{V} \cdot \nabla \vec{V}_h = -\nabla_p \phi - f \hat{\mathbf{k}} \times \vec{V}_h + \vec{F} \quad (3.6)$$

with $\frac{d}{dt} = \frac{\partial}{\partial t} + u \frac{\partial}{\partial x} + v \frac{\partial}{\partial y} + \omega \frac{\partial}{\partial p}$ and the stress tensor in Eq. 3.1 is replaced by a friction vector \vec{F} .

3.3.1. Potential vorticity inversion

One of the strengths of the variable PV in a frictionless atmosphere in hydrostatic balance is that it can be inverted to obtain information about the horizontal wind and mass field. With the use of a tool that can invert a piece of PV back to basic atmospheric variables (piecewise PV inversion, PPI), the atmosphere can be modified by inserting, moving or removing a PV field, and bringing back the atmosphere to approximate non-linear and hydrostatic balance. In this thesis, the invertibility principle of PV will be used to insert a more realistic PV signal of Sinlaku, obtained by observational data, into the initial data for COSMO. Subsequently, the tool will also be used to move the PV feature.

The inversion tool is based on two equations that are numerically solved by several iterations. The first equations is obtained by taking the horizontal divergence of Eq. 3.6. The flow can be divided in a divergent and non-divergent part, where the non-divergent flow can be written in terms of the stream function ψ

$$\vec{V}_\psi = \hat{\mathbf{k}} \times \nabla \psi \quad \Rightarrow \quad u_\psi = -\frac{\partial \psi}{\partial y}, \quad v_\psi = \frac{\partial \psi}{\partial x}$$

where u_ψ and v_ψ are the non-divergent flow components in x- and y- direction, respectively. Assuming that for large-scale atmospheric motions the horizontal divergence is much smaller than the relative vorticity ($\nabla \cdot \vec{V}_h \ll \zeta$), the divergence of Eq. 3.6 can be simplified and written in terms of ψ and ϕ :

$$\nabla^2 \phi = \nabla \cdot f \nabla \psi + 2 \left[\frac{\partial^2 \psi}{\partial x^2} \frac{\partial^2 \psi}{\partial y^2} - \left(\frac{\partial^2 \psi}{\partial x \partial y} \right)^2 \right] \quad (3.7)$$

which is called the (non-linear) balance equation (Charney, 1955). Similarly, the potential vorticity equation (Eq. 2.1) can be re-written in terms of ψ and ϕ also, when assuming hydrostatic balance $\frac{\partial \phi}{\partial \pi} = -\theta$ with $\pi = c_p(p/p_0)^\kappa$ the Exner function and $\kappa = R_d/c_p$, and replacing the horizontal flow by non-divergent flow:

$$PV = \frac{g\kappa\pi}{p} \left[(f + \nabla^2 \psi) \frac{\partial^2 \phi}{\partial \pi^2} - \frac{\partial^2 \psi}{\partial \pi \partial x} \frac{\partial^2 \phi}{\partial \pi \partial x} - \frac{\partial^2 \psi}{\partial \pi \partial y} \frac{\partial^2 \phi}{\partial \pi \partial y} \right] \quad (3.8)$$

For a given PV at a certain pressure level, and with appropriate boundary conditions, Eqs. 3.7 and 3.8 form a closed set of equations. This means that a certain field of PV can be inverted to its corresponding stream function ψ and geopotential ϕ

values, given a first guess of these variables from the model data. Subsequently, the horizontal (non-divergent) wind field can be computed back from the stream function, and the temperature field can be computed from the geopotential according to the hydrostatic balance. The code for the PPI tool was provided by C. Davis and details of how the equations are solved numerically can be found in Appendix A of Davis and Emanuel (1991). The method of PV inversion in combination with the non-linear balance has successfully been used in several studies about ET (e.g. McTaggart-Cowan et al., 2001; Agustí-Panareda et al., 2004, 2005; Agustí-Panareda, 2008; Riemer et al., 2008; Riemer and Jones, 2010, 2014; Grams et al., 2013b) and is therefore thought to be a reliable method to use in this study.

The actual modification that is performed here is described next. The aim was to insert Sinlaku's PV anomaly from the gridded SAMURAI data into the analysis data, and eventually move the anomaly. In order to do this, all data is interpolated onto pressure levels with 25 hPa spacing. Since the PPI tool can only be applied on data with a horizontal resolution of at least 20 km, SAMURAI data is also interpolated onto the 0.25° horizontal grid of the analysis data. In a first step, only the analysis data is modified in the PPI tool, in which the PV field of Sinlaku ($PV > 0.3$ PVU) is removed by setting its value to 0.3 PVU. The remaining fields are inverted back again to obtain horizontal velocity components, temperature field and geopotential. This step is performed in order to have a consistent background field of the environment without Sinlaku for all experiments.

In a second step, this modified analysis data is again used in the PPI tool, but now the SAMURAI data is inserted. The approach is shown schematically in Fig. 3.4. (1) First the PV is computed within the small SAMURAI domain (133.25° - 137.25° , 31.25° - 34.5°) and also within a subset of the modified analysis data (124.0° - 144.0° ,

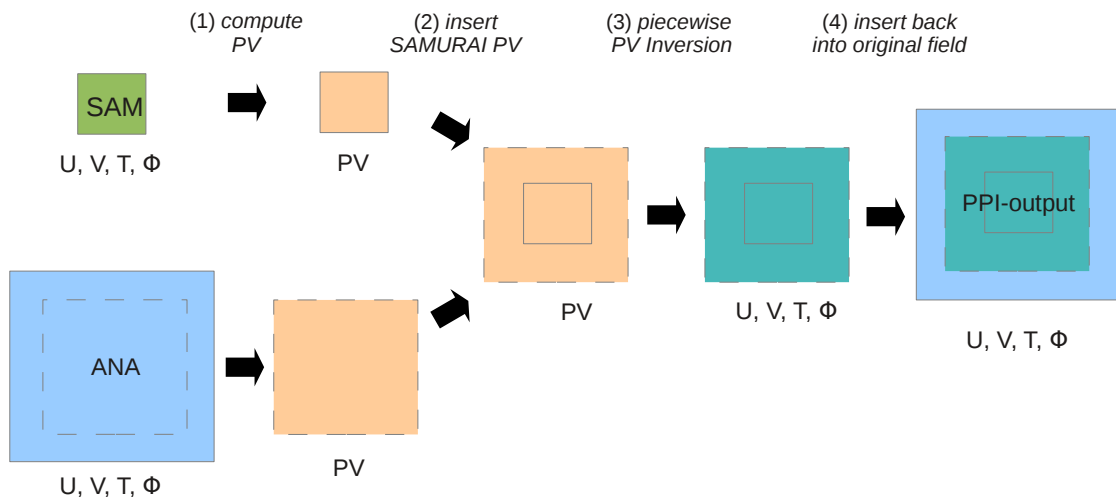


Figure 3.4. – Schematic overview of the implementation of SAMURAI data (SAM) into the analysis data where Sinlaku's PV has been removed (ANA) by the use of the piecewise PV inversion method.

26.0°-39.0°). PPI is only conducted over this subset domain, which is kept relatively small on purpose. At the northern border of the domain, the longitudinal distance of a grid cell still exceeds 20 km (at 39°N $0.25^\circ \approx 21.6$ km), and the PV inversion can therefore be conducted on 0.25° horizontal resolution. If the domain would have extended further northwards, the horizontal grid on which PPI is calculated would have to be coarsened and valuable data about the detailed PV structure from the SAMURAI data would have been lost. (2) As a next step, the SAMURAI PV field is inserted in the analysis PV field (where Sinlaku's PV anomaly was removed earlier), either at the original location of the SAMURAI domain, or moved horizontally (Fig. 3.4). During the insertion of PV, and also during the removal seen earlier, the difference in PV is distributed over the entire domain, so that the total PV in the domain is conserved. The insertion and removal only take place between $p_{\text{top}}=200$ hPa and $p_{\text{bot}}=900$ hPa. 900 hPa is assumed to be above the planetary boundary layer, where the non-linear balance equation holds, and the choice of 200 hPa is justified because Sinlaku's PV tower did not reach above this level and, moreover, SAMURAI data was not available at higher levels. Besides the PV field, the SAMURAI u , v and ϕ fields are inserted into the analysis data, smoothed at the border of the SAMURAI domain, and a first guess of ψ and ϕ is obtained. (3) The PV field is then computed back to a flow and mass field, based on Eqs. 3.7 and 3.8 and (4) finally, the PPI-subset-domain is inserted in the original analysis data again (Fig. 3.4). This version of the PPI tool was adapted to COSMO model data by Christian Grams, and the output data is therefore interpolated to model levels again, which can directly be used to initiate the COSMO model.

3.3.2. Relative vorticity budget

During ET, Sinlaku's vortex evolves with time in a complex manner. A relative vorticity budget approach provides insight into the processes that contribute to the change in vorticity within a closed area. It is therefore a suitable tool for disentangling mechanisms that lead to the intensification or decay during ET from a vorticity perspective. In this subsection it is described how the vorticity budget is computed and how it can be interpreted. Since the vorticity budget will be applied on COSMO output on pressure levels, all equations in this section will be in a pressure coordinates.

Budget calculations

In the first place, it is assumed that in a TC-like vortex the vertical component of the relative vorticity $\zeta = \hat{\mathbf{k}} \cdot \nabla \times \vec{V}_h = \frac{\partial v}{\partial x} - \frac{\partial u}{\partial y}$ is dominant, and this component will from now on be referred to as relative vorticity. Starting with the basic equations, the local change of relative vorticity can be obtained by taking the divergence of the separate components of the horizontal equation of motion (Eq. 3.6)

$$\begin{aligned}\frac{\partial}{\partial x} \left(\frac{\partial v}{\partial t} + \vec{V} \cdot \nabla v = -\frac{\partial \phi}{\partial y} - fu + F_y \right) \\ \frac{\partial}{\partial y} \left(\frac{\partial u}{\partial t} + \vec{V} \cdot \nabla u = -\frac{\partial \phi}{\partial x} + fv + F_x \right)\end{aligned}$$

and subtracting these. After rewriting, this results in the vorticity tendency equation

$$\begin{aligned}\frac{\partial \zeta}{\partial t} &= \frac{\partial}{\partial t} \left(\frac{\partial v}{\partial x} - \frac{\partial u}{\partial y} \right) \\ &= \underbrace{-\vec{V} \cdot \nabla_H \zeta}_a - \underbrace{v\beta}_b - \underbrace{(\eta \nabla_H \cdot \vec{V})}_c - \underbrace{\omega \frac{\partial \zeta}{\partial p}}_d - \underbrace{\left(\frac{\partial \omega}{\partial x} \frac{\partial v}{\partial p} - \frac{\partial \omega}{\partial y} \frac{\partial u}{\partial p} \right)}_e + \underbrace{\hat{\mathbf{k}} \cdot \nabla \times \vec{F}}_f\end{aligned}\quad (3.9)$$

where the terms on the right hand side represent (a) horizontal advection of relative vorticity, (b) advection of planetary vorticity, (c) divergence term, (d) vertical advection of relative vorticity, (e) tilting term and (f) friction term.

Because the interest here lies in the change of vorticity in a certain area, Eq. 3.9 will be rewritten to get the flux of relative vorticity \vec{K} , as shown by Haynes and McIntyre (1987)

$$\frac{\partial \zeta}{\partial t} = -\nabla \cdot \left(\vec{V}_h \eta - \omega \hat{\mathbf{k}} \times \frac{\partial \vec{V}_h}{\partial p} + \hat{\mathbf{k}} \times \vec{F} \right) \equiv -\nabla \cdot \vec{K} \quad (3.10)$$

where the first term in the brackets results from (a), (b) and (c) of Eq. 3.9, and the second term by rewriting (d) and (e).

The flux form of the vorticity tendency is useful because now Gauss's theorem (also known as divergence theorem) can be applied. This theorem relates the behaviour of a vector field within a closed surface to the flux of a vector field through the surface boundary, according to $\iint (\nabla \cdot \vec{f}) dA = \oint \vec{f} \cdot \hat{\mathbf{n}} dl$, where \vec{f} is a vector field, $\hat{\mathbf{n}}$ a unit vector pointing outward normal to boundary l . In simple words, Gauss's theorem states that the net flux out of a region equals the sum of all sources and sinks at the boundary of that region. So when integrating over a closed surface and applying Gauss's theorem, Eq. 3.10 becomes

$$\frac{\partial C}{\partial t} = -\oint \vec{K} \cdot \hat{\mathbf{n}} dl = -\oint \eta \vec{V}_h \cdot \hat{\mathbf{n}} dl + \oint \omega \left(\hat{\mathbf{k}} \times \frac{\partial \vec{V}_h}{\partial p} \right) \cdot \hat{\mathbf{n}} dl - \oint (\hat{\mathbf{k}} \times \vec{F}) \cdot \hat{\mathbf{n}} dl \quad (3.11)$$

where C is the circulation. Assuming that the closed region is a square box, which is suitable when applying it on gridded data, and dividing the perimeter of the box in average values and values that deviate from the average (following Davis and

Galarneau-Jr. (2009), noted by overbars and primes, respectively), the first term on the right hand side in Eq. 3.11 can be rewritten as (Schwendike, 2010)

$$\begin{aligned}
-\oint (\bar{\eta} + \eta')(\bar{\vec{V}}_h + \vec{V}'_h) \cdot \hat{\mathbf{n}} dl &= -\iint \nabla \cdot ((\bar{\eta} + \eta')(\bar{\vec{V}}_h + \vec{V}'_h)) dA \\
&= -\iint \nabla \cdot (\bar{\eta}\bar{\vec{V}}_h + \bar{\eta}\vec{V}'_h + \eta'\bar{\vec{V}}_h + \eta'\vec{V}'_h) dA \\
&= -\bar{\eta} \iint \nabla \cdot (\bar{\vec{V}}_h + \vec{V}'_h) dA - \iint \nabla \cdot (\eta'\bar{\vec{V}}_h) dA \\
&\quad - \iint \nabla \cdot (\eta'\vec{V}'_h) dA \\
&= -\bar{\eta}\tilde{\delta}A - \oint \eta'\vec{V}_h \cdot \hat{\mathbf{n}} dl
\end{aligned}$$

where A is the area of the box, δ the divergence of the wind field and the tilde denotes the average over the area of the box. Eq. 3.11 thus becomes the final vorticity budget equation as used in this thesis:

$$\frac{\partial C}{\partial t} = \underbrace{-\bar{\eta}\tilde{\delta}A}_a - \underbrace{\oint \eta'\vec{V}_h \cdot \hat{\mathbf{n}} dl}_b + \underbrace{\oint \omega \left(\hat{\mathbf{k}} \times \frac{\partial \vec{V}_h}{\partial p} \right) \cdot \hat{\mathbf{n}} dl}_c - \underbrace{\oint (\hat{\mathbf{k}} \times \vec{F}) \cdot \hat{\mathbf{n}} dl}_d \quad (3.12)$$

The terms on the right hand side represent a change of vorticity in the box due to (a) stretching, (b) eddy flux, (c) vortex tilting and (d) friction.

Application of the vorticity budget equation

Eq. 3.12 can now be applied to the hourly gridded COSMO data and an approach similar to Davis and Galarneau-Jr. (2009) is taken. (1) In the first place, the box size is determined, and chosen so that the location of the vortex at sea level lies inside the box during the analysed period. (2) The box moves with the cyclone with a constant translation speed (u, v) . The translation speed is based on Sinlaku's track and is averaged over the analysed time interval. The translation speed is also subtracted from the ground-relative wind field, so that only the storm-relative wind field is considered in the calculations. (3) A box-ensemble approach was introduced by Davis and Galarneau-Jr. (2009) in order to restore the balance of the budget, when small-scale convective cells with high vorticity are present at the border. For the tropical re-intensification phase of Sinlaku, an ensemble was used in which the box was shifted 4 times 2 grid points to the north, south, west and east. This corresponds to a maximum displacement of 0.2° in all directions (on 0.025° resolution) and a box-ensemble with 81 members. For the ET phase, a larger ensemble was needed in order to obtain a nearly balanced situation of the vorticity budget. During this period the box was shifted 8 times 2 grid points, corresponding to a maximum displacement 0.4° and an ensemble with 289 members. (4) The vorticity budget terms are calculated at t and $t + 1$ and first averaged over the box (perimeter), then averaged over the

ensemble of boxes and finally averaged over both time steps. (5) In the last step, the sum of the budget terms is compared to the change in relative vorticity between two timesteps $\zeta(t + 1) - \zeta(t)/\Delta t$, also averaged over the box and over the box ensemble.

Interpretation of the budget terms

The eddy flux term and stretching term arise from rewriting the first three terms (horizontal advection of vorticity and the divergence term) on the right hand side of Eq. 3.9. In their new form they still represent a similar behaviour to the change in vorticity. The stretching term states that in the case of a net divergence (convergence) inside the box there will be a vertical transport of vorticity, and the net vorticity that is present at the border of the box will be transported out of (into) the box at the same level. A developing tropical cyclone has a stretching vortex with convergence and inflow of positive vorticity at lower levels, resulting in a positive stretching term. The eddy flux term accounts for the horizontal advection of a vorticity anomaly into or out of the box. Even without divergence, the inward flow of a positive vorticity anomaly can cause an accumulation of vorticity (Davis and Galarneau-Jr., 2009).

The third and fourth term in Eq. 3.9 (vertical advection of relative vorticity and tilting) together form the tilting term in Eq. 3.12. The vertical advection, however, is cancelled out during rewriting and the use of the flux form, as is further discussed by Kirk (2007). Here the focus lies on the interpretation of the tilting term as given in Eq. 3.12. The underlying mechanism is that horizontal vorticity is associated with vertical wind shear; vertical motion then tilts the horizontal vorticity and creates a dipole of positive and negative vertical vorticity. If the vertical motion occurs on the border of the box, there will be a net change of vertical vorticity inside the box (Fig. 3.5).

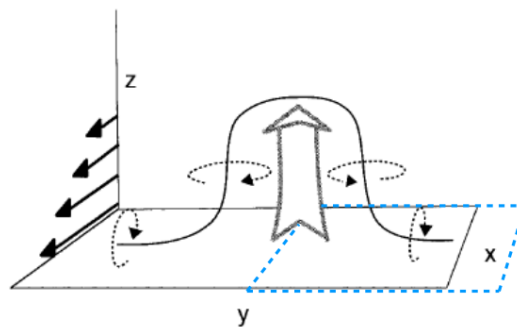


Figure 3.5. – Idealised example of the combined effect of vertical wind shear (arrows along the x-axis) and vertical motion (large arrow) on vorticity generation/destruction (dashed arrows) inside/outside a box of reference (blue line), known as vortex tilting. Reprinted and adapted from Weisman and Davis (1998) © American Meteorological Society. Used and adapted with permission.

The friction term will not be considered in this thesis, following Schwendike and Jones (2010). Above the boundary layer, this has no consequences for the budget, which is nearly balanced without friction. Near the surface, friction cannot be neglected and the budget is therefore not considered below 900 hPa. Additionally, in mountainous regions the box may contain levels that are below the ground and subsequently the budget is not balanced at this level.

3.3.3. Quasi-geostrophic forcing of vertical motion

The contribution of large-scale weather systems to vertical motion can be quantified by the use of a quasi-geostrophic (QG) approach. In the midlatitudes, the horizontal air flow above the boundary layer can be approximated by a balance between the pressure gradient force and the Coriolis force, called geostrophic balance. The equation of motion (Eq. 3.6) then reduces to

$$f\hat{\mathbf{k}} \times \vec{V} = -\nabla_p \phi. \quad (3.13)$$

From this balance follows the geostrophic wind:

$$\vec{V}_g = \frac{1}{f}\hat{\mathbf{k}} \times \nabla_p \phi \quad (3.14)$$

Within the geostrophic balance, the flow can not be divergent. Consequently, it does not account for the occurrence of vertical motion. A more realistic representation of the atmosphere is found when the actual wind is divided in a geostrophic and ageostrophic component $\vec{V}_h = \vec{V}_g + \vec{V}_a$. The assumption that $\vec{V}_g \gg \vec{V}_a$ is called quasi-geostrophic. The geostrophic part of the flow causes advection, while vertical motion only depends on the ageostrophic part of the flow, as seen from the QG-continuity equation

$$\frac{\partial u_a}{\partial x} + \frac{\partial v_a}{\partial y} + \frac{\partial \omega}{\partial p} = 0 \quad (3.15)$$

The QG-approach consists of a set of two equations with two unknowns (ϕ and ω): the barotropic vorticity equations and the QG thermodynamic energy equation. These two equations can be used to derive the QG-omega equation:

$$\sigma \left(\nabla^2 + \frac{f_0^2}{\sigma} \frac{\partial^2}{\partial p^2} \right) \omega = f_0 \frac{\partial}{\partial p} \left[\vec{V}_g \cdot \nabla (\zeta_g + f) \right] + \nabla^2 \left[\vec{V}_g \cdot \nabla \left(-\frac{\partial \phi}{\partial p} \right) \right] \quad (3.16)$$

where $\zeta_g = \frac{1}{f_0} \nabla^2 \phi$ is the geostrophic relative vorticity, and $\sigma = -\frac{RT}{p} \frac{\partial \ln \theta}{\partial p}$ the standard atmosphere static stability parameter. According to the right hand-side of this equation, vertical motion is induced by differential advection of vorticity and temperature. The function of the vertical motion is to keep the mass and thermal field in the atmosphere close to geostrophic and hydrostatic balance (e.g. Martin, 2006).

Within the omega equation, the advection of vorticity and temperature often oppose each other. This problem does not occur when Eq. 3.16 is written in the Q-vector form (Hoskins et al., 1978):

$$\sigma \left(\nabla^2 + \frac{f_0^2}{\sigma} \frac{\partial^2}{\partial p^2} \right) \omega = -2\nabla \cdot \vec{Q} \quad (3.17)$$

where the Q-vector

$$\begin{aligned} \vec{Q} &= -\frac{R}{p} \left[\left(\frac{\partial \vec{V}_g}{\partial x} \cdot \nabla T \right) \hat{\mathbf{i}}, \left(\frac{\partial \vec{V}_g}{\partial y} \cdot \nabla T \right) \hat{\mathbf{j}} \right] \\ &= -\frac{R}{p} \left[\left(\frac{\partial u_g}{\partial x} \frac{\partial T}{\partial x} + \frac{\partial v_g}{\partial x} \frac{\partial T}{\partial y} \right) \hat{\mathbf{i}} + \left(\frac{\partial u_g}{\partial y} \frac{\partial T}{\partial x} + \frac{\partial v_g}{\partial y} \frac{\partial T}{\partial y} \right) \hat{\mathbf{j}} \right] \end{aligned} \quad (3.18)$$

describes the vector rate of change of a temperature gradient along the geostrophic flow. Since the LHS of the Eq. 3.17 is essentially a 3D Laplacian, which is a second derivative operator, this means that when $\nabla^2 \omega$ is positive, ω is negative, corresponding to upward motion. So, when the Q-vector converges ($\nabla \cdot \vec{Q} < 0$), this corresponds to upward motion. The convergence of the Q-vector is the basic principle on which the contribution of quasi-geostrophic flow to vertical motion is computed. A method to solve the differential equations of Eq. 3.18 was provided by Sue Gray and supported by Maxi Böttcher, Christian Grams and Julian Quinting. The method is height attributable, meaning that at a specific level, the QG contribution to ω can be distinguished into lower- and upper-level induced vertical motion, as first introduced by Clough et al. (1996). In midlatitude synoptic scale flow the lower-level forcing can be associated with the forcing by differential temperature advection along the baroclinic zone, and the upper-level forcing can be associated with the differential vorticity advection by the jet stream. Within a TC, however, the differential temperature and vorticity advection are both largest at lower levels.

In this thesis, the QG forcing to vertical motion is computed at a 0.25° resolution grid, so higher resolution simulation data was first re-gridded. The contribution of lower- (1000-750 hPa) and upper-level (650-50) forcing was analysed at a level of 700 hPa. This level is chosen by Deveson et al. (2002) because it is close enough to the surface to express the impact of a near surface cyclone structure and far enough away to avoid boundary layer effects. Since a source of QG vertical motion affects the vertical velocity field on a larger horizontal and vertical extent than the source location itself (similar to the effect of a PV anomaly on its horizontal wind field in Fig. 2.5), both the lower- and upper-level forcing will have a contribution at 700 hPa.

Although the QG-omega forcing is valid for large-scale flow, it has been used and verified on smaller scales as well. However, for the application to smaller scale features it should be noticed that in regions with intense latent heating, the QG diagnostic strongly underestimates the vertical motion (Boettcher and Wernli, 2011). It therefore does not capture convective vertical motion within a TC or along a frontal zone well. Nevertheless, Reasor et al. (2000) applied a Q-vector approach to

a dry vortex with a RMW of only 30 km, and found an upward motion signal to the right of the tilt-vector which corresponded qualitatively to observations. This signal was valid because the vertical motion followed the isentropes of the tilted vortex and no condensational heating was involved. Also for a baroclinic wave, the QG-omega equation turned out to be a qualitatively accurate method, although it is formally invalid (Thorpe and Pedder, 1999). In this study it is therefore justified to use the QG diagnostic qualitatively in order to analyse either the forcing of vertical motion by large-scale midlatitude features, or the smaller scale forcing of non-convective vertical motion near a TC or front.

3.3.4. Frontogenesis function

Frontogenetic processes act to increase or decrease the horizontal temperature gradient (frontogenesis or frontolysis, respectively). Knowledge about the location of frontal activity is useful because it also indicates the expected location of several front-related processes, like cross-frontal vertical motion and precipitation. For the aim of disentangling structural changes and their mechanisms, frontogenesis is therefore a useful tool.

The full frontogenesis function

$$\vec{F} = \frac{d|\nabla_p\theta|}{dt} \quad (3.19)$$

is simplified into a 2D horizontal frontogenesis function by Petterssen (1956), and is written as

$$\vec{F} = \frac{d|\nabla_h\theta|}{dt} = -\frac{1}{2}|\nabla_h\theta|(D - E \cos 2\beta) \quad (3.20)$$

with divergence

$$D = \frac{\partial u}{\partial x} + \frac{\partial v}{\partial y} \quad (3.21)$$

and total deformation

$$E = (E_{st}^2 + E_{sh}^2)^{0.5}. \quad (3.22)$$

The total deformation is divided into stretching deformation $E_{st} = \frac{\partial u}{\partial x} - \frac{\partial v}{\partial y}$ and shearing deformation $E_{sh} = \frac{\partial v}{\partial x} + \frac{\partial u}{\partial y}$. β can be found by the difference between the angle of the local orientation of the axis of dilatation δ and the angle of the local orientation of the isentropes α ($\beta = \delta - \alpha$, Keyser et al., 1988), with

$$\tan \alpha = -\frac{\partial\theta/\partial x}{\partial\theta/\partial y}, \quad \tan 2\delta = \frac{E_{sh}}{E_{st}}$$

The Petterssen frontogenesis function is computed on pressure level output of the COSMO model, and serves in particular as an indicator for the location of ascending and descending motion.

3.3.5. Trajectory calculations

All previously mentioned diagnostic tools have a Eulerian framework in which the state of the atmosphere or its temporal evolution is considered from a fixed frame of reference. The complex interaction of atmospheric air masses may in some applications be better described by a Lagrangian point of view. The temporal evolution of the atmosphere and its properties is then considered along the pathway of an air parcel. In a Lagrangian framework, temporally coherent structures can be analysed which provides insight into the dynamics of the flow (Wernli and Davies, 1997).

In this study, trajectories are calculated with the publicly available tool LAGRANTO (LAGRangian ANalysis TOol, Wernli and Davies, 1997) version 2.0 (Sprenger and Wernli, 2015) which allows calculation of both forward and backward trajectories. The trajectory of a single air parcel is calculated offline by numerically solving $d\vec{x}/dt = \vec{V}(\vec{x})$, where \vec{x} is the 3-D position of the air parcel in geographical coordinates. This is done by three iterations of the location vector $\vec{x}^* = \vec{x} + \vec{V}(\vec{x}, t) \cdot \Delta t$ and wind vector $\vec{V}^* = 0.5[\vec{V}(\vec{x}, t) + \vec{V}(\vec{x}^*, t + \Delta t)]$ where \vec{x}^* and \vec{V}^* are the new position and wind vector, respectively, after an iteration and Δt is 1/12 of the available data time interval (Sprenger and Wernli, 2015). After calculating the position vector of the trajectory over time, atmospheric variables can be traced along the pathway. In this thesis LAGRANTO is applied to hourly output ($\Delta t=5$ minutes) of high-resolution (0.025°) COSMO data on model levels.

In order to define a temporally coherent air mass, an ensemble of trajectories should be calculated and subsequently trajectories with similar physical properties can be selected. The strength of LAGRANTO in comparison to other trajectory tools lies in the possibility for the user to easily select trajectories based on objective criteria (Sprenger and Wernli, 2015). Identification of a coherent ensemble of trajectories (Wernli and Davies, 1997) is an important step in order to get insight into the dynamics of a specific air flow. After applying selection criteria, the ensemble of trajectories can be visualised in many ways. For example, the location of trajectories can be plotted on a geographical map with the development of a particular property along the pathway. This gives an insight in both the pathway and dynamic development along the way, and will be used in this thesis. Another way of visualisation is the application of statistics on atmospheric variables that were traced along the ensemble of trajectories.

Plots of basic statistics will often be shown in this thesis, complementing geographical plots. Therefore, this type of plot is elucidated by an example (Fig. 3.6). 12 Hour forward trajectories were started at 20/00 in a box around Sinlaku at every 25 hPa above 975 hPa. The example aims to find WCB-like trajectories that start in the subtropical warm moist air. Therefore only trajectories are selected that start below 900 hPa and have a θ_{eq} -value > 345 K. Furthermore they should rise and be present above 400 hPa, within the last 6 hours of the trajectories. In the trajectory statistics figures, the behaviour of pressure (Fig. 3.6a) and specific humidity (Fig. 3.6b) is shown against time. $t=0$ represent the starting time of the trajectories (here: 20/00) and in this example $t=12$ the end time (here: 20/12). The trajectory

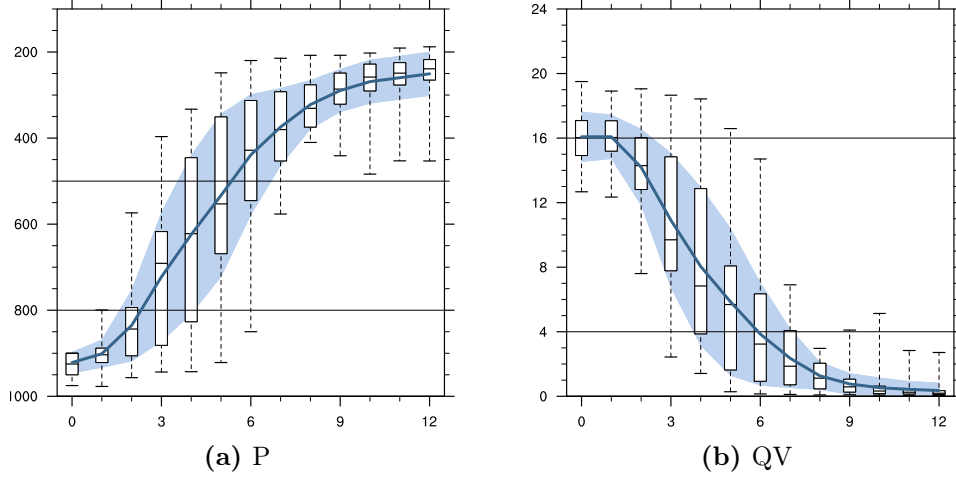


Figure 3.6. – Example of trajectory statistics of an ensemble of trajectories. (a) Pressure (hPa) and (b) specific humidity (g/kg) is shown at the y-axes, and time (hours) on the x-axis, where $t=0$ is the start time of the trajectories. The remaining time depends on the duration of calculation and type of trajectories (forward/backward). Hourly box-whisker plots show the maximum, minimum, 25% and 75% percentiles and the median of the trajectory ensemble. The blue line and shading represent the average and standard deviation, respectively. Additional horizontal black lines are added as a reference value.

statistics consists of a set of box-whisker plots for every timestep, with minimum and maximum values of the trajectory ensemble at the end of the dashed lines, 25% and 75% percentiles at the end of the white boxes and the median represented by the black line within the boxes. Furthermore, the average value and standard deviation is added (blue line and light blue area, respectively). In the interpretation of the physical characteristics along the trajectory ensemble, mainly the median value is considered. In this example that means that trajectories started on average on a level of 925 hPa at $t=0$, and rose to about 250 hPa within 12 hours (Fig. 3.6a). The strongest ascent took place between $t=1$ and $t=7$. At the same time, this air mass started with a moisture content of on average 16 g/kg, and lost its moisture, either by condensation or deposition, during the ascent (Fig. 3.6b). After 10 hours (here: at 20/10) the majority of the air parcels lost so much moisture that the median of the box-whisker plots can no longer be distinguished from zero in Fig. 3.6b. All simple statistic plot throughout this thesis will have the same y-axis scales per variable for inter-comparison between figures.

3.3.6. Additional post-processing tools

From the COSMO model output, additional meteorological variables are computed on all 25 hPa spaced pressure levels. PV is computed according to Eq. 2.1 (Eq. 13 in Hoskins et al., 1985), and where appropriate interpolated onto θ -levels, in order to see the large-scale advection of PV.

Potential temperature (K) is computed as

$$\theta = T \left(\frac{1000}{p} \right)^{R_d/c_p} \quad (3.23)$$

with c_p the specific heat capacity at constant pressure for dry air ($1005.7 \text{ J kg}^{-1} \text{ K}^{-1}$) and $R_d = 287.053 \text{ J kg}^{-1} \text{ K}^{-1}$. Subsequently, the equivalent potential temperature (K) is computed after Bolton (1980) (his Eq. 43):

$$\theta_{eq}(K) = T \left(\frac{1000}{p} \right)^{0.2854(1-0.28r)} \exp \left[\left(\frac{3.376}{T_l} - 0.00254 \right) \times 1000r (1 + 0.81r) \right] \quad (3.24)$$

with temperature T (K) and the mixing ratio r (kg/kg)

$$r = 0.622 \left(\frac{e}{p - e} \right).$$

The water vapour pressure e (hPa) can be computed from the relative humidity RH (%), using the saturated water vapour pressure e_s (hPa) with $e_0 = 6.11 \text{ hPa}$ as a reference saturation vapour pressure at $T = 273.15 \text{ K}$

$$RH = \frac{e}{e_s} \times 100\% \quad e_s = e_0 \exp \left(17.5043 \frac{T - 273.15}{241.2 + (T - 273.15)} \right).$$

Finally, the temperature at the lifting condensation level (K) can be computed according to Bolton (1980) (his Eq. 22):

$$T_l = \left[1 / \left(\frac{1}{T - 55} - \frac{\ln(RH/100)}{2840} \right) \right] + 55.0$$

Freezing and melting processes in the air parcel are neglected in these simplified equations.

The cloud top temperature (CTT) is obtained following Grams (2011) who used a calculation tool provided by A. Penny (NPS), adopted from the program `cttcalc.f` from M.T. Stoelinga (<http://www.mmm.ucar.edu/wrf/users/docs/ripug.htm>). The CTT is computed by interpolating the temperature on model level data to the level of unit optical depth, starting from the model top. The method is quantitatively not accurate but the results are used qualitatively, to compare the locations of high clouds (lowest CTT) in model data with CTT products from satellite images.

The track and pressure intensity of Sinlaku is computed based on the minimum pressure at mean sea level (p_{msl}). First the location of the minimum p_{msl} near the expected location according to the Best Track is found. During ET, the circulation center is not symmetric any more and convective bursts can influence the location of minimum pressure. Therefore, additionally the 'center of mass' is calculated, using a box around the expected center and applying

$$(lon_c, lat_c) = \frac{\left(\iint lon(p_{ref}) dx dy, \iint lat(p_{ref}) dx dy \right)}{\iint (p_{ref}) dx dy} \quad (3.25)$$

where lon and lat represent longitude and latitude, respectively, the subscript c stands for the center, and the reference pressure p_{ref} is 1 where $p_{msl} < p_{msl}+4$, and 0 otherwise. In general, this method turned out to function well for Sinlaku, except when convective bursts were present far away from the circulation center. This occurred in some simulations in a late stage of ET, and is not considered in detail.

4. Challenges in modelling the ET of TY Sinlaku

Modelling of ET is still a challenge, as reviewed in Section 2.3. Nevertheless, there is a need for a simulation of TY Sinlaku that is of sufficient quality to allow to learn more about the relevant physical mechanisms. The main objective is therefore to adequately model the ET of TY Sinlaku. In order to do so, first the quality of the model's initial data is verified by the use of observational data (Section 4.1). Then, the flow diagram of Fig. 2.16 is used to determine different model properties and initialization setups that could improve an ET simulation. In the first place, simulations are initialised with analysis data and the sensitivity of to different initialization times (Fig. 2.16, arrow 6) and horizontal resolutions (Fig. 2.16, arrows 8, 9, 10, 11) is tested (Section 4.2). Afterwards the initial data is modified. Sinlaku's vortex is replaced by a more realistic version of the storm by the use of piecewise PV inversion and the storm is moved horizontally with respect to its original location near Japan (Section 4.3 and Fig. 2.16, arrow 1). It will become clear that it is difficult to simulate the ET of Sinlaku adequately, but not impossible, because two simulations are suitable for analysis of ET dynamics in the next chapter (Section 4.4).

4.1. Sinlaku's development according to observations and analysis data

Several types of observational data the transformation stage of ET were obtained during T-PARC, which makes it an unique dataset for the analysis of structural changes during ET. Sinlaku's structure has already been described based on SAMURAI data on the specific times 19/04 (Foerster et al., 2014) and 20/06 (Quinting et al., 2014). The first aim in this section is to extend the description of Sinlaku's ET over the period 18/12 to 21/00, to get a better overview of the actual development. Therefore, multiple types of observational data are included (see Chapter 3 for details about the data). The second aim in this section is to verify the quality of the analysis data before it is used to initialize the simulations in the next section. In this section, first a general overview of Sinlaku's ET between 18/00 and 21/00 is given, after which the environment and storm structure during are described in more detail for the tropical re-intensification period and the ET period.

4.1.1. General development

The general development of Sinlaku's ET is described based on its track, intensity, cloud structure and surface wind. In general, Sinlaku moves toward the west, along the southern coast of Japan (Fig. 4.1). It intensifies twice; in the early hours of 18 September, when Sinlaku was south of Kyushu, and just before 19 September, south of Shikoku. After 19 September Sinlaku slowly decayed. First a relatively rapid pressure increase from 980 hPa to 990 hPa is seen between 19 and 20 September, when Sinlaku moved parallel to Japan. A second, slower, decay from 990 hPa to 996 hPa occurred between 20 and 21 September, occurred when Sinlaku moved over the open ocean again. In the analysis data, Sinlaku's location fits relatively well with the Best Track, and the translation speed is almost as fast (Fig. 4.1). However, Sinlaku is further north than in the Best Track during the period when it moves near Japan (especially on 18/06, 19/06 and 19/18), with a distinction of a few tenths of a degree. The intensity of Sinlaku in the analysis data is not represented well. The pressure is too high during the entire ET period. Between 18/00 and 19/18 the analysis core pressure is on average 14.6 hPa higher than in the Best Track (997.3 hPa instead

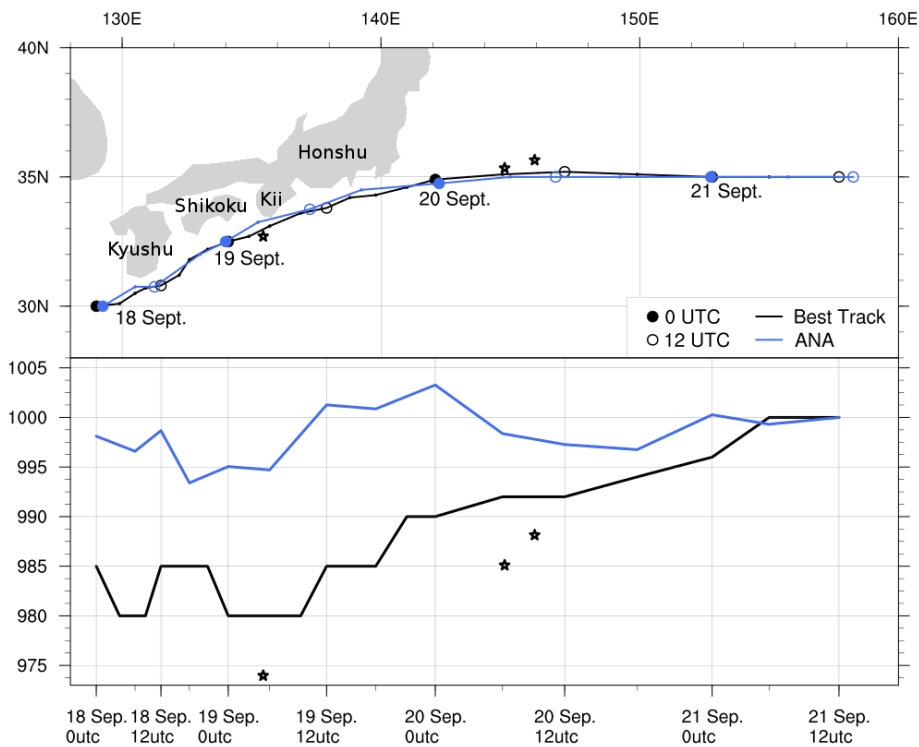


Figure 4.1. – Sinlaku's track (upper figure) and minimum central pressure development at mean sea level (lower figure, hPa) for the Best Track (black) and analysis data (blue). Stars denote the location and pressure of dropsondes nearby the cyclone center. In the track, closed circles represent 0 UTC, open circles 12 UTC at the given days. In this and similar upcoming figures the location and pressure are aligned in time for the Best Track data. For details of data used see Sections 3.1.2 and 3.2.2.

of 982.7 hPa). Also, trends in the pressure development do not fit the Best Track. The re-intensification just before 19/00, for example, is not present in the analysis data. On the contrary, a weak re-intensification is seen on 20 September, although the storm was actually decaying.

The cloud structure and the surface wind field give a first impression of the major structural changes during Sinlaku's evolution. On 17/21 the cloud structure is highly asymmetric (Fig. 4.2a). A vast cloud shield is found over and north of the surface circulation center. Several locations of deep convection (e.g. red spots, CTT < -70 °C in Fig. 4.2a) can be seen, both northwest and northeast of the center. The circulation center is still relatively circular, but this changes within the next 12 hours because the storm impinges on the Japanese island Kyushu (Figs. 4.1 and 4.2b). Although the center is not fully captured by the satellite data on 18/09, it is also not circular. High clouds are still found to the northeast of the suspected center, just above a convergence zone of tropical and coast-parallel air (132-133°E, 32-33°N).

About 10 hours later, on 18/19:15, a convective burst occurs at the same location as the the convergence zone of 18/09 (see Appendix B). This is the beginning of the tropical re-intensification, that took place until about 19/03. During the re-intensification, on 18/21, the surface circulation center is rather elliptic, with the northern branch parallel to the orientation of Shikoku (Fig. 4.2c). In the environment southeast of Sinlaku, subtropical air is advected towards the cyclone. This environmental flow converges with an airstream closer to the center, advected from the west. It forms a convergences line, with associated clouds, stretching from 134°E, 28°N to 135°E, 32°N (Fig. 4.2c). In addition, these two air streams merge with the coast-parallel flow to form a convergence zone east of the center.

After re-intensification, the asymmetric cloud shield is again the dominant structure, with high clouds northeast of the surface circulation center (Fig. 4.2d). When the storm moves eastwards and reaches the eastern border of Japan (Fig. 4.1), a warm frontal structure is indicated by a broad cloud system northeast of the low-level center (Fig. 4.2e). Meanwhile, dry sinking air, as seen by the cloudless air, is advected cyclonically around the center and arrives at the northeastern tip of the center. A cold frontal structure extends as a thin line of clouds to the south. Within the next 26 hours, the cloud structure is dominated by the development of two convective bursts; at the beginning and at the end of 20 September (see Appendix B). On 20/09:15 the decaying burst is present to the northeast of a broad circular surface rotation (Fig. 4.2f). A warm and cold front cannot be clearly distinguished anymore and the convective remnants are the dominant cloud structure.

Based on the intensity and cloud structure, the development of Sinlaku during the period 18-21 September can be divided into two periods. (1) The tropical re-intensification period includes the re-intensification of Sinlaku to typhoon intensity and its decay in the few hours afterwards, until 19/06. Convection in Sinlaku is quite active and the cloud structure is similar to step 2 of the transformation stage of ET (Fig. 2.18). Note that in the conceptual model (Fig. 2.7) this stage is reached by decay, and here the storm intensified. Sinlaku is not a typical case of ET and processes that take place during the development will therefore not necessarily be

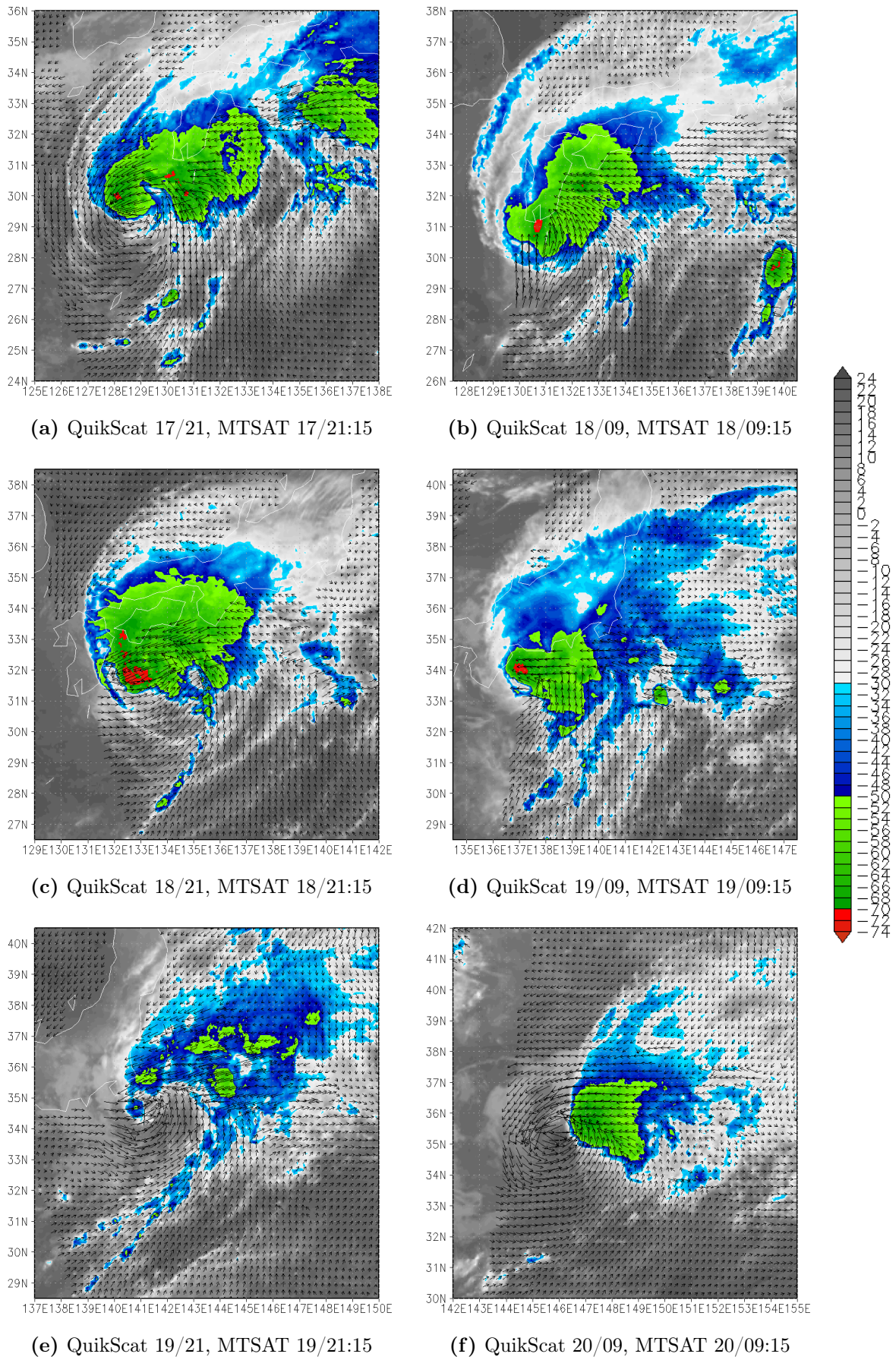


Figure 4.2. – MTSAT cloud top temperature (shaded, °C) and Quikscat surface winds (vectors). Thin white contours represent coastal outlines. For details of data used see Section 3.1.2.

consistent with the conceptual model. (2) The ET-period starts after 19/06 when Sinlaku moves along the southern coast of Honshu, and slowly decays. The storm experiences the inflow of midlatitude air as it moves over the open ocean and its cloud structure is marked, first by a frontal development, and afterwards by convective bursts. Sinlaku is now at step 3 of the transformation stage (Fig. 2.18). The partitioning into a tropical re-intensification period and an ET-period will recur throughout this thesis.

When comparing the CTT of the analysis data with the satellite imagery, it is seen that the re-intensification is not well represented. No eyewall is seen and high clouds are only present to the east of the circulation center (Fig. 4.3a), The area of high convective clouds even decreases during the tropical re-intensification period (18/18

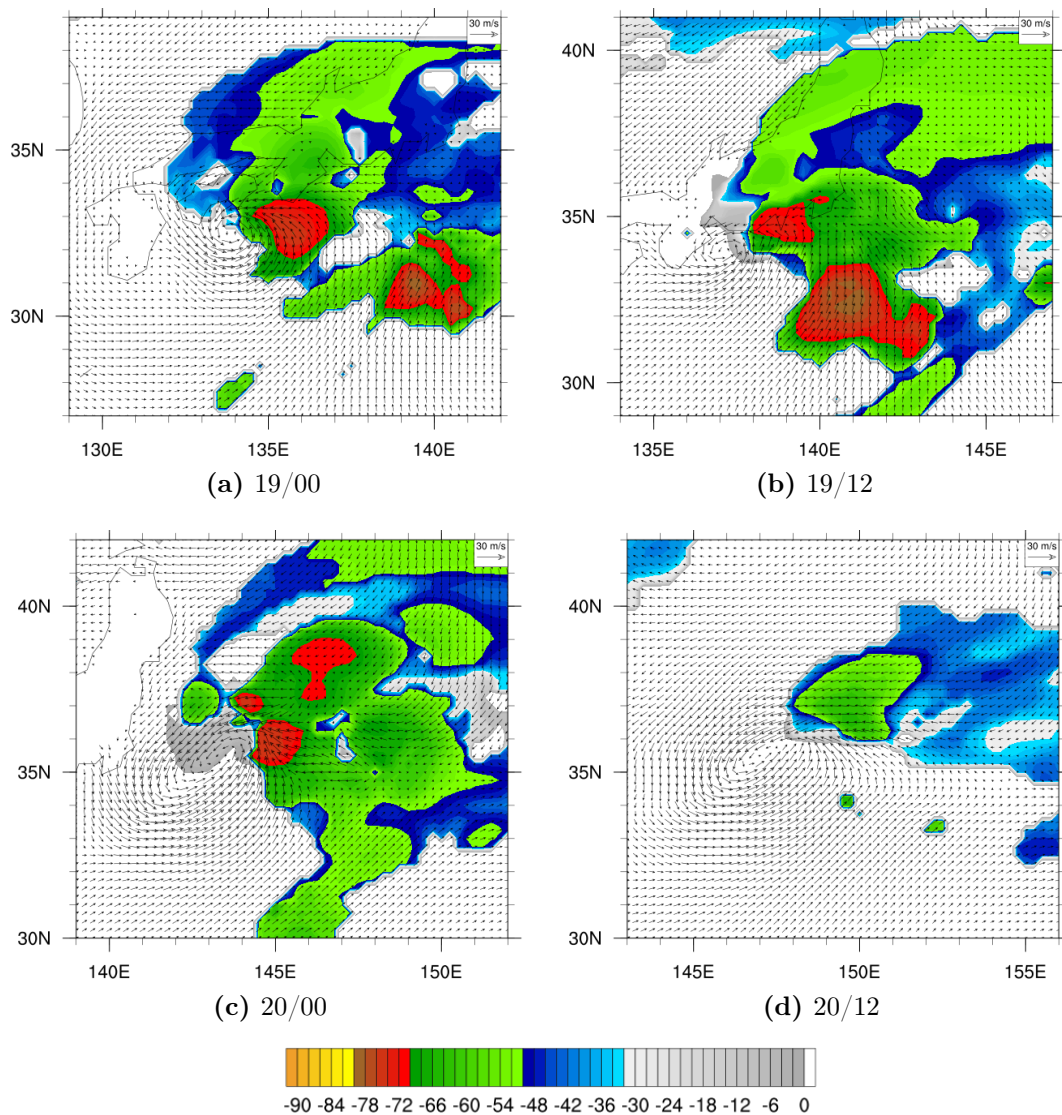


Figure 4.3. – Cloud top temperature (shaded, °C) and 10 m wind (vectors) of the ECMWF research analysis data. Thin black contours represent Japan's coastline. For details of data used see Section 3.2.2.

- 19/00), which corresponds to the pressure development of the analysis data (Fig. 4.1). Also on 19/12, the cloud structure is not well represented in the analysis data, with a major convective area to the southeast, more than 300 km away from the center (Fig. 4.3b). Additionally, Sinlaku's surface center is located too close to Japan. On 20/00, the cloud structure is more similar to the satellite imagery on 19/23:30, with a cloud shield in the northeastern quadrant, extending to 42° N and 156° E (Fig. 4.3c) as observed. The cyclonic inflow of cloudless (dry) air is, however, not well captured in the analysis data. Also the convective burst on 20/06 is not represented and only a shattered cloud shield is observed (Quinting et al., 2014). On 20/12 (Fig. 4.3d), the cloud structure better resembles the satellite data of 20/0915 (Fig. 4.2f), although the 10 m wind field is elliptic instead of circular. Overall, the active convection during tropical re-intensification and the formation of fronts during the ET period is not well captured in the analysis data.

4.1.2. Storm development during the tropical re-intensification period

The evolution of the environment during the tropical re-intensification period (18/12 to 19/06) is described based on AMVs, dropsondes and LIDAR data. During ET, features like the cirrus cloud shield and convection permit the computation of AMVs in the upper troposphere, which give an indication of the outflow of the cyclone. On 18/12, a straight westerly jet is found north of Sinlaku at $40\text{--}42^\circ$ N (Fig. 4.4a). The speed and direction are relatively similar in the analysis data and the AMVs. Outflow from Sinlaku is present northwest of the storm. The outflow has a southerly wind component which turns anti-cyclonically and merges with the jet. In the analysis data, the intensity and direction of the outflow is fairly similar to the AMVs, except for the southerly wind component in the northwestern quadrant (131° E, 34° N). This part of the outflow is weaker in the analysis, with a southwesterly wind direction.

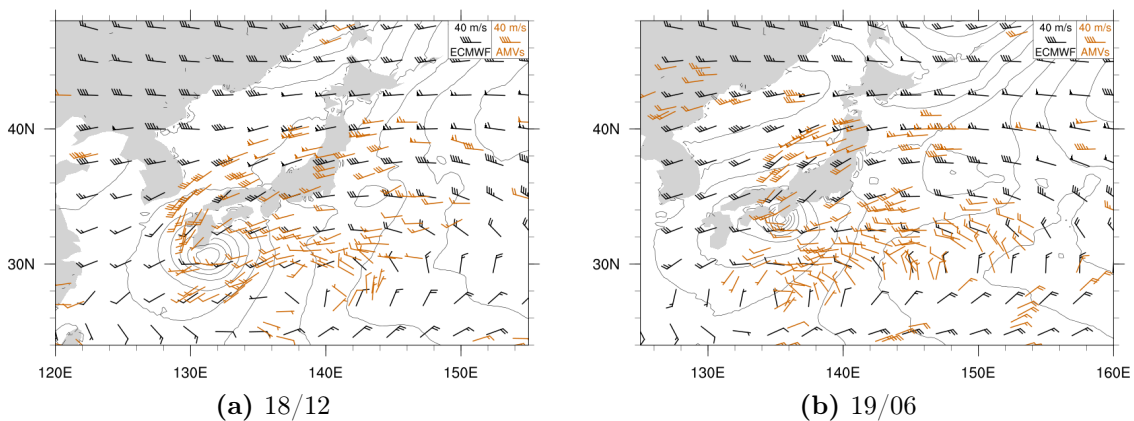


Figure 4.4. – AMVs at 150-250 hPa (orange) and wind barbs at 200 hPa (black) and mean sea level pressure over the ocean (contours, hPa) from the ECMWF research analysis data. For details of data used see Sections 3.1.2 and 3.2.2.

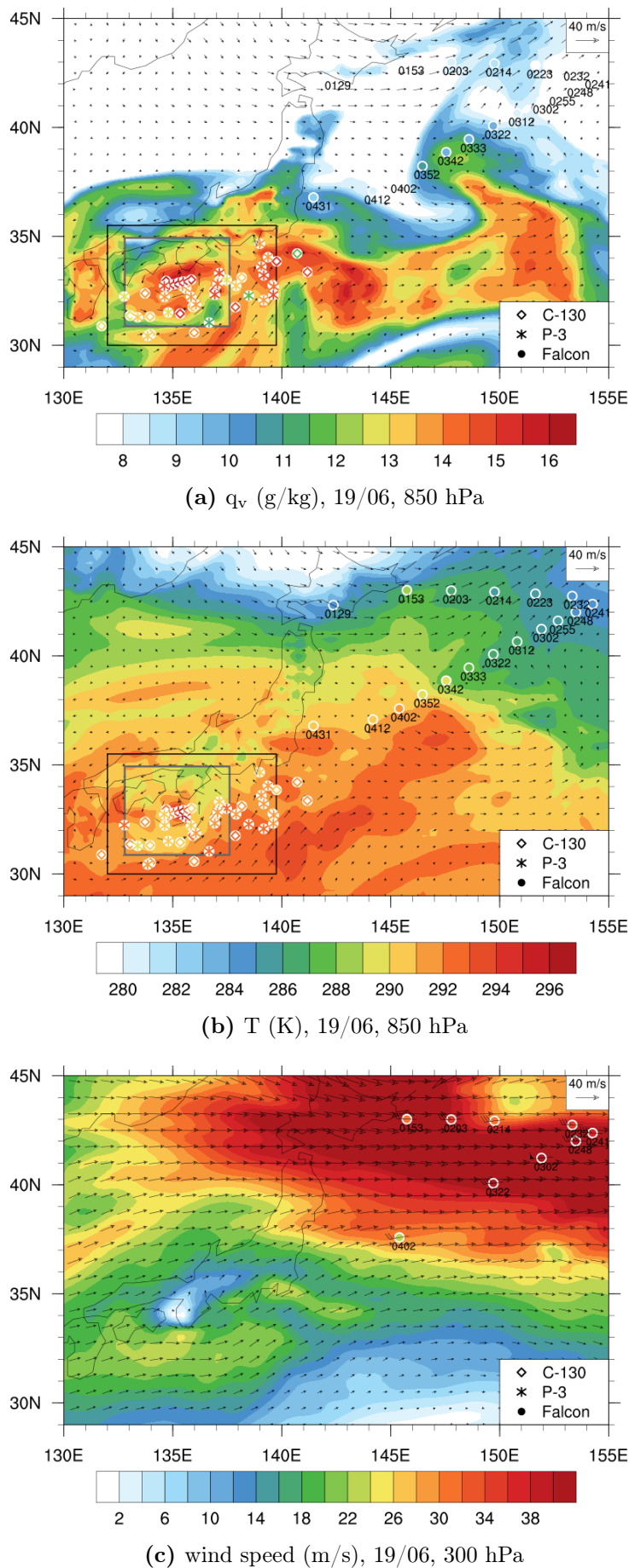


Figure 4.5. – Dropsonde values of (a) specific humidity (g/kg) at 850 hPa, (b) temperature (K) at 850 hPa and (c) wind speed (m/s) and wind direction at 300 hPa, on 19 September, on a background of ECMWF research analysis data on 19/06. Numbers represent the time (hhmm) of the dropsonde launch. A close-up (black box) including SAMURAI data (grey box) is shown in Fig. 4.9. Numbers represent the time of dropsonde launch in hhmm. For details of data used see Sections 3.1.1 and 3.2.2.

On 19/06 Sinlaku weakened after re-intensification and so did its outflow, where the wind direction has shifted from south to southwest in both the AMVs and the analysis (Fig. 4.4b).

Additional detailed information about the environment is obtained from dropsonde data and LIDAR data. DWL and DIAL lidar equipment were on board the Falcon aircraft which flew in the environmental air northeast of Sinlaku at 19 September (Section 3.1.1). A major baroclinic zone is found at this time between $42^\circ - 45^\circ$ N at 850 hPa (Fig. 4.5b). Meanwhile, the anticyclone southeast of Sinlaku transports moist tropical air northwards (Fig. 4.5a). The relatively moist air (> 13 g/kg) arrives at Sinlaku's eastern side at about 33° N. This causes a relatively moist environment south of Japan, where Sinlaku is present. At 300 hPa, a jet streak is present northeast of Sinlaku (Fig. 4.5c). The jet streak is represented well in the analysis data, except for dropsonde Falcon-0402 which is only a local feature of low wind speed around 300 hPa (not shown).

The vertical structure of the wind field along the flight path of Falcon is obtained by the DWL lidar data. Since the flight direction was initially zonally oriented but southwestwards from 02:41 UTC on, the vertical profile will be referred to as northern (southern) side before (after) 02:41 UTC (Fig. 3.1 and Fig. 4.6). The aircraft flew through the jet stream, which had a maximum wind speed of 52 m/s at 10 km height just before 3 UTC (Fig. 4.6). The jet has a steep border to the

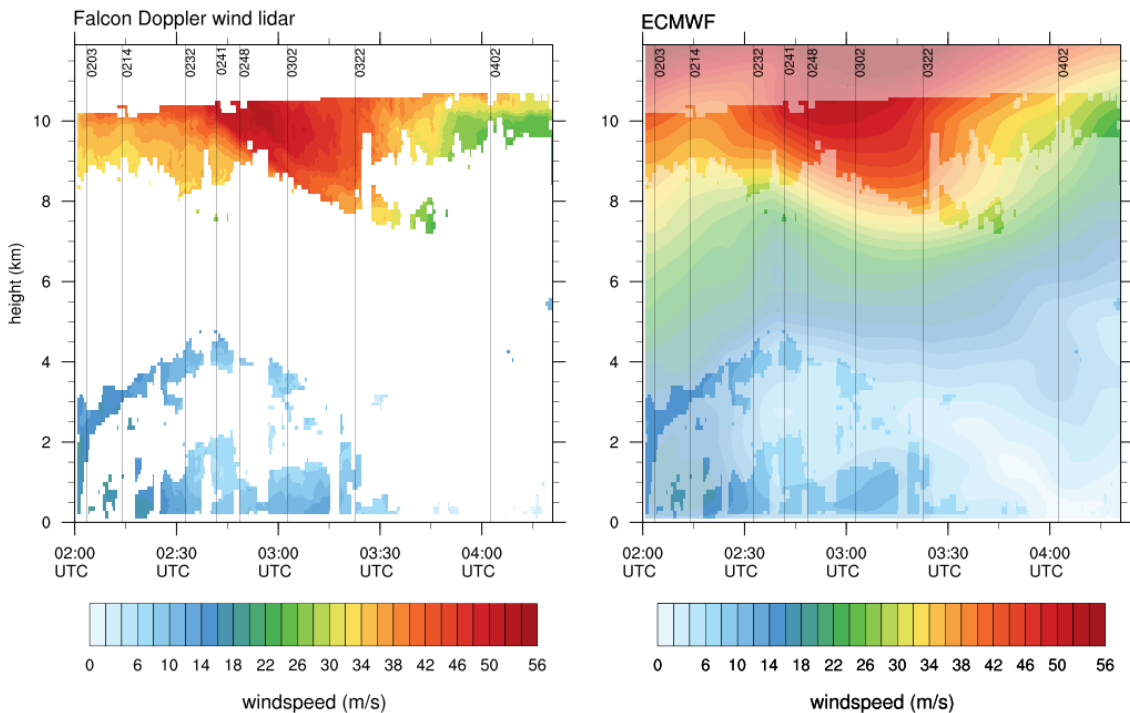


Figure 4.6. – Cross section with wind speed from Falcon DWL lidar (left) and ECMWF research analysis data (right, light colors where no lidar data is available). Locations and launch times (hhmm) of dropsondes along the flight path are given by the vertical lines. For details of data used see Sections 3.1.1 and 3.2.2.

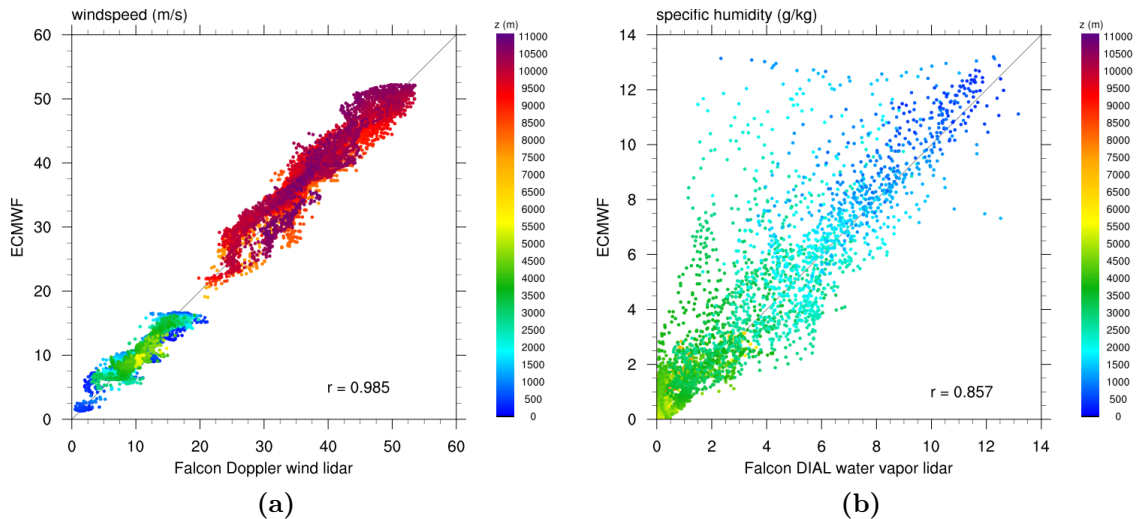


Figure 4.7. – Correlation between lidar and ECMWF research analysis data for (a) wind speed and (b) specific humidity. For details of data used see Sections 3.1.1 and 3.2.2.

south over a height of 7 to 10 km between 3:30 UTC and 3:45 UTC. In the middle atmosphere no data is available due to the presence of clouds. In the analysis data, a similar jet structure is observed (Fig. 4.6) and the two profiles have a high correlation ($r=0.985$, Fig. 4.7a). A maximum value of 50 m/s is present at roughly the same location as in the measurement data. This is, however, not the jet core, which is situated above 11 km height between 2:45 and 3:30 UTC.

The vertical structure of specific humidity along the flight path of Falcon is relatively similar in the lidar and analysis data (Fig. 4.8). Differences exist in the coarser gradients in the analysis data. Also some moist features reach a higher altitude in the analysis data, like the low-level moist plume between 3:30 UTC and 4:00 UTC (Fig. 4.8). In the horizontal overview (Fig. 4.5a) it can be seen that around this time the aircraft flew through a field of moist air that is coupled to the subtropical air, advected from the south. In the lidar data, only a small low-level moist plume is visible at 3:42 UTC (Fig. 4.8). At higher altitudes, between 5 and 8 km, a field with increased moisture content is seen after 4:00 UTC. From the horizontal distribution at 400 hPa (analysis data, not shown) it can be seen that this high altitude moist air is coupled to Sinlaku's outflowing air, and probably belongs to the clouds northeast of Sinlaku. This area of high altitude moist air is too far north and too high in the analysis data (Fig. 4.8). Overall, especially the lower levels (~ 1.5 -3.5 km height) are too moist in the analysis data (Fig. 4.7b), as also concluded by Schäfler and Harnisch (2015), who analysed WCB dynamics based on the moisture characteristics along the same flight. They found that an excess of moisture in the boundary layer near the WCB area, influenced the latent heating, diabatic PV creation and upper-level flow (Fig. 2.16, arrows 18, 19, 20). Nevertheless, besides a too moist boundary layer, the environment is represented quite well in the analysis data.

The cyclone structure shortly after tropical re-intensification can be analysed based

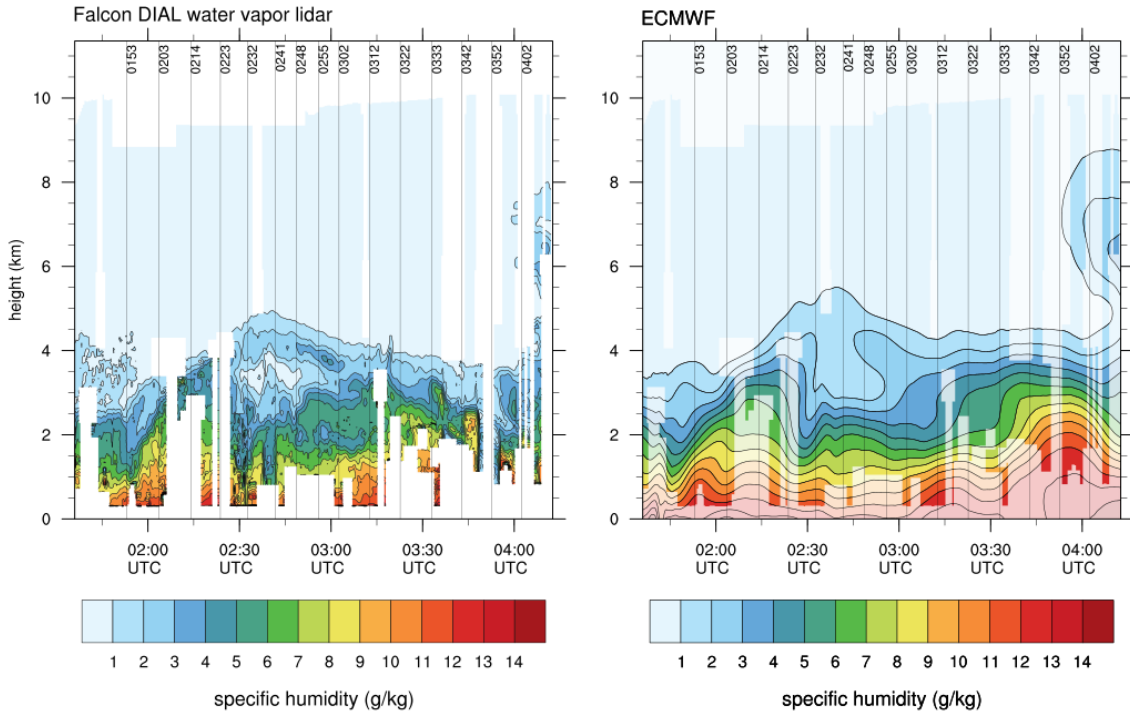


Figure 4.8. – Cross section with specific humidity from Falcon DIAL lidar (left, similar to Fig. 3a from Schäfler and Harnisch (2015)) and ECMWF research analysis data (right), transparent where no lidar data is available. Locations and launch times of dropsondes along the flight path are given by the vertical lines. For details of data used see Sections 3.1.1 and 3.2.2.

on SAMURAI data and dropsonde data (Section 3.1.1) near the storm center (Fig. 4.9). Around 4 UTC, the P3 aircraft flew through the center of the storm. Since the dropsonde values are used in establishing the SAMURAI data, they correspond well with each other (Figs. 4.9a,c,e). The SAMURAI data is now used to describe the storm structure from a different perspective than Foerster et al. (2014) did, and to verify Sinlaku’s structure in the analysis data at 6 UTC (Figs. 4.9b,d,f).

In both SAMURAI and analysis data, the circulation center at 850 hPa is surrounded by an area of relatively moist air (> 13 g/kg) (Figs. 4.9a,b). A tongue of dry air is wrapping cyclonically around the moist air, with its tip east of Sinlaku at 137° E. A tongue of almost cloudless air is seen in satellite imagery of 19/03:15 as well, where the tip reaches the eastern side of the storm also (Fig. .1d). This small-scale structure is, however, not seen in the cloud structure of the analysis on 19/06 (not shown). Differences between the SAMURAI and the analysis data are most apparent near the center of circulation. Maximum specific humidity in SAMURAI is concentrated in the center of the storm (Fig. 4.9a). This area reaches values of > 16 g/kg and has a steep negative gradient in the direction away from the center. In the analysis data, maximum q_v is found over land, to the northeast of the circulation center (Fig. 4.9b).

The temperature in the SAMURAI data at 850 hPa, is 3-4 K warmer in the core

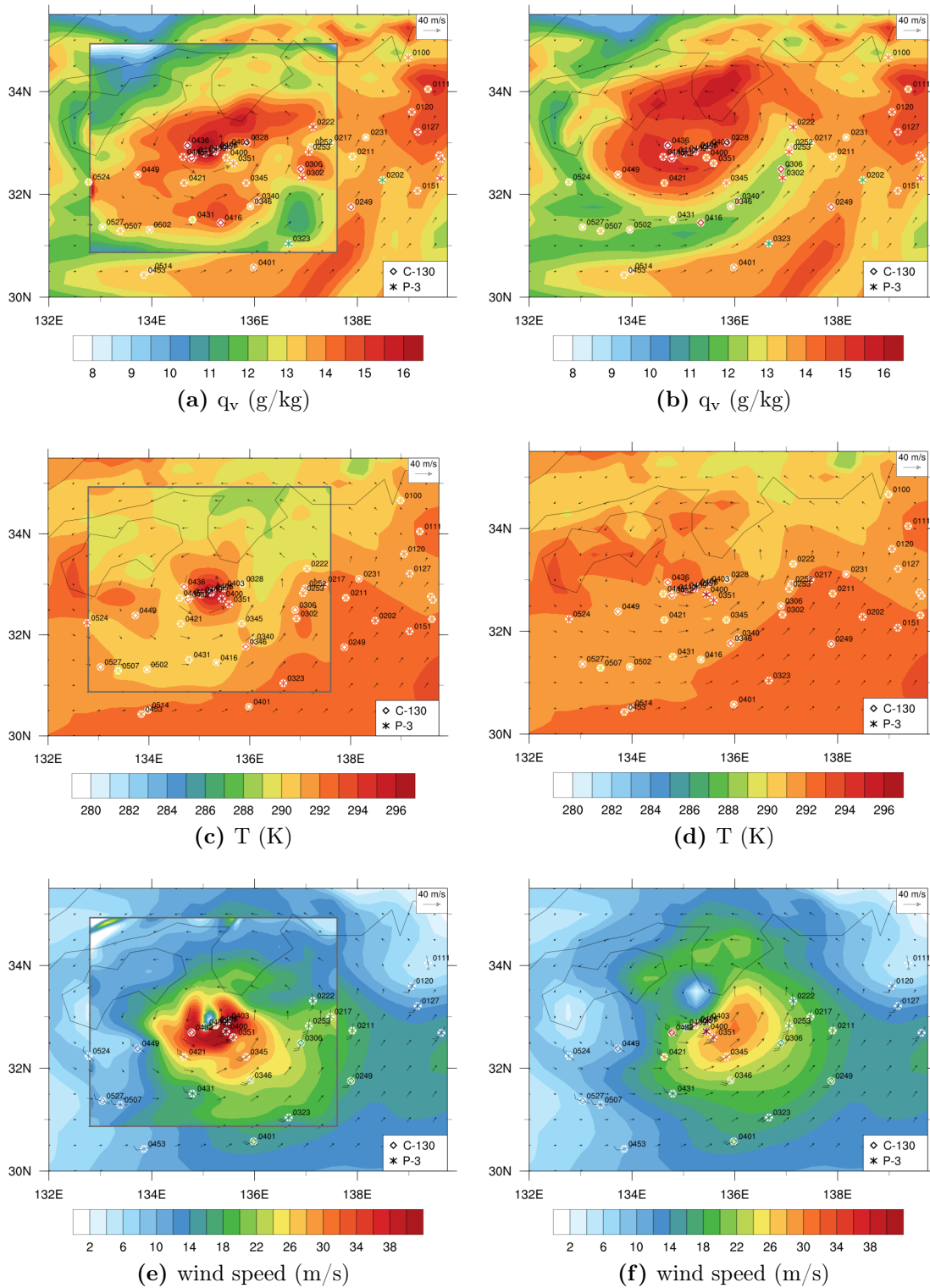


Figure 4.9. – Dropsonde values of (a,b) specific humidity, (c,d) temperature and (e,f) wind speed and wind direction on 19 September, on a background of ECMWF research analysis data on 19/06 (all figures) and SAMURAI data on 19/04 (grey box in Figs. a,c,e), at 850 hPa. Numbers represent the time (hhmm) of the dropsonde launch. Dropsondes are shifted horizontally relative to a reference time of 19/04:00, assuming a linear storm motion of $u=7.95$ m/s and $v=3.54$ m/s, after Foerster et al. (2014). For details of data used see Sections 3.1.1 and 3.2.2.

region compared to analysis data (Figs. 4.9c,d). The highest temperatures are found over sea and are roughly at the same location for both datasets. For the SAMURAI data this means that the warm core lies horizontally aligned with the moist core and circulation center at 850 hPa. In the analysis data, the warm core is present just south of the center. Outside the circulation center, the analysis data is still relatively warm, whereas Sinlaku is a distinct and compact warm anomaly in the SAMURAI data. The temperature gradient is therefore much higher in the SAMURAI data (4 K/0.5° horizontally) than in the analysis (1 K/0.5° horizontally). Since a temperature gradient is indirectly related to wind speed, a higher wind speed is expected in the SAMURAI data. A clear difference in wind field is indeed observed between the SAMURAI and analysis data (Figs. 4.9e,f).

The wind field in SAMURAI data at 850 hPa is of high quality, since the P3 aircraft with the Doppler wind radar on board flew in the core at about 700 hPa. The area of maximum wind speed has southwesterly winds and is located to the southeast of the storm in both datasets. In SAMURAI data wind speed maxima over 40 m/s are found, which is more than 10 m/s higher than in the analysis data. The system is more compact with a radius of maximum winds (RMW) of 0.3° - 0.4° horizontally (~30 - 40 km). The structure has sharper gradients than the wind field in the analysis data and is relatively symmetric over a meridional axis. The core lies over sea, just 0.5° south of the Kii Peninsula. The Kii Mountains are oriented roughly from southwest to northeast and are about 500 - 1000 m high in the southern part, with peaks above 1500 m at the northern part of the peninsula. The entire contour of > 30 m/s wind speed in the SAMURAI data lies south of the mountains (Fig. 4.9e). Only a small part of the > 20 m/s wind contour is situated over the peninsula. To the northwest, Sinlaku's outer core touches Shikoku, with, among others, the >1900 m high Mount Tsurugi at the eastern side of the island. In the analysis data, the 850 hPa windfield is twice as broad, with a RMW of about 1.0°, and highly asymmetric with a maximum wind speed of 30 m/s in the southeast (Fig. 4.9f). The core is impinging on the tip of the Kii Peninsula, so from a dynamical perspective, all air has first to be transported over the Kii mountains, and secondly over the mountains on Shikoku. Orographic effects like lifting, blocking and surface shear will highly affect the cyclonic development, in a way that does not agree with observations. Therefore, the structure of Sinlaku is not represented well in the analysis data during the tropical re-intensification period.

4.1.3. Storm development during the extratropical transition period

The description of Sinlaku's evolution is continued with the ET-period, from 19/06 to 21/00. Sinlaku was slowly decaying and influence of the jet stream became more dominant during this period. Nevertheless, the convective burst on 20/06 was accompanied by an increased area of outflow above 250 hPa, which is seen by the AMVs with southwesterly wind direction (Fig. 4.10a). The analysis data did not represent the convective burst (Quinting et al., 2014), which is reflected by the

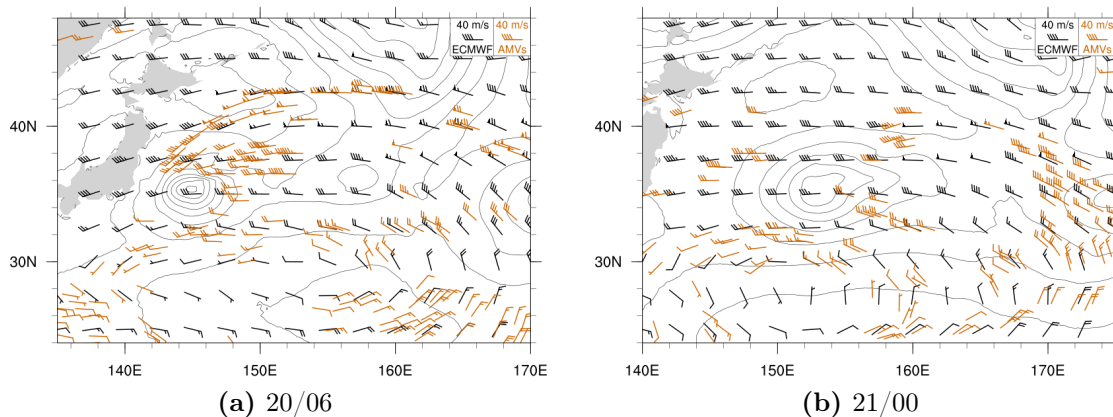


Figure 4.10. – AMVs at 150-250 hPa (orange) and wind barbs at 200 hPa (black) and mean sea level pressure over the ocean (contours, hPa) from analysis data. For details of data used see Sections 3.1.2 and 3.2.2.

wind barbs that follow the westerly direction of the jet stream. On 21/00, again a convective burst occurred. A small deviation from westerly winds is found in the AMVs in the northeastern quadrant of Sinlaku (Fig. 4.10b). The burst was, again, not observed in the analysis data, neither was a deviation in the wind barbs due to cyclonic outflow.

Around 20/06, the P3 and C130 aircrafts flew at about 700hPa, near the storm center and the WCB-like cloud structure northeast of it (Fig. 3.1). The SAMURAI data is already partly analysed by Quinting et al. (2014), who focused on the convective burst development. In vertical cross sections to the east side of the center, an upward flow from the south is seen (Quinting et al., 2014, Fig. 8). Above 5 km height this flow splits into slantwise ascent to the north, representing the warm front, and straight ascent, representing the convective burst. Deep convection is not represented in the operational analysis data, where only slantwise ascent is present (Quinting et al., 2014, Fig. 12). Quinting et al. (2014) note that the dry air intrusion is not captured well in the analysis data also (Figs. 4.11a,b).

The SAMURAI data show a comma-shaped q_v structure with highest values of 15.5 g/kg just north of the rotational center (Fig. 4.11a). At the same time, midlatitude dry air is advected from the west and arrives in the southwestern quadrant of the storm. In the analysis data the q_v field has a similar but less compact comma-shaped structure (Fig. 4.11b). The clear inflow of midlatitude dry air, however, is missing. Highest temperatures are found in the southwestern quadrant, for both the SAMURAI and analysis data (Figs. 4.11c,d). The high temperatures are co-located with the dry air, which suggests the presence of adiabatic sinking motion in the southwestern quadrant of the storm. In the SAMURAI data, the air is warmer and drier than in the analysis data. Sinlaku's wind field has a circular shape in the SAMURAI data with a center at about 145.25° E, 35.25° N (Fig. 4.11e). The wind field is asymmetric, with maxima of 34 m/s in the southeastern quadrant. In the analysis data the cyclone wind field is wider and elongated in shape (Fig. 4.11f).

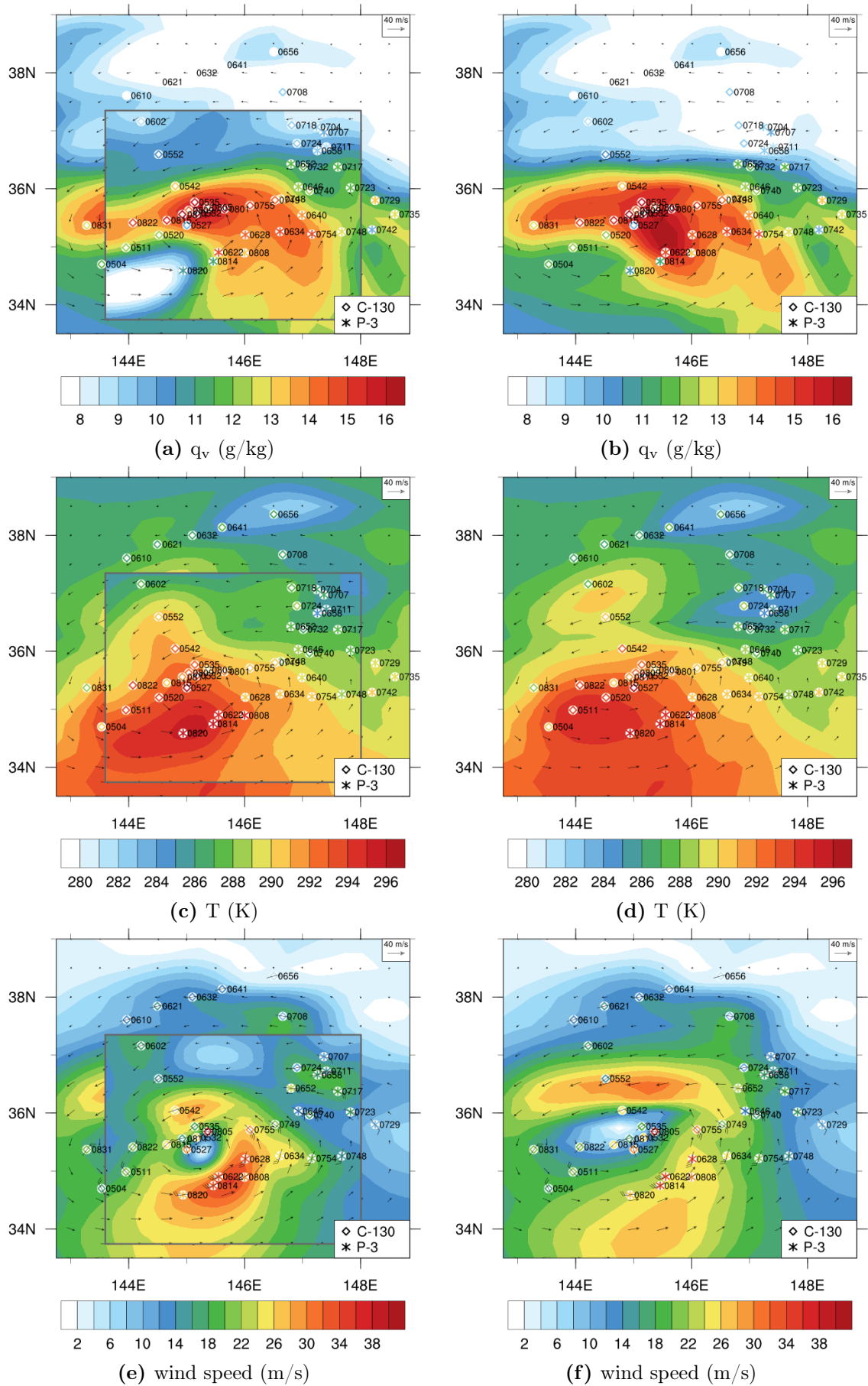


Figure 4.11. – Similar to Fig. 4.9, but on 20 September and an ECMWF research analysis background on 20/06. Dropsondes are shifted horizontally relative to a reference time of 20/06:00, assuming a linear storm motion of $u=10.5$ m/s and $v=0.6$ m/s, after Quinting et al. (2014). For details of data used see Sections 3.1.1 and 3.2.2.

The center lies more to the northwest at about 144.7° E, 35.8° N, and maximum wind speeds > 30 m/s are now found in the northern branch of the wind field.

18 hours later, on 21/00, Sinlaku is located more than 1000 km away from the Japanese coast (Fig. 4.1). The P3 aircraft was not operational at this time and consequently no radar data was available. Thus there was not enough additional data to warrant a SAMURAI analysis. The Falcon aircraft did not reach the storm, but instead measured the environment upstream of the storm. Since the dropsonde data was already assimilated in the analysis data (Section 3.2.2), they agree fairly well for both wind speed, wind direction, temperature and specific humidity (Fig. 4.12). The wind field on 21/00 at 850 hPa is not a closed circulation any more. It has broadened (RMW $\sim 2.5^\circ$), with maxima below 30 m/s are located south of the center (Figs. 4.12a,b). At 300 hPa, a small trough-structure is embedded in the straight westerly jet (Fig. 4.12c). The convective burst on 21/00 did not influence the flow at 200 hPa (Fig. 4.10b), but is co-located with the eastern flank of the trough at 300 hPa, suggesting a small modification of the flow at this level. The convective burst is accompanied by a high q_v at 300 hPa (not shown). At 850 hPa, relatively moist air is still transported from the west towards the system, but the magnitude of advection has decreased compared to 19/06 (Fig. 4.5a). A warm front is present east of Sinlaku at 36° N, seen by the maximum in moisture, a high horizontal temperature gradient and a shift in the wind vectors (Figs. 4.12a,b). The convective burst is present in this region as well and it probably developed along the warm front. Apart from that, Sinlaku is mainly embedded in midlatitude air. Dry air is still wrapping cyclonically around the center and co-located with a temperature maximum to the south, interpreted as adiabatically descending air.

4.1.4. Discussion

From the observations it can be seen that Sinlaku has a rather unusual development. It re-intensified as a tropical cyclone although ET was expected. After re-intensification, the intensity of the cyclone decreased only slowly. Sinlaku moved close to Japan during tropical re-intensification and the inflow of midlatitude cold dry air started first when the cyclone moved over the open ocean again. The low-level wind field is almost circular before and after the storm interacts with Japan. In between, the northern branch of Sinlaku's circulation has a surface wind field that is parallel to the coast. The presence of land and orography may therefore play a role in the development of Sinlaku's ET.

In the analysis data, Sinlaku was often located north of the Best Track and closer to Japan. The differences are in the order of only 0.25° latitude but, considering that the radius of the major storm axis was about 50 km at that time, significant. Nevertheless, the interaction with the land did not agree with the observations, since no coast-parallel flow is observed and the cyclone stays relatively circular near Japan, and becomes elliptic in shape over the ocean. The structure of the storm was not well represented in the analysis data either. In the first place Sinlaku is too

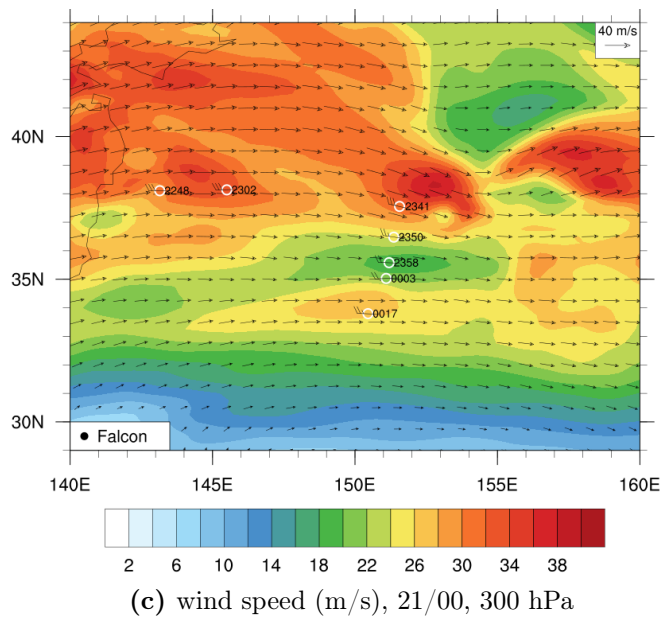
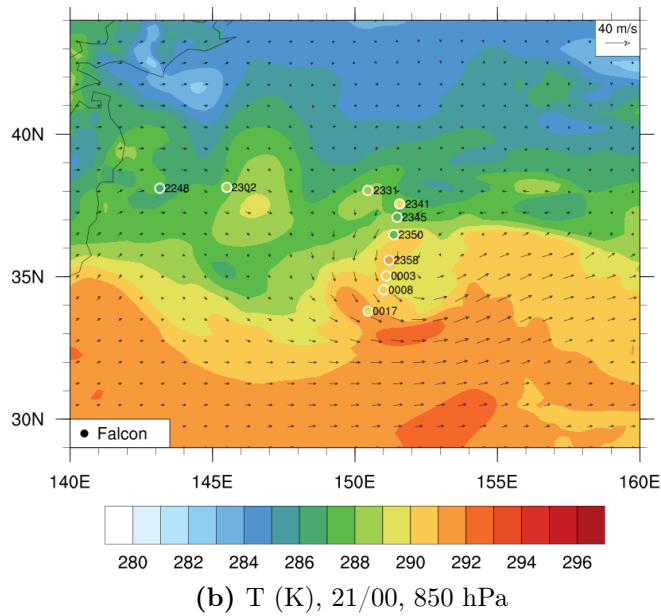
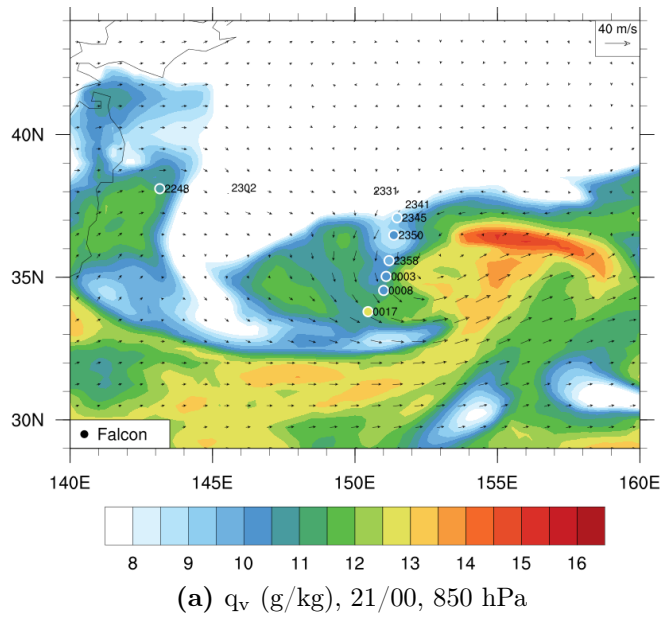


Figure 4.12. – Similar to Fig. 4.5, but for an ECMWF research analysis background on 21/00. Dropsondes are shifted horizontally relative to a reference time of 21/00:00, assuming a linear storm motion of $u=10.7$ m/s and $v=-0.3$ m/s, based on interpolation of the Best Track data. For details of data used see Sections 3.1.1 and 3.2.2.

broad and too weak in magnitude of wind speed, specific humidity and temperature. Secondly, the location of maxima and minima are not represented right.

Convective activity was observed during the tropical re-intensification (18/12 - 19/06) and a frontal structure, followed by convective bursts were observed during the ET period (19/06 - 21/00). The analysis data did not represent the timing and location of the convective clouds and the frontal development right. The upper-level outflow, following high convection was therefore also missing in the analysis data, and the jet over Sinlaku remained zonal. A different representation of Sinlaku in the analysis data has implications on, for example, the PV field and frontogenesis (Quinting et al., 2014). As a consequence, this can alter the structural development of both the storm and the environment in a model simulation

The environment in which Sinlaku moves is represented well by the analysis data, except for an excess of moisture in the boundary layer. A misrepresentation of lower-level moisture may have implications on the low-level development of fronts, clouds and diabatic PV production, when the data is used as initial data for modelling. Together with the weak representation of Sinlaku in the analysis data, it will be a challenge for a regional numerical model to produce a realistic ET development. Sinlaku's location close to Japan and the interaction with orography will only increase this challenge. In the next section the development of Sinlaku with this initially weak representation, will be tested.

4.2. Challenges in modelling with standard COSMO simulations

In this section, simulations are conducted using the analysis data as initial and boundary data (hindcasts). Five different initialisation times are used (Fig. 2.16, arrow 6), at different stage of Sinlaku's life cycle: before tropical re-intensification (18/00, 18/06, 18/12), during re-intensification (18/18) and just afterwards (19/00). Also Sinlaku's location with respect to orography is different at each timestep. Subsequently, three different setups of horizontal resolution and convection parametrisation are used (Fig. 2.16, arrows 8, 9, 10, 11): 0.25° (~ 28 km) and 0.0625° (~ 7 km), both with parametrised convection, and 0.025° (~ 2.8 km) in which deep convection is resolved and shallow convection is parametrised (for more details about the specific model setup see Section 3.2.2). These are referred to as 'LoRes', 'MiRes', and 'HiRes', respectively. For HiRes simulations, a more accurate representation of smaller scale structures is expected. The LoRes and MiRes simulations indicate how well past and present global models can capture the cyclone structure.

A combination of the different model setups results in a set of 15 hindcasts. An overview of the simulations and their abbreviations is given in Table 4.1. All hindcasts have the same domain size of $115^\circ\text{E} - 180^\circ\text{E}$, $24^\circ\text{N} - 50^\circ\text{N}$ without nesting and without a rotated pole. This corresponds to 261×105 grid points for LoRes, 1041×417 grid points for MiRes and 2601×1041 grid points for HiRes. The latter reaches the

<i>initialization time</i> (<i>dd/hh</i>)	18/00	18/06	18/12	18/18	19/00
<i>horizontal resolution</i>					
0.25°, ~28 km	H1800-lo	H1806-lo	H1812-lo	H1818-lo	H1900-lo
0.0625°, ~7 km	H1800-mi	H1806-mi	H1812-mi	H1818-mi	H1900-mi
0.025°, ~2 km	H1800-hi	H1806-hi	H1812-lo	H1818-hi	H1900-hi

Table 4.1. – Overview of the starting date and resolution of simulations that are initialised with standard initial data (ECMWF research analysis data). The code names are composed by 'Hindcast' (H), date of initialisation (ddhh) and the resolution (e.g. -hi for HiRes).

limits of what was computationally possible at the time the hindcasts were calculated. The domain is kept relatively large to give the model the freedom to develop according to the underlying physics without restrictions at the boundaries. For reliable comparison, unless otherwise stated, all simulations are interpolated to an identical grid of 0.25° horizontal resolution. SAMURAI data is not interpolated.

4.2.1. General development

The general development of Sinlaku in the hindcasts is best described based on a comparison with the Best Track data (Fig. 4.13). First, focussing on the different initialisation times for all horizontal resolutions, it is seen that Sinlaku in H1800 and H1806 has a relatively high central pressure and makes landfall over Japan (Fig. 4.13). The cyclone in these simulations is north of the Best Track after 18/12 and close to land. The cyclone cannot properly intensify from its weak initial structure to a typhoon, and the weak system moves more slowly than in the Best Track. A small intensification on the order of 1-2 hPa is observed near Shikoku. Nevertheless, the intensification is too weak, and the cyclone continues to decay. In the remaining three initialisation times (H1812, H1818 and H1900), Sinlaku does not make landfall, despite moving close to or even partly over Japan (Fig. 4.13). H1812 and H1818 both show a tropical re-intensification stage until shortly after 19/00. In these hindcasts Sinlaku is initialised as a weak system, but it had the right environmental conditions to intensify. In H1900 Sinlaku is initialised after tropical re-intensification. It does not have these favorable conditions and its central mean sea level pressure therefore stays relatively high. Continuing with the ET-period, Sinlaku is located north of the Best Track in all simulations. Its intensity decreases as expected while moving along the Japanese coast, but unexpectedly increases again by 2 to 10 hPa between 19/18 and 20/00. This unexpected intensification is observed for all hindcasts, and occurs as Sinlaku moves from the south-eastern tip of Honshu (near Tokyo) over the open ocean again.

Now, focusing on the influence of horizontal resolution on the general development, it is seen that the HiRes hindcasts show a lower central pressure during the tropical

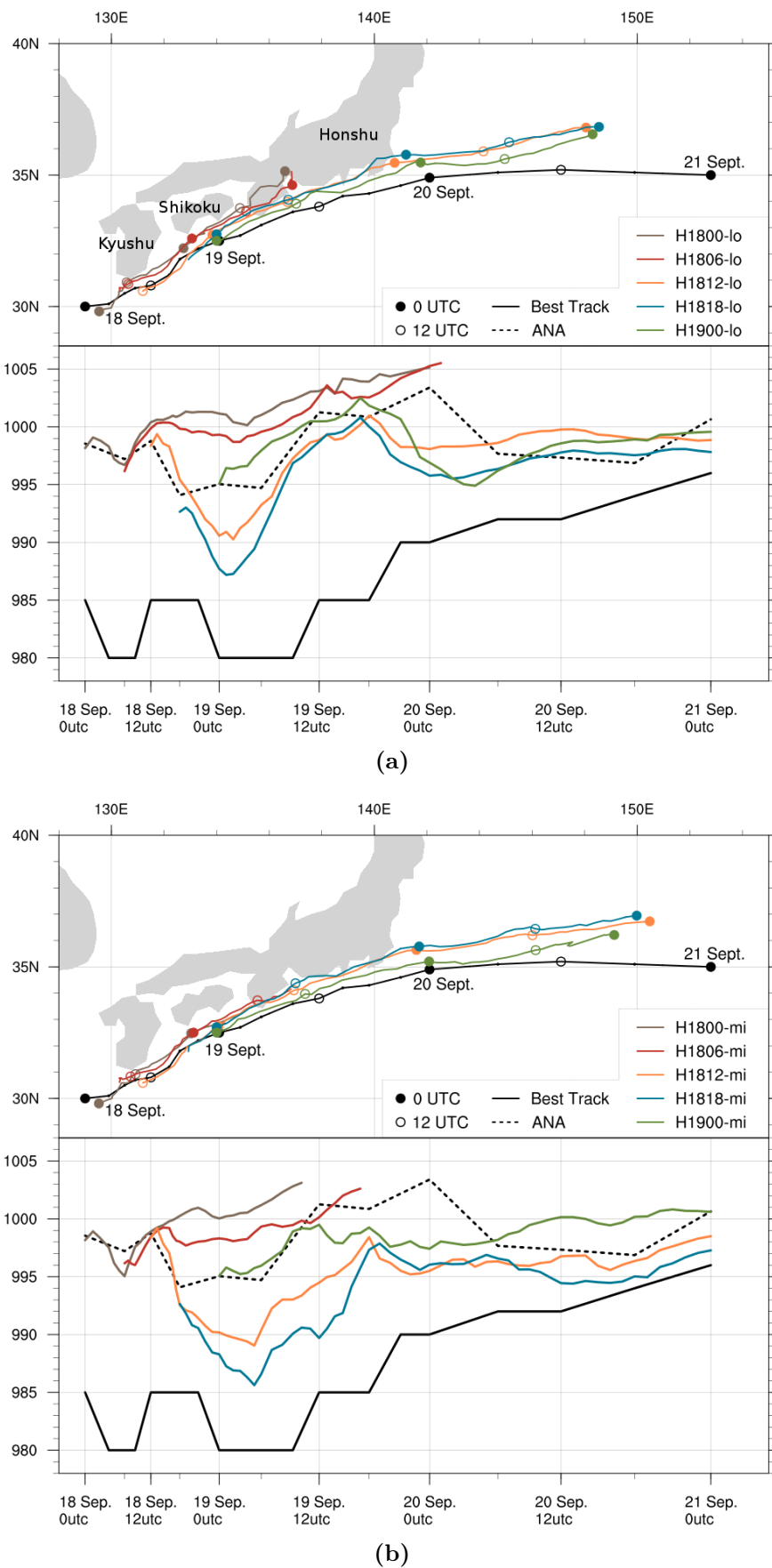


Figure 4.13. – Sinlaku’s location and minimum pressure at mean sea level (hPa) of the hindcasts given in Table 4.1 at (a) LoRes, (b) MiRes and (c) HiRes, from their starting date until 21/00. The simulations starting on 18/00 and 18/06 are only shown until landfall. Best Track and ECMWF research analysis data are shown in black (for details of data used see Sections 3.1.2 and 3.2.2).

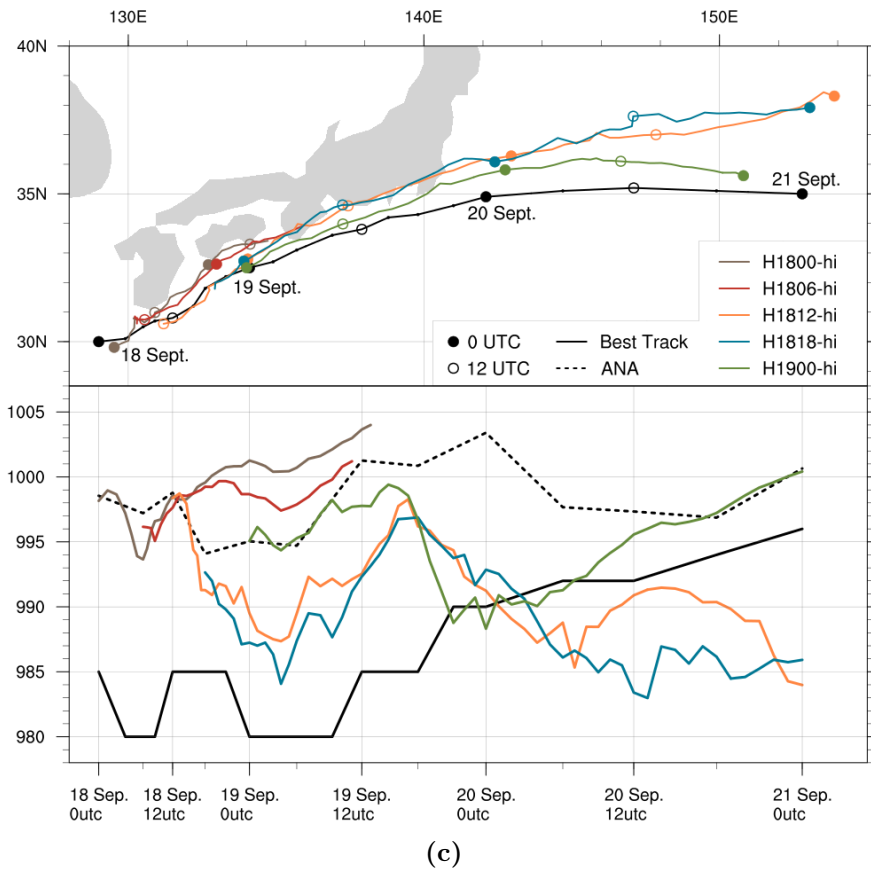


Figure 4.12. – Continued.

re-intensification period than MiRes and LoRes, as could be expected. The storm also has a faster translation speed for higher resolutions. For example on 20/12, the LoRes simulations have a difference of about 1° longitude compared to the Best Track location (Fig. 4.13a). At MiRes the difference is about 0.5° longitude (Fig. 4.13b) and at HiRes the longitudinal location is on average similar to the Best Track (Fig. 4.13c). A difference in translation speed can be related to the difference in intensity and associated vertical extent of the storm, where a higher reaching system can be influenced more by the deep layer mean steering flow in the midlatitudes.

Another remarkable difference in development between hindcasts of different resolution is found after the unexpected re-intensification of 19/18 - 20/00. Whereas the LoRes and MiRes hindcasts start to decay again with an average of 1-4 hPa in one day (Fig. 4.13a,b), the HiRes hindcasts (except H1900-hi) continue to intensify (Fig. 4.13c). In these simulations, Sinlaku reaches a central pressure in the order of 985 hPa, which is close to its intensity during tropical re-intensification, and lower than in the Best Track data. Since there is confidence in the Best Track data used here (Appendix A), this evolution is unreliable. H1812-hi and H1818-hi also show the largest northward deflection from the Best Track. The intensification and northeastward movement of Sinlaku during ET indicate an extratropical re-intensification and strong interaction with the jet stream. This would also follow

the false-alarm intensification as documented by Harr et al. (2010). In H1900-hi Sinlaku had a different development along its path and was located further south than the other HiRes simulations. It is likely that a different interaction with both the topography and the upper-level flow caused the cyclone to decay again after 20/00 (Fig. 4.13c).

Additional AMV analysis (Appendix C) shows that the upper-level flow during tropical re-intensification is captured relatively well in all hindcasts, up to 19/06. Afterwards the bias between AMVs and model output suddenly increases. A comparison of the modelled environmental wind, temperature and moisture fields with LIDAR data of the environment on early 19 September, shows a high correlation for all hindcasts (Appendix C). This suggests that the environment is represented well in all hindcasts and there is no significant difference between HiRes, MiRes and LoRes.

4.2.2. Storm structure during the tropical re-intensification period

The analysis of the general development showed that only the tropical re-intensification period is hindcasted sufficiently, and therefore only this period is considered in a more detailed analysis. For a verification of the structure of Sinlaku, the hindcasts are compared to SAMURAI data on 19/04, focussing on differences due to resolution (Figs. 4.13). The structures in H1800, H1806 and H1900 are not taken into account in this comparison because they are either unrealistic due to landfall, or still in the spin-up time of the model. The structure of H1818 is relatively similar to H1812, and therefore not shown.

Sinlaku's wind field at 900 hPa in the SAMURAI data shows an asymmetric but compact closed circulation with a RMW of $0.3^\circ - 0.4^\circ$ ($\sim 30 - 40$ km, Fig. 4.13a). In the hindcasts the wind field is less compact. Most similar is the wind field of H1812-hi, with a RMW varying between $0.4^\circ - 0.6^\circ$ around the center ($\sim 40 - 60$ km, Fig. 4.13c), whereas all LoRes simulations have a relatively broad structure with a RMW in the order of 1.0° (~ 100 km, Fig. 4.13b). Quantitatively, the HiRes hindcasts are the only hindcasts that come close to the observed maximum wind speeds. Furthermore, in the original (non-interpolated) resolution, smaller scale structures are visible in the wind field (Fig. 4.14a). SAMURAI data shows two branches of maximum wind speeds: southeast and west of the center. All simulations do represent the southeastern branch well. The second wind maximum is, however, found at different locations. In H1812-lo, it is found north of the center, where the wind starts flowing offshore (Fig. 4.13b). In H1812-hi, on the other hand, a second wind maximum is located in the northwestern quadrant of Sinlaku, parallel to Shikoku. From the vertical cross section it is seen that the strongest wind speeds are channelled between the orography and the cyclone center (Fig. 4.13c).

The warm and moist core in the SAMURAI data at 900 hPa is surrounded by air that is about 4°C colder (Fig. 4.13a, middle panel). In H1812-hi, the warm moist

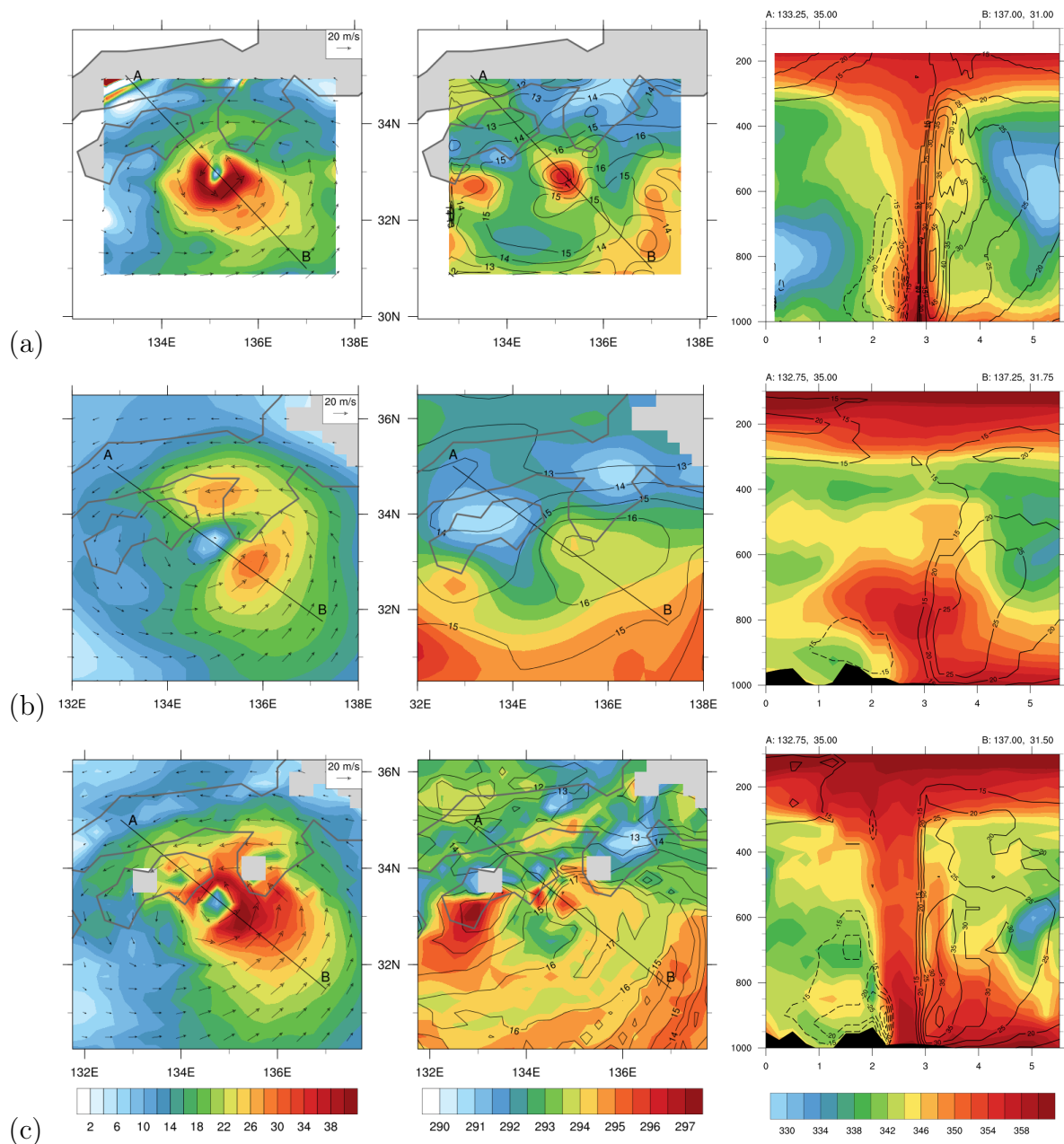


Figure 4.13. – Horizontal cross sections at 900 hPa of (left) wind speed (m/s) and wind vectors, (middle) temperature (K, shaded) and specific humidity (g/kg, contours), and (right) vertical cross sections (x-axis in $^{\circ}$) of equivalent potential temperature (K, shaded) and horizontal wind speed perpendicular to the cross section (black contours every 5 m/s, continuous/dashed into/out of the section) for (a) SAMURAI data on 19/04, (b) H1812-lo on 19/06 and (c) H1812-hi on 19/03. The grey contour represents the coastline of Japan, grey areas in the simulated data represent orography and the black lines show the locations of the cross sections. For details of SAMURAI data see Section 3.1.1.

core with surrounding colder air wrapping around the center is represented relatively well (Fig. 4.13c). A difference, however, is the transport of warm moist air to the east of the center, which is not clearly observed in the SAMURAI data. In the

LoRes simulations the horizontal temperature and moisture structure represents a baroclinic wave pattern with a weak warm core (Fig. 4.13b). This pattern resembles the third step of the ET transformation stage, although at this time tropical re-intensification just ended and Sinlaku was at the second step of its transformation (Foerster et al., 2014).

In the vertical structure, Sinlaku exhibits a tower of warm moist air in the SAMURAI data (Fig. 4.13a), co-located with a PV tower reaching up to 300 hPa (Fig. 4.14c). The PV tower has two maxima, above and below 600 hPa, and a warm core throughout the troposphere. The cyclonic circulation exhibits wind speeds > 15 m/s up to 600 hPa although maximum wind speeds are found at 900 hPa (800 hPa) in the northwest (southeast) (Fig. 4.13a). A relatively similar structure is found in H1812-hi, with a warm moist tower through the troposphere and a > 15 m/s cyclonic wind field up to 600 hPa with maxima at 900 hPa (Fig. 4.13c). Also the PV tower has two maxima, divided at 600 hPa and a warm core at least to above 400 hPa (Fig. 4.14b). In H1812-lo Sinlaku did not develop a vertically stacked warm moist core (Fig. 4.13b). Also the > 15 m/s closed cyclonic circulation does not extend up to 600 hPa, and there is no clear level of maximum wind.

Up to now, Sinlaku's structure has been compared to observational data. The description of the structure will be continued with two examples at times when no observational data are available. The focus lies on the influence of resolution and initialisation time with respect to the structural development near topography. In the first example on 18/22, Sinlaku has moved towards Shikoku and was re-intensifying tropically. The low-level wind speed increased between the circulation

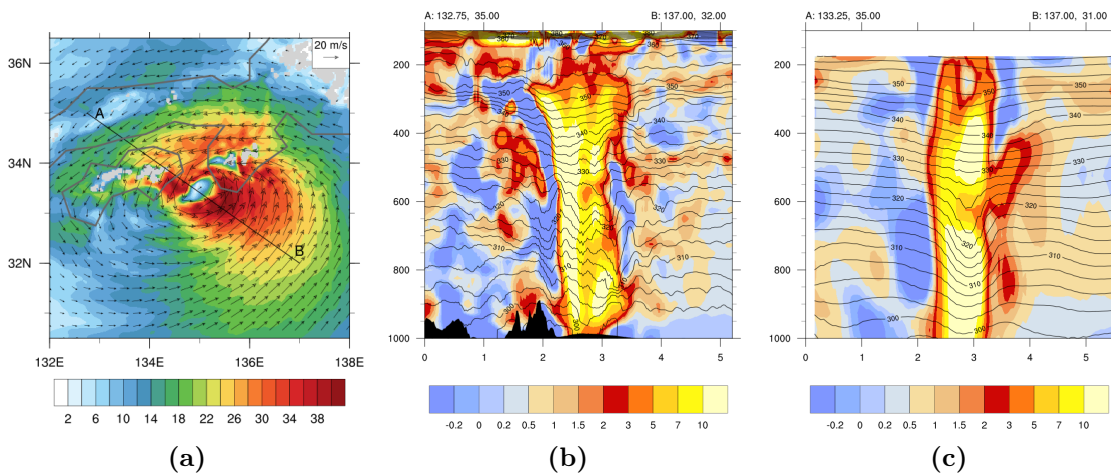


Figure 4.14. – Horizontal cross section on 19/04 and 900 hPa of wind speed (m/s) and wind vectors for (a) H1812-hi (on 0.025° resolution). Vertical cross sections of PV (PVU, shaded) and potential temperature (K, contours) for (b) H1812-hi on 19/04 (on 0.025° resolution, location of cross section is given by the black line in (a)) and (c) SAMURAI data on 19/04 (location of cross section is given by the black line in Fig. 4.13a). For details of SAMURAI data see Section 3.1.1.

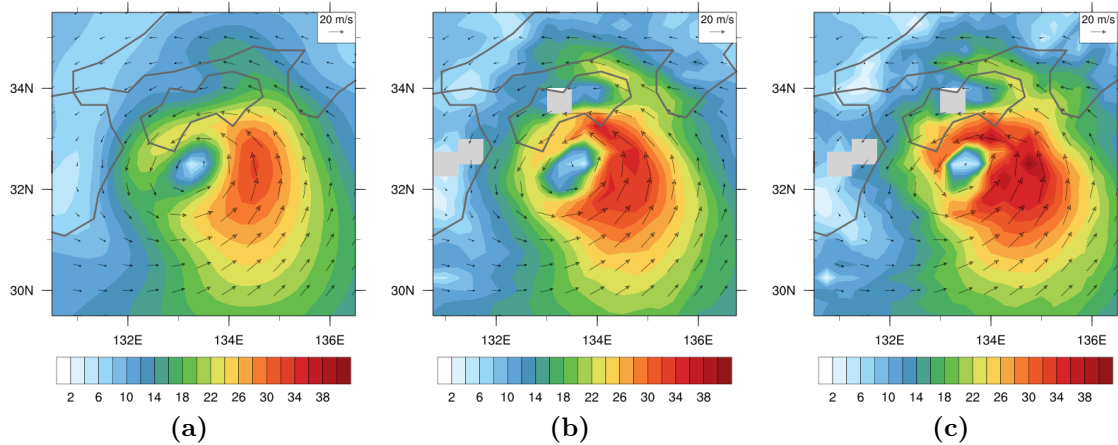


Figure 4.15. – Wind speed (m/s) of H1812 at 900 hPa on 18/22 for (a) LoRes, (b) MiRes and (c) HiRes. The circulation center is placed in the center of the figure. The grey line represents Japan’s coastline and grey areas are orography higher than 900 hPa.

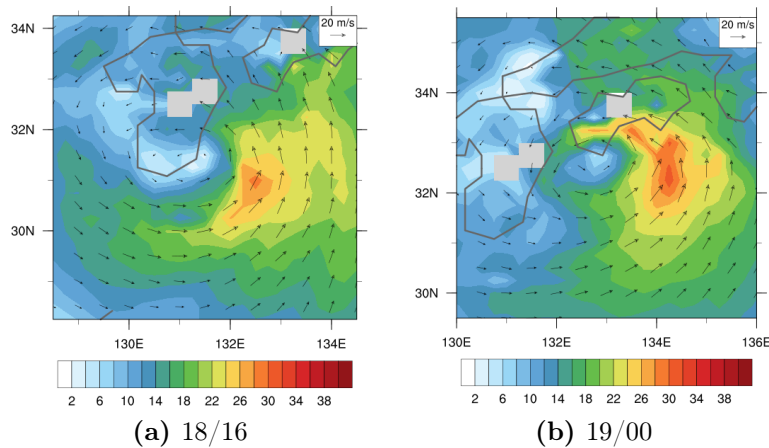


Figure 4.16. – Wind speed (m/s) of simulation H1806-hi at 900 hPa on (a) 18/16 and (b) 19/00. The circulation center is placed in the center of the figure. The grey line represents Japan’s coastline and the grey areas are orography higher than 900 hPa.

center and the island topography (Fig. 4.15). At LoRes the orography is not as high, gradients in the wind speed are small and therefore the northern branch of increased wind speed is less developed (Fig. 4.15a). In MiRes a stronger northern branch is able to develop (Fig. 4.15b) and in HiRes even more small-scale gradients in the wind speed are present (Fig. 4.15c). This indicates that the structural development of the storm is influenced by the horizontal resolution in the presence of topography.

In the second example, the hindcasts of H1806, in which Sinlaku made landfall, are considered. In these hindcasts, Sinlaku’s location just after initialization was closer to Kyushu than according to the Best Track (Fig. 4.13). Therefore, the initially

weak cyclone interacted with the topography and could not develop properly, even on HiRes. The resulting cyclonic asymmetric wind field was broad and stretched over the entire southern tip of Kyushu (Fig. 4.16a). A small re-intensification was seen when Sinlaku's circulation was present over water again and near Shikoku. Similar to the hindcasts in Fig. 4.15, a small branch of increased wind speed between the cyclone center and topography developed (Fig. 4.16b). The circulation center was, however, closer to the island (in the order of 50 km) and when a few hours later, the cyclone circulation was partly over land again, its intensity decreased.

4.2.3. Discussion

The aim in this section was to investigate how well the ET of Sinlaku could be modelled with analysis data used as initial data. The influence of initialization time and resolution are analysed, and model output is compared with observations. During tropical re-intensification and shortly afterwards (up to 19/06) the environment was represented relatively well in all hindcasts. However, the structural development of Sinlaku was diverse. The initialisation time and horizontal resolution turned out to have a major influence on the structural evolution. Initialisation time (Fig. 2.16, arrow 6) did not only influence the forecast lead time, but also Sinlaku's location with respect to topography. An early initialization (H1800 and H1806) gave an incorrect interaction with land and resulted in a decay instead of an intensification. The two hindcasts that started just before tropical re-intensification (H1812 and H1818) did represent the re-intensification well. A high horizontal resolution simulation with resolved convection (Fig. 2.16, arrows 8, 9, 10, 11) was expected to better represent the compact structure of Sinlaku than a lower resolution simulation. In the case of Sinlaku, this was beneficial to its development near orography also. LoRes hindcasts, on the other hand, represented Sinlaku as a broad cyclonic structure, with a different typhoon-terrain interaction. MiRes hindcasts represented Sinlaku relatively well but are still weaker and less compact than the HiRes hindcasts.

ET was not simulated adequately in any of the hindcasts. Despite the smaller forecast lead time, H1900 showed an ET development that departed from the observed development also. All hindcasts showed to some extent an unexpected re-intensification between 19/18 and 20/00, when the storm moved away from the Japanese coast towards the open ocean. Remarkable is that the two HiRes simulations that showed the best representation of tropical re-intensification (H1812-hi and H1818-hi), had the worst representation of ET. Their 'false alarm' extratropical re-intensification (Harr et al., 2010) is further discussed in Chapter 5. So, none of the hindcasts represented the development of both Sinlaku's tropical re-intensification and ET adequate in comparison to observations, and it is clearly a challenge to simulate Sinlaku well. This has two main reasons. (1) Sinlaku is represented in the initial data as too weak, and (2) the development near orography is an additional challenge for the model. Nevertheless, the storm structure of Sinlaku during its tropical re-intensification phase was best captured by H1812-hi and H1818-hi, and greatly improved compared to the analysis data.

4.3. Modifying the initial data for COSMO simulations

The goal of this chapter to obtain a realistic enough simulation of Sinlaku's unusual ET, including the tropical re-intensification phase and ET phase, is not fully accomplished yet. An adequate simulation was obtained only for the first phase. In this section the aim is to obtain a suitable simulation of the ET phase also. The challenges in the previous section were the weak representation of Sinlaku in the initial data and its location relative to land. To overcome these challenges, the initial conditions will be modified. This will be done in two steps. In the first place the storm structure is replaced by a more realistic structure based on observational data. Secondly, Sinlaku is moved relative to land. According to the flow diagram of Fig. 2.16, these modifications cause a difference in initial structure (arrows 1 and 5) and initial location (arrows 1 and 4), which leads to a different development and typhoon-terrain interaction (arrows 26, 27 and 28).

4.3.1. SAMURAI as initial data

The storm structure in the initial data will be improved using measurement data in the form of the gridded SAMURAI data on 19/04. Since the borders of the SAMURAI data do not match the environment of the analysis data, the SAMURAI data can not be used to initiate the COSMO model directly. Instead, the piecewise PV inversion method is used to balance the storm and smooth the borders, but retain the essential storm structure based on observations (see Section 3.3.1 for technical details on the method).

After applying the PV inversion method, the resulting PV tower has the same order of magnitude as the PV tower in the analysis data (Fig. 4.17a), which is lower than in SAMURAI data (Fig. 4.17b). This is as expected, since the SAMURAI data has a 5 km horizontal resolution. The piecewise PV inversion was only possible on a coarser grid, resulting in a new PV field with 0.25° horizontal resolution (~ 28 km, see Section 3.3.1). Nevertheless, the essential structure of the new PV field is similar to that in the SAMURAI data. An upright PV tower is seen that extends to about 250 hPa (Fig. 4.17c). A minimum in PV is seen at 600 hPa and two maxima are found, at 450 hPa and 800 hPa. This is an improvement to the tilted PV tower with a maximum at mid-levels in the analysis data (Fig. 4.17a). The cyclonic wind field in the new data is relatively weak due to the coarse resolution. Nevertheless, it has maxima in the lower troposphere associated with the low-level PV maximum (Fig. 4.17c) and the RMW is smaller than in the analysis data (Fig. 4.17a). Overall, the cyclone characteristics in the new data show a more realistic structure than in the analysis data, with potential to develop as a realistic cyclone during the spin-up time.

Although the new structure is improved, it is still relatively weak in magnitude. When a relatively weak cyclone has to develop in the first few hours of the simulation

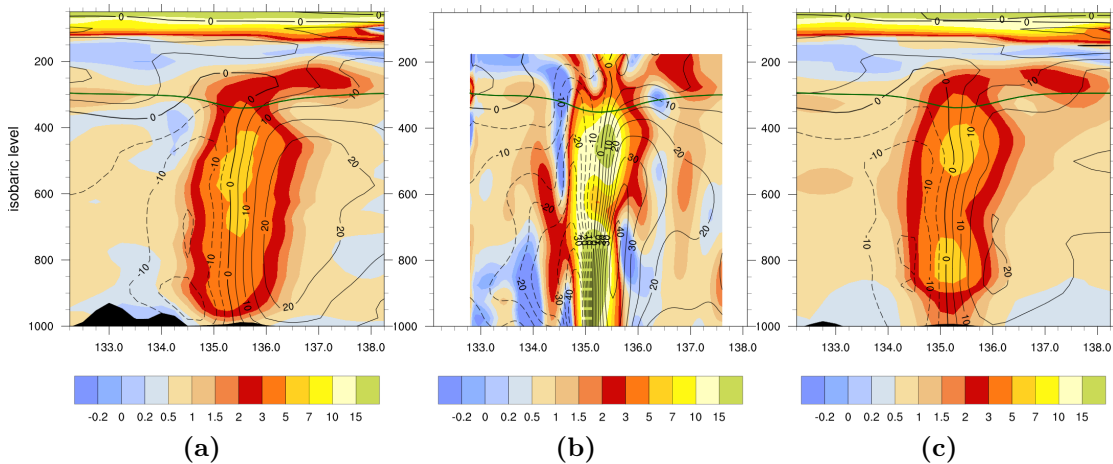


Figure 4.17. – Vertical cross section of PV (shaded, PVU) and wind speed perpendicular to the section (every 5 m/s, continues/dashed lines into/out of the section) of the (a) ECMWF research analysis data on 19/06(at 33.5°N), (b) SAMURAI data on 19/04 (at 32.9°N) and (c) the output after piecewise PV inversion (at 33.0°N). For details of data used in (a) and (b) see Sections 3.1.1 and 3.2.2.

it may not develop properly when it directly interacts with land. An improved simulation is expected when the storm is moved away from land. Thus a further modification of the initial conditions is to test the sensitivity to moving the storm away from land. For the movement of the storm, the piecewise PV inversion tool is used as well. The SAMURAI PV field is now shifted horizontally, before the corresponding wind and temperature field is computed (see Section 3.3.1). In the first place Sinlaku is shifted 0.5° south (SmS in Fig. 4.18). Secondly, a shift of 1.0° east (SmE in Fig. 4.18) is chosen because Sinlaku then has time to intensify during the spin-up time without immediately being delayed compared to the Best Track. Moving the storm more than 1.0° away from its initial position would not have improved the forecast, but instead would have altered Sinlaku’s location relative to the jet stream, the baroclinic zone and the SST field, which is unrealistic. Thirdly, it is attempted to place Sinlaku at the same location as it has in the analysis data (SmANA in Fig. 4.18). The aim of this third movement is not to improve the forecast, but to test the sensitivity of the typhoon-terrain interaction for an improved initial storm structure. Since the storm could be moved in intervals of 0.25° only, SmANA is close to but not co-located with the storm in the analysis data on 19/06 (H1906 in Fig. 4.18).

An overview of the simulations in this section is given in Table 4.2. For comparison, one simulation is a hindcast, based on the non-modified analysis data (H1906)¹. All simulations start on 19/06 and the setup of the simulations is identical to the approach in the previous section. So the only difference is the initial data. Sm0 is the simulation in which the SAMURAI PV is not moved, but implemented corre-

¹H1906 was not added in the previous section because the aim was there to include the tropical re-intensification in the simulation, which occurred before 19/06.

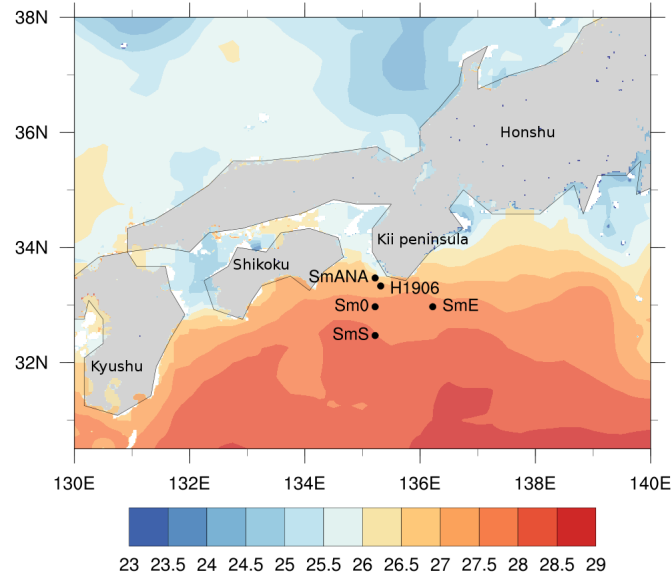


Figure 4.18. – Location of minimum sea level pressures of Sinlaku in the simulations SmANA, Sm0, SmS, SmE and H1906, relative to Japan (grey shading) and the SST as used in the COSMO model (colored shading, °C, see Section 3.2.2 for details).

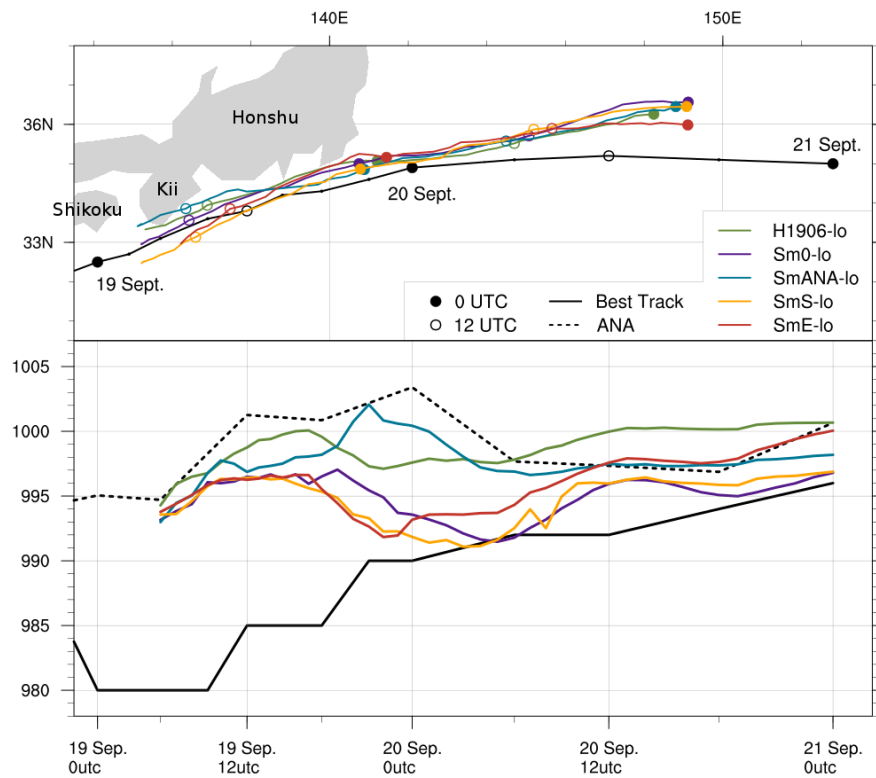
<i>data</i>	ANA	MOD	MOD	MOD	MOD
<i>movement</i>	-	-	ANA	0.5° S	1.0° E
<i>horizontal res.</i>					
0.25°, ~28 km	H1906-lo	Sm0-lo	SmANA-lo	SmS-lo	SmE-lo
0.025°, ~2 km	H1906-hi	Sm0-hi	SmANA-hi	SmS-hi	SmE-hi

Table 4.2. – Overview of the resolution and movement of simulations that are initialised with either analysis data (ANA) or modified data (MOD). The code names are composed by 'Simulation' (S), 'movement' (m), direction of movement (e.g. S for southwards) and the resolution (e.g. -hi for HiRes).

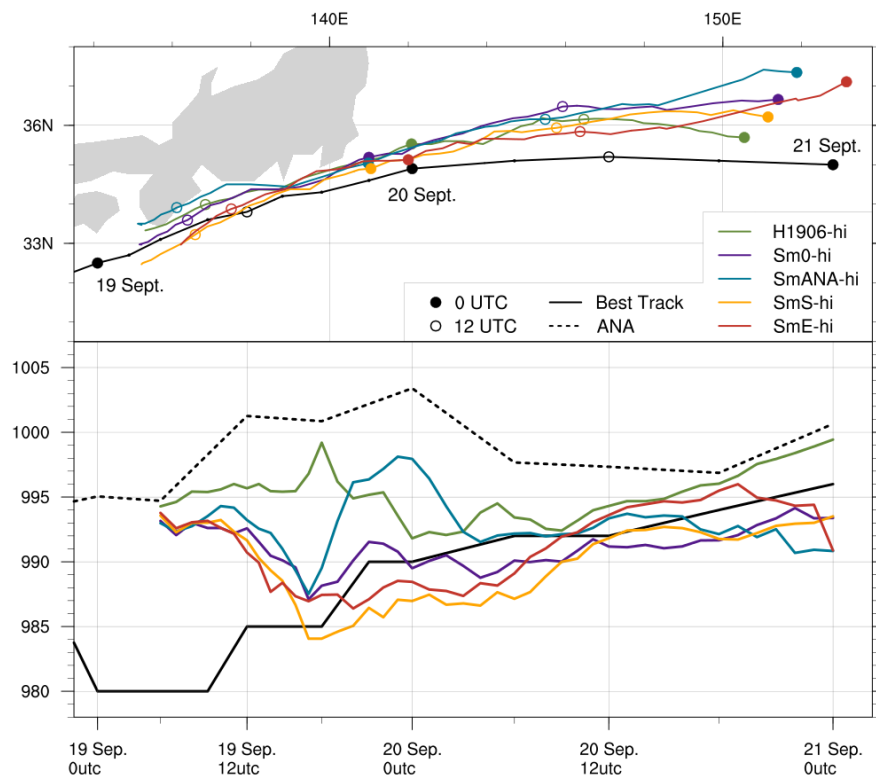
sponding to its longitude and latitude data. Nevertheless it is about 0.5° south of Sinlaku's location in the analysis data (Fig. 4.18).

4.3.2. General development

Despite different initial locations, Sinlaku moves towards Japan in all simulations and is located north of the Best Track within 12 hours after initialisation (Fig. 4.19). Instead of moving over Japan, all tracks follow the coastline and merge close to the coast on about 19/18. This suggests an influence of the Japanese coastline on the steering of the cyclone. After moving over the open ocean again, the tracks of the LoRes simulations are similar to each other, whereas the HiRes simulations show a variation in the latitudinal extent, especially in the last twelve hours of



(a)



(b)

Figure 4.19. – Sinlaku’s location and minimum pressure at mean sea level (hPa) of the simulations given in Table 4.2 at (a) LoRes and (b) HiRes, from 19/06 until 21/00. Best Track and ECMWF research analysis data are shown in black (for details of data used see Sections 3.1.2 and 3.2.2).

the simulations. At this time, Sinlaku is extratropical and more difficult to track based on the minimum p_{msl} . SmE-hi, for example, develops a burst of convection in the northeastern corner of the circulation center (not shown) which becomes the dominant minimum p_{msl} and causes a 'jump' in the track. Up to 20/12, the tracks were reliable.

In the simulations with modified data Sinlaku's minimum p_{msl} is initially only about 1° lower than in the hindcast (H1906). Despite this small difference, Sinlaku shows a different pressure development in the LoRes simulations (Sm0-lo, SmS-lo and SmE-lo), although not necessarily better. An intensification is observed between 19/18 and 20/00, which is was seen in all the hindcasts in the previous section as well, and does not agree with the Best Track. In the HiRes simulations (Sm0-hi, SmS-hi and SmE-hi), a period of intensification is observed in the first eleven hours, until 19/17, without the unexpected intensification between 19/18 and 20/00. Afterwards, Sinlaku slowly decreases its intensity. This is a more realistic behaviour and agrees with the Best Track.

A comparison between SmANA and H1906 shows differences as well. Although Sinlaku in SmANA-lo is initially only 0.17° (~ 17 km) removed from the initial storm in H1906, it moved northeastward over the Kii-peninsula in the first few hours of the simulation, instead of around the peninsula as H1906-lo did. The movement over land modified Sinlaku's structure (not shown) due to which the cyclone could not reach the same low p_{msl} as the other modified initial storms (Sm0-lo, SmS-lo, SmE-lo). So SmANA-lo did not give an improved simulation compared to H1906-lo. In the HiRes simulations, however, SmANA-hi did show a similar increase in intensity as the other modified storms, despite the fact that it was still moving over the Kii-peninsula in its spin-up time. Nevertheless, the intensity rapidly decreased when Sinlaku moved straight towards the Japanese coast on 19/18. Overall, the modified structure and movement of the initial cyclone did improve the intensity development of Sinlaku in the HiRes simulations.

4.3.3. Storm structure during the ET period

Sinlaku's structure is analysed on 20/06, when it is located over the open ocean (Fig. 4.20). From the SAMURAI data it can be seen that the wind field is asymmetric but relatively compact (RMW $\sim 0.75^\circ$) with a closed circulation (Fig. 4.20a). Two branches with wind speeds > 30 m/s are seen in the northwest and southeast. In all simulations the wind field is relatively broad (RMW within 0.75° - 1.5°). Sinlaku's circulation in H1906 resembles an almost north-south oriented ellipse with only one branch of increased wind speed at the eastern side (maximum winds < 30 m/s, Fig. 4.20b), which does not agree with the SAMURAI data. Sm0 shows a more similar shape and higher maximum wind speeds (> 30 m/s), but with only one branch of increased wind speeds (Fig. 4.20c). Sinlaku's low-level wind field is best captured in simulation SmE-hi (Fig. 4.20d). Especially the relative location and magnitude of increased wind speeds agree well with the SAMURAI data.

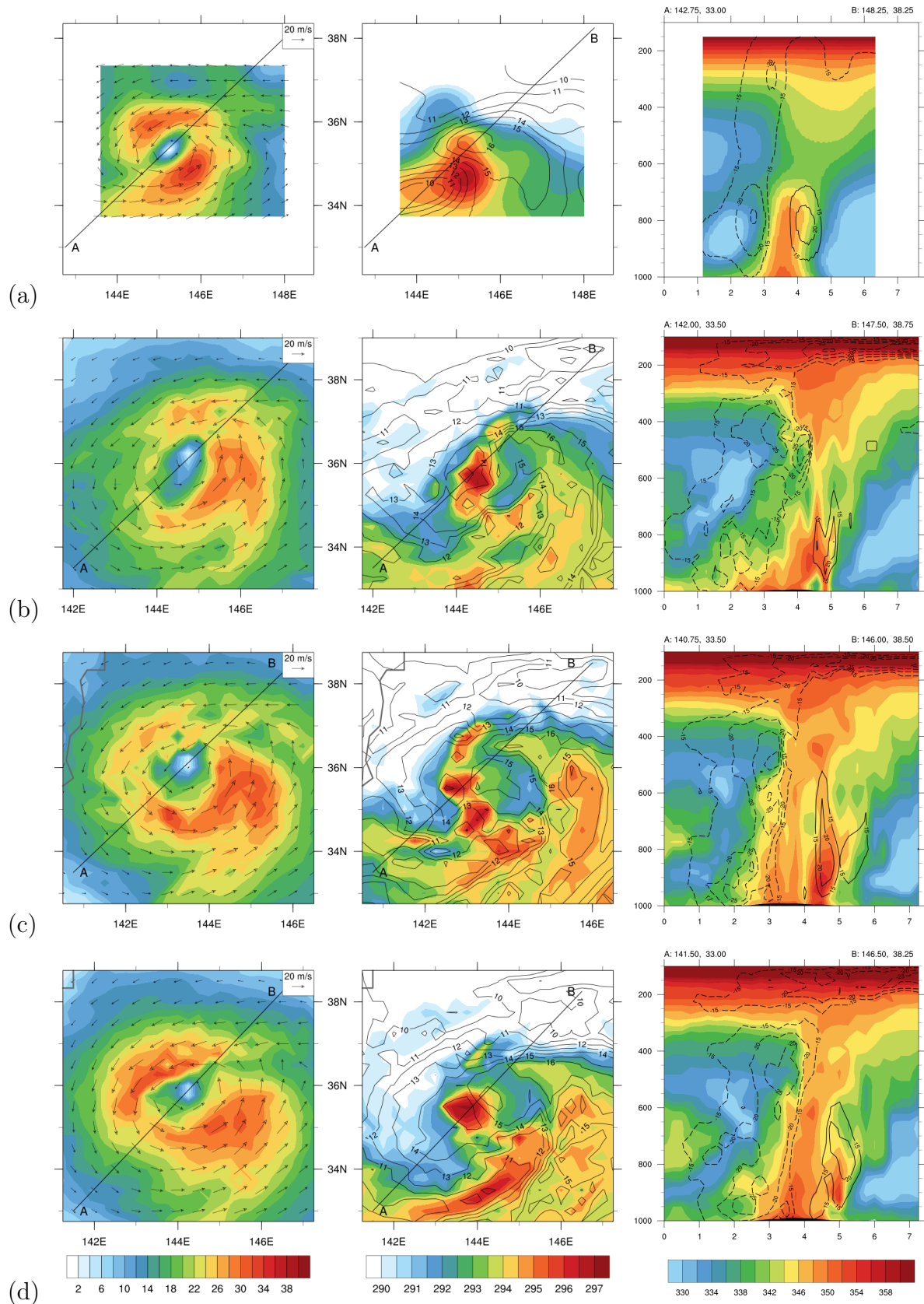


Figure 4.20. – Horizontal wind speed (left), T and q_v (middle) and vertical sections of θ_{eq} and horizontal wind speed (right) similar to Fig. 4.13 for (a) SAMURAI data, (b) H1906-hi, (c) Sm0-hi and (d) SmE-hi, all at 900 hPa on 20/06. The black lines represents the location of the cross sections. For details of SAMURAI data see Section 3.1.1.

The circulation center in the SAMURAI data is located in the area of maximum moisture, and an area of anomalous warm and dry air is present just southwest of it (Fig. 4.20a). The warm dry air was interpreted before as adiabatic sinking air. The temperature and moisture fields in SAMURAI are based on only a few dropsondes and do not necessarily give a full picture of the real situation. The HiRes simulations therefore show smaller scale features of moisture and temperature. One or more smaller scale areas of anomalously warm air are found to the southwest of the center all HiRes simulations. In H1906-hi, the moist air is only present to the east of the circulation center (Fig. 4.20b) and in Sm0-hi, dry air has already encircled the center (Fig. 4.20c). This does both not agree with the SAMURAI data. The distribution of subtropical and midlatitude air masses is best represented in SmE-hi (Fig. 4.20d). The circulation center is located in the tip of a comma-shaped moist feature, with warm and drier air directly southwest of it. In all HiRes simulations, cold and dry air (< 12 g/kg) wraps around the center at a radius of $\sim 2^\circ$, which cannot be seen in the small area of SAMURAI (Fig. 4.20).

In the vertical cross sections a tilted warm moist tower is seen, surrounded by low- θ_{eq} air (Fig. 4.20a). The structure of the tower in the HiRes simulations fluctuates over short horizontal distances (not shown) due to, for example, convective plumes which give upright regions of anomalously high θ_{eq} air. Nevertheless, the warm moist tower of the SAMURAI data is best represented in SmE-hi, with a consistent field of high- θ_{eq} air and highest magnitudes near the boundary layer (Fig. 4.20d). In all simulations, the low-level vertical wind field is relatively similar to the SAMURAI data with a maximum in (perpendicular) wind speed at 800 hPa. At the data-sparse upper levels, the quality of the SAMURAI data is less reliable.

The development of ET and structural changes is better represented in HiRes than in LoRes, as will be shown in the following example (Fig. 4.21 and 4.22). The times of the HiRes and LoRes figures are chosen so that the circulation center is at the same location. No observations are present at this time. Sinlaku has just started its interaction with the baroclinic zone which is seen by the inflow of midlatitude air to the west of the storm (Figs. 4.21). Although the location of wind speed maxima are similar in LoRes and HiRes, the magnitude is higher in the HiRes simulation (Fig. 4.21). Subsequently, the stronger wind speed in HiRes accounts for a stronger advection of midlatitude air, which circles around the center and reaches the southeastern quadrant in HiRes, while it reaches only the southwestern quadrant in LoRes (Fig. 4.21). Furthermore, the warm moist tower is undercut by midlatitude air, due to the coarse gradients in LoRes (Fig. 4.22a). In the HiRes simulation smaller scale features, with a high horizontal gradient, maintain the warm moist center below 900 hPa while midlatitude air is circling around it instead of undercutting it (Fig 4.22b).

Smaller scale features dominate the differences between the cyclone structure in HiRes and LoRes. In the HiRes simulation the cyclone center is still relatively moist (> 15 g/kg) but strong moisture gradients are present towards the dry air just to the north, west and south of it (Fig. 4.21b). A corresponding small but upright and well mixed θ_{eq} tower indicates convective activity, although slantwise ascent over

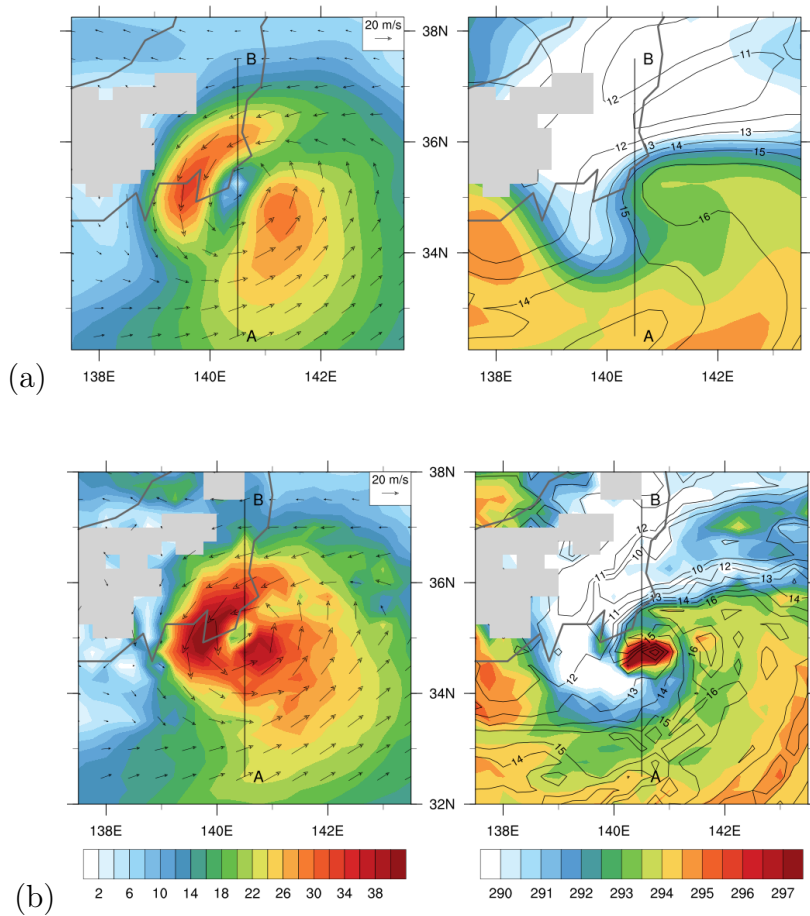


Figure 4.21. – Horizontal cross sections at 900 hPa of (left) horizontal wind speed (m/s) and (right) temperature (K) and moisture (g/kg), similar to Fig. 4.13, for (a) SmE-lo at 19/21 and (b) SmE-hi at 19/20.

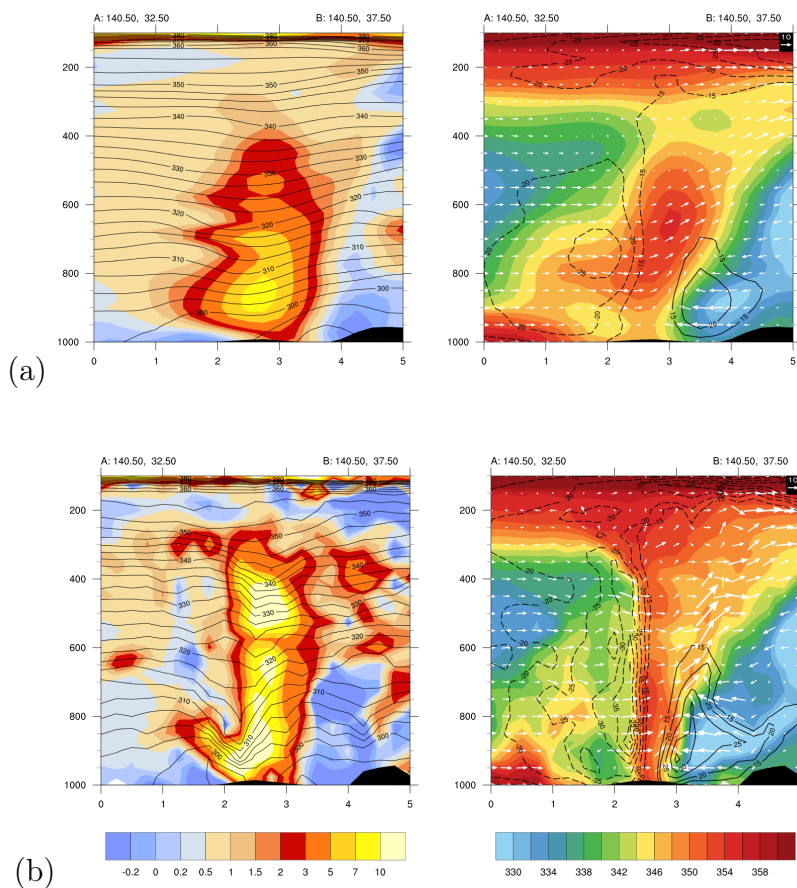


Figure 4.22. – Vertical cross sections of (left) PV (PVU, similar to Fig. 4.14) and (right) θ_{eq} (K, similar to Fig. 4.13) for (a) SmE-lo at 19/21 and (b) SmE-hi at 19/20. The locations of the cross sections is given Fig. 4.21 a and b, respectively.

the warm front north of the center is present as well (Fig 4.22b). In the LoRes simulation, a larger portion of the center is relatively moist due to coarser gradients (Fig. 4.21a), resulting in a relatively broad tilted θ_{eq} tower where only slantwise ascent is present (Fig 4.22a). Another small-scale feature only seen in HiRes at this time is the anomalous warm and dry area just south of the cyclone center, which was earlier interpreted as adiabatic sinking (Fig. 4.21b). This warm stable area coincides with the dip in isentropes and increased low-level PV south of the PV tower (at 2.2°, 900 hPa) in Fig. 4.22b. The dynamics of this feature is discussed further in the next chapter. In LoRes simulations the anomalous warm air does develop a few hours later (not shown) and is less intense and further away from the center. Overall, Sinlaku has a much compact, intenser and higher reaching cyclone structure in HiRes, as seen by the shape of the PV tower as well (Fig. 4.22). Although there are similarities between HiRes and LoRes, especially differences in smaller scale intense features like stronger inflow of midlatitude air and convective activity, may influence the complex interaction that are important for a reliable forecast.

4.3.4. Discussion

In this section Sinlaku's ET period was modelled with modified initial data. Where others used PV inversion for the goal of sensitivity analysis, here the technique was used in the first place to improve the simulation of Sinlaku's ET. In the second place, a sensitivity analysis was conducted as well. The model was initialised on both HiRes and LoRes with standard analysis data, modified data without storm movement, and modified data in which Sinlaku was shifted by 0.5° S and 1.0° E. Despite the modified structure, Sinlaku is still relatively weak in the new initial data. It needs a spin-up time to develop towards its observed intensity. In hindcasts of the previous sections it was shown that the development during the spin-up time is sensitive to Japan's topography. Therefore the storm was shifted southward, away from the terrain. Additionally, the initially weak storm may experience a weaker steering flow. Therefore the storm has also been moved eastwards, which is both downstream and further away from Japan. The eastward moved storm (SmE-hi), indeed shows a relatively good agreement with the longitudinal progression in the Best Track, whereas the southward moved storm (SmS-hi) showed a delay which originates in the first few hours of simulation.

In terms of structure, a more realistic representation of Sinlaku in the initial data, did improve the simulation, especially at HiRes (Fig. 2.16, arrows 1, 5). The additional re-location of the cyclone in the initial data resulted in a track and pressure development that agreed to the Best Track and was an improvement to the conducted hindcast (Fig. 2.16, arrows 1, 4). Consequently, there was a better timing of the interaction with the baroclinic zone, and therefore structural changes during ET were represented well. HiRes simulations were thereby of advantage in comparison to LoRes simulations. In HiRes simulations smaller scale structures are present and these are essential in the investigation of mechanisms that are responsible for

the structural changes during the complex interaction of an ET event. The storm structure of Sinlaku during its ET phase was best captured by SmE-hi, and greatly improved compared to the structure in the analysis data.

4.4. Conclusions

Modelling of ET is still a well known challenge. Still, it is aimed to model the ET of Sinlaku in a sufficient quality to justify using the simulation to explore physical mechanisms responsible for structural changes during ET. In order to do this, the overview of challenges in modelling, summarized in the flow diagram of Fig. 2.16 is used as a red thread. The initialisation of a model plays a key role in a proper simulation. Therefore it was first tested how well Sinlaku's structure and the environment are represented in the initial data (here: analysis data). The model is initialised with different setups and the initial data is modified with the use of observational data and piecewise PV inversion. The research questions regarding modelling can be answered and are given below:

How well does the analysis data represent Sinlaku's development?

The analysis data, with relatively low resolution does represent the environment relatively well, although the boundary layer is too moist. The storm structure is not represented well. The storm is too weak and the location is often too close to Japan.

How well can Sinlaku be simulated with standard initial data?

All simulations at different horizontal resolutions and different initialisation time did not represent the ET of Sinlaku properly. The intensity development was different compared to the Best Track data and the cyclone either stayed too weak or even re-intensified extratropically. Only one relatively good simulation was obtained for the period when tropical re-intensification took place, and none for the ET phase.

What is the influence of different initialization times on the simulation of Sinlaku?

An initialisation of 6 hours difference can have a significant impact on Sinlaku's development. Not only forecast lead time but also the location close to orography played a role. A short forecast lead time before tropical re-intensification gave the best results. Furthermore, when Sinlaku was close to Japan in the initial data, the storm interacted with orography during the spin-up time and was not able to intensify.

Can the piecewise PV inversion method be used to improve the initial data and thereby the simulation?

A change in storm structure did change the development of the storm when a high horizontal resolution was used. On a low horizontal resolution the storm could not properly develop near the terrain of Japan. The additional relocation of the storm by the PV method further improved the HiRes simulations. The piecewise PV inversion method would be even more helpful when it could be applied on a higher resolution grid, which is a topic of future research.

What is the influence of orography on a proper simulation of Sinlaku, from a technical perspective?

The cyclone is very sensitive to land, and cannot properly develop when it is initialized close to orography. This is valid for all horizontal resolutions that were tested.

Is a computationally expensive high horizontal resolution needed to properly simulate Sinlaku during its ET?

Yes. Sinlaku is a relatively small cyclone and its ET is influenced by the terrain of Japan. At LoRes a relatively broad structure evolves which has a different interaction with the less well represented terrain, and the baroclinic zone. At HiRes the structural changes are in better agreement with the observations.

Are any of the simulations sufficiently close to the observed evolution of Sinlaku to justify them being used to investigate mechanisms that determine the structural evolution during an ET event?

In hindcast H1812-hi, Sinlaku has a structure that is close to the observed structure during the tropical re-intensification period. Its low-level wind field is relatively compact and the vertically straight PV tower and warm moist core agree well with the SAMURAI data on 19/04.

In simulation SmE-hi, Sinlaku's structure agrees well with the observed structure during the ET-period. The shape and relative location of maxima in the low-level wind field are captured well, together with the distribution of midlatitude and subtropical air masses.

Considering model error propagation by errors in the initial data (Fig. 2.16) the simulation of Sinlaku benefited from a higher resolution including resolved convection, a better representation of orography and higher gradients for stronger wind speed in the center region (arrows 8, 9, 10, 11). The initialization time influenced the initial location and cyclone structure (arrow 6) and the initial data has been modified by changing the TC structure and location of the storm (arrows 1, 4, 5). This gave a better typhoon-terrain interaction (arrows 26, 27, 28) and a more realistic development of the storm after Sinlaku moved over the open ocean again. In this case study it was therefore of great importance to properly initialize the simulation in order to get a reliable simulation. Finally two simulations are selected that will be analysed in the next chapter: one simulation for the tropical intensification period (H1812-hi) and one simulation for the extratropical transition period (SmE-hi), both at high horizontal resolution.

5. Structural changes during the ET of TY Sinlaku

In this chapter the focus lies on the dynamical development of Sinlaku during ET. The aim is to find mechanisms that are responsible for the intensification and the decay of the cyclonic system. This chapter is divided in two main sections that represent two time periods: the tropical re-intensification phase and the ET phase. In both sections the analysis is conducted based on high resolution simulations, allowing a detailed depiction of relevant flow features.

5.1. The re-intensification as a tropical cyclone

The tropical re-intensification of Sinlaku is analysed from 18/18 to 19/06, based on the high resolution simulation H1812-hi. The contributing mechanisms are investigated by the use of trajectory analysis and vorticity budget analysis.

5.1.1. Overview

The general development of Sinlaku can be described as an intensification during the first 18 hours of simulation H1812, a decay in the middle 12 hours, and a second intensification period afterwards (Fig. 5.1). The first intensification period has a tropical character and is the main focus of this section. The second intensification period has an extratropical character and will be discussed in section 5.2.3. The first hours of the simulation are marked by an intensification between 18/12 and 18/17, that belongs to the spin-up time. Afterwards, the pressure at mean sea level stays relatively constant until a sudden intensification is seen on 19/00 and a rapid decay on 19/06. The PV and relative vorticity in the center (within a circle of 1° radius) show a constant increase until 19/00, after which both decrease.

During the period of 18/18 to 19/06 Sinlaku moved northeastward, with a translation speed that increases from 8 to 9 m/s. The direction and speed of the track is relatively similar to the 950-250 hPa average environmental flow, which suggests that Sinlaku is mainly steered by the environmental flow. A strong variation in hourly translation speed suggests, however, that also other processes play a role, although they are of minor importance. Topography, for example, turns out to have no major influence on the distribution of vertical motion, and therefore it also has no

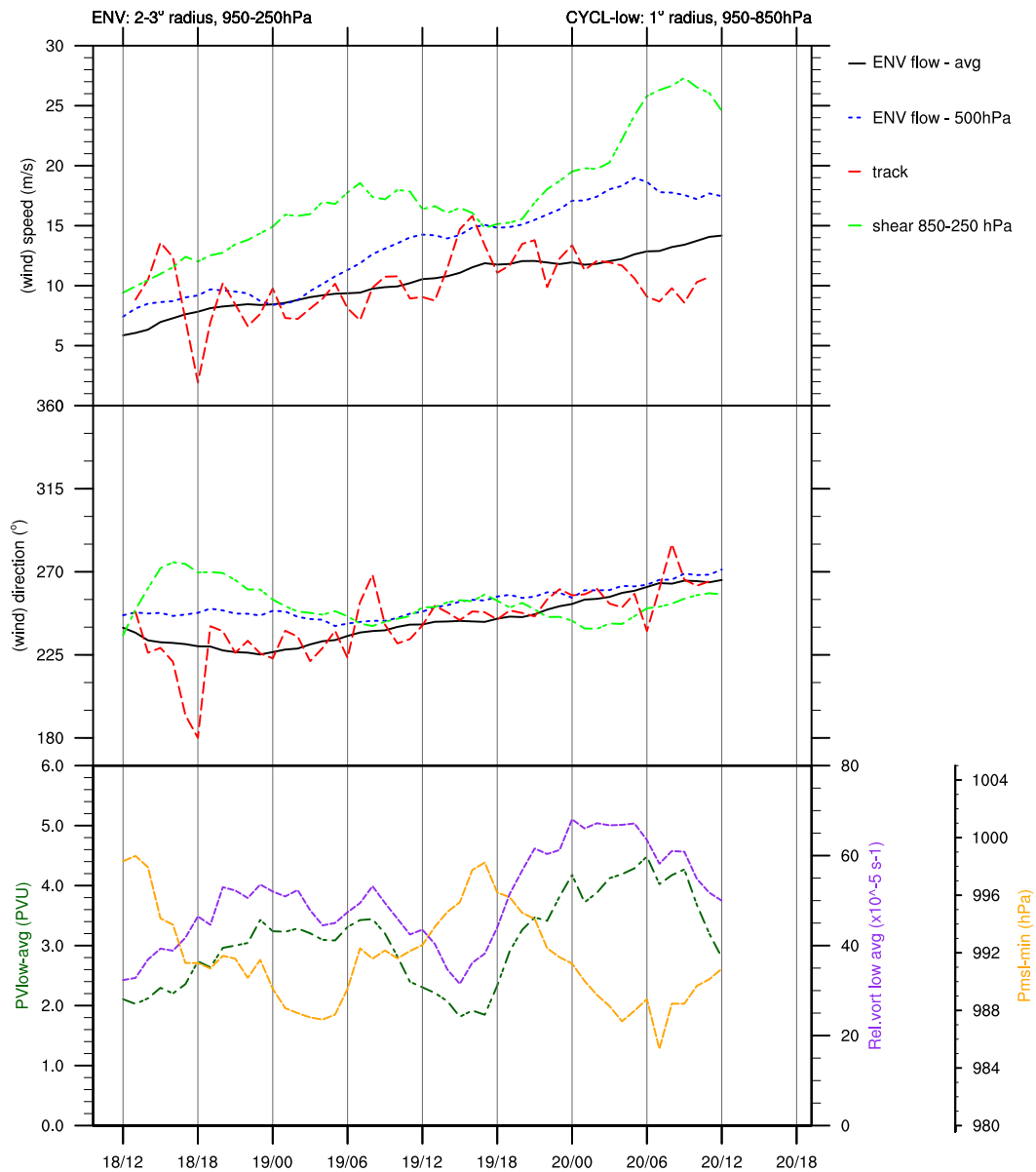


Figure 5.1. – Overview over time of the speed (upper panel) and direction (middle panel) of Sinlaku’s track (red), the environmental flow within a circle between 2° and 3° radius around the cyclone center at 500 hPa (blue) and averaged over the layer 950-250 hPa (black), and the vertical wind shear within the same circle around the center, between 850 and 250 hPa (green). The lower panel shows the minimum mean sea level pressure of Sinlaku (yellow) and its average PV (dark green) and relative vorticity (purple) within a circle of 1° radius around the cyclone center in the 950-850 hPa layer.

significant influence on the location of maximum diabatic heating that could cause track deflection. During this period, the environmental shear increases from 12 to 18 m/s and has a westerly direction. The magnitude of shear is still below 20 m/s which is in the range that the cyclone is resilient to the shear, so that the vertical mass flux is enhanced (Davis et al., 2008).

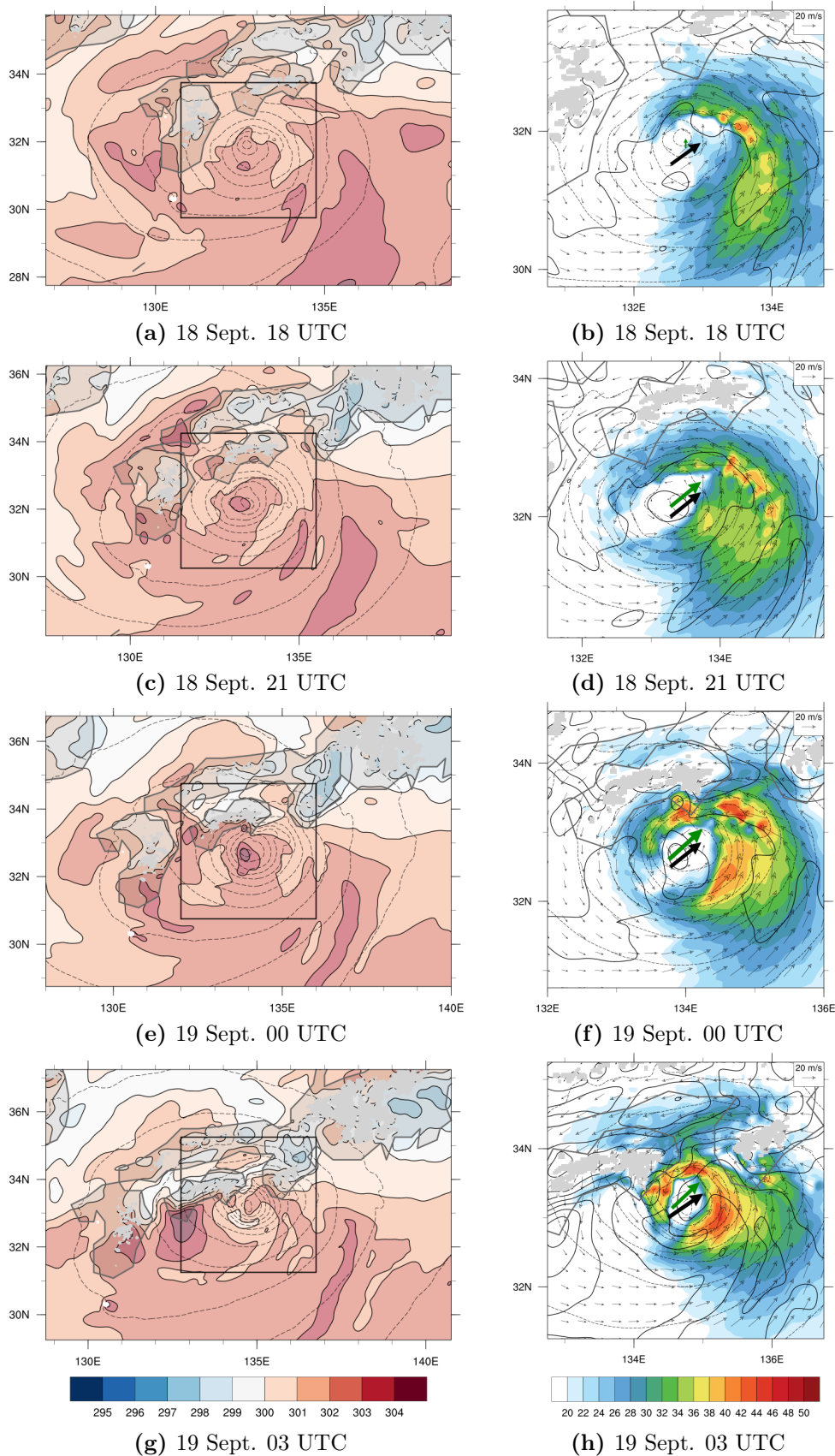


Figure 5.2. – Overview of potential temperature (shaded, K) and geopotential height (dashed contours) at 925 hPa. The black box marks the area of the panels to the right, which zoom in on horizontal wind speed (shaded), potential temperature (contours) and wind vectors, at (a,b) 18/18, (c,d) 18/21, (e,f) 19/00, (g,h) 19/03 and (i,j) 19/06. The green arrow represents the direction and speed of the cyclone, the black arrow represents the environmental flow and the grey areas represent orography.

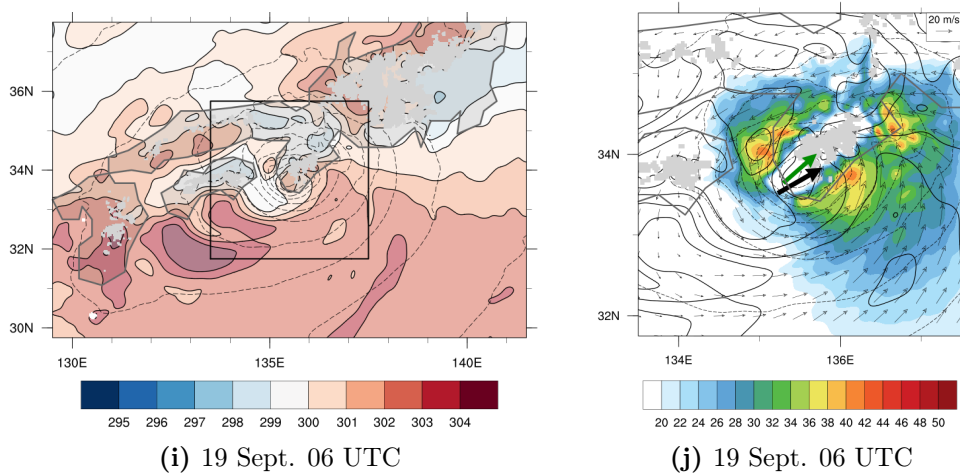


Figure 5.1. – Continued.

During the tropical re-intensification period, Sinlaku moved close to Japan. On 18/18, its center is still warmer than its environment, and the storm has an asymmetric wind field, with a branch of increased wind speeds to the northeast (Fig. 5.2a,b). When Sinlaku moved closer to Shikoku¹ on 18/21, its northern branch flows parallel to the island and a sharp change in wind direction is seen at 134°E, 32.75°N (Fig. 5.2d). An explanation of this behaviour can be the channelling of air between the cyclone center and the orography at Shikoku. At this time, the warm air has become more aligned with the geopotential height center, suggesting a more axi-symmetric system (Fig. 5.2c). Six hours later, on 19/00, when the central pressure has increased, Sinlaku has an almost closed circulation with increased wind speeds of >20 m/s (Fig. 5.2f). Also the temperature in the center has increased and Sinlaku is still warmer than its environment (Fig. 5.2e). On 19/03, both the northeastern and northwestern branches of the cyclonic motion are parallel to the orography and may be influenced by channelling (Fig. 5.2h). The wind field becomes stronger and contracts, and colder air is flowing cyclonically around the center (Fig. 5.2g). Finally on 19/06, Sinlaku moves over mountainous terrain, which weakens its circulation, while additional cold air flows in at the west side, resembling cold air inflow during ET (Figs. 5.2i,j). Additional features that can be observed are the fields of warm air southwest of Shikoku on 19/03 and 19/06, indicating adiabatically warmed downslope winds.

The re-intensification of Sinlaku to typhoon intensity, with tropical properties like an eyewall, was quite remarkable. There are multiple circumstances that can promote a re-intensification. In the first place, the ocean temperature south of Shikoku was still > 26 °C, favorable for TC development (Fig. 4.18). Secondly, Foerster et al. (2014) argued that the re-intensification was supported by the influence of vertical wind shear. An additional mechanism can be the influence of topography, since Sinlaku was able to undergo tropical re-intensification when it was close to

¹For a map of Japan with the names of relevant locations, see e.g. Fig. 3.3

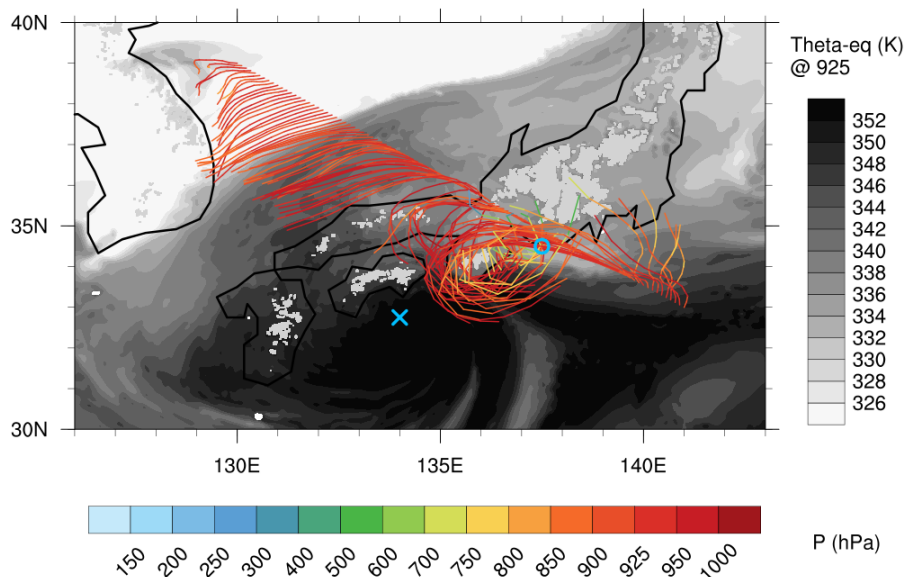


Figure 5.2. – 12-hour forward trajectories starting at 925 hPa on a northwest-southeast directed line crossing Japan (solid black line) on 19/00. The colors of the trajectories show the pressure (hPa). Equivalent potential temperature at 925 hPa at trajectory starting time is given in gray shades. The location of minimum mean sea level pressure of Sinlaku is marked by a blue cross (at trajectory start) and circle (at trajectory end). This Figure is shown in Evans et al. (2017) also.

Japan. The main influence of the land is orographic blocking of air flow in the lower troposphere. Trajectories reveal that midlatitude air at lower levels moves around the Japanese mountains (Fig. 5.2). South of Japan Sinlaku was located in a sub-tropical warm-moist air mass and protected from the intrusion of cold dry midlatitude air. At the time that a local pool of cold air is advected from the east and southwards between the islands Shikoku and Honshu (Fig. 5.2, 135°E, 34°N, and Fig. 5.2i), the system weakens suddenly. This leads to the hypothesis that cold air was blocked by the islands of Japan and the protected warm and moist area in which Sinlaku was present, was favourable for re-intensification.

5.1.2. Mechanisms behind tropical re-intensification

At the beginning of re-intensification, a rain band is observed to the northeast of the center. This region is marked by convergence and ascending motion and a band of high PV (Figs. 5.3a,b). A vertical cross section through the band reveals an almost barotropic environment (Fig. 5.4a). The ascent crosses the isentropes and has therefore a convective character instead of being slantwise. Only near the surface is a sharp temperature gradient observed, above which the ascending motion is present (Fig. 5.4a,b, at 2°). This area of cooler air may as well be present due to evaporative cooling of the precipitation below the convective area. Within the deep convection, condensation causes the diabatic production and destruction of PV, and a horizontally small PV tower is seen, reaching up to 200 hPa. North

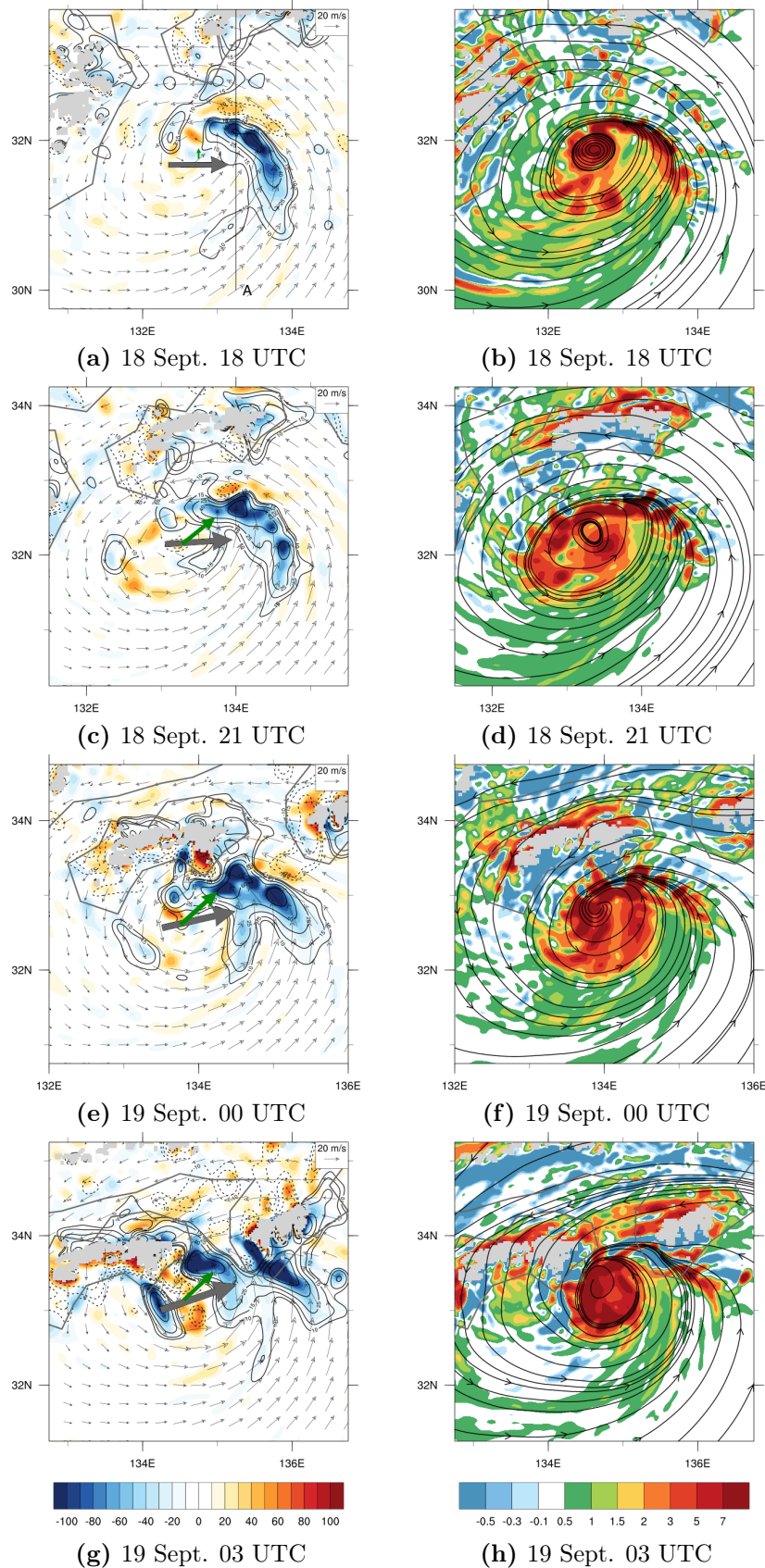


Figure 5.3. – Left: divergence (shaded, $\times 10^{-5} \text{ s}^{-1}$), vertical wind speed (ascent: solid, descent: dashed) and horizontal wind vectors at 925 hPa. Right: 950-900 hPa averaged PV (shaded, PVU) and streamlines at 925 hPa. At (a,b) 18/18, (c,d) 18/21, (e,f) 19/00 and (g,h) 19/03. The green (grey) arrow represents the direction and relative speed of the cyclone (vertical wind shear), the grey areas represent orography.

of the convective area, an easterly flow is observed, between the convergence area and the mountains of Shikoku (Fig. 5.4b). The maximum wind speed is found at 925 hPa, below the strongest updrafts, while the air perpendicular to the low-level easterly wind is rising over it, northwards.

The convection starts in a potentially unstable environment where low- θ_{eq} air is situated above high- θ_{eq} air, which is still present south of the rainband (Fig. 5.4b). In this potentially unstable environment, convergence forced by the TC circulation could have triggered the convection. Another process that can support vertical motion in a TC in general is vertical wind shear, where enhanced convection is found in the downtilt left side (see Section 2.2.1). Here, the direction of tilt is in the same direction as the vertical wind shear, and upward motion is indeed mainly found in on the downtilt left side (grey arrows in Fig. 5.3). Over the next 6 hours, the convergence zone stays at the same location, relative to the cyclone center. The band of PV is wrapping around the center cyclonically, while new PV is created diabatically in the rainband to the northeast (Figs. 5.3c-f). On 18/18 and 18/21, streamlines suggest that the PV is only advected around the center or even outward from the center. On 19/00, however, the streamlines show a cyclonic flow inwards and the PV feature contracts. This coincides with the time that the mean sea level pressure suddenly decreased (Fig. 5.1). On 19/03, the PV in the center has contracted further, suggesting intensification. However, the field of convergence and ascent now becomes highly influenced by orography (Figs. 5.3g,h). On 19/06, Sinalaku was located over Japan, and convection was fully influenced by orography.

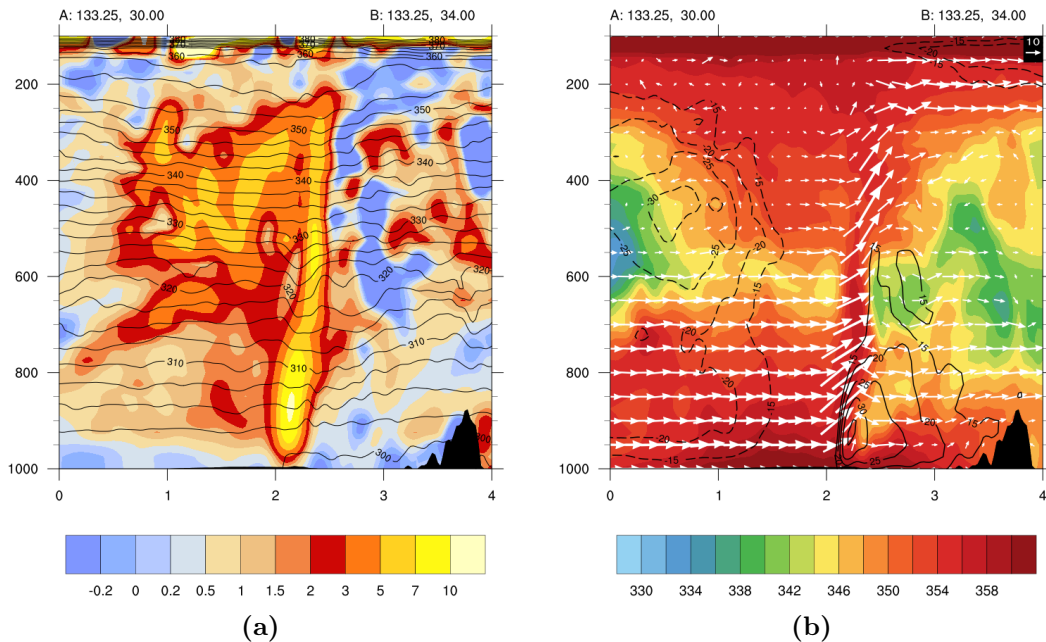


Figure 5.4. – Vertical cross sections on 18/18 of (a) PV (shaded, PVU) and θ (contours, K) and (b) θ_{eq} (shaded, K), horizontal wind speed perpendicular to the section (contours, m/s) and parallel wind vectors (m/s), where the vertical wind speed is multiplied by a factor 10. The location of the cross section is given in Fig. 5.3a.

Diagnostic tools will now be used to analyse how the area of convergence develops, whether the band of high PV is indeed transported into the center and if there are also other mechanisms according to the vorticity budget, that supported the intensification of Sinlaku.

To analyse the development of the convergence zone, both forward and backward trajectories are calculated, starting at lower levels (950 - 800 hPa) in a box around the area of convergence (Fig. 5.5). Trajectories with an anomalous initial PV value are assumed to represent the PV band. They are analysed later and therefore not considered here. Overall, the trajectory analysis shows that the mechanism respon-

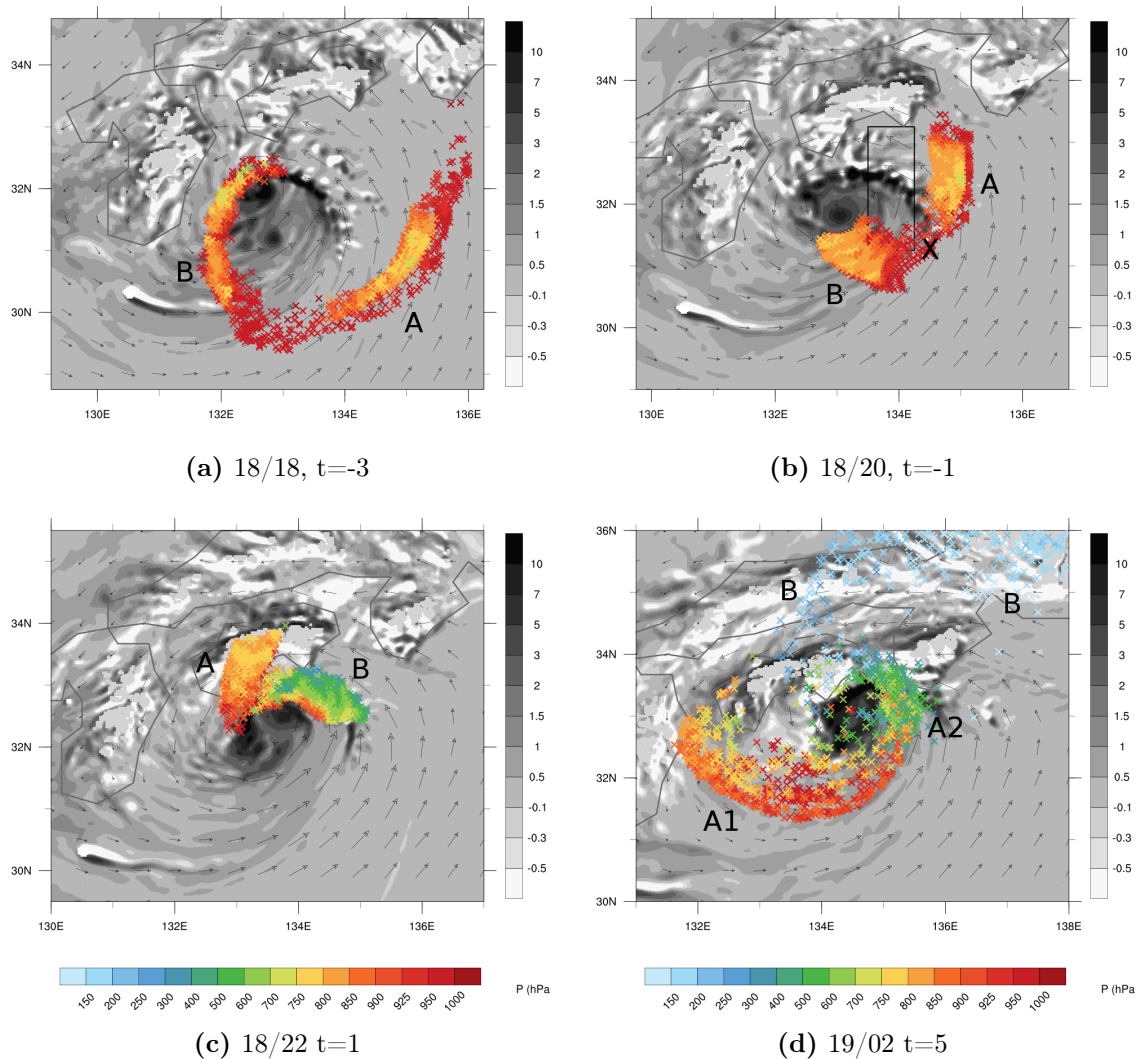


Figure 5.5. – Location of backward (a,b) and forward (c,d) trajectories starting on 18/21 ($t=0$) outside the PV band ($-0.5 < PV < 2$ PVU) in a box ($133.75 - 134.5, 31.5 - 33.5$ at $t=0$, black box in (b), moved relative to the center at $t=-1$) at 950, 900, 850 and 800 hPa, at (a) 18/18 ($t=-3$), (b) 18/20 ($t=-1$), (c) 18/22 ($t=1$) and (d) 19/02 ($t=5$). Wind vectors are at 925 hPa, the grey shades show PV (PVU) averaged over 950-900 hPa, and the colors the pressure of the air parcels (hPa).

sible for the convergence consists of two separate air flows, whose development will now be explained. Before the two air masses arrive at the convergence zone, the first air mass is present in the eastern environment of Sinlaku and it is advected by the outer circulation at lower levels (Figs. 5.5a,b, marked by 'A'). The second air mass originates closer to the center of the cyclone, mainly west of the center, and follows the cyclonic motion of the storm (Fig. 5.5a,b, marked by 'B'). The environmental air mass (A) is channelled between the cyclone center and the mountains of Shikoku, increasing the wind speed of the air parcels, and changing the wind direction to westwards (Figs. 5.5c). At the same time, air mass B has still a northward direction and both air masses therefore converge northeast of the center. Sinlaku's movement towards the northeast, which is perpendicular to the convergence line, may enhance this convergence (green arrows in Fig. 5.3). After arriving at the convergence zone, the air parcels of air mass B are lifted over the environmental air and become part of the deep convection (Fig. 5.5c). They rise to a height above 250 hPa and turn anti-cyclonically into the jet stream (Fig. 5.5d, blue crosses in the northeast quadrant). Meanwhile, the air parcels of air mass A stay at lower levels (950 - 750 hPa) and are advected cyclonically around the center (Fig. 5.5c,d). A part of these air parcels move radially outward (A1 in Fig. 5.5d), and a part of these air parcels stay close to the center and eventually rise within the convergence zone, following a similar path as air mass B did six hours earlier (A2 in Fig. 5.5d). It is therefore hypothesized that the convergence zone could develop due to the channelling of the environmental air (A) near orography, over which the air mass near the cyclone (B) was forced to rise.

The air that arrives in the band with high PV, below the convection in the convergence zone, originates from in between air mass A and B, marked by an X in Fig. 5.5b. This air mass is compressed, and according to the mass continuity, the air is therefore accelerating. Consequently, the highest wind speeds are found below the convection (Fig. 5.4b). Due to the high wind speed, the development near the center occurs rather fast also. Forward trajectories that start in the area of high PV (> 10 PVU) are therefore calculated three times, every two hours, and analysed at $t=2$ (Fig. 5.6). A part of the trajectories flow radially outward, as seen from air mass A1, another part of the trajectories in the rain band follows the path of air mass B, where they ascend in the convective area (Fig. 5.6). A third part follows the leading edge of air mass A2, as it wraps around the cyclone near the center. This last part of the air parcels spirals into the cyclone center in the first two hours of calculation while keeping its high average PV value (> 3 PVU, Fig. 5.7c). High PV air is therefore transported into the center. After three to four hours the leading edge of the trajectories arrives at the convergence zone and finally ascends (Fig. 5.7a). Since there is a continuous production of PV in the rainband, the high-PV band grows while circling around the center, and the amount of trajectories with $PV > 10$ PVU increases over time (Fig. 5.6a,b,c). Therefore, there is a continuous advection of high PV air into the center.

The rising air of air masses A and B along the convergence zone loses specific humidity by condensation (Fig. 5.7b) and creates PV below the level of maximum latent heating. The air parcels however rise and move above the level of maximum

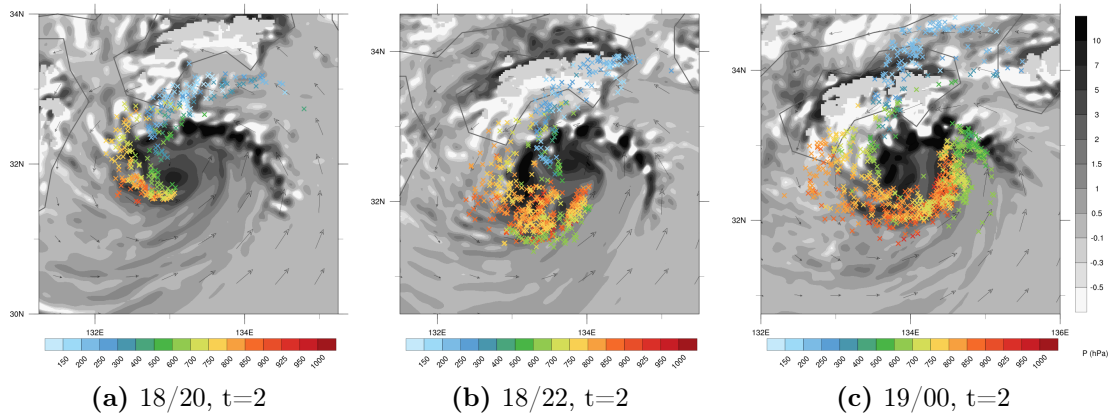


Figure 5.6. – Location of forward trajectories that started on (a) 18/18, (b) 18/20 and (c) 18/22 in the PV band at locations with $PV > 10$ PVU. The current trajectory location and background are given at $t=2$, on (a) 18/20, (b) 18/22 and (c) 19/00. The grey shades show PV (PVU) averaged over 950-900 hPa, and the colors the pressure of the air parcels (hPa).

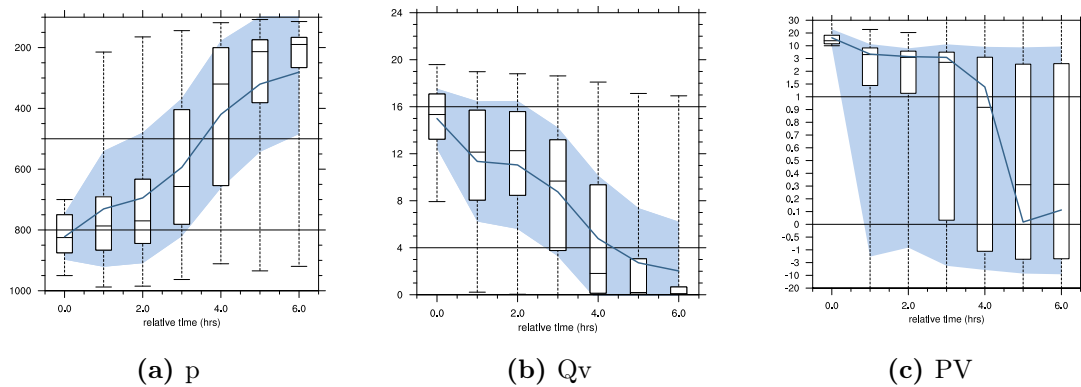


Figure 5.7. – Statistical development along 6 hr forward trajectories that start on 18/22 in the PV band at locations with $PV > 10$ PVU, shown for (a) pressure (hPa), (b) specific humidity (g/kg) and (c) PV (PVU). For details of the statistic figures see Section 3.3.5.

latent heating, where PV is destroyed and therefore relatively low (Fig. 5.7c). The outflow of the rising low-PV air into the environment at upper levels, is marked by an anticyclonic turning and accelerating into the westerly jet stream. On 18/18 Sinlaku can be recognized by the high PV air south of a sharp PV gradient (Fig. 5.8a). A jet streak is already present over northern Japan between 40°N and 42°N and has a curved pattern. The low PV outflow is present northeast of Sinlaku, but still about 2° south of the jet streak. Twelve hours later, just after re-intensification, the area of low-PV air northeast of Sinlaku has increased in horizontal extent and both Sinlaku and the low-PV air have moved northward (Fig. 5.8b). The upper-level PV gradient has now been influenced by Sinlaku. The gradient has increased and moved northward as well, where it has modified the initially curved pattern. Asso-

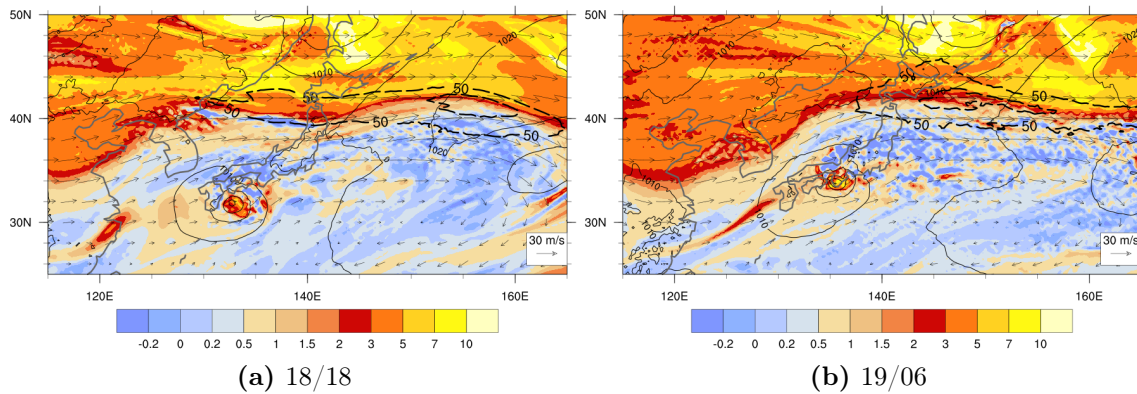


Figure 5.8. – PV (shaded, PVU) and wind vectors at the 345 K level, and the mean sea level pressure (thin black contours) on (a) 18/18 and (b) 19/06. The jet streak is marked by a thick black dashed line (wspd > 50 m/s, every 10 m/s). Grey contours represent the location of topography.

ciated with the strengthened PV-gradient, the magnitude and meridional extent of the jet streak have increased. So, although Sinlaku was a relatively weak storm, it nevertheless appeared to influence the midlatitude flow.

To further analyse the intensification period, the vorticity budget is computed over the period 18/18 to 18/21 and the budget terms are accumulated (Fig. 5.9). This period is taken, because it has a relatively good balance between $\Delta\zeta$ and the sum of the budget terms. At later times, orography was located within the box and the budget was out of balance. In general, this period is marked by an increase in vorticity in the lower troposphere and a decrease in the upper troposphere (Fig. 5.9). The lower-level increase in vorticity is caused by the eddy flux and tilting term. A positive eddy flux term is mainly found at the east side of the box (Fig. 5.10a). At this side, an area of increased relative vorticity is present along a convergence line, co-located with the band of high PV (Fig. 5.11b and 5.3b). Anomalously high values of relative vorticity are advected into the box (Fig. 5.11b). The behaviour of the eddy flux is similar to what was previously seen by the trajectory analysis, where PV instead of relative vorticity was transported towards the cyclone center. At the same time, air moves radially outward at the southwest, similar to the trajectories in Fig. 5.5d (although at another time and level). This accounts for a net divergence over the box. Together with a positive mean vorticity at the border, this gives a negative stretching term (Fig. 5.11b).

At upper levels, the negative vorticity tendency is dominated by the eddy flux, and present at the eastern side of the box (Fig. 5.10a). Since the influence of the westerly jet stream increases at upper levels, the westerly wind becomes dominant over the cyclonic circulation at this level (Fig. 5.11a). Therefore, the outflow of positive vorticity at the southern east side of the box (near corner A) is larger than the inflow of positive vorticity at the northern east side (near corner B, Figs. 5.10a and 5.11a). So, the upper-level vortex is advected by the westerlies.

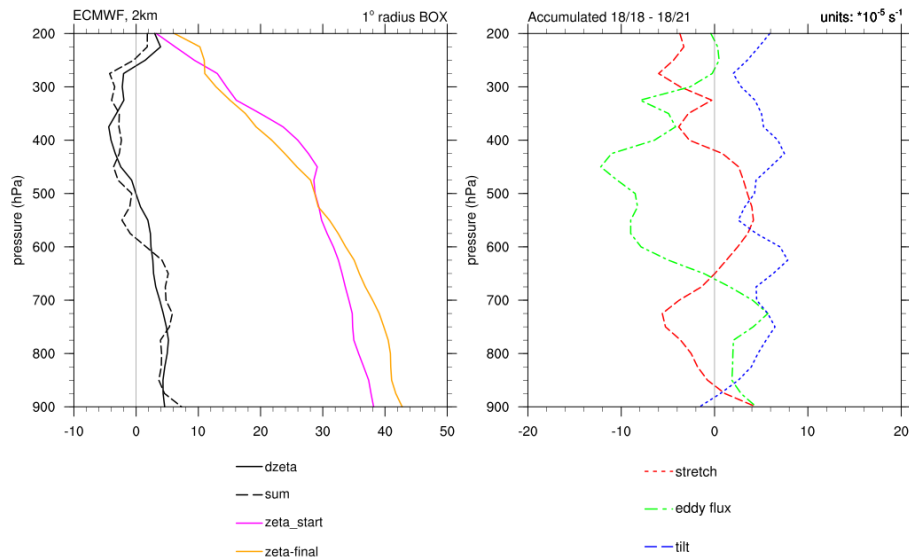


Figure 5.9. – Average vorticity ($\cdot 10^{-5} \text{ s}^{-1}$) in a square box with radius 1° around the cyclone center on 18/18 (pink, start), 18/21 (orange, end), and the change in vorticity (black) and sum of the vorticity budget terms (black dashed) over this period. The separate budget terms of stretching (red), eddy flux (green) and tilting (blue) are shown at the right.

A positive tilting term is found through the entire troposphere (Fig. 5.9) and is dominant at the eastern side of the box also (Fig. 5.10b). The mechanisms behind the positive tilting term is related to VWS. In the first place, the environmental VWS tilts² the cyclone vortex. The cyclonic center at upper levels is therefore present in the eastern half of the box (Fig. 5.11a), while the cyclone center at lower levels is present in the middle of the box (Fig. 5.11b). The vortex tilting thereby induces an internal VWS (see Fig. 2.13a) with strongest winds in the lower troposphere at the eastern box side (Fig. 5.10b). Additionally, the cyclonic circulation is strongest at lower levels, amplifying the internal VWS. Finally, the upward motion in the rainband causes the horizontal vorticity, created by the VWS, to tip over to become vertical positive vorticity inside the box (see Section 3.3.2, Fig. 3.5), creating a positive tilting term (Fig. 5.10b). In general, environmental VWS does tilt a cyclone vortex, induce an internal VWS and causes upward motion in the downtilt left quadrant (Section 2.2.1). The enhanced upward motion makes a cyclone resilient to the environmental VWS. Additionally, from a vorticity budget perspective, the environmental VWS indirectly supports the creation of vorticity near the center, which strengthens the cyclone.

From the previous analyses it was seen that Sinlaku intensified in a potentially warm and moist environment, which was present because the inflow of midlatitude air was blocked by the orography of Japan. The intensification started with the development

²Note the difference between the tilting of the cyclone, due to which the cyclone has not a vertically straight vortex any more (hereafter called 'vortex tilting'), and the tilting term of the vorticity budget, in which horizontal relative vorticity is tilted to become vertical relative vorticity (hereafter called 'tilting term').

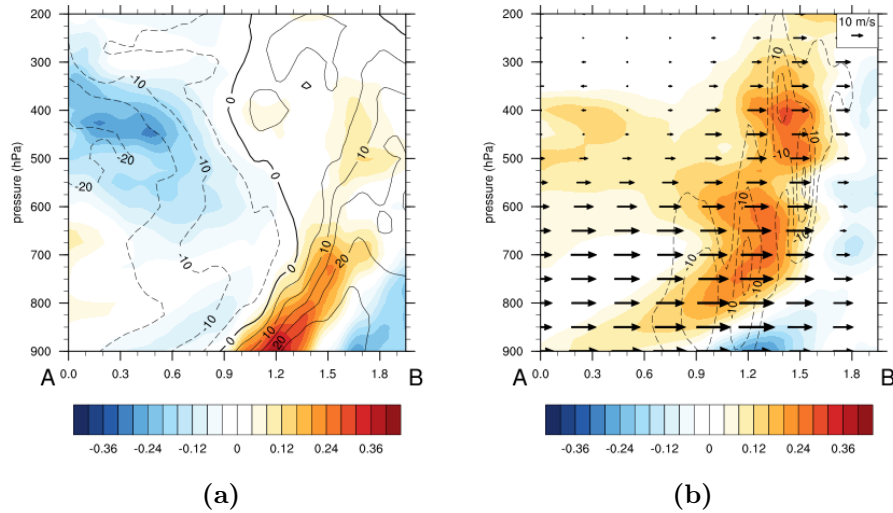


Figure 5.10. – Vertical cross section of the box at side AB in Fig. 5.11 of (a) accumulated eddy flux (shaded, $\times 10^{-5} \text{ s}^{-1}$) and averaged perpendicular wind speed (solid/dashed into/out of the box, m/s) and (b) accumulated tilting term (shaded, $\times 10^{-5} \text{ s}^{-1}$), averaged vertical motion (solid/dashed contours downward/upward motion, Pa/s) and averaged parallel horizontal wind vectors (m/s) over the period 18/18 - 18/21. The location of the box and side AB on 18/19 is given in Fig. 5.11.

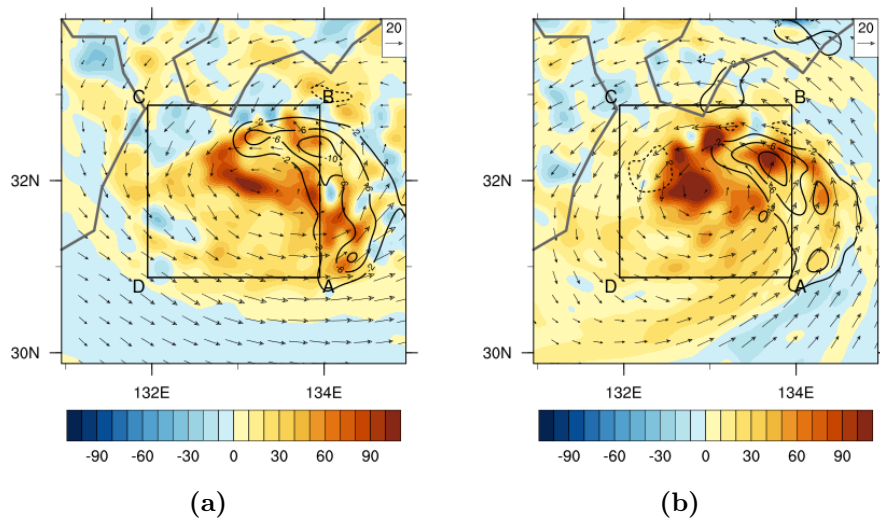


Figure 5.11. – Relative vorticity (shaded, $\times 10^{-5} \text{ s}^{-1}$), ω (solid/dashed contours for rising/sinking motion, Pa) and cyclone-relative wind vectors (without translation speed, m/s) on 18/19 at (a) 450 hPa and (b) 725 hPa. The black box shows the location over which the vorticity budget is calculated.

of a rainband along a convergence zone. The convergence existed between an air mass in Sinlaku's lower-level outer circulation, that was channelled and deflected near orography, and an air mass near the inner circulation, that rose over the convergence zone. Below the convection of the resulting rain band, PV was produced diabatically. The anomalously high PV was then transported cyclonically inwards and supported

the re-intensification of Sinlaku. Additionally, Sinlaku's vortex was tilted by the environmental VWS and the upward motion in the rainband caused the horizontal relative vorticity to tip over into positive vertical relative vorticity near the center, amplifying the tropical re-intensification.

5.1.3. Mechanisms behind tropical decay

The decay after tropical re-intensification is clearly seen in the sea level pressure on 19/06. The low-level relative vorticity, however already starts to decrease on 19/02 (Fig. 5.1), although the PV in the center seems to contract, which would be a sign for TC intensification (Fig. 5.3h). This is clearly a complex situation. With the use of vorticity budget and trajectory analysis it is aimed to disentangle the processes behind this complex situation. Since the storm is in between mountainous areas, its structure including its vorticity changes every hour. The vorticity budget is therefore not balanced most of the time, except between 19/02 and 19/03. During this time interval the budget reflects a similar signal as in the non-balanced budgets between 19/00 and 19/04, and is therefore chosen to be representative for the processes during the complex development (Fig. 5.12). In general, the vorticity of Sinlaku has a negative tendency in the lower troposphere, below 700 hPa and a tendency close to zero above. The contracting PV feature is reflected in the positive stretching term at 700 hPa. Net convergence and upward motion in the box, cause a positive stretching term (Fig. 5.13a). Vorticity is transported upwards, due to which the vortex tube is stretching and contracting, causing an intenser cyclone. The cyclone also became more axi-symmetric during this time, as previously seen in Figs. 5.3h and 5.2h. This would suggest TC formation.

Nevertheless, the cyclone is not entirely axi-symmetric. It is still in the stage where originally ET was expected and the situation is more complex than only TC intensi-

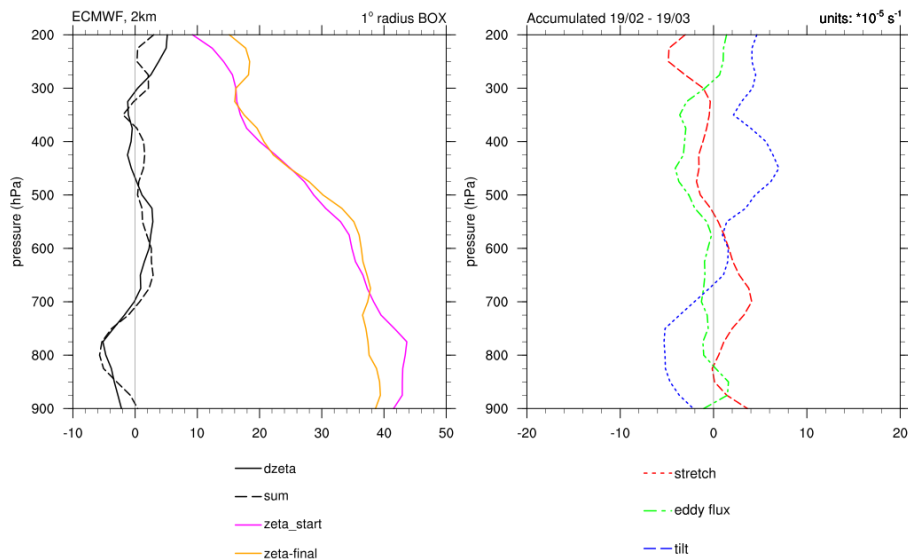


Figure 5.12. – Similar to Fig. 5.9, for the time interval 19/02 - 19/03.

fication. Negative tendencies of eddy flux and tilting influence the low-level vortex. Their influence is (again) mainly found at the eastern side. This time, topography may influence the budget. Orography is only present below 900 hPa, and the budget was not considered at this level. Nevertheless, the orography will influence the low-level wind field above 900 hPa as well. It is expected that friction becomes more dominant as well, but even without the friction term, the vorticity budget is nearly balanced (Fig. 5.12).

In the northeastern corner, the low-level horizontal wind speed is decreasing near orography which causes a positive vertical wind shear, while a negative vertical wind shear is found around 500 hPa (Fig. 5.13c). Together with upward motion, this gives a negative contribution to the vorticity budget by the tilting term at lower levels and positive contribution at middle to upper levels. Diabatic PV is created along the ascent region, and this is transported into the box, causing a positive eddy flux (Fig. 5.13b). At the same time, negative vorticity is seen along the hill slope which is advected into the box also, resulting in a negative eddy flux term (Fig. 5.13b). Above 900 hPa, this mainly cancels out the positive inflow of vorticity, except for a small peak at 850 hPa. Positive tilting at mid- to higher levels is also seen at the northern box side (not shown). This is because Sinlaku's vortex has now tilted northwards. Similar to in the previous section, the vortex tilting caused a vertical wind shear, which was favourable for a positive tendency of vorticity by the tilting term, but now at the north side.

Tropical re-intensification ended abruptly on 19/06, according to the central pressure. At this time cold air could flow in at the west side of the center (Fig. 5.2i) causing a pressure rise without PV and vorticity fall. Locally, the orography was favourable for the advection of low- θ_{eq} air from the east (Fig. 5.16b, at 6°). This

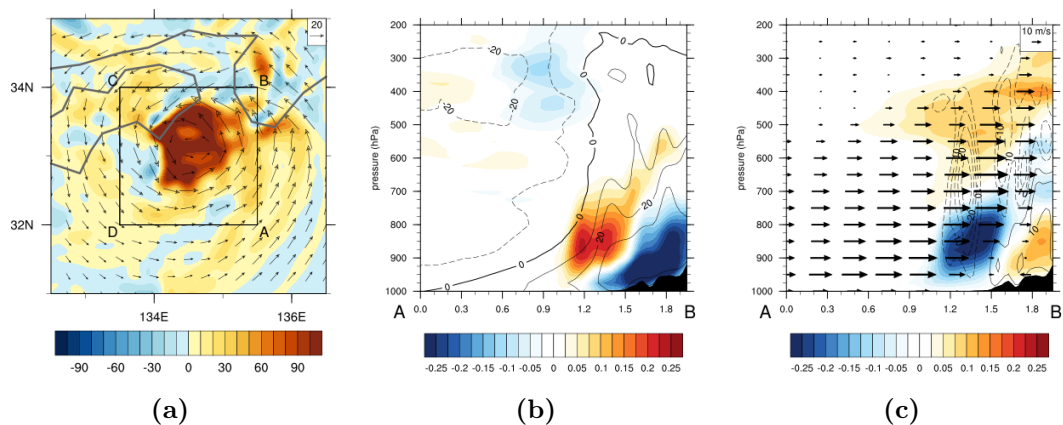


Figure 5.13. – (a) Relative vorticity (shaded, $\ast 10^{-5} \text{ s}^{-1}$) and cyclone-relative wind vectors (m/s) on 19/02 at 700 hPa, and corresponding vertical cross sections along side AB of the black box, of (b) eddy flux (shaded, $\ast 10^{-5} \text{ s}^{-1}$) and average perpendicular wind speed (solid/dashed contours into/out of the box, m/s) and (c) tilting term (shaded, $\ast 10^{-5} \text{ s}^{-1}$), vertical motion (solid/dashed contours downward/upward motion, Pa/s) and average parallel horizontal wind vectors (m/s).

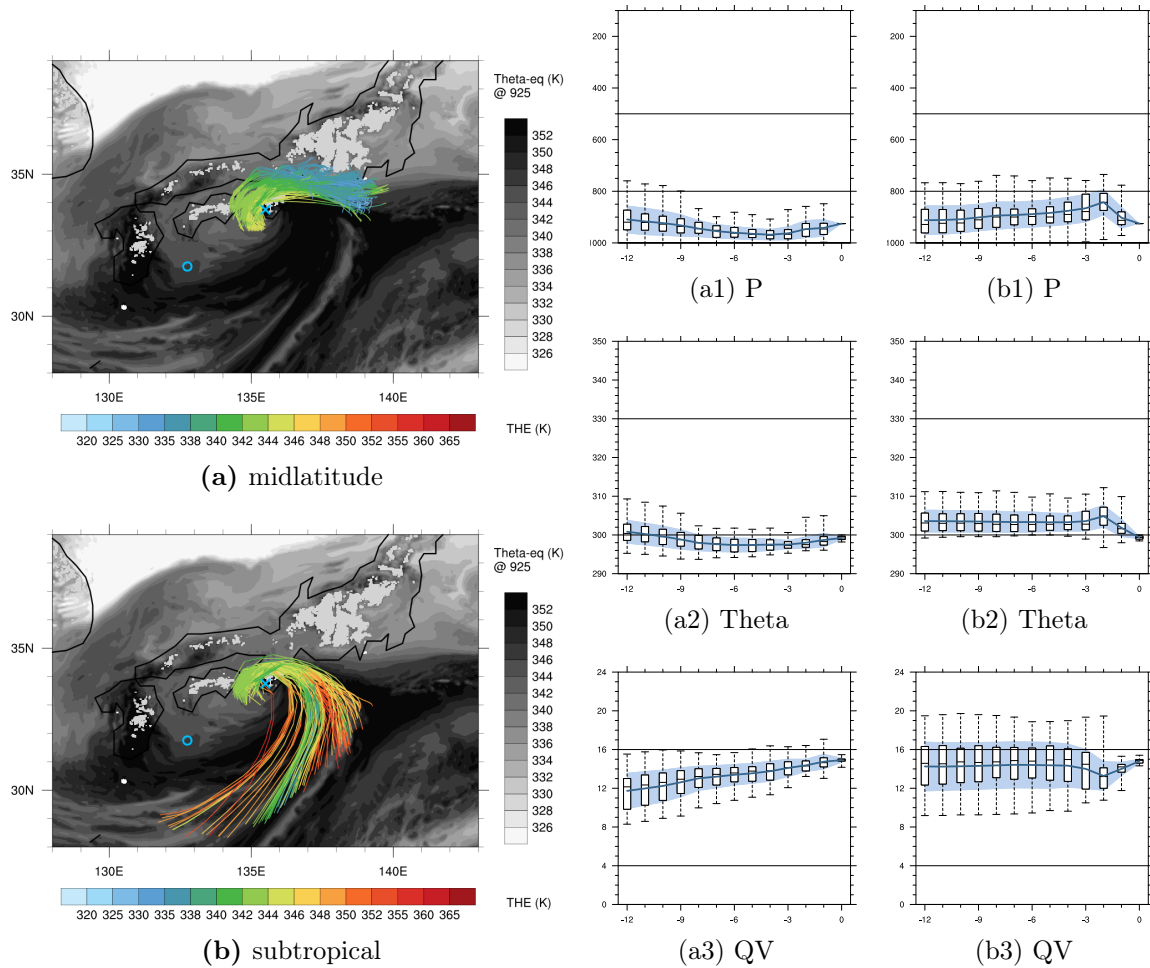


Figure 5.14. – 12 hour backward trajectories and corresponding statistics, starting on 19/06, west of the cyclone center in air with $\theta < 300$ K for (a) air of midlatitude origin and (b) subtropical origin. The colors represent θ_{eq} along the trajectories and the grey shades represent θ_{eq} on 19/06 at 925 hPa. For details of the statistic figures see Section 3.3.5.

air was transported around the Kii-mountains (Fig. 5.16b, at 5°), and arrived to the west of the mountains (Fig. 5.16b, at $3-4^\circ$). West of this mountain range, the colder air was transported over the sea between the mountains of Shikoku and the Kii-peninsula (Fig. 5.2, $134-137^\circ\text{E}$, $34-35.5^\circ\text{N}$). This local cold air inflow influenced the warm moist area in which Sinlaku resided during the previous hours. The colder air inflow is therefore analysed in more detail by the use of trajectories. Backward trajectories that are started in the cold inflowing air, reveal that the air consists of two masses with different origin and properties (Figs. 5.14).

Air parcels that start near Japan have relatively low θ_{eq} values (Fig. 5.14a). They are located below a precipitation field that is associated with the asymmetric cloud shield that belongs to Sinlaku's ET and developed before tropical re-intensification took place (Fig. 5.15a). It is not clear if this air mass is either of midlatitude

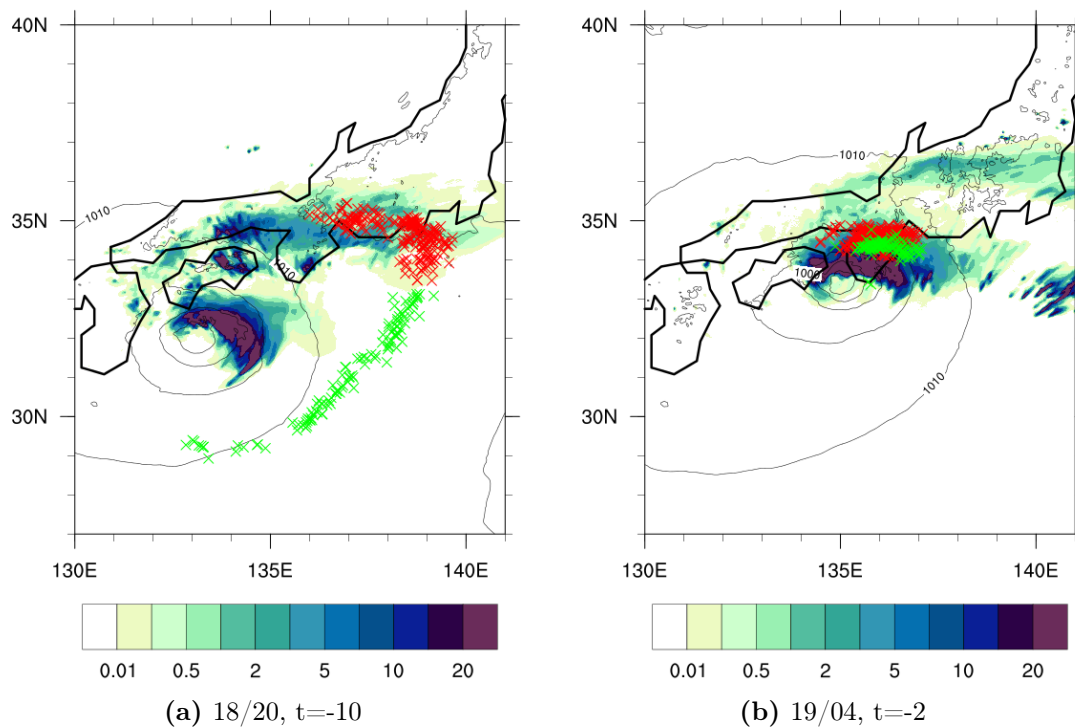


Figure 5.15. – Trajectory location of the midlatitude air mass (red crosses) and subtropical air mass (green crosses) of Fig. 5.14, in comparison to precipitation (shaded, 1h accumulated, mm) and mean sea level pressure (contours, hPa) at (a) 18/20 ($t=-10$) and (b) 19/04 ($t=-2$).

origin, or cooled due to evaporation from the precipitation. The air parcels are at very low levels and sink even further (Fig. 5.14a1), while their specific humidity increases a little (Fig. 5.14a3) and the potential temperature decreases, interpreted as evaporative cooling (Fig. 5.14a2). These air parcels are advected eastward, along the coast, around a mountain range but still over local hills of the Kii-peninsula where the air parcels rise and warm (Fig. 5.14a). There is still an increase in water vapour from evaporating precipitation, now from the rain band that advanced over the Kii-peninsula (Fig. 5.15b). These air parcels end west of Sinlaku with a higher θ_{eq} than they originally had, due to the gain in water vapour (Fig. 5.14a3).

The second air mass is spread over the entire environment southeast of Sinlaku in an initially precipitation free area (Fig. 5.15a). These trajectories are present at lower levels as well (Fig. 5.14b1). They are of subtropical origin, with a higher potential temperature and water vapour content than the first air mass (Fig. 5.14b2,b3). When these trajectories are near Japan and a convective zone, they rise a little, in which the potential temperature increases and water vapour is lost, probably by condensation (at $t = -3$ in Fig. 5.14b1,b2,b3). At $t=-2$, however, they arrive near the area of Sinlaku's rainband with high amounts of precipitation (Fig. 5.15b). Evaporative cooling (Fig. 5.14b2,b3) causes the air parcels to suddenly sink (Fig. 5.14b1). They then turn cyclonically, to arrive as relatively cold air to the west of Sinlaku (Fig. 5.14b). The sudden evaporative cooling and sinking in the last two

hours is not observed for the northern air mass because it was mainly located in the area of weaker precipitation (Fig. 5.15b). Sinlaku thereby influenced the inflow of colder air near the center by evaporative cooling from its own precipitation.

5.1.4. Additional influences of topography

In the previous sections, it was seen that Sinlaku was influenced by topography in several ways. There are however additional mechanisms of how the topography can change the structure of a typhoon (see Section 2.2.3). These mechanisms contained, among others, (1) orography induced convergence, (2) changes in vertical motion due to dry air inflow from land and (3) differential friction. Also, (4) track deflection towards the area of maximum diabatic PV creation can occur.

Starting with the orography induced convergence (mechanism 1), Tang and Chan (2014) mentioned that the larger scale circulation over the orography induced a PV stretching and consequent positive vorticity anomaly where the air was advected away from the mountains. As a result, cyclonic deflection of the air flow, which was parallel to the mountains, caused an area of convergence near the cyclone. For Sinlaku, a similar situation is observed. On 19/03 an area of positive PV is found south of the orography at 133.5°E, 33°N (Fig. 5.3h). Negative PV is found directly east of it (134.2°E, 33.5°N), at the location where the cyclonic flow is partly over land and channelled between the circulation center and the orography (similar to Tang and Chan, 2014, their Fig. 8b). The positive and negative PV anomalies deflect the

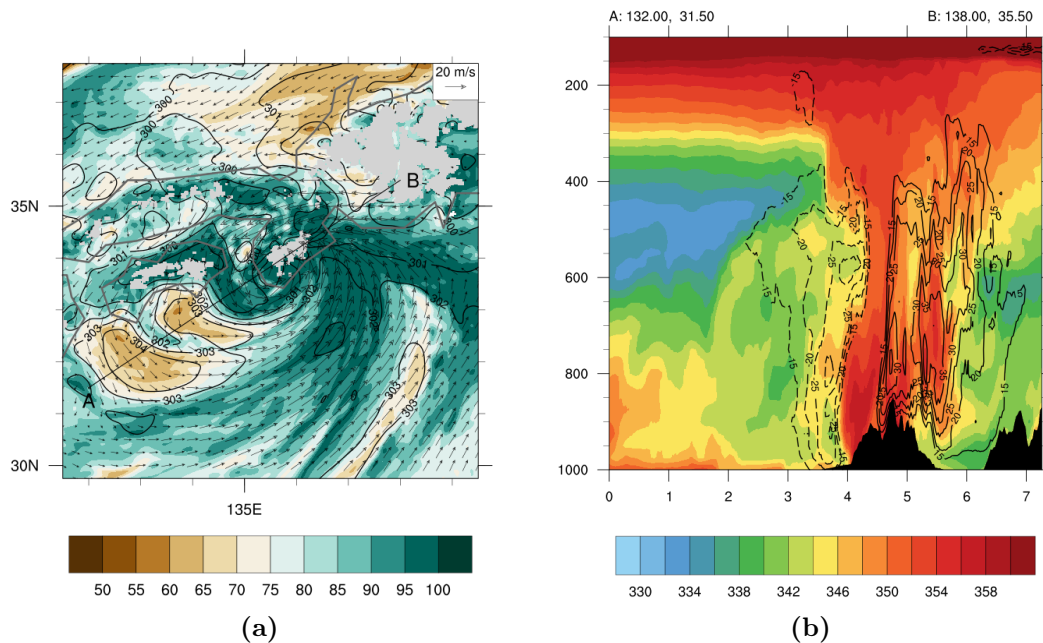


Figure 5.16. – (a) Horizontal overview at 925 hPa of RH (shaded, %) and θ (contours, K). Line AB represents the location of the (b) vertical cross section of θ_{eq} (shaded, K) and perpendicular horizontal wind speed (contours, m/s), on 19/06.

flow so that the streamlines converge, and a convergence zone is indeed found here (Fig. 5.3g,h, 134.2°E, 33°N). This is, however, a minor effect in comparison to the rainband, and accounts for an area of weak precipitation up to 3 mm/h (also seen 1 hr later, Fig. 5.15b, 134.5°E, 33.2°N).

Dry air from land (mechanism 2) is seen in the outer circulation of Sinlaku. Due to the presence of orography, the dry air is present in the form of downslope adiabatically warmed wind (foehn) (Fig. 5.16a, 132°E-135°E, 31.5°N-33.5°N). Very moist, high- θ_{eq} air lies near the surface and below low- θ_{eq} air (Fig. 5.16b, $\sim 0.5^\circ - 3^\circ$). This creates a potential instability at the west side of Sinlaku's outer circulation. Without a clear triggering mechanism, however, the potential instability does not have an effect on the vertical motion field. The dry air also does not reach the inner core of Sinlaku. Although streamlines indicate that the dry air would flow into the center, the translation speed of the storm is so high that this does not actually happen and the dry foehn air stays to the south and southwest of the cyclone center. The effect of differential friction on ascending motion on the onshore side (mechanism 3) is not observed, because the effect of orography was dominant. Even when the cyclone moves over land and the central pressure increases, still a cyclonic circulation is observed, reaching up to 400 hPa (Fig. 5.16b). Also, a clear track deflection (mechanism 4) is not observed and Sinlaku's track is dominated by the environmental steering flow (Section 5.1.1).

5.1.5. Discussion

In this Section it is argued that Sinlaku re-intensified as a tropical cyclone. The re-intensification occurred, however, not as a classical TC-intensification. Sinlaku could intensify in a protected warm moist area because the orography of Japan prevented the midlatitude air to flow southwards and interact with the cyclone. The re-intensification took place under the influence of diabatically created PV in a rainband that was advected around and into the cyclone. At the same time tilting of the vortex, caused at positive tilting term in the vorticity budget. Galarneau-Jr. et al. (2013) found a similar profile of the vorticity budget for the intensification of Hurricane Sandy (2012), although Sandy was clearly in the ET phase and in a baroclinic environment at that time. The positive eddy flux has a similar origin: inflow of high PV air, along a band of diabatically created PV (here: rainband, Galarneau-Jr. et al. (2013): warm front). The tilting term, however, was in their study obtained due to vertical windshear along the front, while here the vortex tilt is responsible.

Orography played a key role in the development of Sinlaku, although not all aspects described in Section 2.2.3 were observed or as important. In the studies, described in section 2.2.3, the cyclone had either no translation speed, or it moved towards land. Here the translation speed was relatively high, and Sinlaku moved parallel to land. Due to this high translation speed, many influences due to topography, as seen in previous studies were only of minor influence on the structural changes here. Nevertheless, the translation speed in combination with orography may have

contributed to the existence of a convergence zone and subsequent rainband, that was present perpendicular to the direction of Sinlaku's track. A similar deformation of the wind field and subsequent convergence zone was not observed in the study of Tang and Chan (2014), where the translation speed was about half as low as in this study. After landfalling over the Kii-peninsula, the inflowing air of Sinlaku is diabatically cooled by the evaporation of Sinlaku's own precipitation field. Sinlaku therefore plays a role in its own destruction.

5.2. The development during extratropical transition

In this section the extratropical transition of Sinlaku is analysed, based on simulation SmE-hi from the previous Chapter. During the transformation stage, Sinlaku's structure changes from a tropical to an extratropical cyclone and it is analysed how this change develops. In the case of Sinlaku, the cyclonic system also slowly decays, and the reason behind the decay is investigated. In order to do this, first a chronological overview of the ET development is given in which extratropical characteristics are shown. Secondly, the interaction of the midlatitude and subtropical air masses and their influence on the maintenance of the cyclonic systems is analysed in more detail than has been done in previous literature. Thirdly the behaviour of the different air masses and the mechanisms by which they influence the intensity are described. Fourthly, the consequences of the mechanisms for the development of extratropical cyclone features is explained, and finally the connection between all previously described air masses, mechanisms and extratropical characteristics is discussed.

5.2.1. Overview

After a spin-up time in the first few hours of the simulation, Sinlaku moves with an average speed of 10 m/s in the north-east to eastern direction (Fig. 5.17). This speed and direction agree fairly well with the average environmental flow between 950 and 250 hPa. In the absence of an environmental steering flow and the advection of PV, the direction of movement is towards the location of maximum diabatic PV tendency, which is often located over land (see Section 2.2.3). Sinlaku moved south of Japan until 19/18, so when the storm's motion was influenced by the topography, a northward deflection towards the land would have been expected. Nevertheless, no clear sign of a track deflection is seen. Overall, Sinlaku just follows the environmental steering flow.

The intensity of Sinlaku can be based on minimum surface pressure tendency, or (potential) vorticity development, whose tendencies do not necessarily coincide. The minimum pressure of Sinlaku decreases in the first hours of the simulation after which it fluctuates around 988 hPa. After 20/06, Sinlaku decays. The low-level

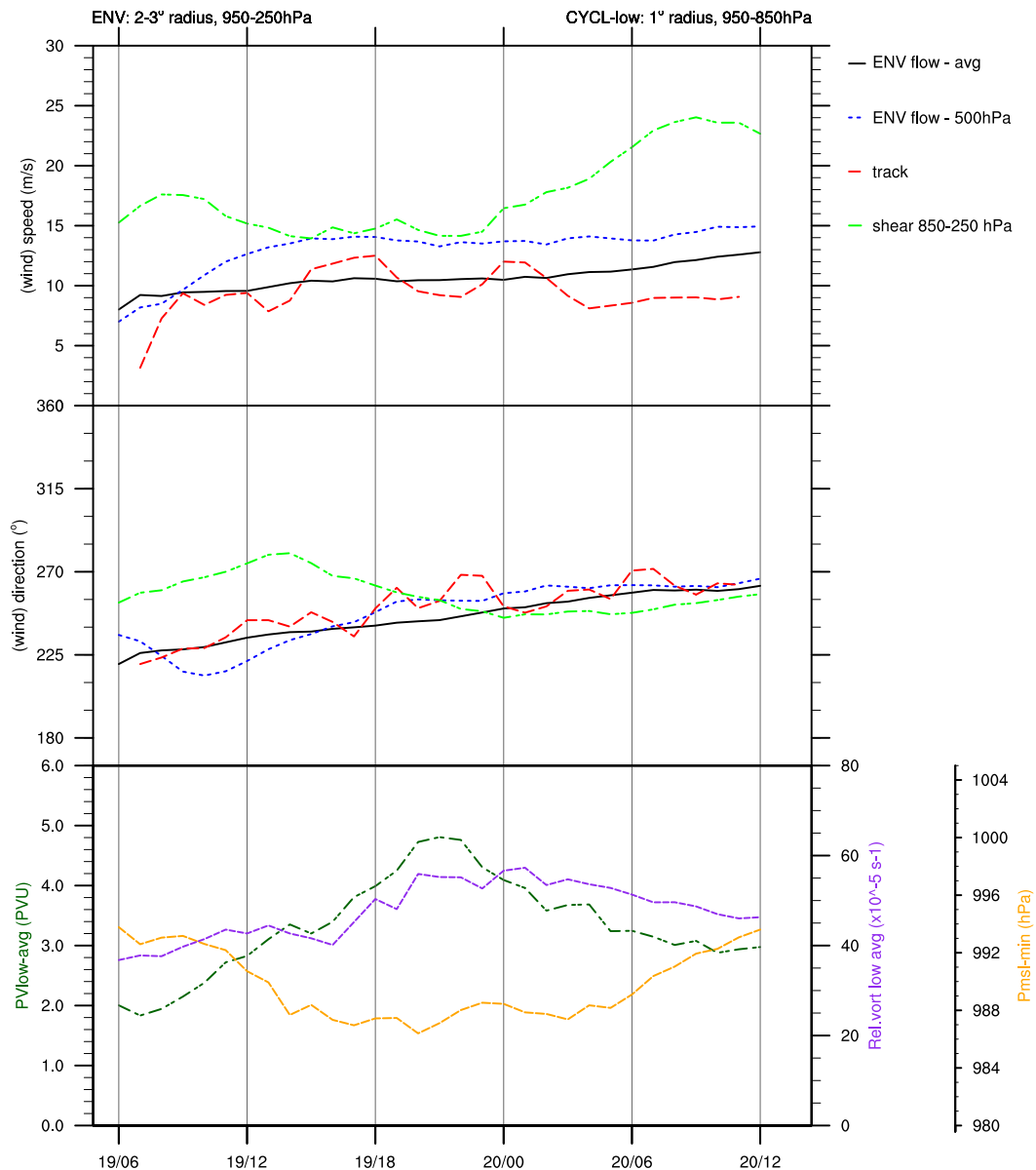


Figure 5.17. – Overview over time of the speed (upper panel) and direction (middle panel) of Sinlaku’s track (red), the environmental flow within a circle between 2° and 3° radius around the cyclone center at 500 hPa (blue) and averaged over the layer 950-250 hPa (black), and the vertical wind shear within the same circle around the center, between 850 and 250 hPa (green). The lower panel shows the minimum mean sea level pressure of Sinlaku (yellow) and its average PV (dark green) and relative vorticity (purple) within a circle of 1° radius around the cyclone center in the 950-850 hPa layer.

(950-850 hPa average) (potential) vorticity field, on the other hand, showed Sinlaku was intensifying as it moved south of Japan. Even after Sinlaku moved over the open ocean again, from 19/18 on, and experienced the inflow of midlatitude air, the vorticity field in the center was still increasing. The low-level PV decreases after 19/22, and the low-level relative vorticity after 20/03, showing that the cyclone is

decaying

The vertical wind shear (VWS) of the environmental flow is of importance for the tilting and upper-level advection of the vortex. During the spin-up time, the VWS is still relatively high, but decreases when the storm and its upper-level outflow develops. A semi-steady value of about 15 m/s is reached, which is present until the storm starts to decay. A VWS up to 20 m/s, causes an enhanced vertical mass flux (Davis et al., 2008), so Sinlaku was still resilient to VWS at this time. After 20/00 the VWS rapidly increases to 24 m/s which is not favourable for cyclone development anymore. At the same time Sinlaku started to decay and VWS may be one of the responsible factors for the decay.

During the period of 19/12 to 19/18, Sinlaku moved parallel to the southeastern coast of Japan including its highest mountain range (Fig. 3.3). Sinlaku remained in a relatively warm environment (Fig. 5.18a). As during the tropical re-intensification period, the inflow of midlatitude air is blocked by orography (Fig. 5.18a). Northwest of Japan, the low-level air flows in a large circle around the mountains, but never arrives near the cyclone. Sinlaku therefore remains in a relatively warm moist environment. Relatively colder air is found over the Kanto Plain³, east of the mountains (Fig. 5.18a) and increased low-level winds, that were channelled between the mountains and the cyclone center (Fig. 5.18b), were able to advect the first cold air from the Kanto Plain into the system, before the major cold air advection started (Fig. 5.18a). The cold air is only present at lower levels and wraps around the center where it undercuts the warm moist air. Meanwhile, a warm front has build to the east of Sinlaku (Fig. 5.18a), and subtropical air ascends instead of being transported towards the cyclone center (Fig. 5.18a). To the west of Sinlaku, air parcels that flowed from the Kanto Plain over the mountains, descend as adiabatically warmed downslope winds (Fig. 5.18a). Although the resulting air is relatively warm, this is not a classical foehn, since the air flows beneath the precipitation of the warm front and gains water vapour as it cools diabatically. Trajectory analysis shows that in the next 12 hours, the warm dry air parcels stay at roughly the same location south of the mountains, and do not follow Sinlaku as it moves eastwards (not shown). The downslope wind does therefore not influence the development of Sinlaku during its ET.

When Sinlaku moved eastward, away from Japan and thus from the orographic barrier, the cool and dry midlatitude air to the north could directly interact with the transitioning TC (Fig. 5.18b). A pronounced cold and warm sector evolved, as is typical for step 3 of the transformation stage of ET (Klein et al., 2000). This interaction with the midlatitude baroclinic zone east of Japan was the begin of the actual ET of Sinlaku. A cold front can now develop, is present south of the center on 19/18, and advances to the east of the center on 19/22 (Figs. 5.18c and 5.18e). A bent-back frontal structure around the warm area is seen most clearly at 18 UTC and on 19/22 the major part of Sinlaku's low-level circulation and warm anomaly is embedded in the midlatitude air. The frontal evolution between 19/18 and 19/22 develops similar to a Shapiro-Keyser cyclone, although there are differences. Because

³For a map of Japan with the names of relevant locations, see e.g. Fig. 3.3

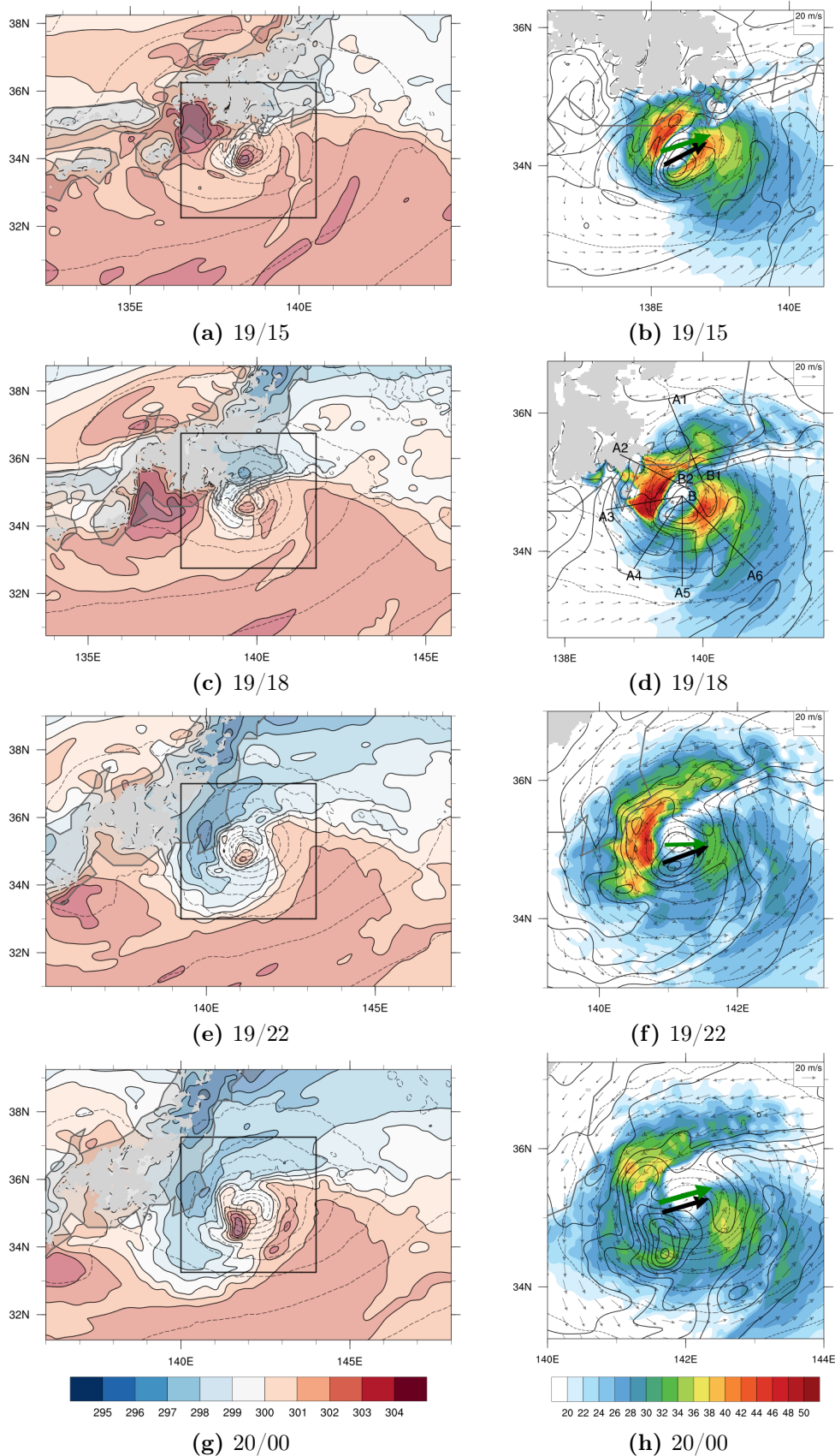


Figure 5.18. – Overview of potential temperature (shaded, K) and geopotential height (dashed contours) at 925 hPa. The black box marks the area of the panels to the right, which zoom in on horizontal wind speed (shaded), potential temperature (contours) and wind vectors, at (a,b) 19/15, (c,d) 19/18, (e,f) 19/22, (g,h) 20/00, (i,j) 20/06 and (k,l) 20/12. The green (black) arrow represents the direction and relative speed of the cyclone (environmental flow), the grey areas represent orography and black lines in (d) the location of cross sections.

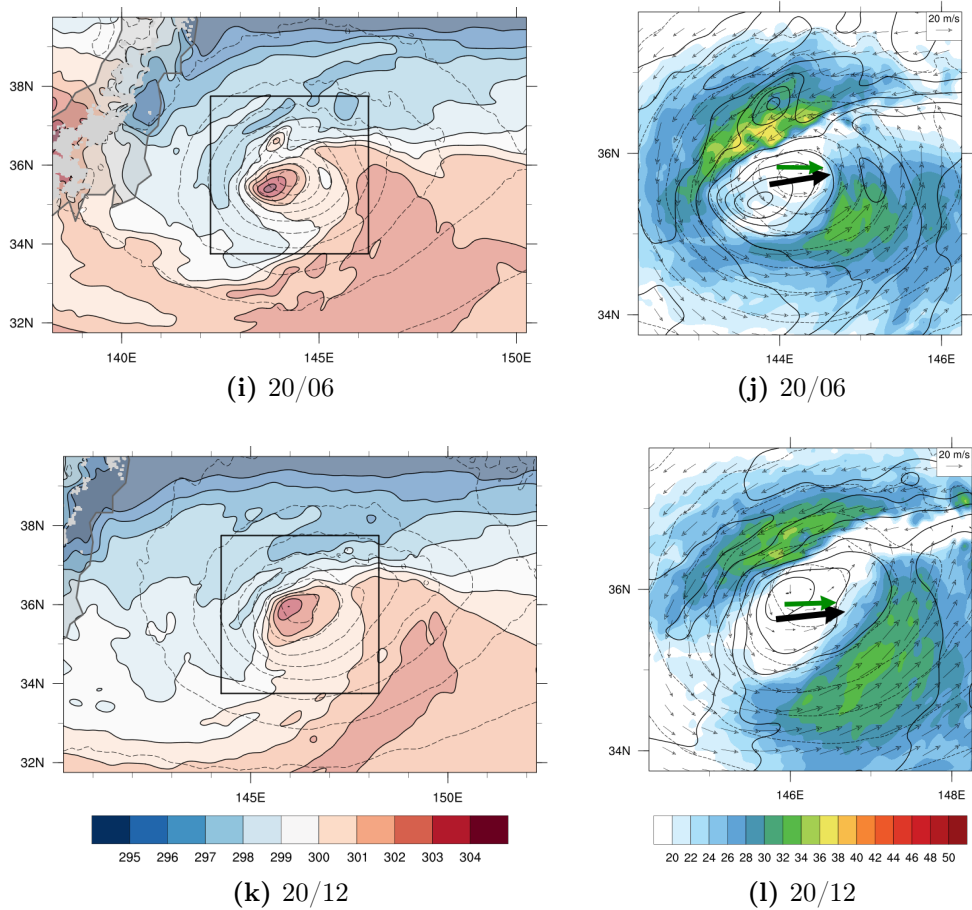


Figure 5.17. – Continued.

Sinlaku does not develop along the baroclinic zone, but starts as a rotational field with high translation speed superimposed on a baroclinic zone, the development occurs more rapidly: within a few hours, instead of one to several days. The wind field during the Shapiro-Keyser-like cyclone development, shows two maxima of > 40 m/s near the cyclone center (Figs. 5.18d and 5.18f). The first low-level wind maximum is present northwest of the cyclone center, parallel to the isentropes of the bent-back warm front, and to the left of the direction of motion of Sinlaku. The second low-level wind maximum is located to the southeast of the center and near the region where a frontal fracture is expected but not clearly observed. A third region of relatively high wind speed (> 25 m/s) is seen southeast of Sinlaku in the warm sector, just ahead of the cold front (Fig. 5.18f). The possibility of these features being a cold jet, sting jet and warm jet will be analysed in Section 5.2.4.

After 20/00, the cyclone starts to decay. Trajectories that started in the cold sector north of Sinlaku, stay at lower levels and show cyclonic and anticyclonic motion (Fig. 5.18b, around 141°E , 35°N). In the warm sector, air parcels rise and also show both cyclonic and anticyclonic behaviour (Fig. 5.18b, around 143°E , 36°N). This pattern corresponds to the air streams of classical extratropical cyclones, as described by Thorncroft et al. (1993). Sinlaku is therefore thought to be extratropical at this stage. The maxima in the wind field have decreased (< 40 m/s, Figs. 5.18h, 5.18j

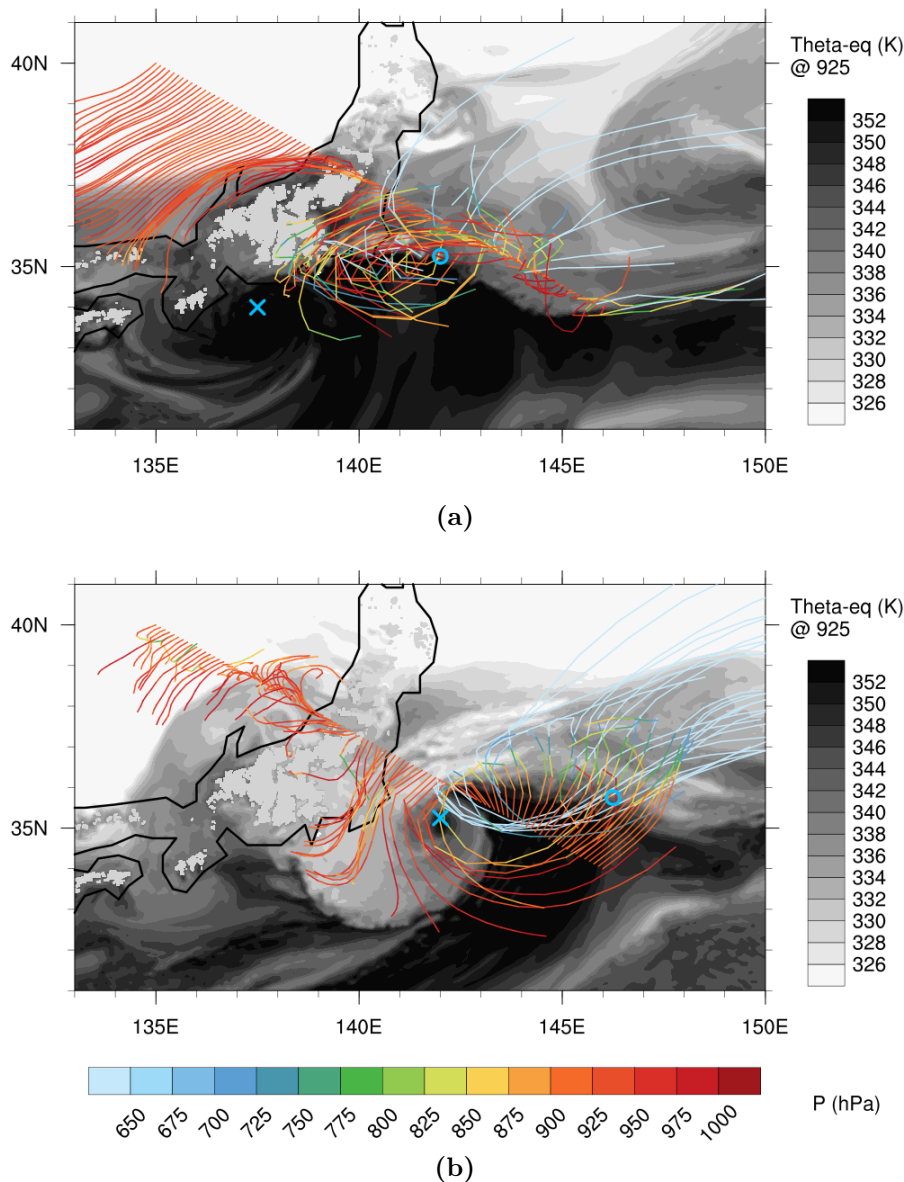


Figure 5.18. – 12-hour forward trajectories starting at 925 hPa on a northwest-southeast directed line crossing Japan (solid black line) on (a) 19/12 and (b) 20/00. The colors of the trajectories represent the pressure (hPa). Equivalent potential temperature at 925 hPa at trajectory starting time is given in gray shades. The location of minimum mean sea level pressure of Sinlaku is marked by a blue cross (at trajectory start) and circle (at trajectory end). Figure (b) is shown in Evans et al. (2017) also.

and 5.18l), and the cyclonic wind field has broadened from an almost axi-symmetrical circulation with $RMW < 0.5^\circ$ on 19/15 to an asymmetric circulation with $RMW > 1.0^\circ$ on 20/12. There are two areas of maximum wind still, in which the flow is parallel to the isentropes of a warm anomaly, that was first present south of the center but moves towards the west and center of the circulation over time.

From a quasi-3D perspective, 20/00 is representative for the structure of Sinlaku during its ET development. Considering the temperature and moisture distribution

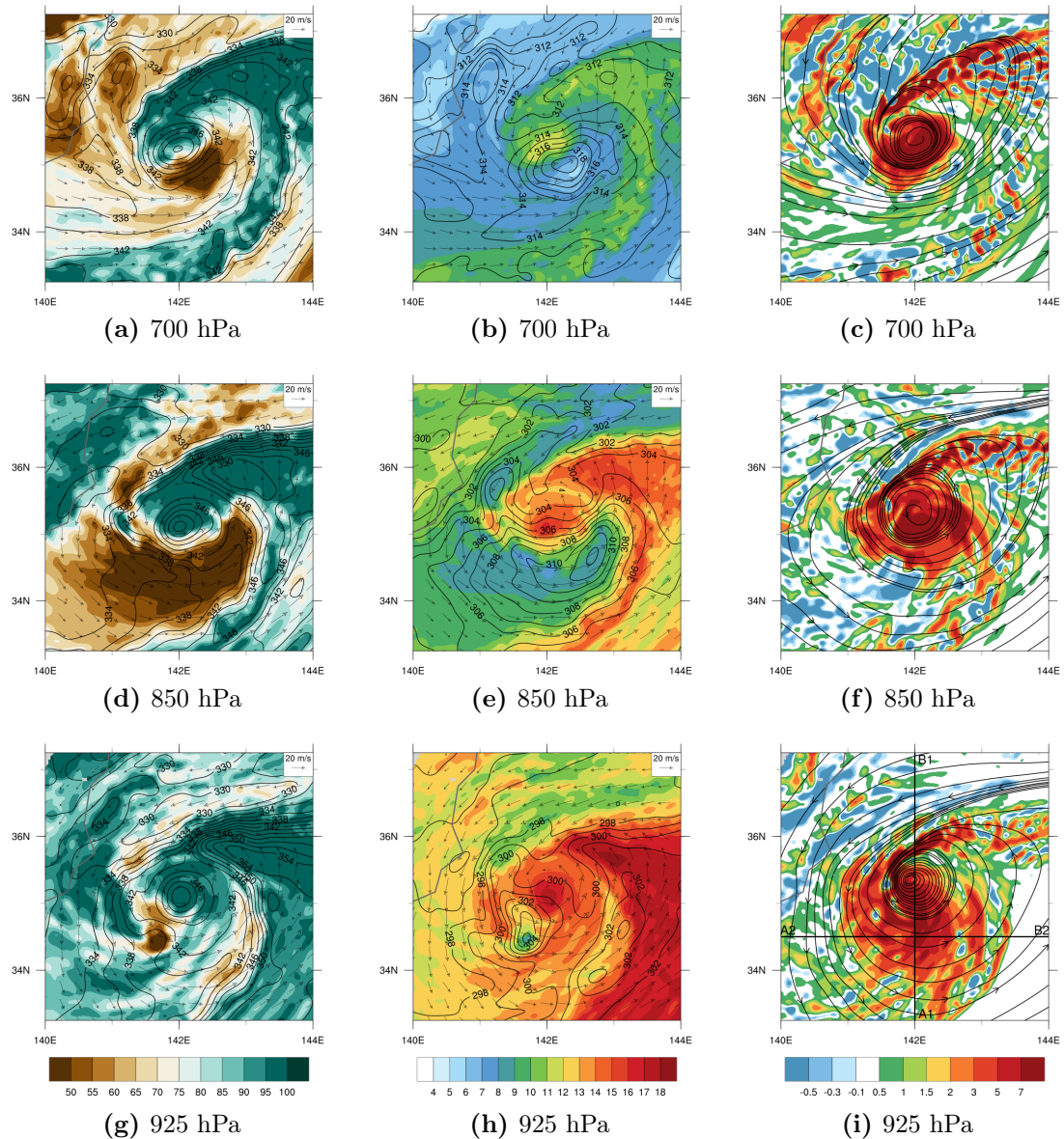


Figure 5.19. – Overview of the structure of Sinlaku’s center with (a,d,g) relative humidity (shaded, %) and θ_{eq} (contours, K); (b,e,h) specific humidity (shaded, g/kg) and θ (contours, K); (c,f,i) PV averaged over the shown level ± 25 hPa (shaded, PVU) and streamlines, at (a,b,c) 700 hPa, (d,e,f) 850 hPa and (g,h,i) 925 hPa, on 20/00.

the most remarkable feature is the warm and dry anomaly south of the circulation center (Fig. 5.19). This feature of stable air is best visible at 850 hPa (Fig. 5.19e), and present to a smaller horizontal extent at 700 hPa (Figs. 5.19a,b). Ritchie and Elsberry (2001) also recognized a stable area of warm dry air on the upshear side of the cyclone at 850 hPa. They associated this feature with the area of suppression of convection, free of clouds and precipitation. The development of this remarkable feature and its consequences for the further development of ET have not, however,

been investigated in detail in previous studies. This stable feature is therefore one of the key topics in the next subsections, and will be referred to as the 'warm anomaly'.

Below the warm anomaly, at 925 hPa, colder but relatively moist midlatitude air is present with a localized warm dry anomaly (141.7°E, 34.5°N, Figs. 5.19g,h). Despite the inflowing dry air, the rotational center still consists of moist saturated air at all heights considered (Figs. 5.19a,d,g). The inflow of subtropical air towards the warm front east of Sinlaku (142°E-144°E, 36°N) occurs at lower levels only (Fig. 5.19h). At 850 and 700 hPa, moist saturated air is dominant along a spiral band that wraps around the center (Fig. 5.19a,b,d,e). The moist band consists of the cold front to the southeast of the center and the warm front to the northeast. When considering the intensity of Sinlaku, it is seen that high PV air is present in the rotational center at all heights. At 700 and 850 hPa, there is also positive PV seen along the warm front, spiralling into the center (Fig. 5.19c,f). At 925 hPa, this frontal PV is less intense, and the dominant PV feature is present south of the center, just below the warm anomaly at 850 hPa (Fig. 5.19i). This low-level PV feature south of the center is a topic of interest also and will be explained in Section 5.2.3. But first the midlatitude and subtropical air masses that seem to spiral around each other on 20/00 (Fig. 5.19) are analysed from a Lagrangian perspective.

5.2.2. Distribution of midlatitude and subtropical air masses

The interaction of a TC with the baroclinic zone is characterised by the inflow of cold and dry midlatitude air that weakens the cyclonic system, as was reviewed in Chapter 2. The actual path of the inflowing midlatitude air, and the mechanism behind the weakening are, however, not yet described. Next to the midlatitude air, the advection of warm moist subtropical air towards the cyclone is investigated also, in order to analyse the role of the warm moist air in the maintenance of Sinlaku's intensity during ET. Most features in this subsection are based on Sinlaku's reference structure on 20/00 (Fig. 5.19).

Subtropical air supply

The supply of subtropical air is of importance for the maintenance of the cyclone. In a TC, the warm moist air flows in at the boundary layer and serves as a source for diabatic heating and PV creation as it rises in deep convection. During ET, a warm front develops, and the subtropical air rises over the warm front in a warm conveyor belt (WCB) like flow, creating PV diabatically along the front. This is seen for Sinlaku as well (Fig. 5.20). Air parcels that start in the subtropical air southeast of Sinlaku move towards the baroclinic zone. There they rise and the trajectories split into two branches. One branch rises up to 200 hPa, loses q_v and gains θ during ascent, reaches the jet stream and turns anti-cyclonically (Fig. 5.20a,a1,a2,a3). It resembles WCB-1 in Fig. 2.14, although the process occurred within 12 hours, which

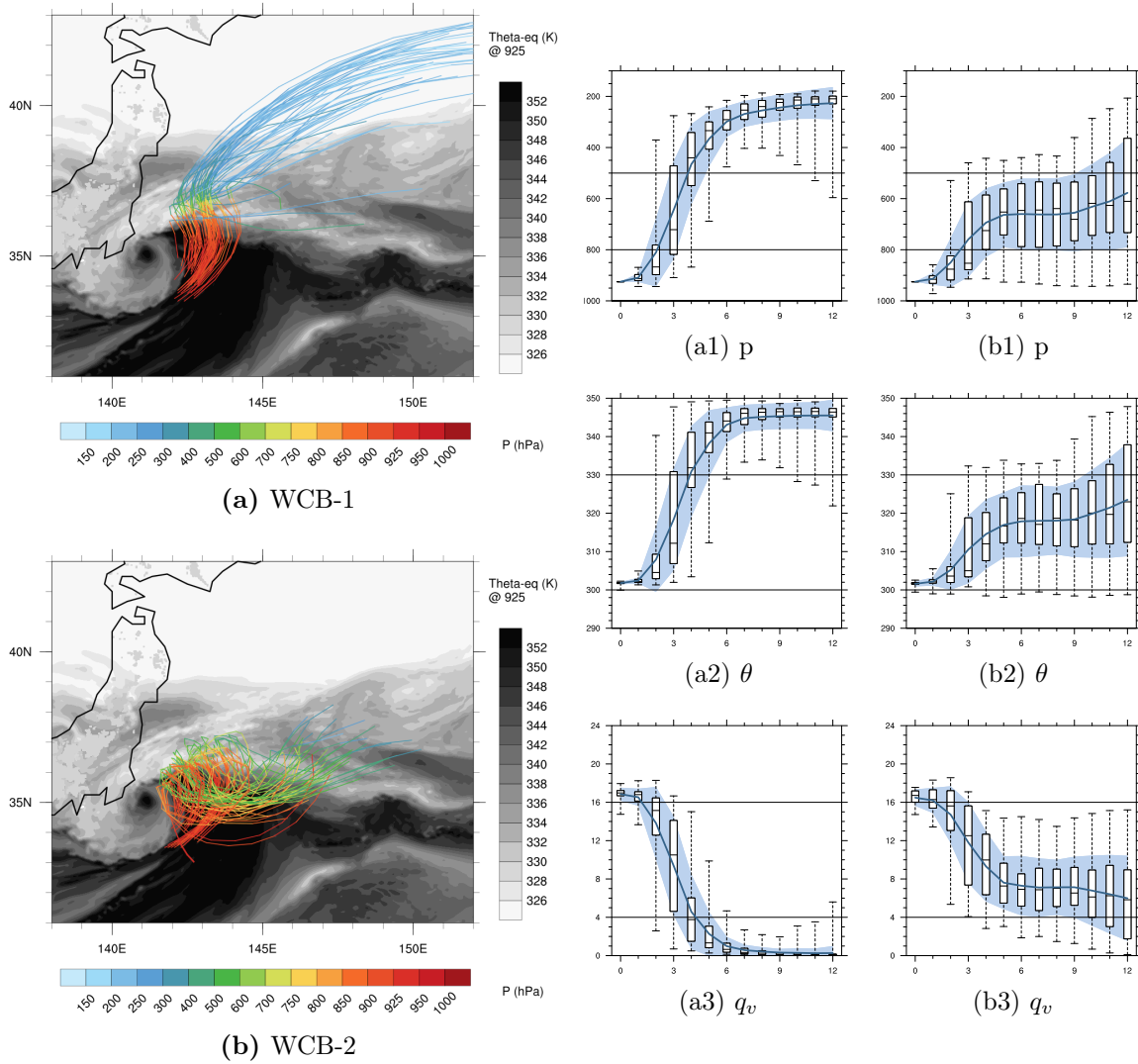


Figure 5.20. – 12 hour forward trajectories and corresponding statistics, starting on 19/22, east of the cyclone center in air with $\theta_{eq} > 345$ K and wind speed > 25 m/s, for (a) WCB-1 and (b) WCB-2. The colors represent the pressure along the trajectories and the grey shades represent θ_{eq} at 925 hPa on 19/22. For details of the statistic figures see Section 3.3.5.

is rapid for a WCB. The second branch rises up to 650 hPa (Fig. 5.20b1). During the ascent, clouds form and the specific humidity decreases from ~ 16 g/kg to 7 g/kg (Fig. 5.20b3). After turning cyclonically around the cyclone center at a relatively steady level of 650 hPa, the air stream continues with a second ascent along the baroclinic zone (Fig. 5.20b,b1). This branch resembles WCB-2 in Fig. 2.14. These two classical WCB branches, that transport subtropical air towards Sinlaku’s warm front, will serve as an example for comparison with air streams in other sections.

The WCB trajectories were selected for their wind speed > 25 m/s. This refers to the area of increased wind speeds, in the warm sector, ahead of the cold front and east of the center (Fig. 5.18f, 142.5°E , 34.5°N). From additional backward trajectories

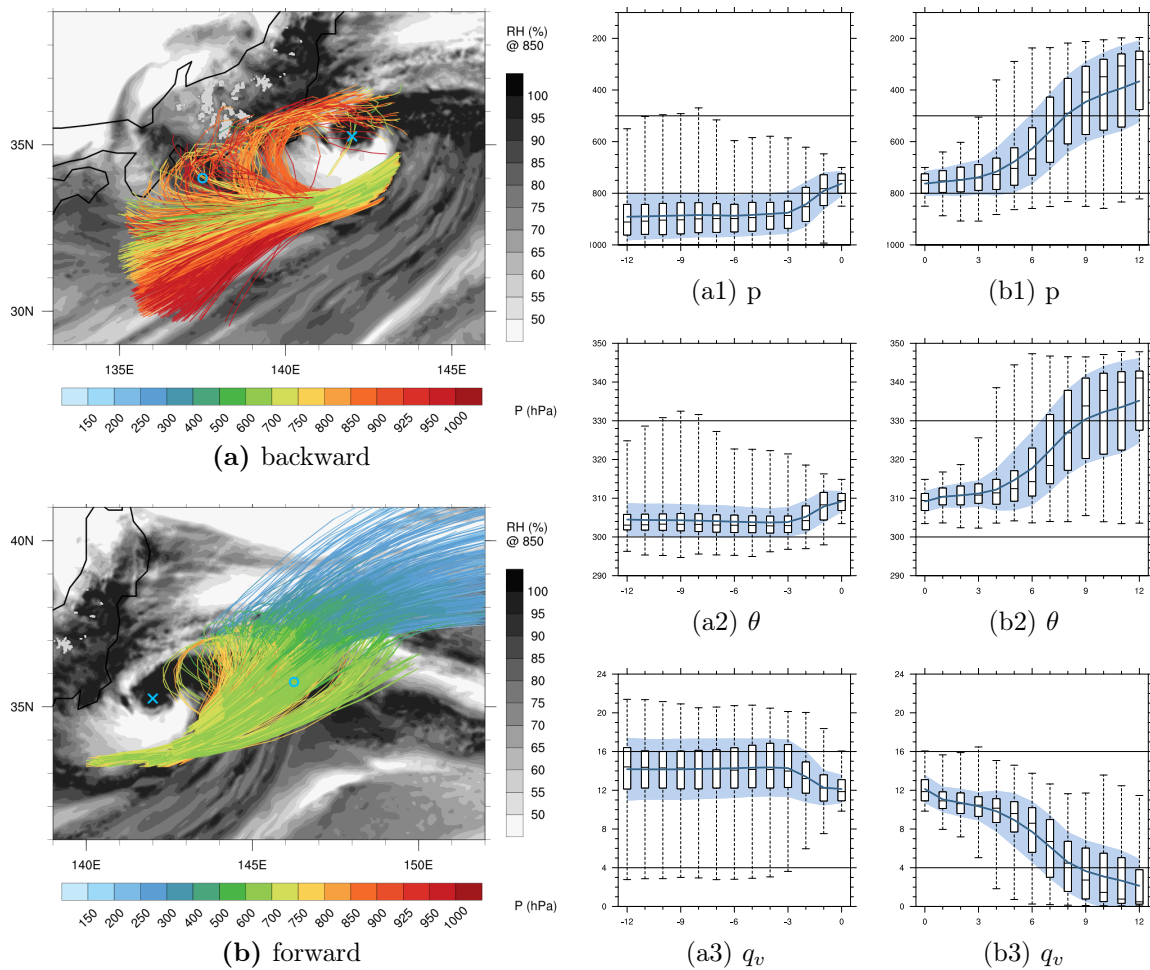


Figure 5.21. – 12 hour (a) backward and (b) forward trajectories and corresponding statistics, starting on 20/00, south of the cyclone center in air with $RH > 98\%$. The colors represent the pressure along the trajectories and the grey shades represent RH at 850 hPa on 20/00. For details of the statistic figures see Section 3.3.5.

that started at the same location (not shown) it could be seen that the wind speed increased on average from 17 m/s to 27 m/s within 6 hours. These air parcels thereby remained at a level below 900 hPa, embedded in subtropical air. Since this increased wind field in the warm sector is related to the WCB, it is thought to be a warm jet-like feature (see Fig. 2.14). Although it is weaker than a WJ (> 30 m/s, e.g. Hewson and Neu (2015)), the increase in wind speed may be related to warm jet dynamics.

Not all subtropical air reaches the warm front by inflow below 900 hPa. The mid-latitude air to the southwest of Sinlaku undercuts part of the subtropical air inflow, which is therefore lifted along the cold front. Backward trajectories that are started in the band of saturated air (here: $RH > 98\%$) of the cold front, between 850 and 700 hPa (see also Fig. 5.19a,d) mainly originate in the subtropical air southeast of Sinlaku (Fig. 5.21a). As in the case of the air parcels that arrive at the WCB,

these trajectories increase their ground-relative speed from 11 m/s to 25 m/s (not shown). This speed is higher than the translation speed of the storm and may indicate a weak form of the warm jet. Due to the acceleration the air parcels arrive at the south and southeast of Sinlaku. The air parcels flow at a constant height of on average 900 hPa and rise along the cold front to 750 hPa in the last three hours where they become saturated, lose water vapour by condensation and increases its potential temperature (Fig. 5.21a1,a2,a3). Only a minority of trajectories originates in the midlatitude sector along the warm front. In the next 12 hours, the air parcels rise a second time, now along the warm front (Fig. 5.21b), where they lose water vapour again before arriving in the jet stream (Fig. 5.21b1,b3). These trajectories resemble WCB-1.

The air parcels that arrive in the cyclonic and anti-cyclonic WCB (Fig. 5.20) arrive with on average 16 g/kg water vapour, and lose 8 g/kg and 16 g/kg respectively along the warm front (Fig. 5.20a3,b3), thereby supplying the front with latent heat and diabatically modifying the PV. The air that is lifted along the cold front, originates at a higher altitude and with a lower water vapour content (14.5 g/kg, Fig. 5.21a1,a3). Due to its lifting along the cold front, at least 2 g/kg of water vapour is transformed into liquid water before the air arrives at the warm front (Fig. 5.21b3). The warm front therefore becomes drier, and subsequently a lower amount of latent heat is released. So the undercutting midlatitude air to the southwest of Sinlaku modifies the subtropical air supply and thereby plays a role in reducing the diabatic PV creation with consequences for weakening Sinlaku's warm front with associated precipitation and cross-frontal circulation.

The saturated cyclone center

Within a TC, warm moist air flows into the cyclone in the boundary layer. When the air rises, potential energy (related to θ_{eq}) is converted into kinetic energy when the water vapour condenses and diabatically creates PV. Subsequently, the air flows out of the system at the top, and is replaced by new high- θ_{eq} air at the bottom. During ET, the newly inflowing air can also consist of midlatitude cold dry (low- θ_{eq}) air, decreasing the available water vapour that can condense and create PV diabatically. Nevertheless, on 20/00 the center still consisted of saturated and relatively high θ_{eq} air (Fig. 5.19a,d,g). The development of this center is investigated by the use of trajectories. Processes that influence the temperature and water vapour content are analysed, assuming that an increase in water vapour together with an increase in temperature cause an increase in θ_{eq} (Eq. 3.24, where $r \approx q_v$). 12-hour backward trajectories are calculated, starting at 975 - 700 hPa in the saturated (here $RH > 98\%$) and relatively warm air in the center (141.5-142.5, 34.8-35.6). The resulting trajectories can be divided into three categories: originating in the subtropics ($\theta_{eq} > 350$ K), originating in midlatitudes ($\theta_{eq} < 350$ K) and originating in the center of the storm (136.75-137.75, 33.5-34.5 with $\theta_{eq} > 350$ K) 12 hours earlier.

The locations of the trajectories and their magnitude of θ_{eq} are given at t=-12, t=-9, t=-6 and t=-3 (Fig. 5.22). A minority of the air parcels (7 %) originate

from the original TC core and remain in the center during the full 12 hours (Fig. 5.22, crosses). Their θ_{eq} decreases, however, first by a decrease in q_v during ascent, and later by a decrease in temperature, possibly due to mixing with colder air (Fig. 5.23a1,a2,a3,a4). The remainder of the trajectories originate from outside the center and spiral inwards, bringing air with different properties into the center.

The majority of the trajectories (69 %) arrive from the northern midlatitude air (Fig. 5.22, circles). Trajectories start in the cold sector along the warm front and circle around the cyclone before arriving in the center. They start above 900 hPa and undergo evaporative cooling when they are advected beneath the warm frontal precipitation (Fig. 5.23b3,b4). Subsequently, the increased density causes the air parcels to sink (Fig. 5.23b1). At $t=-3$, almost all air parcels are in or near the center. The air parcels rise and θ_{eq} rises due to an increase in potential temperature, while the water vapour content is relatively constant (Fig. 5.23b2,b3,b4). The wind speed in the last few hours is relatively high in the midlatitude and subtropical air masses

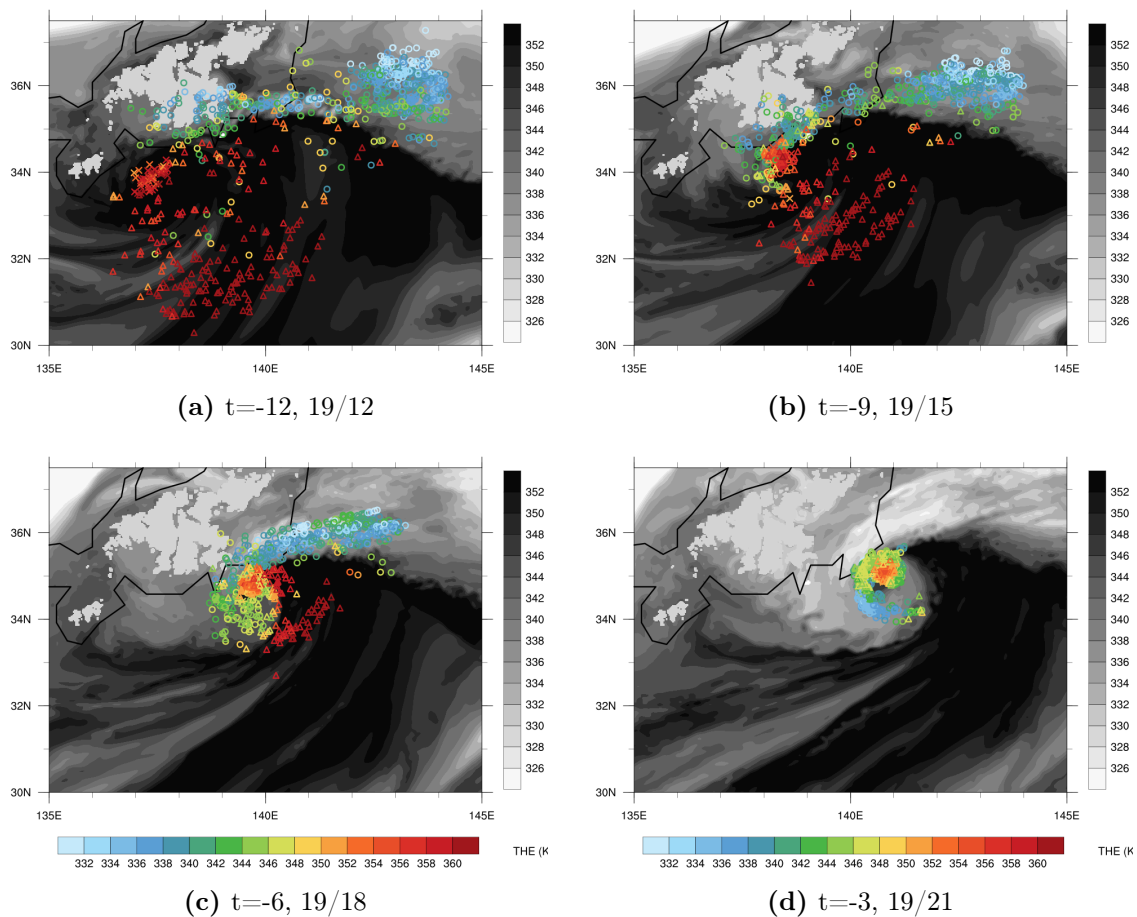


Figure 5.22. – Location of individual trajectories that end in the center of Sinlaku with $RH > 98\%$ on 20/00. Colors represent the actual θ_{eq} of the air parcels and grey shades represent θ_{eq} at 925 hPa on (a) 19/12, (b) 19/15, (c) 19/18 and (d) 19/21. Parcels that start in the center, subtropical air mass ($\theta_{eq} > 350$ K) or midlatitude air mass ($\theta_{eq} < 350$ K) on 19/12 are marked by a cross, triangle or circle, respectively.

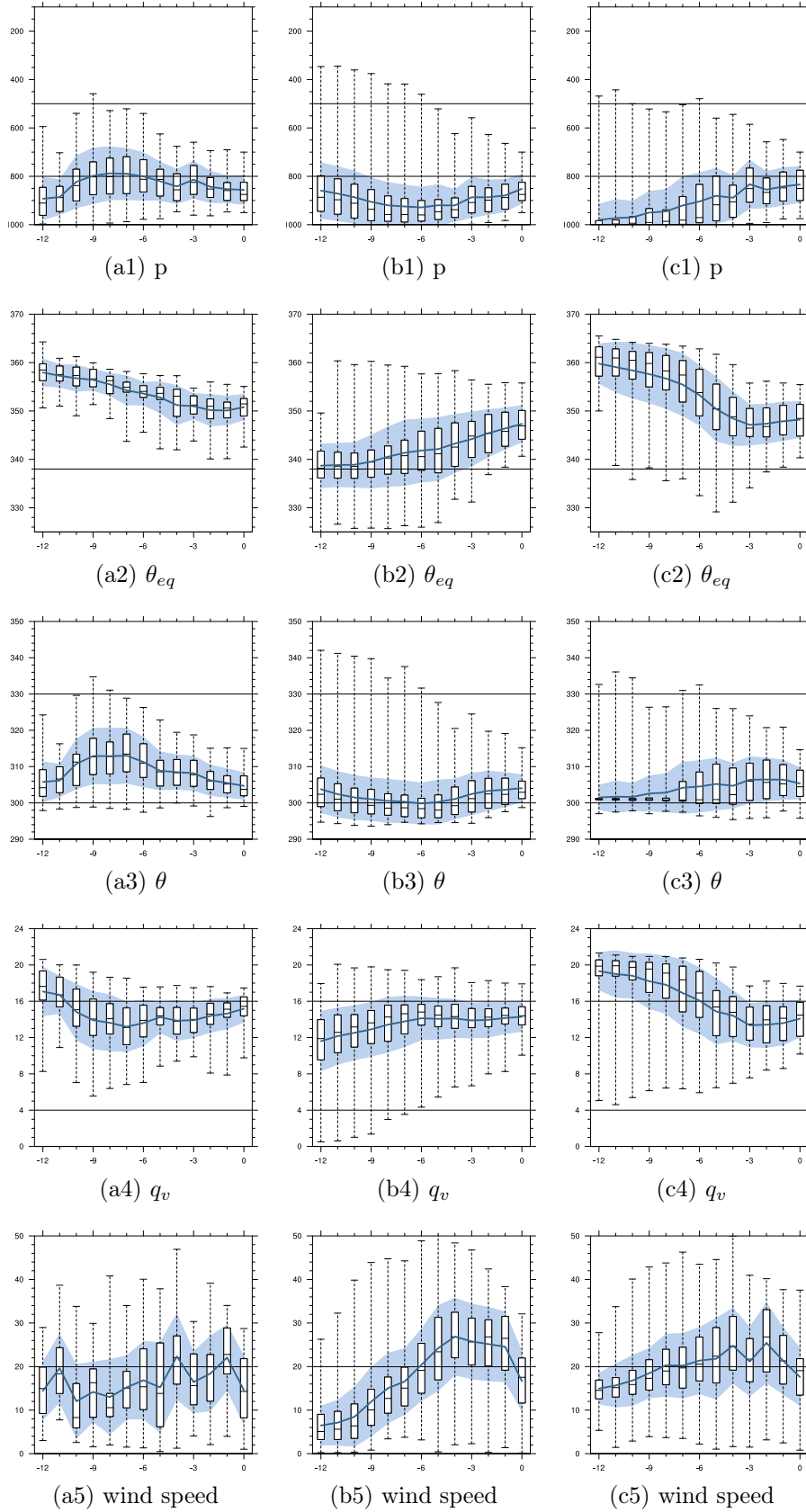


Figure 5.23. – Statistics corresponding to the trajectories of Fig. 5.22, with (a) the center air mass, (b) the midlatitude air mass and (c) the subtropical air mass. For details of the statistic figures see Section 3.3.5.

(> 20 m/s, Fig. 5.23b5,c5). It is suggested that the potential temperature could rise due to mixing of the colder midlatitude air with the warmer subtropical and center air masses, in a relatively turbulent environment. Despite the increase in θ_{eq} , the air has still a lower θ_{eq} value than the air that originates in the core, thereby decreasing the intensity of the cyclone warm core (Fig. 5.23b2).

A quarter of the trajectories (24 %) arrive from the southern subtropical air and flow over the ocean surface towards the center via the warm front close to the center (Fig. 5.22, triangles). The air rises, first adiabatically and afterwards diabatically, losing water vapour along the way (Fig. 5.23c1,c3,c4). Most air parcels are near the warm front during this time or already turning around the center and are expected to either lose water vapour by condensation or by mixing with dry midlatitude air that also circles around the center. The loss of θ_{eq} is dominated by the loss of q_v (Fig. 5.23c2,c4), and, despite the initially high magnitude of θ_{eq} , these air parcels end in the center with a relatively low θ_{eq} (Fig. 5.23c2). Thereby they contribute to the intensity decrease of the center also.

So, whereas in a TC the rising high- θ_{eq} is replaced by new high- θ_{eq} air, here the baroclinic situation of the warm front and, in particular the part close to the center, influences the development. The air that was already present in the center did also sink due to evaporative cooling near the front. Besides, subtropical air loses water vapour (decreasing θ_{eq}) and midlatitude air gains water vapour (increasing θ_{eq}), either along the warm front or possibly by mixing near the center, bringing both air masses at a relatively similar magnitude of θ_{eq} (Fig. 5.23b2,c2). This magnitude is, however, lower than in the original center and thereby decreases the potential energy, related to θ_{eq} , in the center (Fig. 5.23a2).

The warm anomaly near the center

In literature it has often been mentioned that at the west side of the cyclone, midlatitude air sinks and forms a stable cloud-free area. This stable area is located near the center and it therefore highly influences the convective character of the transitioning TC. The development of this area has, however, never been analysed in detail, and is the objective of this subsection. Since the warm anomaly is best seen at 850 hPa, 12-hour backward trajectories are started at this level in the relatively warm and dry region ($Q_v < 10$ and $\theta > 306$, Fig. 5.19e). The resulting trajectories can be separated into four categories, based on their location and height 12 hours earlier: northwest of Sinlaku above 700 hPa (Fig. 5.24a), south of Sinlaku at lower levels (Fig. 5.24b) and northeast of Sinlaku along the warm front, either at low (Fig. 5.24c) or high (Fig. 5.24d) levels. The air masses will be referred to as NW-high, S-low, E-low and E-high, respectively. This shows that the stable air does not simply consist of inflowing midlatitude air. Instead it consist of a mixture of one subtropical and three different midlatitude air streams.

The air masses all have their own characteristics during the first 9 hour of the trajectories. Airmass NW-high arrives from altitudes above 500 hPa (Figs. 5.24a

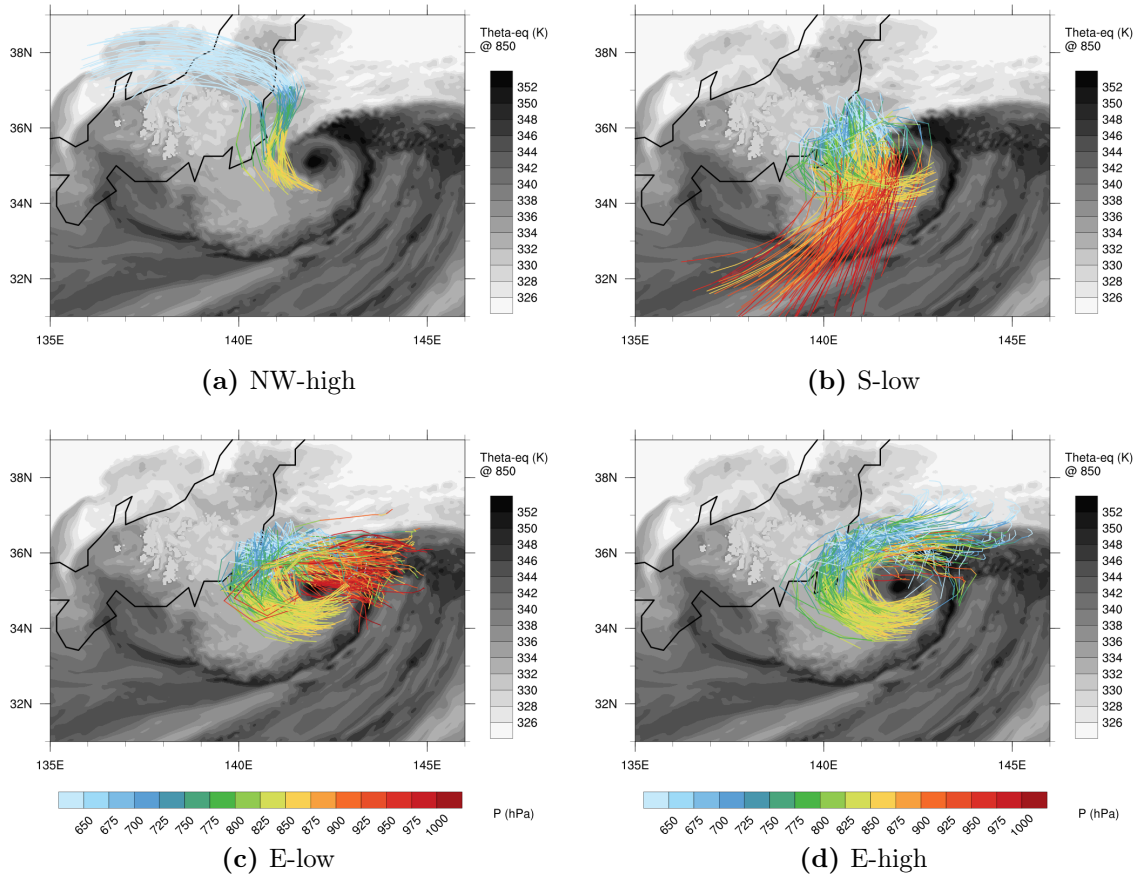


Figure 5.24. – 12 hour backward trajectories, starting on 20/00, south of the cyclone center at 850 hPa in air with $\theta > 306$ K and $q_v < 10$ g/kg. The colors represent the pressure along the trajectories and the grey shades represent θ_{eq} at 850 hPa on 20/00. The trajectories are divided into air streams (a) NW-high, (b) S-low, (c) E-low and (d) E-high, based on their specific paths, initial location and height.

and 5.25a1). It has a very low water vapour content and is relatively dry ($RH < 40$ % on average, Fig. 5.25a3,a4). Between $t=-6$ and $t=-3$ the air parcels arrive below the precipitation field of the WCB-like structure (Fig. 5.24a). They gain water vapour from the evaporation of precipitation and the air cools during the phase change from the liquid to the gas phase (Fig. 5.25a2,a3). The denser air starts to descend (Fig. 5.25a1) and now follows the cyclonic rotation of the cyclone. Although the air becomes relatively moist along the way, this air stream still represents the dry air intrusion (see Fig. 2.15). Airmass S-low starts south of Sinlaku below 900 hPa and represents subtropical air (Fig. 5.24b). It rises to the east of Sinlaku over the warm front. When the RH is on average above 90%, the air in many trajectories is saturated and loses water vapour by condensation (Fig. 5.25b2,b3,b4). The air turns cyclonically and arrives in the cold sector ahead of the warm front. Subsequently the air cools diabatically and starts sinking (Fig. 5.25b1,b2,b3, $t=-4$ to $t=0$). Airmass E-low behaves in a similar manner to S-low, although its starting location is along the warm frontal zone, far away from the cyclone center (Fig. 5.24c), and with initially a

lower amount of water vapour (Fig. 5.25c3). The air starts with evaporative cooling and sinking motion while gaining water vapour (Fig. 5.25c1,c2,c3). It then arrives in the rising part of the frontal zone and behaves like air mass S-low (Fig. 5.25b,c, $t=-7$ to $t=0$). Airmass E-high starts along the front also, but at higher altitudes (Fig. 5.24d). It behaves in a relatively similar manner to NW-high, although here the air parcels are initially not extremely dry (Fig. 5.25a,d). The air is always below the precipitation area and evaporative cooling therefore occurs at a relatively steady rate (Fig. 5.25d2,d3).

During the last three hours, all four air streams are near the cyclone and now have similar characteristics (Fig. 5.25). They descend from about 700-750 hPa towards 850 hPa. Air masses S-low, E-low and E-high have mixed at this time, and arrive all spread over the warm anomaly. A warm anomaly was already there before they arrived and resulted in locally downward sloping isentropes. Due to a lack of precipitation in this stable area, the air parcels could sink purely adiabatically along the isentropes. Because the potential temperature stays constant during adiabatic sinking, the air parcels are relatively warm compared to the environment (Fig. 5.25b2,c2,d2, $t=-1$ to $t=0$). Additionally, the adiabatic sinking along the isentropes of the warm anomaly maintains or even increases the intensity of the warm anomaly, depending on the characteristics of the descending air. Airmass NW-high arrives at the western side of this air mass, just on the border of the warm anomaly temperature gradient. It sinks on average almost 100 hPa within the last hour, but the descent is not fully adiabatic (Fig. 5.25a2).

Overall, it can be said that close to the cyclone, all four air streams descend diabatically below Sinlaku's own precipitation area, until they arrive near the stable precipitation-free area, where they sink adiabatically and arrive as air that is warm relative to its environment. Beside this behaviour, it can be observed that the air parcels all increase in wind speed during their descent (Fig. 5.25a5,b5,c5,d5). Air masses S-low and E-low in particular show an increase in wind speed of about 10 m/s that coincides with a decrease in relative humidity from an almost saturated level towards less than 50%, while descending more than 100 hPa from the region of precipitation (Fig. 5.25b1,b4,b5,c1,c4,c5). Although these air masses do not reach a wind speed of > 40 m/s, their characteristics correspond very well to those of a sting jet. This feature is analysed further in Section 5.2.4.

Now, the consequence of this warm dry air for the subsequent development of Sinlaku's ET will be analysed. 12-hour forward trajectories are started at the same location as where the backward trajectories started from. The forward trajectories can be divided into two parts (Fig. 5.26). Both parts show rising air along the warm front but with different characteristics. Part 1 ascends rapidly from 850 to 300 hPa, losing water vapour on the way (Fig. 5.26a1,a2,a3). The remaining dry air turns eastwards as it moves into the jet stream (Fig. 5.26a). This air flow is relatively similar to WCB-1 (Fig. 5.20a), although here the ascent occurs over a longer time period. Part 2 remains around 850 hPa for the first few hours (Fig. 5.26b,b1). These air parcels move first eastward, with the cold frontal zone ahead of them. When they are located close enough to the cold front, they gain water

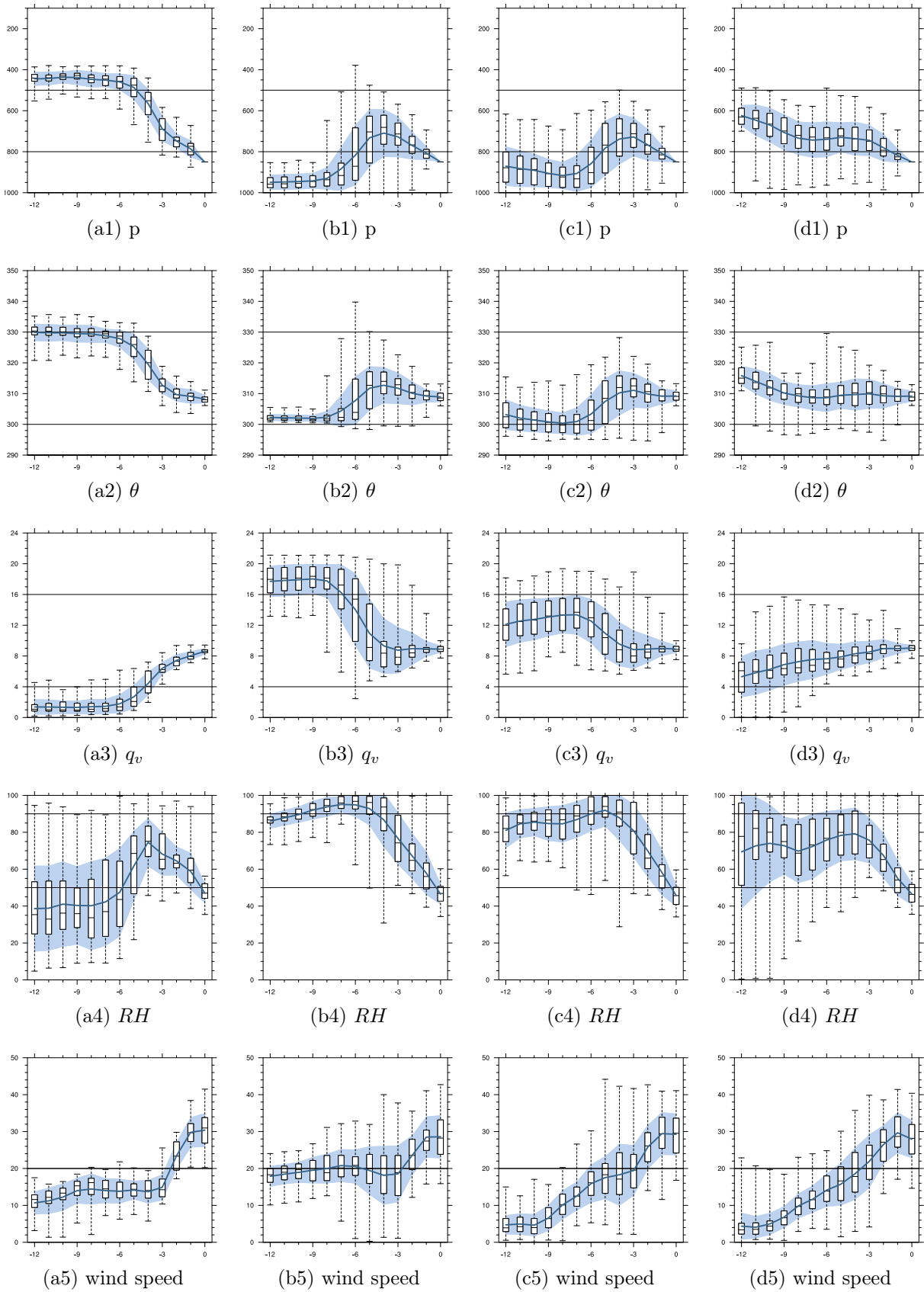


Figure 5.25. – Statistics corresponding to the trajectories of Fig. 5.24, for (a) NW-high, (b) S-low, (c) E-low and (d) E-high. For details of the statistic figures see Section 3.3.5.

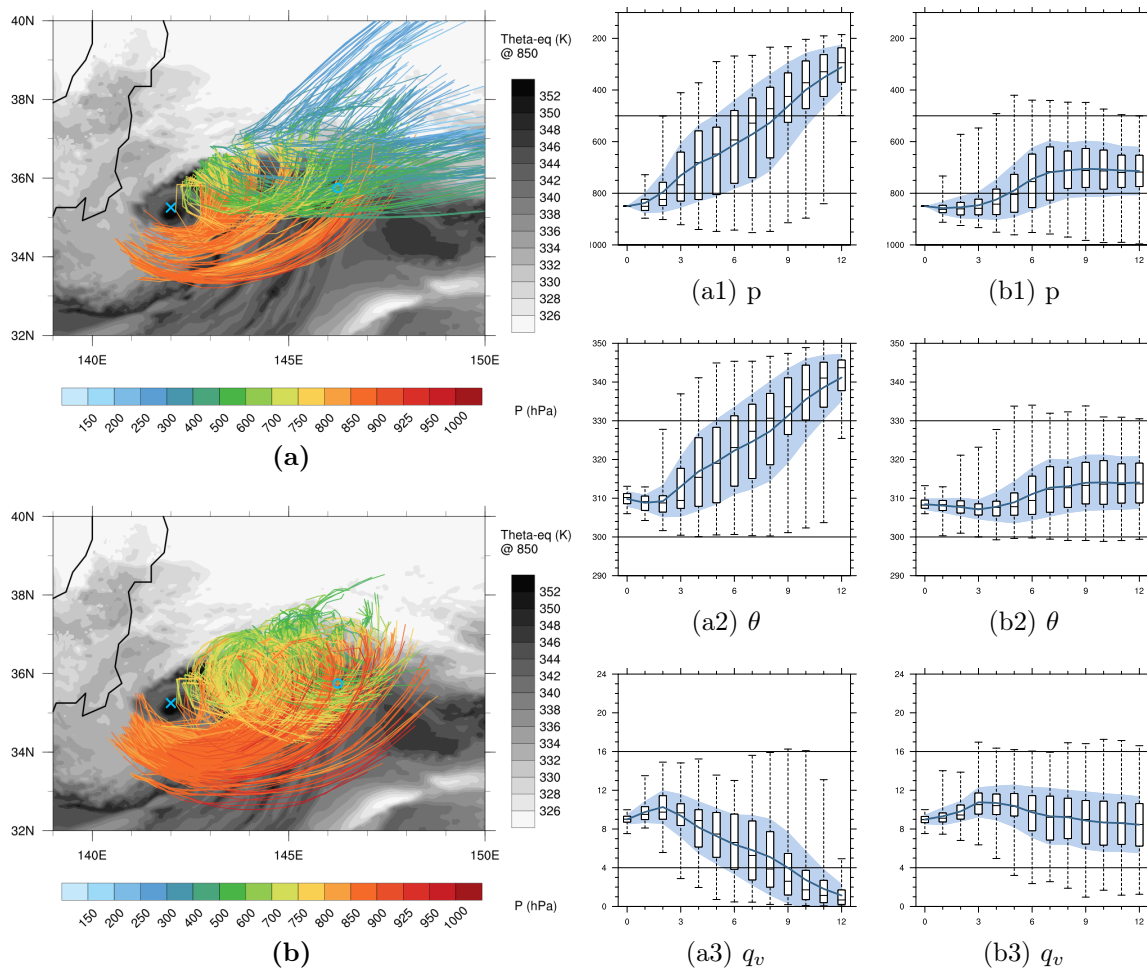


Figure 5.26. – 12 hour forward trajectories and corresponding statistics, starting on 20/00, south of the cyclone center at 850 hPa in air with $\theta > 306$ K and $q_v < 10$ g/kg. The colors represent the pressure along the trajectories and the grey shades represent θ_{eq} at 850 hPa on 20/00. The trajectories are divided into (a) an air stream that rises to above 500 hPa and (b) and air stream that stays below 500 hPa. For details of the statistic figures see Section 3.3.5.

vapour from cold frontal precipitation (Fig. 5.26b2,b3) and turn cyclonically to rise at the warm front from 850 to on average 700 hPa and lose water vapour again (Fig. 5.26b,b1,b3). After 12 hours the amount of water vapour in these air parcels is on average similar their initial value in the warm dry anomaly (8.5 g/kg instead of 9 g/kg, Fig. 5.26b3). This air flow is relatively similar to WCB-2. Both WCB-like features that arise from the warm air anomaly, transport 9-11 g/kg water vapour towards the warm front, in comparison to the > 16 g/kg from the actual WCB features (Fig. 5.20). Especially the WCB-2-like warm anomaly outflow results in relatively dry air that stays near Sinlaku's center (Fig. 5.26b). As a consequence, the warm front and associated processes are weakened.

From these backward and forward trajectory analyses, it can be said that in the first 12 hours, evaporative cooling by Sinlaku's rain field increases the temperature

gradient across the front and initiates the sinking motion of both the midlatitude and subtropical air. The front is therefore strengthened, as was the warm air anomaly by the adiabatic sinking in the last hour, representing a positive feedback mechanism. However, in the next 12 hours, the relatively dry air that has sunken to 850 hPa, infiltrates the warm front again. The dry air cannot cause as much condensational heating as the subtropical air does and thereby weakens the warm front. When the front decreases, also the associated processes like precipitation, evaporative cooling and subsequent sinking, decrease in intensity. As a consequence, the downward motion into the stable air decreases. This cycle of processes represents a negative feedback mechanism from downward motion initiated along the warm front resulting into the warm anomaly, toward a weakening of the warm front, the downward motion and the warm anomaly.

Midlatitude air inflow in the environment

The midlatitude air mass west of the storm ($\theta < 298$ K, $q_v < 13$ g/kg) at 925 hPa, can be divided in four air masses with similar characteristics to NW-high, S-low, E-low and E-high. The air masses will here be named with an additional "env-". The majority of the trajectories are now present in env-E-high and env-E-low (Table 5.1). They start ahead of the warm front and therefore the air west of Sinlaku consists indeed mainly of midlatitude air (Fig. 5.27). Only a minority has its origin in subtropical air (env-S-low) or in the dry intrusion air stream (env-NW-high, Table 5.1). The focus lies therefore on the air masses env-E-low and env-E-high. A small difference in starting location can be distinguished between the E-low/E-high and env-E-low/env-E-high air streams. The trajectories of env-E-low can be traced back to mainly north of 36°N and remain at relatively lower levels (Fig. 5.27a), while E-low is traced back to mainly south of 36°N, and is therefore captured by the rising motion of the warm front (Fig. 5.24c). Env-E-high, on its turn, is traced back to a location that is on average more east than in E-high (Fig. 5.27b and 5.24c). Env-E-high has therefore more time to be influenced by the precipitation field of Sinlaku and descends relatively quickly. Both env-E-low and env-E-high arrive west of Sinlaku at roughly the same time and location as E-low and E-high, but then at a lower level and with a southward direction of motion towards the environment, rather than turning cyclonically around the center.

	Center		Environment	
NW-high	58	11 %	30	5 %
S-low	126	24 %	20	3 %
E-low	187	35 %	303	49 %
E-high	157	30 %	267	43 %

Table 5.1. – Number and percentage of trajectories that end in either the center region of Sinlaku (see Fig. 5.24) or the environmental region (see Fig. 5.27) on 20/00, divided over the air masses NW-high, S-low, E-low and E-high.

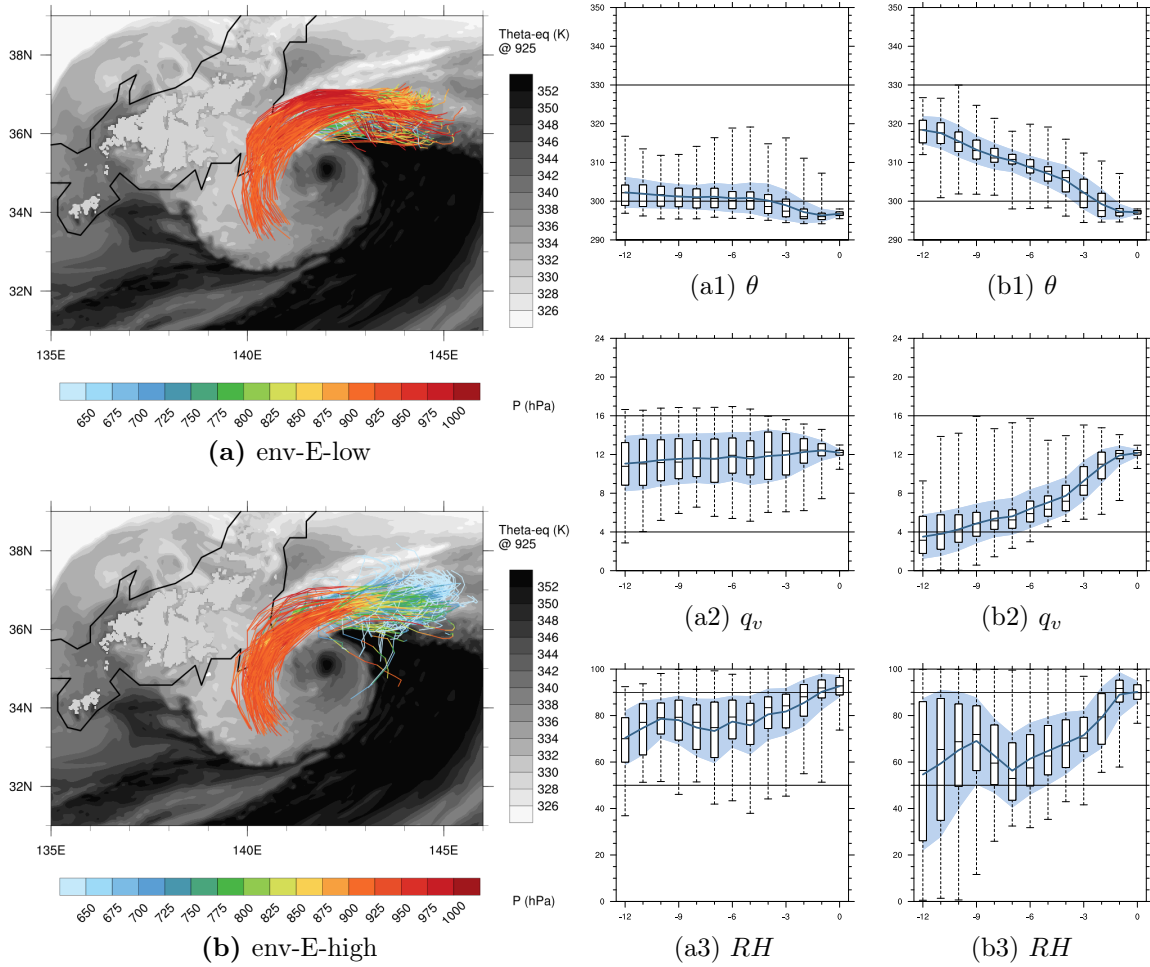


Figure 5.27. – 12 hour backward trajectories, starting on 20/00, west of the cyclone center at 925 hPa in air with $\theta < 298$ K and $q_v < 13$ g/kg. The colors represent the pressure along the trajectories and the grey shades represent θ_{eq} at 925 hPa on 20/00. The trajectories are divided into air streams (a) env-E-low and (b) env-E-high, based on their specific paths, initial location and height. For details of the statistic figures see Section 3.3.5.

The small difference in origin, results in a marked change in the characteristics of the air streams. The env-E-low air stream stays at lower levels and, although it sinks a little, its characteristics stay relatively constant (Fig. 5.27a1,a2). Therefore, this air stream transports air with midlatitude properties to the west of Sinlaku. Env-E-high starts on average at 600 hPa (Fig. 5.27b). The first 2 hours the air parcels stay at this height, and start descending from $t=-10$ to $t=0$, until they arrive at 925 hPa. The descent coincides with evaporative cooling and an increase in specific humidity (Fig. 5.27b1,b2). The last two hours before arriving to the west of the storm the air parcels sink adiabatically (Fig. 5.27b1). Due to a constant addition of water vapour, env-E-high starts with $q_v = \sim 3$ g/kg and ends with 11 g/kg (Fig. 5.27b2), while the air parcels that end near the center (E-high) start with 6 g/kg and end with 9 g/kg (Fig. 5.25d3). The intenser diabatic cooling causes env-E-

high to arrive in the environment west of Sinlaku with a relatively low potential temperature (298 K instead of 310 K in E-high) and higher rate of humidity (12 g/kg instead of 9 g/kg). Relative humidity therefore also increases (Fig. 5.27b3), due to which some air parcels become saturated and some clouds may be seen in the environmental air. So, in comparison to the dry air near the center, the environment to the west of the Sinlaku is relatively moist, due to evaporation below the warm frontal precipitation.

5.2.3. Mechanisms behind structural changes during ET

A TC intensifies by the conversion from potential energy into kinetic energy. The main mechanism here is convection that causes diabatic PV creation due to latent heat release. During ET, however, the TC moves into a baroclinic environment and the mechanisms that are responsible for the change in intensity and structure, change also. In the previous subsection a first impression is already given about mechanisms that influence the structure and intensity, based on warm moist air that is related to potential energy. In this subsection, multiple mechanisms that additionally influence the structural changes during ET are disentangled. The focus lies in the first place on the vertical motion field. Focussing on this field is motivated by the downward motion that played a key role in the creation of the stable warm anomaly in the previous subsection. Secondly, the low-level PV field is analysed, which was observed to be large outside the center at lower levels (Fig. 5.19i). Thirdly, the change in intensity of Sinlaku's vortex is analysed from a vorticity budget perspective.

Asymmetric vertical motion field

The vertical motion field is important in the development of ET because it determines the distribution of clouds and precipitation, but also latent heating, diabatic PV modification and the associated horizontal wind field. In the previous subsection it was seen that downward motion contributed to the development of the warm anomaly, which is a stable and cloud free area and characteristic for ET. Ritchie and Elsberry (2001) also found a feature of downward motion in their 15 km resolution simulation, that reached from roughly 200 hPa to 900 hPa and ended near a stable area with its maximum at 850 hPa. They explained it by upper-level convergence between the TC circulation and the midlatitude westerlies, but did not illustrate this further. For Sinlaku, no clear convergence area is found at upper levels. This raises the question what mechanisms actually influence the vertical motion field to the west of Sinlaku during its ET. From the trajectory analysis in the previous subsection it became clear that downward motion initially occurred at the same time as cooling of the air and the increase of water vapour. This was interpreted as evaporative cooling and diabatic sinking. At the end, however, the descent of most air parcels was adiabatic. Therefore, two additional causes of subsidence will be analysed here: vertical motion related to vortex tilting in vertical shear and cross-frontal circulation. Both mechanisms are analysed on 19/22, when Sinlaku was in

the period of its maximum intensity during ET, located over the open ocean with an intense low-level wind field, and on 20/06, when Sinlaku was weakening.

Starting with the vortex tilting in vertical shear, in the first place the vortex is tilted by the environmental vertical wind shear. During the tropical re-intensification period (Section 5.1), Sinlaku was tilted in the direction of the shear vector. In the ET phase, environmental vertical wind shear still tilts the vortex, but the tilt has turned, due to precession (e.g. Jones, 1995; Reasor et al., 2004). On 19/22, mainly a north-northwestward tilt is observed almost perpendicular to the shear vector, with a small directional change towards the northeast above 500 hPa (Fig. 5.28a).

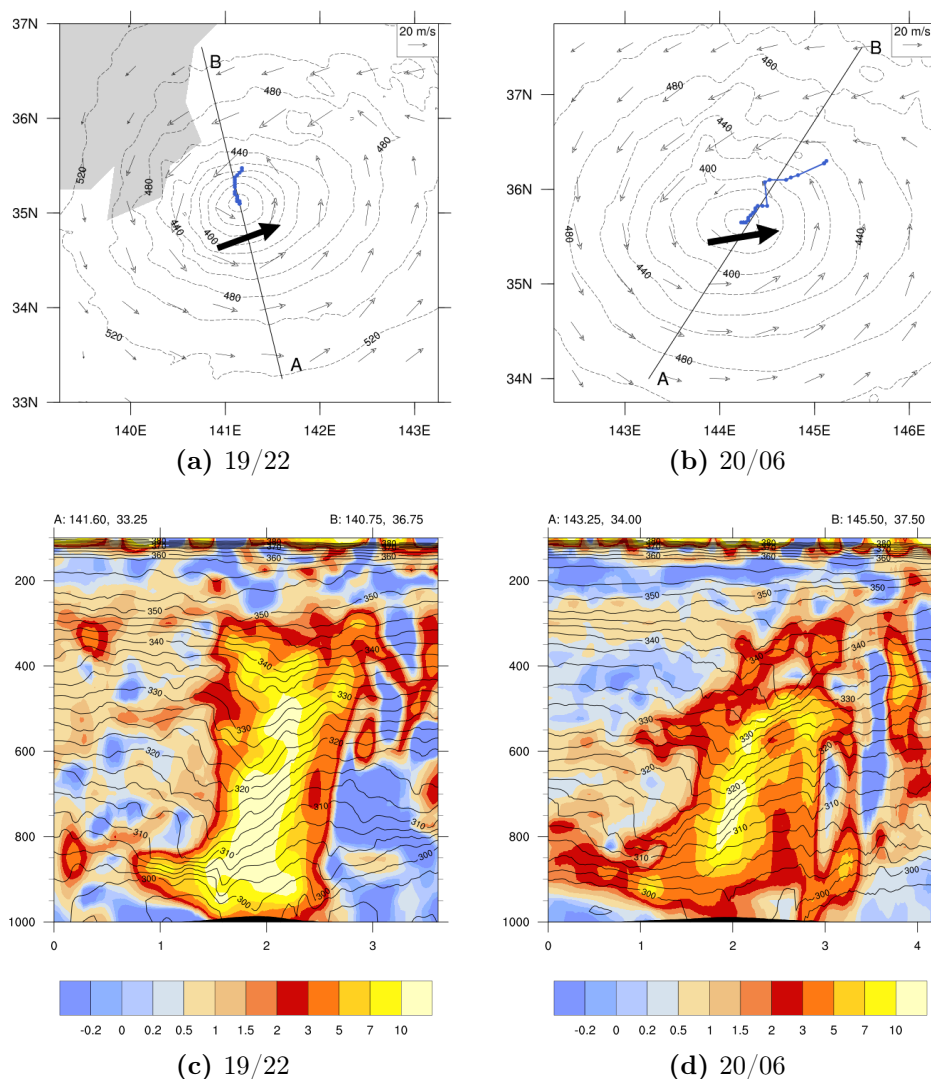


Figure 5.28. – Geopotential height (contours, m) and wind vectors (m/s) at 950 hPa, the location of minimum GPH at every 25 hPa between 950 and 400 hPa (blue dots and lines), and the environmental shear vector between 950 and 250 hPa (black arrow). The cross sections along line AB give PV (shaded, PVU) and isentropes (contours, K) on (a,c) 19/22 and (b,d) 20/06.

On 20/06 the tilt has changed to north-northeastwards up to 600 hPa, and east-northeast above 550 hPa, both in the downshear left direction (Fig. 5.28b). Cross sections along the direction of tilt show lowered isentropes at the uptilt side (left side of the PV tower in Figs. 5.28c,d) and raised isentropes at the downtilt side (right side of the PV tower in Figs. 5.28c,d). This pattern is similar to the idealised situation of isentropes in a balanced tilted vortex (Fig. 2.13b). Consequently, there is a warm anomaly at the uptilt side and a cold anomaly downtilt. This indicates that there might indeed be a relation between the warm anomaly and a tilted vortex in VWS. The uptilt warm anomaly is located at the same place as the warm and stable air from previous subsections. Whereas in the previous trajectory analysis the influence of moist dynamics on the development was discussed, here the influence of the dynamically driven secondary circulation of a tilted vortex is discussed. On 20/06, a similar situation is seen, although the isentropes are less steep and the entire PV tower is weaker, reaching less high. Meanwhile the vertical wind shear is stronger and tilts the vortex more.

The relation between the vortex tilt and the temperature field shows that Sinlaku's vortex is close to a balanced state. This would be best described by a non-linear balance, but e.g. Reasor et al. (2000) showed that using the QG-approximation provides useful qualitative information about the vertical motion field forced by dry dynamics. The vertical motion field is therefore diagnosed with the balanced dynamics of the QG- ω equation (Eq. 3.17). This results in a dipole of QG-forced vertical motion along the horizontal temperature anomaly (Figs. 5.29a,b). This configuration is similar to the distribution of temperature and vertical motion anomalies of a vortex in VWS following dry dynamics (Fig. 2.13c), although the vortex is not entirely dry yet (Figs. 5.29e,f). The maximum in QG-forcing is indeed co-located with fields of ascent and descent at 700 hPa (Figs. 5.29c,d). The vertical motion field can therefore partly be explained by the dry dynamics of a vortex in VWS. Consequently, the vertical motion along the horizontal temperature anomaly inside the vortex consists, at least partly, of slantwise ascent, rather than convection.

The magnitudes of the QG-forced vertical motion cannot be used quantitatively, but gives qualitative information. The QG-forcing to vertical motion is strongest at lower levels (Figs. 5.29a,b). This could be expected since the strongest temperature gradient is present at lower levels (Fig. 5.28c,d). Also, the differential vorticity advection will be stronger at lower levels because that is where the vorticity is strongest. Nevertheless, there is an upper-level forcing as well. On 19/22, the upper- and lower-level forcing are co-located (Fig. 5.29a). On 20/06, the lower-level forcing has decreased and the center of maximum upper- and lower-level QG vertical motion do not overlap anymore (Fig. 5.29b). This can be explained by the change in direction of the tilt above 500 hPa (Fig. 5.28b). The QG-forced vertical motion at 700 hPa is therefore strongest on 19/22, when the vortex tilt is in one direction and the upper- and lower-level forcing are co-located

Part of the vertical motion in Fig. 5.29c,d is not explained by the QG forcing. The elongated line of ascent and descent represents the warm front and the vertical motion is the cross-frontal circulation. Also, a less pronounced cold front is seen to

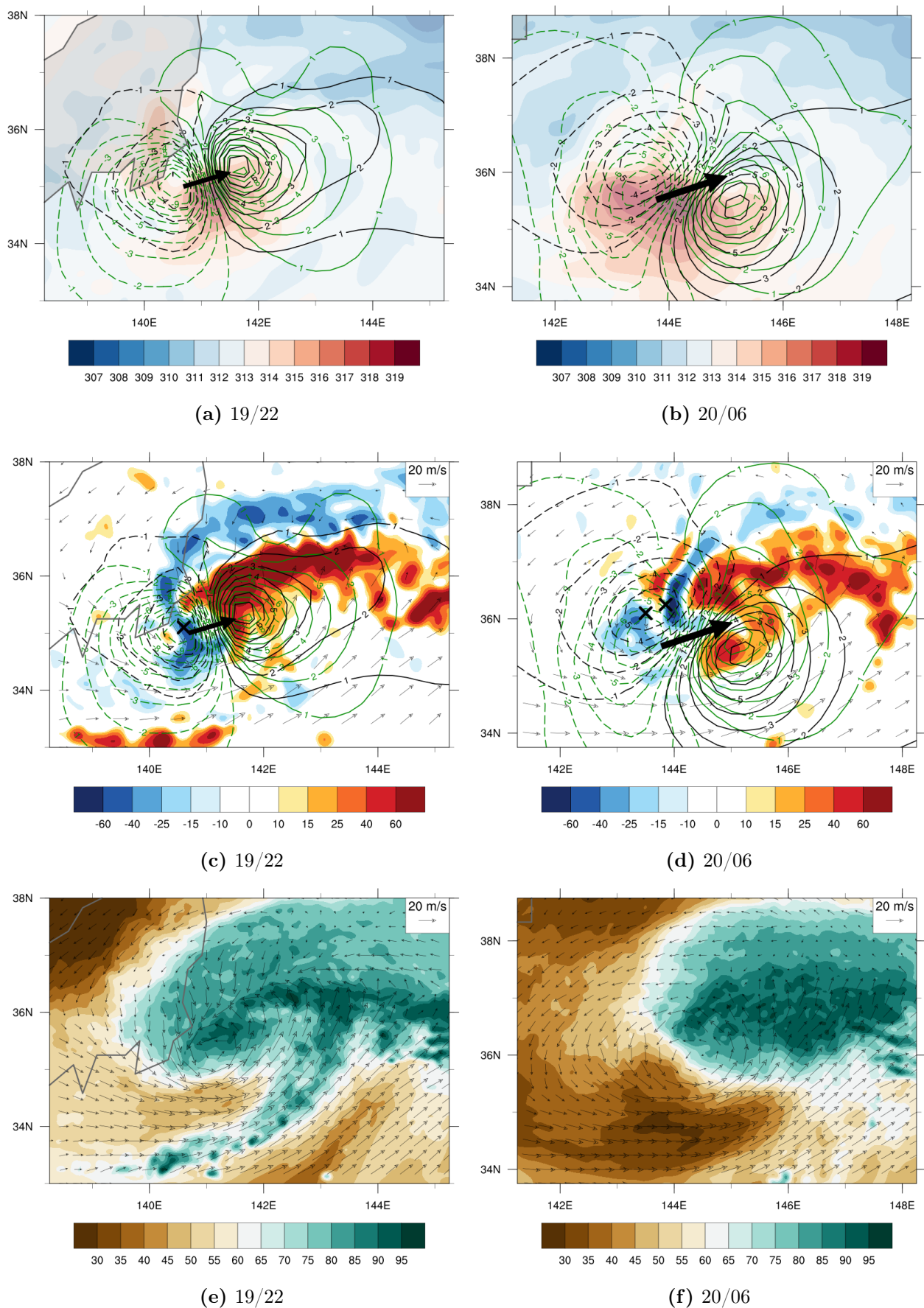


Figure 5.29. – 700 hPa fields on (a,c,e) 19/22 and (b,d,f) 20/06 of (a,b) θ (shaded, K) and (c,d) vertical motion (shaded, cm/s) and (e,f) average 900-250 hPa relative humidity (shaded, %), (a-d) including QG forcing of w (lower-/upper-level contribution in green/black contours, cm/s) at 700 hPa. The thick black arrow shows the 900-250 hPa shear vector and the crosses are reference locations (see text).

the south. In case of frontogenesis, a thermally direct circulation is expected, and in case of frontolysis, a thermally indirect circulation. On 19/22, there is indeed frontogenesis seen along the warm front northeast of the cyclone center at 925, 850 and 700 hPa (Figs. 5.30c,e,g). The location of the front and its vertical motion turns cyclonically with height, especially above 700 hPa, with an orientation from roughly west-east (925-700 hPa) to north-south (at 400 hPa). The frontogenesis has weakened at 400 hPa, but the associated vertical motion from the low-level frontogenesis is still present (Fig. 5.30a). Frontolysis is seen mainly to the west of the circulation. Especially at 925 and 850 hPa it is located between an area of sinking and rising motion to the west of the center, representing a thermally indirect circulation (Figs. 5.30e,g). It also amplifies the downward motion west of the storm. A similar pattern of frontolysis to the west of a transitioning cyclone is found by Harr and Elsberry (2000) and Quinting et al. (2014), where the frontolysis is dominated by deformation. An explanation for the frontolysis can therefore be the high translation speed of the cyclone, but this is a topic of further research. On 20/06, the warm front has weakened at all levels (Figs. 5.30b,d,f,h), and the baroclinic zone at 925 and 850 hPa is located further away from the circulation center. Although there is still vertical motion present at 700 and 400 hPa, there is almost no frontogenesis or frontolysis seen near the warm front at these levels. The frontolysis and associated vertical motion pattern to the west of the center has decreased as well and maximum downward motion is rather seen to the northwest and north of the center, in comparison to west of the center on 19/22.

Now the different mechanisms for vertical motion can be combined. On 19/22, a 'tower of descent' is observed, stretching through the entire troposphere from about 100 hPa to 975 hPa. This tower of descent is present at the same location as the maximum upper- and lower-level QG-forced downward motion (reference cross in Fig. 5.29c). It also coincides with the location of the sinking motion, either due to frontolysis at 925 and 850 hPa, or due to the frontogenesis along the cyclonically turned bent-back warm front (reference crosses in Figs. 5.30a,c,e,g). Additionally, this was also the location through which the trajectories moved that were in the first place influenced by diabatic sinking (Fig. 5.24). All three mechanisms may therefore contribute to the downward motion at the west of Sinlaku. The maximum of ascending motion by the QG-dynamics and the warm front do not coincide but are cyclonically shifted. On 20/06, the orientations of the tilt, warm anomaly, QG forced vertical motion and the warm front have all been shifted. Their maxima of downward motion do not coincide any more (reference crosses in Figs. 5.29d and 5.30b,d,f,h). Still there is downward motion found in a vertical column through the troposphere, but it reaches only up to 400 hPa and has a lower intensity. The tower of descent is similar to what Ritchie and Elsberry (2001) found, although here, different mechanisms for the downward motion are proposed. The air parcels themselves, however, are not transported all the way from 200 to 900 hPa, but just sink and rise again within 2 consecutive hours, after which they continue their cyclonic circulation at the level where they started (not shown). A maximum in downward velocity is found between 700 and 850 hPa and this corresponds to the air parcels that descend from 700 hPa and arrive in the 850 hPa stable air (Fig. 5.25). This descent is in

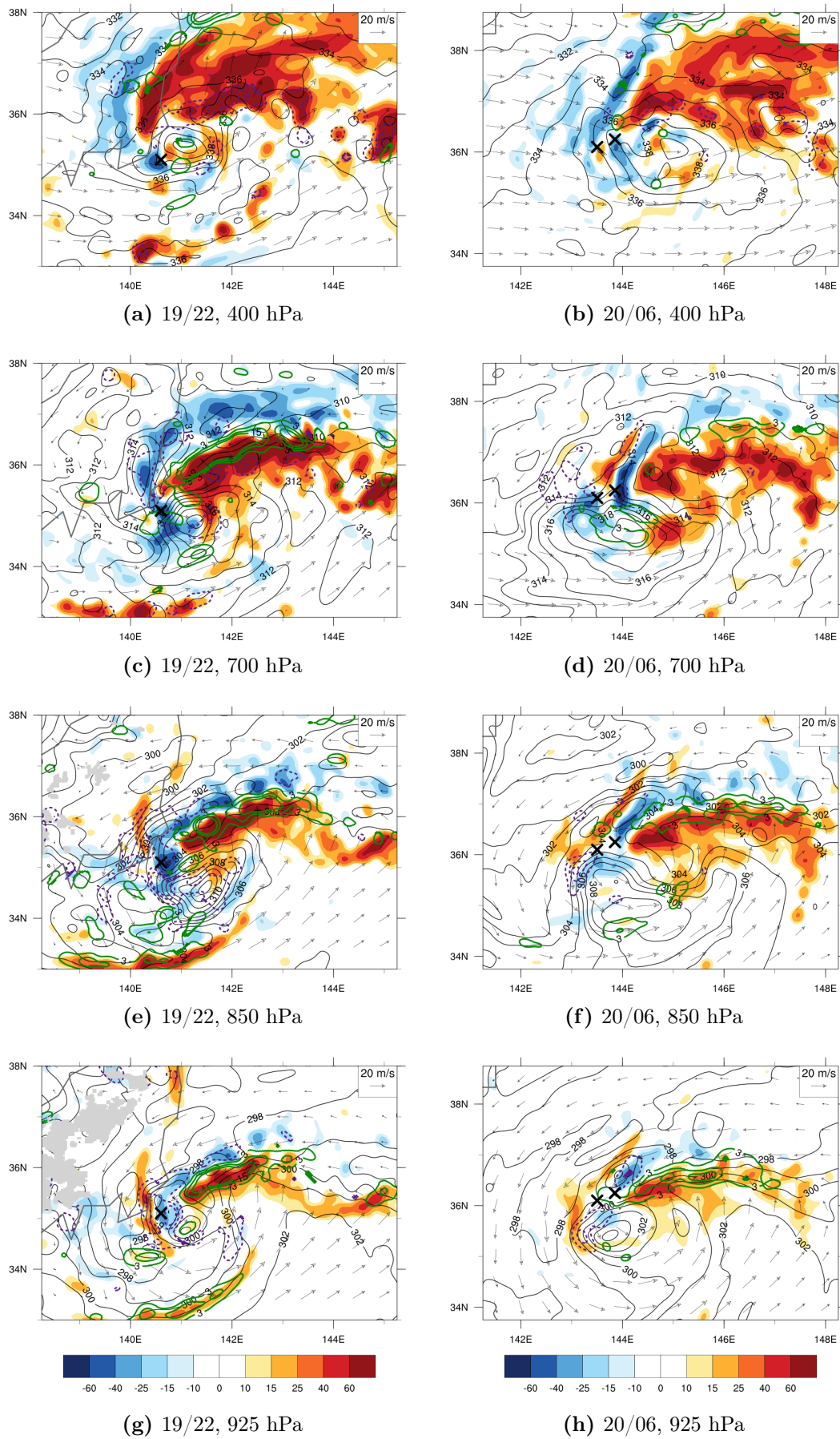


Figure 5.30. – Vertical wind speed (shaded, cm/s), θ (black contours, K), frontogenesis (green contours) and frontolysis (purple contours) at (a,b) 400 hPa, (c,d) 700 hPa, (e,f) 850 hPa and (g,h) 925 hPa, on (a,c,e,g) 19/22 and (b,d,f,h) 20/06.

the same order of magnitude as the 1500 m sinking that was mentioned by Ritchie and Elsberry (2001). Interestingly, the location of the reference crosses coincides not only with a tower of descent, but also with the location of strongest horizontal wind speeds at 925 hPa. This will be discussed further in Section 5.2.4.

Low-level positive PV anomaly

Up to now, the development and consequences of the low-level warm anomaly south of Sinlaku have been identified. One aspect that has been neglected so far, is a positive PV anomaly, that is well co-located with the warm anomaly, and present just below it (Fig. 5.19e,i, 141°E-143°E, 34°N-35°N). It is a relatively small feature south of the PV tower between 900 and 850 hPa on 19/22 and between 950 and 850 hPa on 20/06 (Fig. 5.28). According to Eq. 2.1, a PV anomaly is associated with a circular wind field around it. A low-level cyclonic circulation up to 800 hPa is indeed found, which is broader than the cyclonic circulation above 800 hPa (Fig. 5.31b). This low-level PV features is therefore important in the structural change of the low-level wind field.

A change in PV at a given location can in general be caused by either advection of PV or by modification of PV due to diabatic heating or frictional forces (Eq. 2.4). The development of this PV anomaly must therefore be governed by one or more of these processes. Since the area above the PV anomaly is relatively stable, diabatic heating by convection is the least likely and also not found (not shown). A trajectory analysis is conducted to analyse the source of PV in this area. 6-Hour backward trajectories are calculated, starting on 20/00 at 975 - 850 hPa in a box

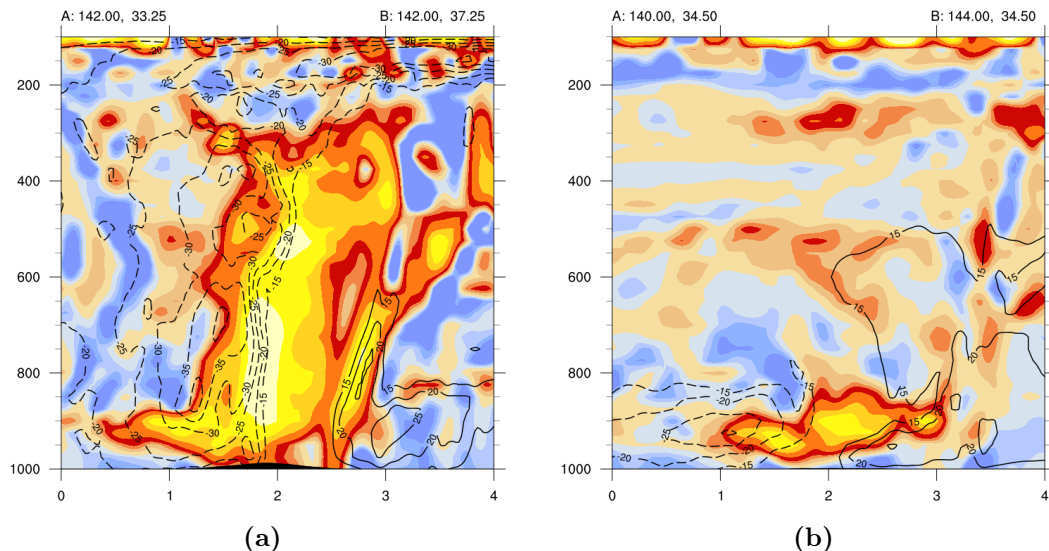


Figure 5.31. – Cross sections of PV (shaded, PVU) and perpendicular horizontal wind speed into/out of the section (solid/dashed contours, m/s) for (a) section AB1 and (b) section AB2 in Fig. 5.19i.

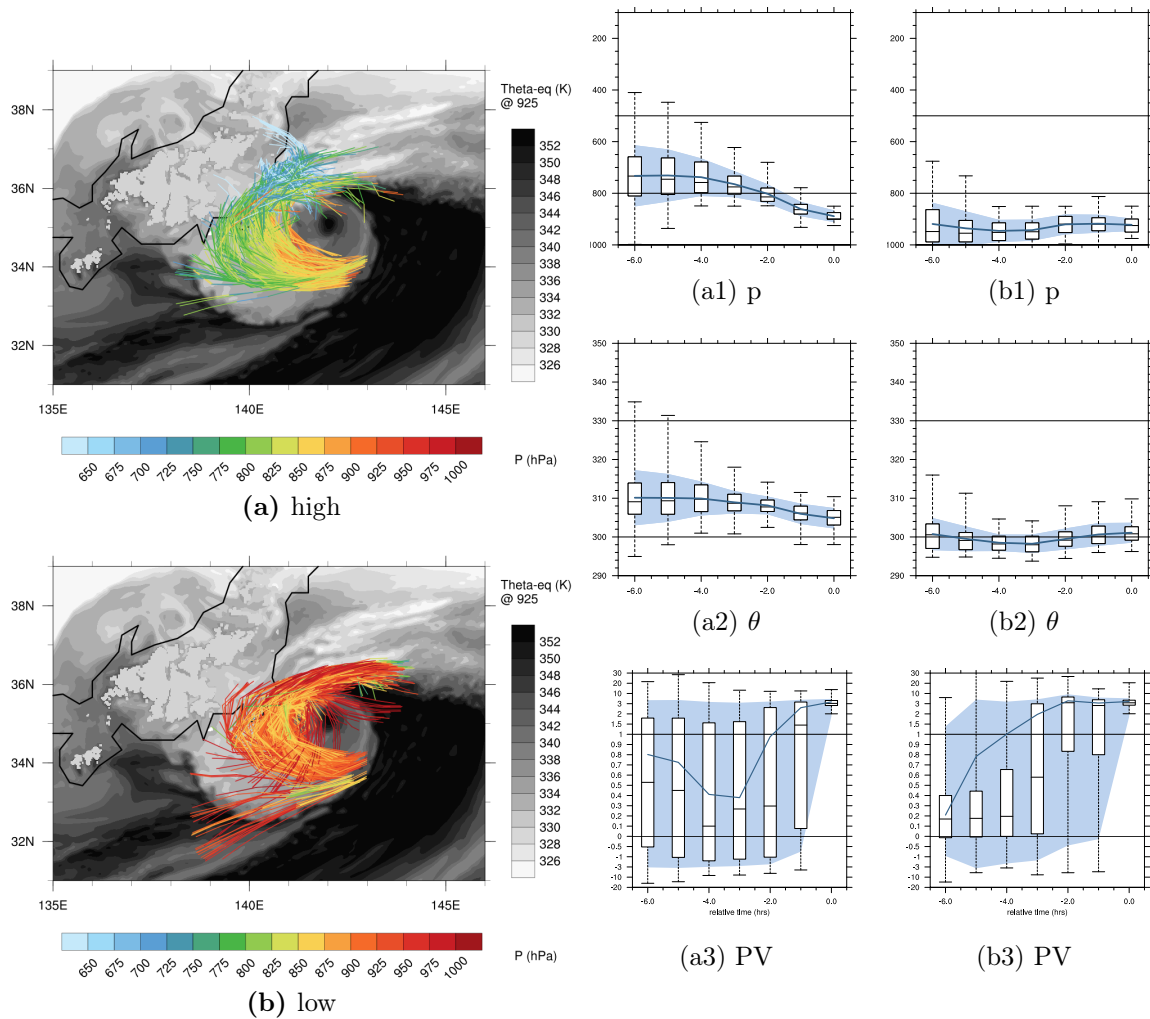


Figure 5.32. – 6 hour backward trajectories, starting on 20/00, south of the cyclone center between 975 and 850 hPa where $PV > 2$ PVU. The colors represent the pressure along the trajectories and the grey shades represent θ_{eq} at 925 hPa on 20/00. The trajectories are divided into air streams that (a) originate above 850 hPa and (b) originate below 850 hPa. For details of the statistic figures see Section 3.3.5.

south of the center ($141-143^\circ$, $33.5-34.3^\circ$) where $PV > 2$ PVU (Fig. 5.19i). The resulting trajectories are divided into two categories: originating above or below 850 hPa.

The trajectories that originate at lower levels start either along the warm front or nearby the cyclone center (Fig. 5.32b). The majority of the trajectories are located just north of the center near the warm front between $t = -4$ and $t = -2$, where they on average rise from 950 to 925 hPa (Fig. 5.32b, b1). During this period, the PV along these trajectories increases (Fig. 5.32b3). It is hypothesized that these air parcels are present beneath the maximum of latent heat release due to condensation within air rising up the warm front and therefore they are in the area where PV is created diabatically. This diabatic PV is then transported around the cyclone towards the

south, which is seen by the almost adiabatic motion of the trajectories (Fig. 5.32b2, $t=-1$ to $t=0$). The low-level PV at the south side of Sinlaku therefore consists of advected positive PV that was diabatically created along the warm front.

The trajectories that start above 850 hPa (Fig. 5.32a) have a similar path and development as seen before, in the trajectories that end in the warm anomaly (Fig. 5.24). They originate from north of Sinlaku, either from the dry intrusion or from along the warm front and sink while turning around the center. The difference is that these trajectories sink to below 850 hPa and on average cool during the descent. They do therefore not show adiabatic descent in the last hour (Fig. 5.32a1,a2) as the trajectories in the warm anomaly did (Fig. 5.25, sinking while θ remained constant). The PV is therefore not necessarily transported and may be created locally. In absence of diabatic PV creation, an explanation for the high PV air is the creation by frictional processes. The air should therefore be turbulent. Just above the PV anomaly and warm anomaly lies a maximum in wind speed (Fig. 5.31a) which could induce a turbulent atmosphere in which PV is created locally. Turbulence is, however, a subgrid-scale process, which is beyond the scope of this research.

Most trajectories originate from along the warm front (Fig. 5.32). Condensation inside the warm front causes a PV dipole with a positive PV anomaly below the maximum in latent heating. Evaporative cooling below the warm frontal precipitation, on the other hand, causes a PV dipole with a negative PV anomaly below the maximum in diabatic cooling. Thus, the trajectories originate from an area with high gradients in PV. This may explain the strong variability in the PV magnitude along the trajectories (high standard deviation in Figs. 5.32a3,b3), since the trajectories originate from different heights (Figs. 5.32a1,b1) and may be near a positive or negative PV anomaly.

A vorticity budget analysis

The vorticity budget analyses gives an indication of the processes that play a role in the intensity development of Sinlaku. Since the wind field broadens over this period and the vortex is tilted, a box size of $4^\circ \times 4^\circ$ (2° radius) was most suitable to capture the entire circulation. For comparison, a smaller box size of $2^\circ \times 2^\circ$ (1° radius), including the low-level inner circulation, is analysed as well.

Starting with the large box, different budget terms have a large variation over time and height (Fig. 5.33). The average change in vorticity over time is positive to neutral throughout the entire troposphere up to about 20/02 (Fig. 5.33a). This is dominated by a positive eddy flux and stretching term in the lower troposphere (Fig. 5.33b,c), counteracted by a negative tilting term (Fig. 5.33d). Similarly, a positive tilting term is found in the upper troposphere, counteracted by a negative eddy flux and stretching term. After 20/02, Sinlaku shows an average increase in vorticity in the lower troposphere and a decrease in the upper troposphere (Fig. 5.33a). Now the tendency is dominated by the eddy flux and stretching in both the

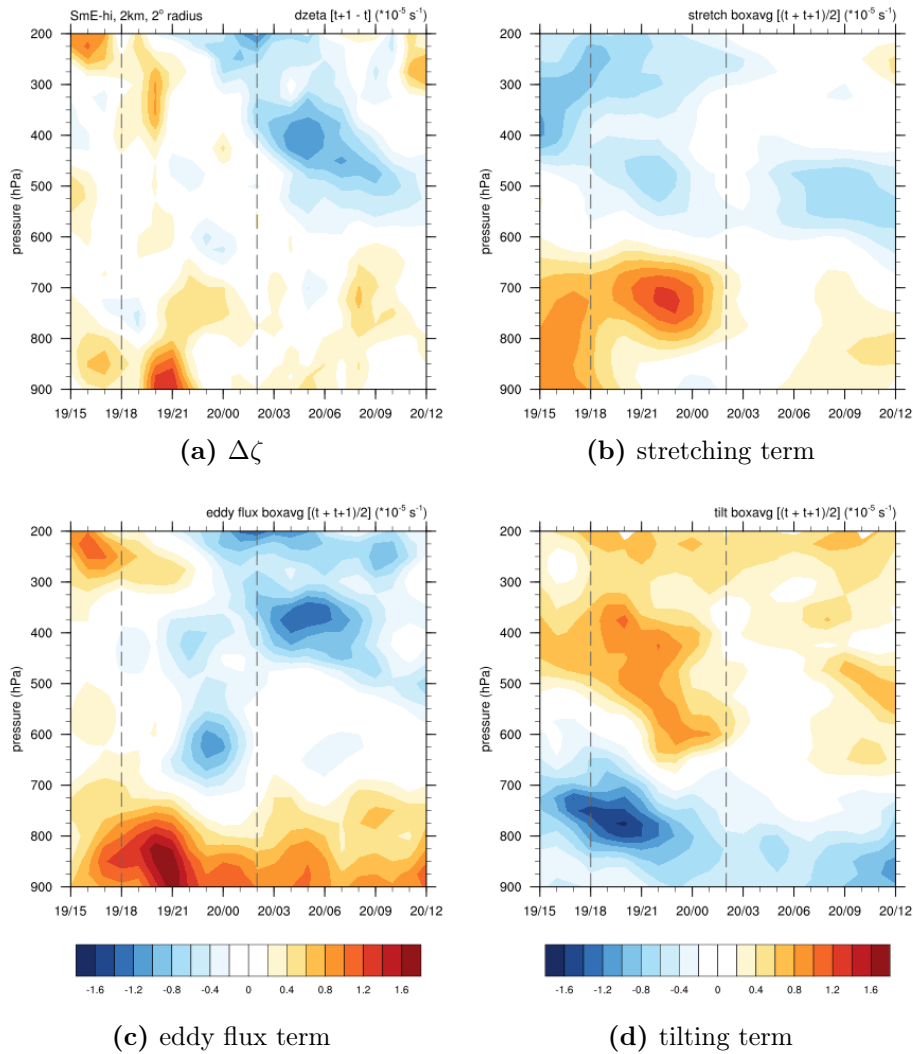


Figure 5.33. – Development of (a) the change in relative vorticity $\Delta\zeta$, and the contribution by (b) the stretching term, (c) the eddy flux term and (d) the tilting term, over time and height, within a box of 4° around the surface cyclone center.

lower and upper troposphere (Fig. 5.33b,c). So, two periods with different dynamics can be distinguished and they are analysed in more detail and compared to the same intervals with a smaller box (Fig. 5.34). The first period is analysed from 19/18 to 20/02, because before 19/18 Sinlaku moves close to the Japanese mountains, and the vorticity budget box intersects the surface and includes a layer of surface friction. The first few hours of this period still includes areas where orography is present at the edge of the box, but the balance at lower levels is relatively good, and there is confidence in the overall features. The second period is from 20/02 to 20/13. The division into these two periods also fits with the vorticity development seen in Fig. 5.17 where the low-level vorticity within 1° radius from the center is 'jumpy' but increasing up to about 20/02, with a steady slow decay afterwards.

A comparison of the results for both box sizes shows large differences between the

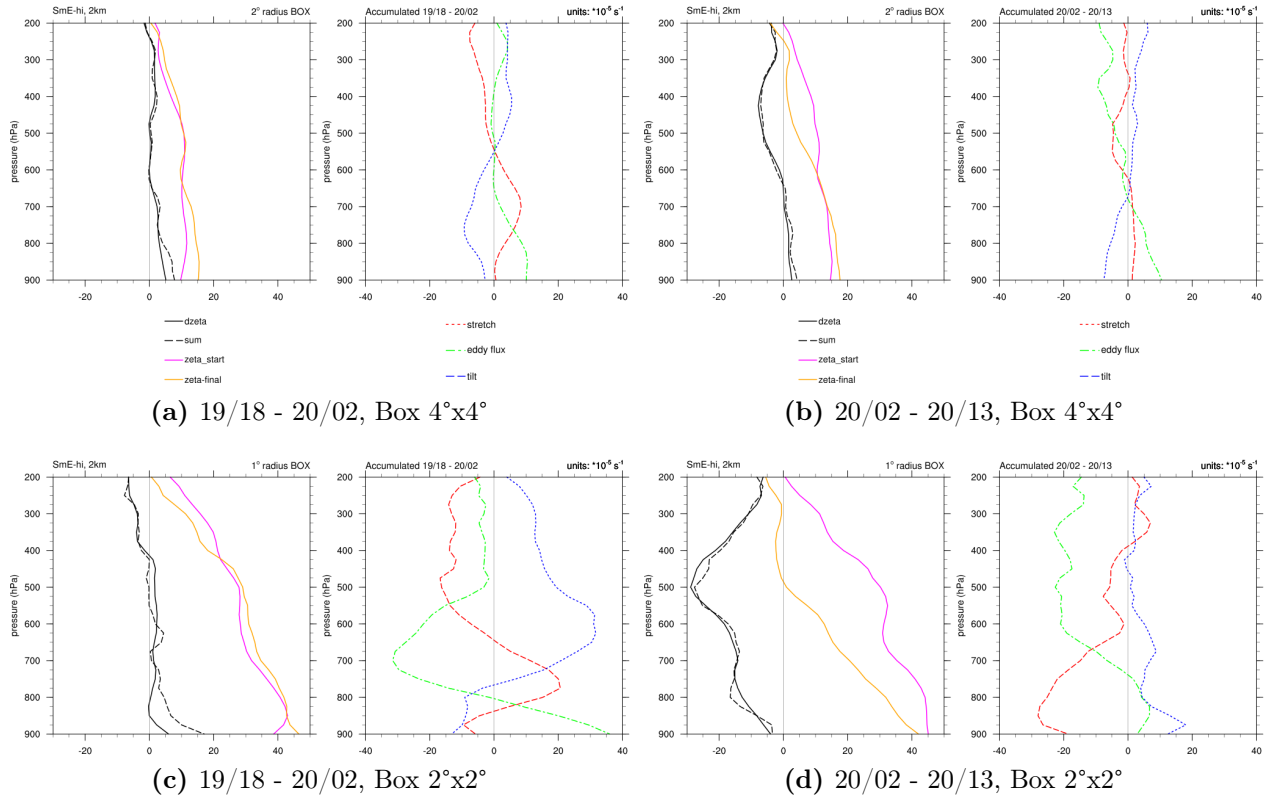


Figure 5.34. – Average vorticity ($\cdot 10^{-5} \text{ s}^{-1}$) in a square box of (a,b) radius 2° and (c,d) radius 1° around the cyclone center at (a,c) 19/18 (pink, start), 20/02 (orange, end) and (b,d) 20/02 (pink, start), 20/13 (orange, end), and the change in vorticity (black) and sum of the vorticity budget terms (black dashed) over these periods. The separate budget terms of stretching (red), eddy flux (green) and tilting (blue) are shown at the right of each figure.

vorticity budget and processes that play a role near the center and further away from the storm (Fig. 5.34). In the large box, the vorticity increases at the lower levels over both periods and is either neutral or decreases at upper levels (Fig. 5.34a,b). In the small box, the vorticity only increases weakly in the lower troposphere in the first period, while the vorticity decreases markedly throughout the troposphere in the second period (Fig. 5.34c,d). So during the entire ET period, the lower-level vorticity is increasing in the large box and decreasing in the small box. This indicates that the circulation is broadening, which is consistent with previous results. At upper levels, the decreasing vorticity in the second period influences the vertical extent of the vortex.

In the first period, from 19/18 to 20/02, the eddy flux is positive in both boxes at 900 hPa (Fig. 5.34a,c), due to the inflow of positive vorticity, mainly along the frontal zone (Fig. 5.35e). Due to a northward tilt of the vortex and a cyclonic turn of the frontal zone with height, the orientation of the front at 725 hPa is so that there is mainly outflow of positive and inflow of negative vorticity on the northern side of the small box (Fig. 5.35c), causing the negative eddy flux in the middle

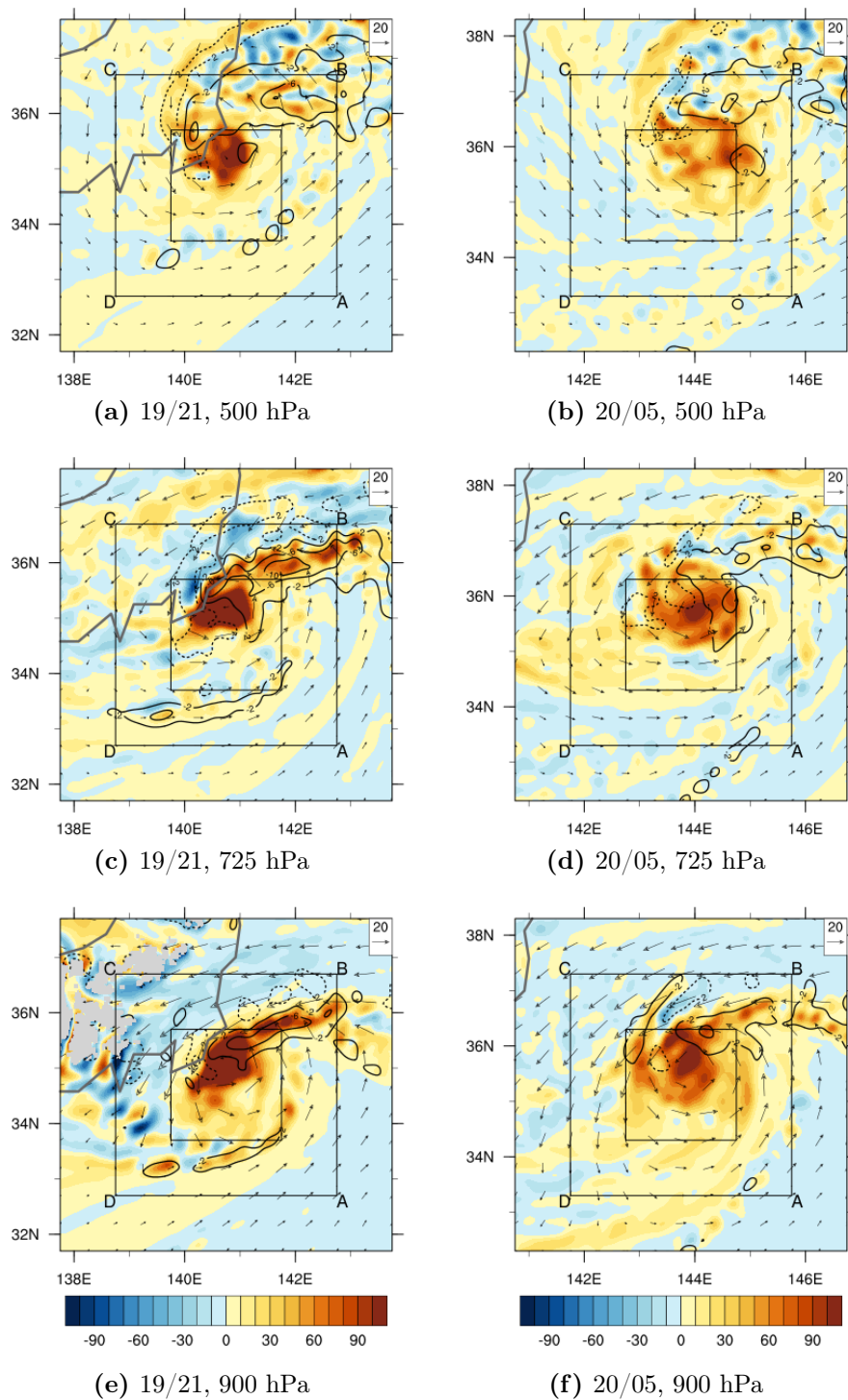


Figure 5.35. – Relative vorticity (shaded, $\times 10^{-5} \text{ s}^{-1}$), ω (solid/dashed contours for rising/sinking motion, Pa) and cyclone-relative wind vectors (without translation speed, m/s) on (a,c,e) 19/21 and (b,d,f) 20/05 at (a,b) 500 hPa, (c,d) 725 hPa and (e,f) 900 hPa. The black lines indicated the location of the $4^\circ \times 4^\circ$ and $2^\circ \times 2^\circ$ boxes, the grey contours represent Japan's coastline and the grey patches are orography.

troposphere (Fig. 5.34c). A positive stretching with net inflow is found in both boxes in the lower troposphere, with a negative stretching term and net outflow in the upper troposphere. This would indicate a maximum of rising motion in the middle troposphere. The change from positive to negative stretching lies at a lower level in the small box (Figs 5.34a,c), again because the front and therefore vertical motion is tilted and turning, due to which the maximum vertical motion is present in the small box at a lower level. The negative stretching term in the small box, just above 900 hPa (Fig. 5.34c), is dominated by a wind speed maximum on the west side of Sinlaku, which is present at the border of the box directed outwards, causing divergence (Fig. 5.35e). This wind speed maximum is present inside the large box, and therefore does not give a net convergence or divergence. Negative tilting in both boxes is mainly caused by a vertical shear along the eastern box side, due to the tilted front, in combination with rising motion along the front. This is very similar to that seen during the tropical decay (Fig. 5.13c), although now the air rises in the warm front instead of over orography. The positive tilting in the small box is also similar to the positive tilting during tropical re-intensification, and caused by the tilted vortex toward the north, that induces an internal vertical wind shear, in combination with rising motion. In the large box, it is the front that changes its orientation with height, causing a vertical wind shear at the border of the box, together with upward motion causing a positive tilting term.

In the second period, from 20/02 to 20/13, the front has weakened and therefore also the positive low-level eddy flux. The negative upper-level eddy flux is now dominated by the northwestward tilt of the vortex due to which high vorticity is located at the border of the small box. Positive vorticity is advected out of the box at the east side near point B, and negative vorticity is advected into the boxes at the west side, near point D (Fig. 5.35b). The front has not only weakened, but is also located further away from the circulation, and relatively more sinking motion is present near the center (Fig. 5.35d) This causes a negative stretching in the small box and a very weak stretching in the large box. The orientation of the front is also important for the tilting. It is located almost west-east in the lower troposphere, due to which it is perpendicular to the eastern side of the large box, giving a negative tilt, and parallel to the northern side of the small box, giving a positive tilting term (Fig. 5.35f). In the upper troposphere, it is again the vortex tilt that causes a positive tilting term for the small box. For the large box, orientation of the front causes vertical wind shear in combination with vertical motion at the east side of the box, near point B that cause a positive tilting term.

5.2.4. Development of extratropical cyclone characteristics

In previous sections it was seen that Sinlaku's ET resembled a Shapiro-Keyser-like cyclone development. In this section it will be analysed to what extent typical features of a Shapiro-Keyser cyclone are present during Sinlaku's ET. The focus lies on the warm core seclusion, bent-back warm front, cold jet and sting jet and the

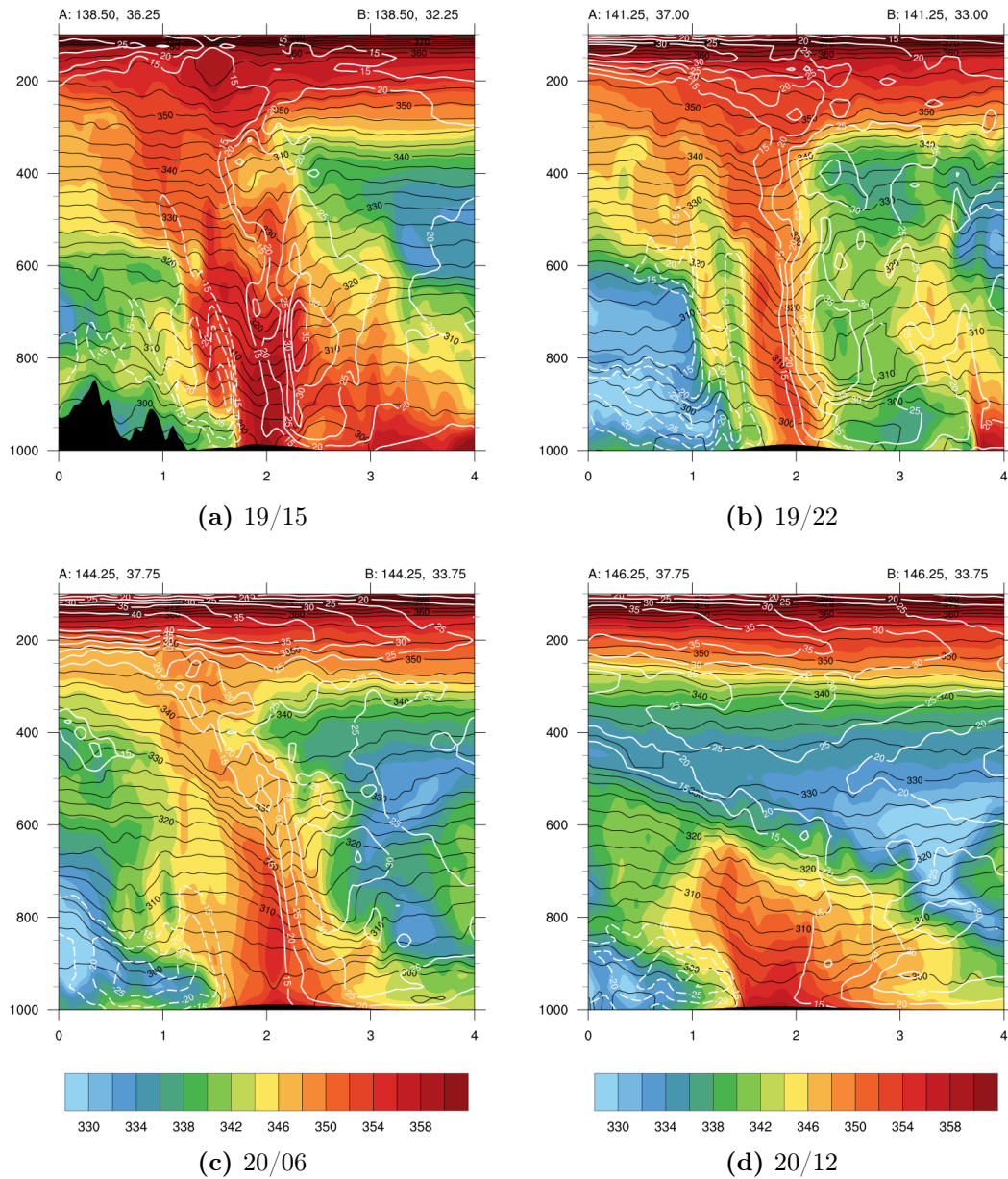


Figure 5.36. – Vertical cross sections of 4° width from north to south (left to right) through the center of the storm, with θ_{eq} (shaded, K), θ (black contours, K) and perpendicular horizontal wind speed into/out of the section (solid/dashed white contours, m/s) on (a) 19/15, (b) 19/22, (c) 20/06 and (d) 20/12.

observed features are explained by the mechanisms that have been discussed in the previous section.

Warm core seclusion

Before Sinlaku interacts with the midlatitude air, its center consists of a vertically straight warm moist tower (Fig. 5.36a). The first cold air starts to flow in at the

north side, advected between the mountains and the cyclone center below 900 hPa. When the actual interaction with the midlatitude air starts, colder drier air starts to circle around the center at lower levels (Fig. 5.36b). Nevertheless, a warm moist θ_{eq} -tower remains present through the entire troposphere, although it has decreased in magnitude. The warm anomaly is present south of the center at 850 hPa, so the warmest air is not present in the center and no warm seclusion is seen yet. On 20/06, Sinlaku's vortex has tilted and at lower levels it has become broader (Fig. 5.36c). The warm anomaly is still present south of the center between 900 and 800 hPa, but has weakened. In the mean time, a new warm anomaly has formed in the center below 900 hPa, and θ_{eq} has increased at lower levels also, although the θ_{eq} -tower has weakened at the top. This development continues in the next 12 hours, until on 20/12, the newly formed warm anomaly in the center at lower levels has increased and has even a higher magnitude than during the beginning of ET, while the top of the θ_{eq} -tower is not present anymore (Fig. 5.36d). The stable air to the south of the center has further decreased in intensity, and at the same time it has moved

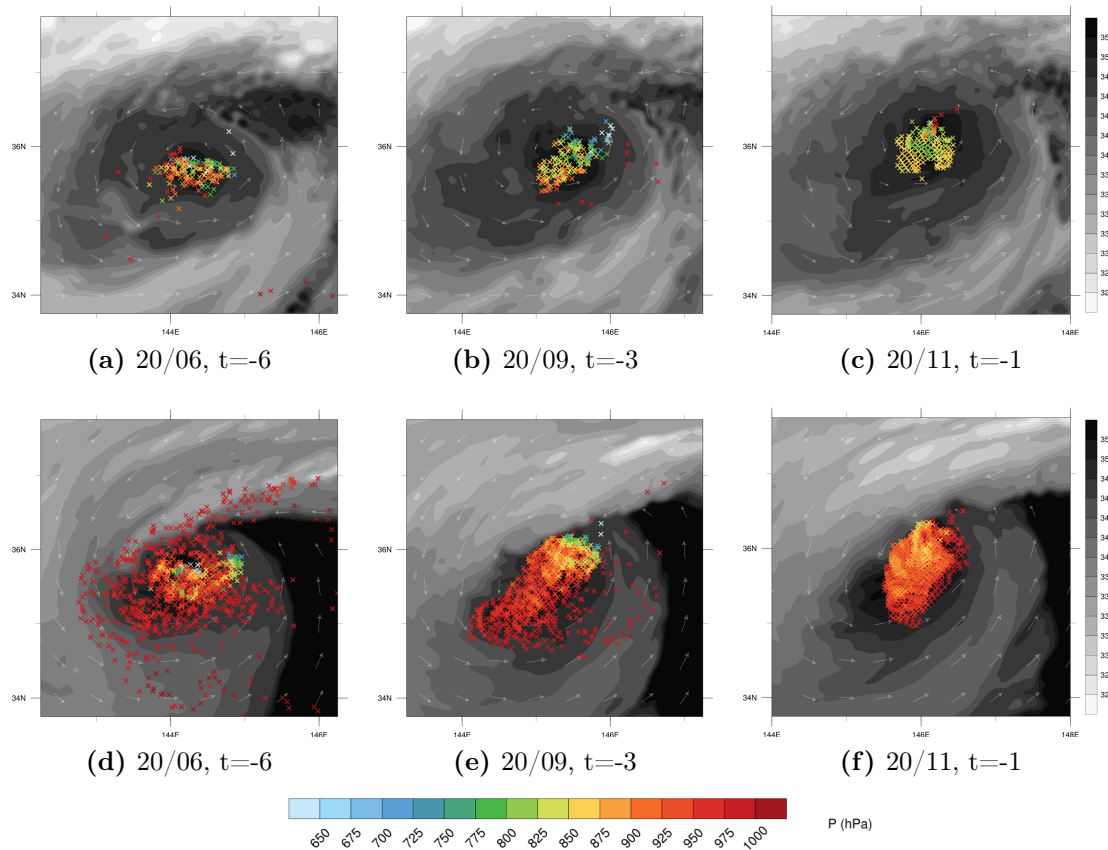


Figure 5.37. – Location of backward trajectories that were started in a box around the center of Sinlaku (145.75° - 146.75° , 35.4° - 36.4°) on 20/12, at (a,b,c) 850 hPa where $\theta > 308$ K and $\theta_{eq} > 350$ K and (d,e,f) below 900 hPa where $\theta > 300$ K and $\theta_{eq} > 350$ K. Colors represent the pressure level of the air parcels (hPa), grey shadings the θ_{eq} (K) at (a,b,c) 850 hPa and (d,e,f) 975 hPa and wind vectors at these levels, on (a,d) 20/06, (b,e) 20/09 and (c,f) 20/11.

a little towards the cyclone center. It now forms outward sloping isentropes to the south of Sinlaku, while to the north, isentropes are also sloped due to the warm frontal zone and tilted cyclone. The isentropic configuration with outward sloping isentropes at both sides of the center indicates a warm core seclusion that is similar to Neiman et al. (1993) (their Fig. 22), although the isentropes do not intersect with the surface here.

The development of the warm seclusion is analysed with trajectories that are started at two locations. In the first place, 6-hour backward trajectories start on 20/12 in the warm moist air below 900 hPa, since the warm moist area developed at lower levels. Furthermore, trajectories are started in the warm anomaly at 850 hPa, since this is the height of the warm stable air south of the center at previous time steps. The low-level warm seclusion consists of air parcels that were either present near the center already, or arrive from a level near the surface (1000 - 950 hPa, Figs. 5.37d,e,f). The air parcels on average gain water vapour (1 g / 6 hr) and heat (2K / 6 hr) and therefore increase their θ_{eq} . This increase is explained by the uptake of warmth and water vapour through surface fluxes from the ocean. At 850 hPa, the air parcels already started in the center and stay there over time (Figs. 5.37a,b,c). Most of the air parcels rise from below 900 hPa, while some sink from above 800 hPa. On average they increase in temperature while specific humidity is lost and relative humidity decreases from on average 90% (some air parcels were saturated) to below 80% (no saturated air parcels anymore). The temperature increase can be interpreted as being due to either latent heat release or due to the mixing of warm dry air from higher levels with colder moist air from lower levels. At least the warm core seclusion forms locally and this development takes about 12 hours, although the frontal development of the Shapiro-Keyser-like cyclone occurred within about 4 hours.

The low level cyclone wind field

The low-level wind field of a cyclone undergoing ET is one of the most important factors as it can cause direct damage to property and ocean waves that influence shipping. The low-level wind field of Sinlaku on 19/18 was in the simulations located near Honshu and the densely populated area of Tokyo. The focus here lies on 19/18, which shows the strongest wind speeds, although two maxima in the wind field, at opposite sides of the cyclonic wind field, were observed during the entire ET period (Fig. 5.18). Since the development of Sinlaku occurred as a Shapiro-Keyser-like cyclone, it is well possible that a cold jet and sting jet are present. There are indeed two phenomena of increased wind speed, which may be like a cold and sting jet, but with slightly different properties. Therefore, two new names are introduced here: the cold low-level jet (CLJ) and sinking dry jet (SDJ). The wind field will first be described based on cross sections through the circulation, which gives a good impression of the quasi-3D development around the center (Fig. 5.38). After describing the wind field from a Eulerian perspective, the areas of strongest

low-level wind speed will be analysed from a Lagrangian perspective by the use of trajectories.

Cross section AB1 is perpendicular to the warm front, showing a field of high θ_{eq} air along the sloping isentropes (Fig. 5.38a). North of it, a CLJ of 35 m/s is present at 900 hPa, in the cold sector near the maximum horizontal temperature gradient. The CLJ increases in speed to 40 m/s in cross section AB2 (Fig. 5.38b). Also its vertical extent increases and the CLJ is now present between 950 and 800 hPa, below the sloping feature of the bent-back warm front. An additional field of strong winds is found above 600 hPa, which is the beginning of the SDJ. At cross section AB3, the SDJ has sunken to 700 hPa, whereas CLJ has sunken to below 900 hPa. The SDJ and CLJ are vertically co-located now, and they both increased in magnitude (Fig. 5.38c). This is also the location of the strongest low-level wind (> 45 m/s). The bent-back warm front has been replaced by the area of warm dry sinking air, with its maximum warm air at the location of the SDJ (Fig. 5.38c). A similar configuration as in cross sections AB1 to AB3 is observed by Smart and Browning (2014) (their Fig. 6a-d), where a cold jet starts at lower levels in the cold sector below the bent-back warm front and a sting jet develops further away from the center and sinks. In their study, the strongest wind speeds in the cold jet were also found where the sting jet is at 700 hPa, and almost vertically aligned with the cold jet (Smart and Browning, 2014, their Fig. 6d). It is therefore hypothesized that the SDJ has sting jet characteristics and the CLJ has cold jet characteristics. The only difference to literature is that a cold jet is expected to stay either at the same height or rise a little. Here the CLJ sinks to below 900 hPa.

The cyclonic circulation continues with a radially outward movement of the CLJ at the southwest and south side of Sinlaku (Figs. 5.38d,e), due to the broadening low-level wind field around the low-level PV anomaly at south of Sinlaku (Section 5.2.3). The SDJ stays closer to the center. In cross section AB4, it is at roughly the same height as in AB3, but with a magnitude of 15 m/s higher than in AB3. This is due to the orientation of the cross section, relative to the inflowing SDJ, which has a dominant direction from the northwest. In cross section AB5, the SDJ core has sunken to 750 hPa and increased to 40 m/s. The warm anomaly has also sunken cyclonically and is now the dominant feature at lower levels. The colder air in which the CLJ resides, has relatively warmed and is present only below 900 hPa. Southeast of Sinlaku, in cross section AB6, the CLJ and SDJ are vertically aligned again and represent a column of strong wind speeds (> 40 m/s), that includes the secondary maximum of the low-level wind speed (Fig. 5.38f).

After analysing the wind structure at one particular time step, now the development over time is investigated. First, 6-hour backward trajectories are started every 10 hPa, between 1000 and 700 hPa in the area to the southeast of the center (Fig. 5.18d), where the wind speed is larger than 40 m/s (including the SDJ and CLJ jet cores in Fig. 5.38f). The strong wind is present at the (cyclonic) end of the warm anomaly and especially the SDJ is dominant here. It shows sting jet characteristics, as did the sinking air in the trajectory analysis of the warm anomaly on 20/00 (Fig. 5.25). Therefore, this feature is mainly analysed on sting jet characteristics,

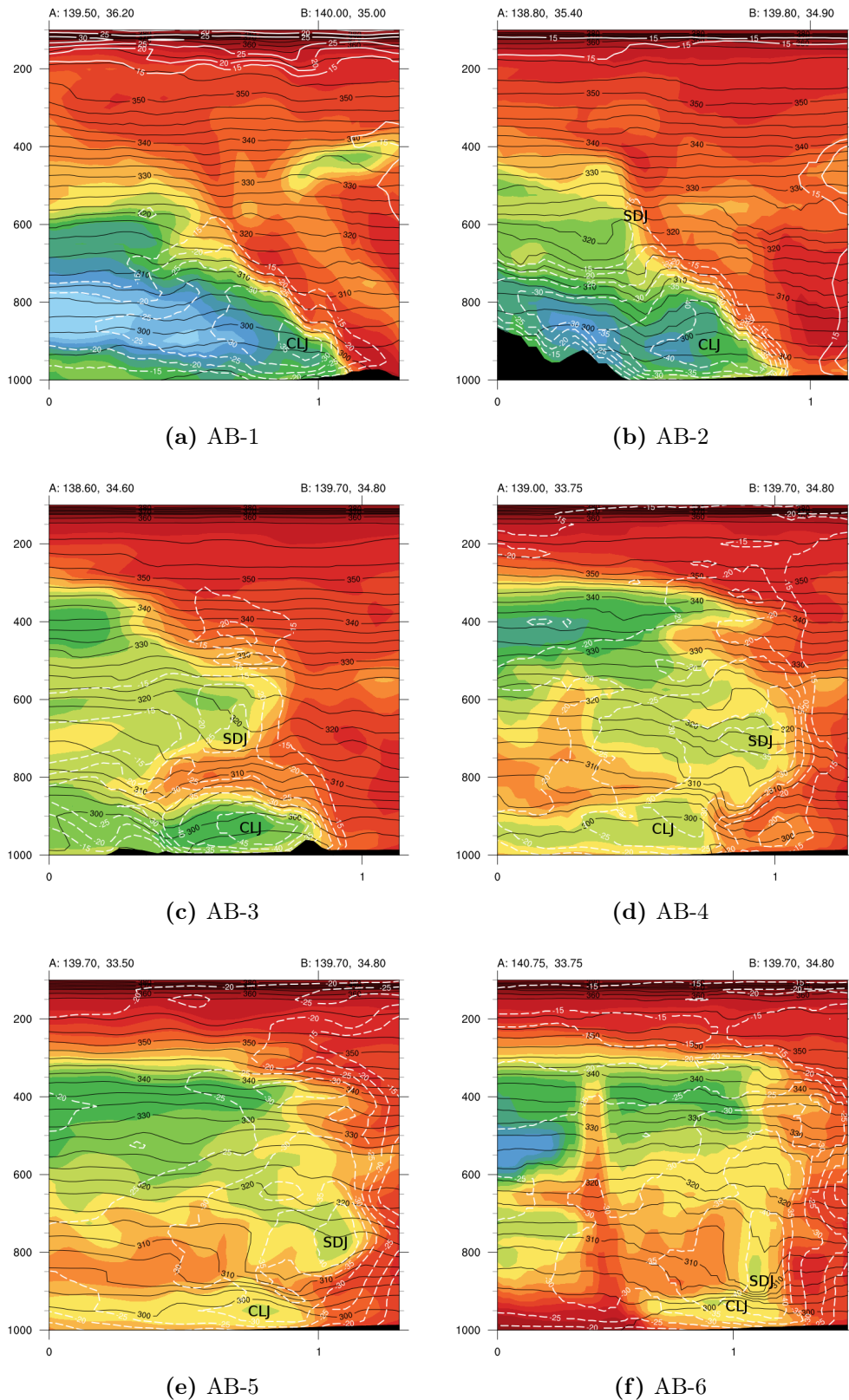


Figure 5.38. – Vertical cross sections of θ_{eq} (shaded, K), θ (black contours, K) and perpendicular horizontal wind speed into/out of the section (solid/dashed white contours, m/s) through the cyclonic circulation of Sinlaku on 19/18. The cyclone center is present at the right side of the figures, and the location of the cross sections is given in Fig. 5.18d. The location of the sinking dry jet and cold low-level jet is given by SDJ and CLJ, respectively.

and trajectories are selected on the low relative humidity at the end location ($RH < 50\%$) and almost saturated air somewhere along the way ($RH > 98\%$). It is remarkable that the resulting trajectories were not only sinking, as was expected for the sting jet. Two groups could be distinguished: one sinking in the last three hours and one rising (Figs. 5.39 and 5.40). The sinking air originates from east of the cyclonic circulation and first rises over the warm front (Fig. 5.39a). The air is relatively moist but condensation occurs along the warm front due to which the specific humidity decreases (Fig. 5.40a3). Between $t=-3$ and $t=-1$ the air parcels turn cyclonically, and become located northwest of the center, in the part of the warm front where frontal and diabatically driven sinking motion take place (Fig. 5.39c). The transition from the moist and rising side of the warm front towards the sinking side where it starts to become dry (Fig. 5.40a1,a3,a4), may be referred to as what in literature is called 'air descending from the cloud head'. While sinking, the wind speed increases from < 10 m/s to > 40 m/s (Fig. 5.40a5). During the last hour, the air sinks on average adiabatically, over the temperature gradient of the warm anomaly (Figs. 5.39e,g and Fig. 5.40a2).

The rising part of air originates from two different locations (Fig. 5.39b). Part of the air parcels have a subtropical origin and move radially inward. The other part originates in the cold sector ahead of the warm front. Although these trajectories have a small difference in initial temperature and water vapour, they show very similar characteristics, and are therefore taken as one group. The air parcels originate mainly below 950 hPa and have a high relative humidity (Fig. 5.40b1,b4). Over time, the air parcels become closer to the radius of maximum winds and their wind speed increases (Fig. 5.40b5). When they move just north of the center they rise within the warm front and lose an initial amount of water vapour (Figs. 5.39d,f). The last time step is the most interesting one. The air parcels stay (on average) on the same height, but still they lose water vapour and gain heat (Fig. 5.40b1,b2,b3). Subsequently, their relative humidity decreases (Fig. 5.40b4). Also the wind speed increases with about 10 m/s (Fig. 5.40b5). The air parcels of the rising and sinking air streams are now roughly at the same height (Fig. 5.40a1,b1) and it is hypothesised that both air masses mix, due to which the area is possibly turbulent and high momentum air can be transported downward. Therefore the wind speed at lower levels can increase. The sinking air in this trajectory analysis can be associated with the SDJ and shows indeed sting jet characteristics. The situation is, however, more complex than just sinking air that transports high momentum downward. Also the rising air along the inner circulation of the cyclone contributed to the high wind speeds at lower levels.

The second area of high wind speeds, to the west of Sinlaku (Fig. 5.18d), is dominated by the CLJ at lower levels and showed characteristics of a cold jet (Figs 5.38a,b,c). The situation is, however, also here, more complex than having a strong jet along the temperature gradient of the bent-back warm front. 6-Hour backward trajectories are started at the west side of the cyclone center where the wind speed is > 40 m/s, at every 10 hPa between 1000 and 800 hPa. As in the previous trajectory analysis, air parcels originate from both the subtropics and from the midlatitudes along the warm front (Appendix D, Fig. .5). The situation is rather complex and

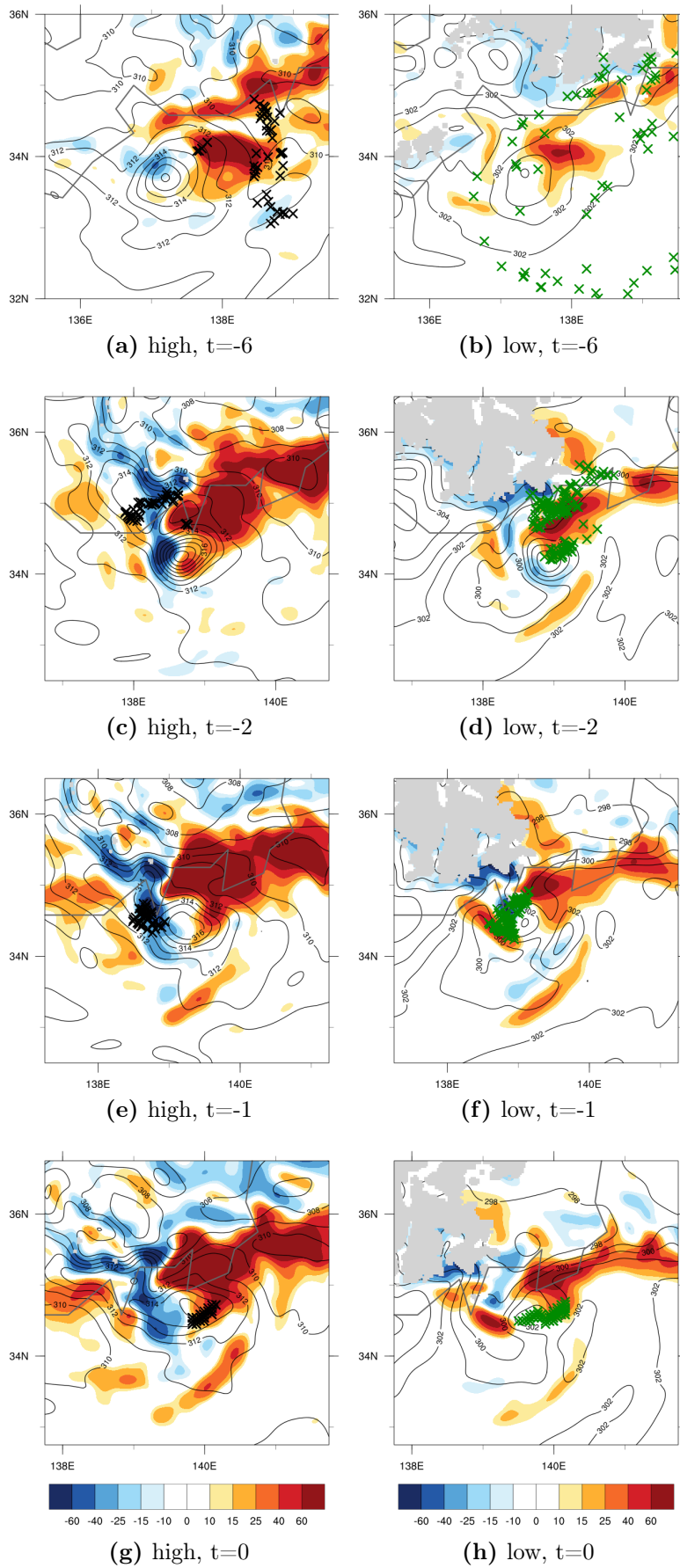


Figure 5.39. – Location of backward trajectories that end in the area southeast of the center on 19/18, between 700 and 1000 hPa, with windspeed > 40 m/s. The trajectories are divided into a group that sinks from above 700 hPa (a,c,e,g, black crosses) and a group that rises (b,d,f,h, green crosses), shown relative to the vertical wind speed (shaded, cm/s) at 750 hPa and 925 hPa, respectively, in a frame moving with the cyclone, with the center in the middle of the figures. Grey areas are orography.

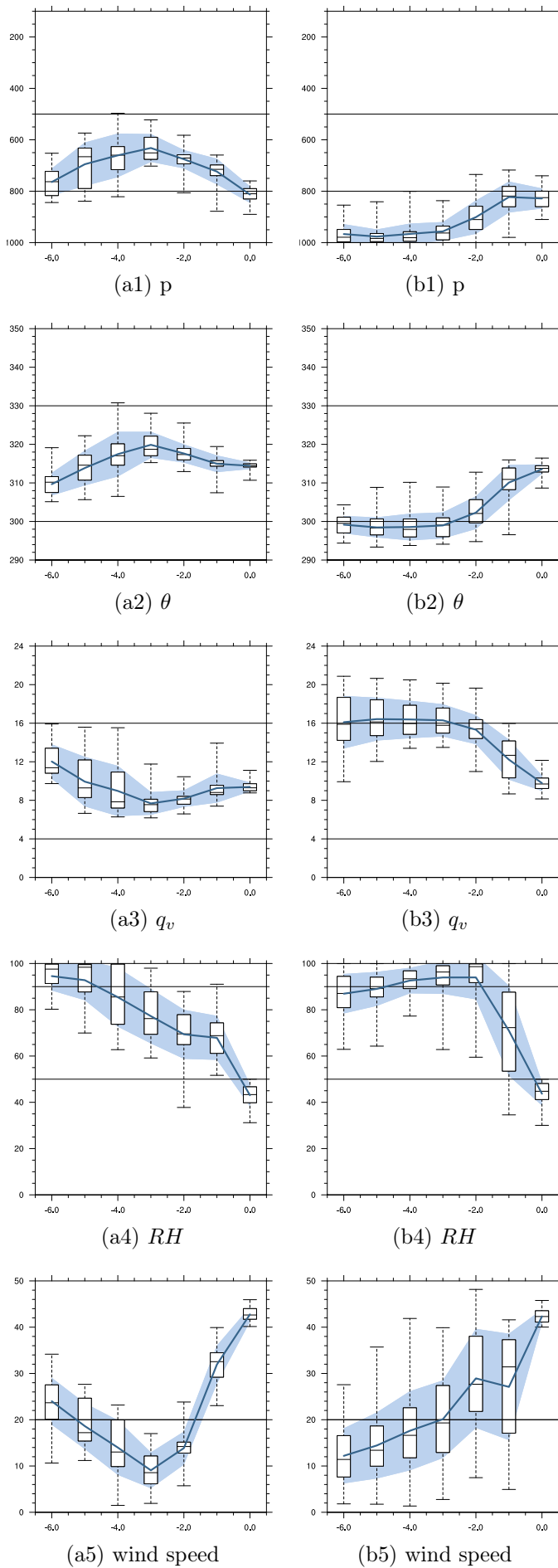


Figure 5.40. – Statistics corresponding to the trajectories of Fig. 5.39, for (a) the sinking and (b) the rising trajectories. For details of the statistic figures see Section 3.3.5.

the area of highest wind speeds consists of both rising and sinking air, and air parcels that stay at a relatively constant height. The trajectories are therefore split into the groups 'rising' (red), 'sinking' (orange), residing relatively 'low' (green, below 875 hPa) and residing relatively 'high' (blue, above 875 hPa) air parcels, based on their pressure level at $t=-3$ and $t=0$ relative to a boundary of 875 hPa (Fig. 5.41). The boundary is artificially chosen and based on the level of the subtropical air parcels at $t=-3$, and the height of the CLJ, from which the majority is present below 875 hPa (Fig. 5.38b,c).

The CLJ consists of different air masses with different properties (Appendix D, Fig. .6) and they all mix at the location of the strongest low-level wind speed. All four groups of air parcels merge to the northeast of Sinlaku, near the warm front, but at a larger radius than the air parcels in the previous analysis (here $\sim 1^\circ$ instead of $\sim 0.5^\circ$). Along the warm front part of the air parcels rise on the warm side, others sink at the cold side, while in the meantime they turn cyclonically towards the west (Fig. 5.41). Moist air is mainly advected by the initially low trajectories. Part of the water vapour is lost along the warm front, while sinking air parcels gained water vapour during evaporation. At the last time step, the low trajectories stay on average at 925 hPa, although their water vapour content decreases. This is an indication of mixing of the air. Overall, all trajectories have a relatively high relative humidity, fluctuating around 90% on average. Together with a wind speeds over 40 m/s and the location in the cold sector along the bent back warm front, makes the CLJ feature a cold jet like feature. At the same time, the sinking trajectories show a sinking motion of about 100 hPa / 3 hrs (from 825 to 925), which would be similar to what was previously found for a sting jet. These sting jet-like trajectories are, however, not dry when they sink, but even gain water vapour.

When the air parcels come closer to the cyclone center, their wind speed increases (Fig. 5.42). In the last hour, the wind speed suddenly increases from $< \sim 30$ m/s to > 40 m/s and the wind speed profile becomes a bell-shaped structure with its maximum just above 950 hPa (Fig. 5.42d). The area of maximum wind speed is co-located with a tower of descending motion, similar to that seen on 19/22 (Section 5.2.3, reference cross in Figs. 5.29c and 5.30a,c,e,g). It is therefore hypothesized that the rising and sinking motion of air parcels moving cyclonically over and below the (bent-back) warm front, creates a potentially unstable and turbulent area. Within this area, high-momentum air could be transported downward in a column of downward motion, and the high-momentum air causes an increase in low-level wind speed. Additional mechanisms that may influence the strong wind speeds at this location are the channelling between the cyclone center and orography (Fig. 5.38b). Furthermore, the strongest winds are found where the air moves from land offshore and a reduction of shear may have contributed to an increased low-level wind speed as well. On 19/22, however, Sinlaku was over open ocean again, still with a very strong low-level wind field to the west of the center. Trajectory analysis showed a similar behaviour as on 19/18 (not shown). The topography may therefore have influenced the wind field, but did not play a key role.

On 19/18, but also during the remainder of ET, the strongest 925 hPa wind speeds to

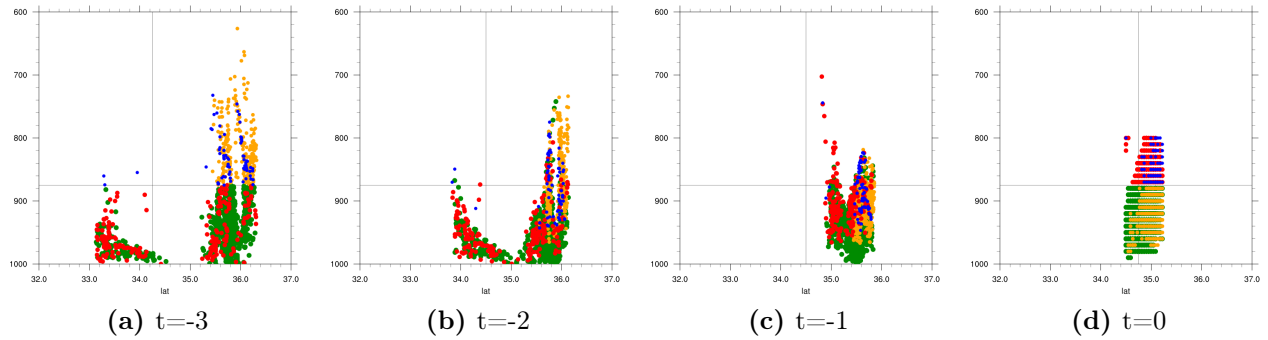


Figure 5.41. – Development of pressure and latitude along backward trajectories that end in the $> 40\text{m/s}$ wind speed area to the west of Sinlaku on 19/18. The colors represent air masses of rising (red), sinking (orange), low (green) and high (blue) air in comparison to a reference level of 875 hPa. A reference line is given at the latitudinal location of Sinlaku.

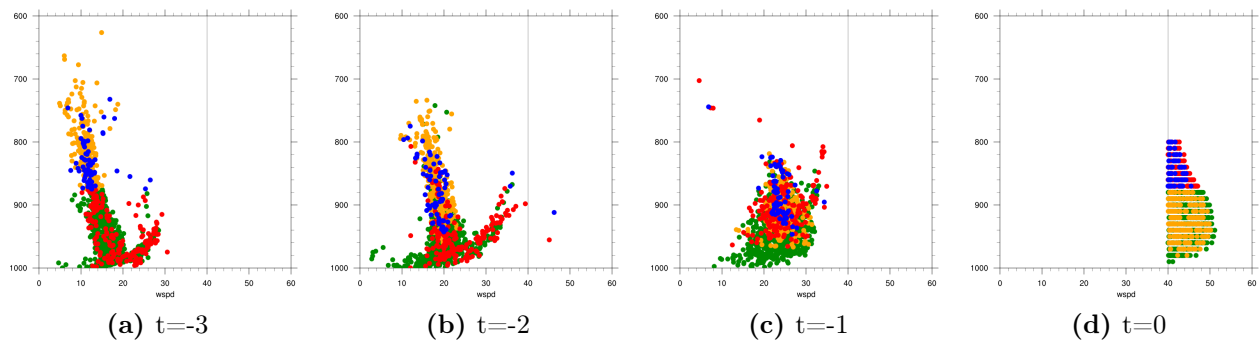


Figure 5.42. – Development of pressure and wind speed along backward trajectories that end in the $> 40\text{m/s}$ wind speed area to the west of Sinlaku on 19/18. The colors represent air masses of rising (red), sinking (orange), low (green) and high (blue) air in comparison to a reference level of 875 hPa.

the west and northwest of Sinlaku's center are co-located with a tower of descending motion. Since the tower of descent is influenced by frontolysis, diabatic descent and QG-forcing due to the tilting of the cyclone, all three mechanisms contributed to the destructive low-level wind speeds. The intensity, however, decreases over time, because all three mechanisms for downward motion decrease in intensity and are not co-located any more so that the tower of descent decreases both in vertical extent and magnitude. The high wind speed to the east and southeast of Sinlaku was strongest for only a few hours (19/16 - 19/18, $> 44\text{ m/s}$) but remains present as a field of high wind speeds ($< 35\text{ m/s}$) for the next 18 hours. This field is co-located with a location just cyclonically upstream of the maximum QG-forcing for ascent. An explanation for this location can be that the downward motion of the SDJ is at its lowest level before it is forced to rise again, in combination with low-level rising air at this location that causes a potentially unstable environment in which high momentum air can more easily be mixed downward.

Unexpected extratropical re-intensification

An unexpected re-intensification was observed during ET in simulation H1812-hi. When ET systems re-intensify, this often occurs when the low-level TC remnants move beneath an upstream upper-level trough (type B cyclogenesis, Petterssen and Smebye (1971)). For Sinlaku, no upstream upper-level trough is seen in the QG forcing (Figs. 5.43a,b). Only a downstream trough is seen, which is in general unfavourable for extratropical re-intensification (Harr and Elsberry, 2000). Nevertheless, Sinlaku is close to the jet entrance (Figs. 5.43c,d), which may contribute to the increased upper-level forcing. Sinlaku is also close to an upstream trough of PV at upper levels (Figs. 5.43c,d). From a horizontal perspective they almost seem to merge, and on 20/12, Sinlaku's mean sea level pressure signal is even below the upper-level PV trough (not shown). Nevertheless, from a vertical perspective they do not merge. Sinlaku's vortex does not tilt backwards, and the upper-level PV anomaly does not extent downwards (Fig. 5.44). Additionally, the PV tower of Sinlaku decreases in height over time and reaches only up to 500 hPa on 20/12 (not

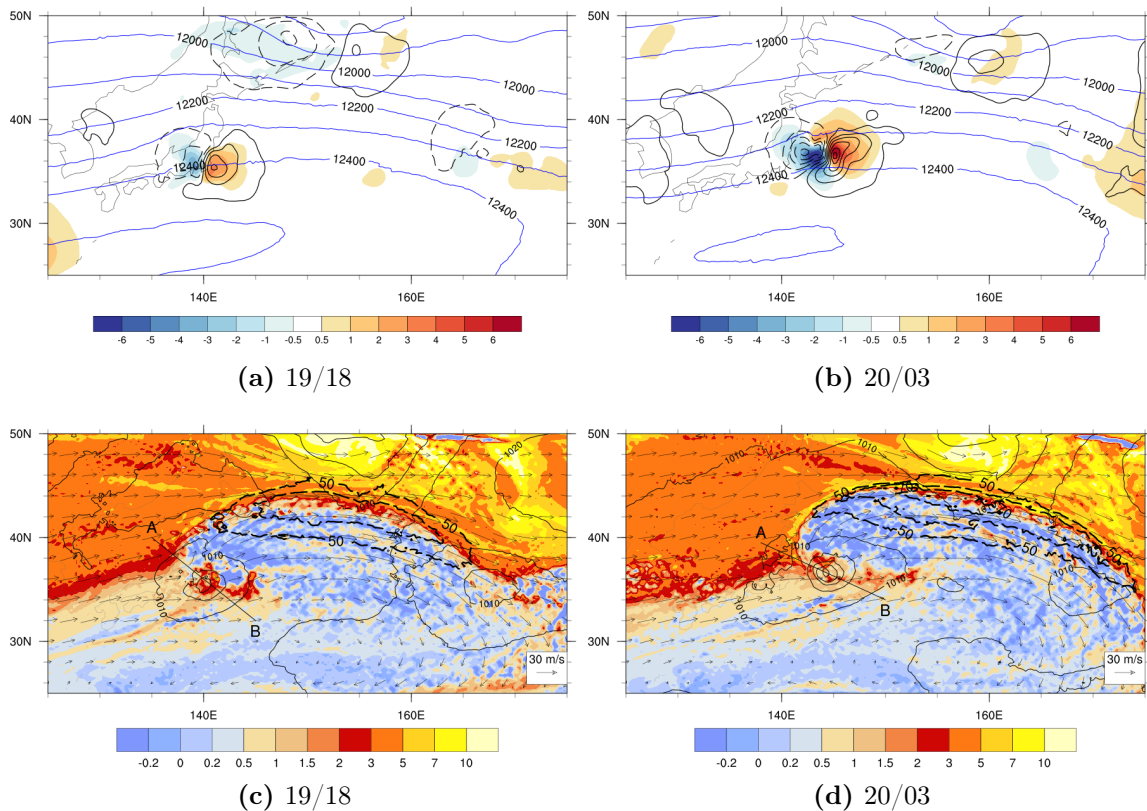


Figure 5.43. – Upper figures: QG forcing of vertical motion at 700 hPa (upper-/lower-level forcing in black contours/shaded) and geopotential height at 200 hPa (blue contours, m). Lower figures: PV (shaded, PVU) and wind vectors at the 345 K level, and the mean sea level pressure (thin black contours) on (c) 19/18 and (d) 20/03. The jet streak is marked by a thick black dashed line (wspd > 50 m/s, every 10 m/s). Grey contours represent the location of topography. All for simulation H1812-hi.

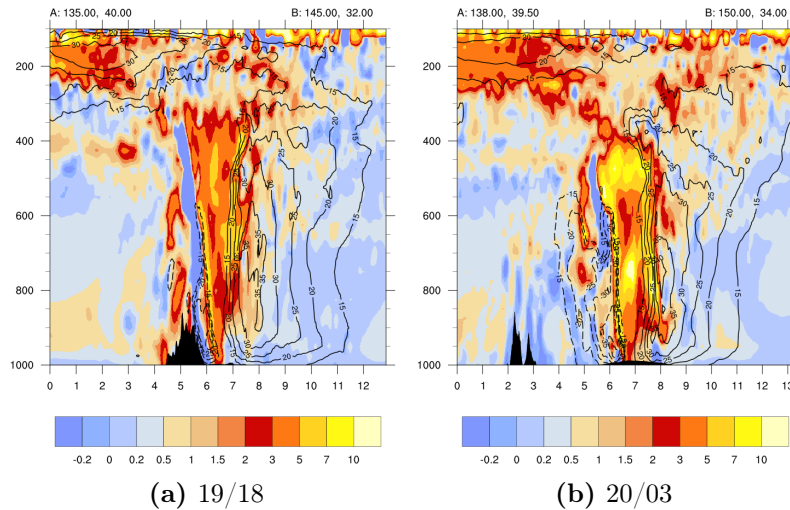


Figure 5.44. – Vertical cross section of PV (shaded, PVU) and perpendicular horizontal wind speed (solid/dashed into/out of the section, m/s) along the line AB in Fig. 5.43, on (a) 19/18 and (b) 20/03, for simulation H1812-hi

shown).

The strong intensification must therefore be influenced by another mechanism. In absence of a type B cyclogenesis, re-intensification as a type A cyclone (Petterssen and Smebye, 1971) is examined. This type of cyclone develops on a front, with no pre-existing upper-level trough, so lower-level temperature advection is dominant over upper-level vorticity advection. Both the upper- and lower-level QG-forcing for vertical motion near the cyclone increase between 19/18 and 20/03, and the increase in lower-level forcing is strongest (Figs. 5.43a,b). This was seen in simulation SmE-hi as well, where even the upper-level QG-forcing was dominated by temperature advection, due to the tilting of the cyclone (Section 5.2.3). Additionally, the vertical wind shear up to 20 m/s until 20/03, was favourable for the resiliency of the vortex. This agrees with a type A cyclogenesis.

From a vorticity budget analysis, it can also be seen that the cyclone intensifies in the period 19/18-20/02 due to the eddy flux in the lower troposphere, stretching in the middle troposphere and tilting in the upper troposphere (Fig. 5.45). The mechanisms are similar to simulation SmE-hi, but intenser (Fig. 5.33). Additionally, a strong low-level eddy flux is seen between 20/03 and 20/06, extending the low-level intensification (Fig. 5.45c). Despite the positive fluxes, there is also a strong negative lower-level tilting and upper-level stretching term (Fig. 5.45b,d). A net positive vorticity tendency flux is therefore seen especially in the lower levels, from 19/20 on, dominated by the eddy flux term (Fig. 5.45a,c). It then develops toward a level of 700 hPa, dominated by stretching on 20/00 (Fig. 5.45a,b). Finally on 20/04, the low-level vorticity budget is dominated by the eddy flux again (Fig. 5.45a,c), by the advection of high vorticity air which is present along the warm front (not shown). The unexpected extratropical intensification is therefore mainly a rapid low-level baroclinic cyclone development. This is different from most often

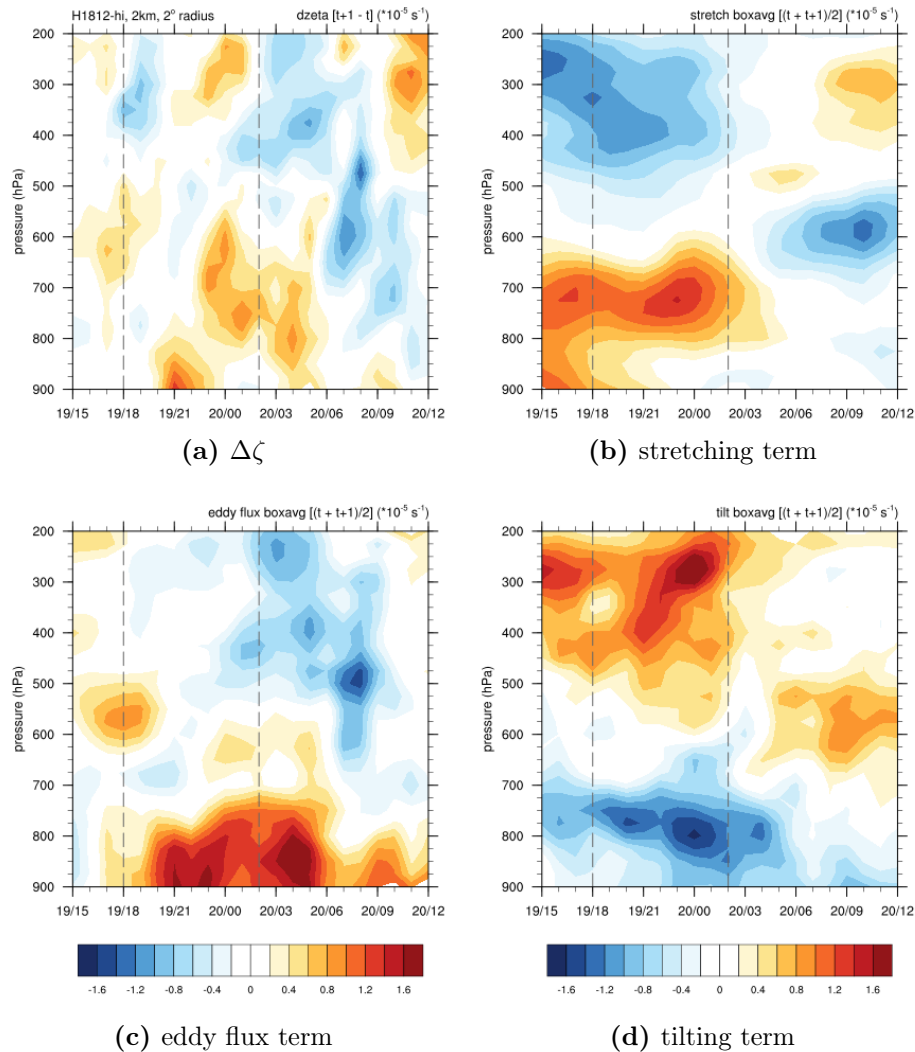


Figure 5.45. – Development of (a) the change in relative vorticity $\Delta\zeta$, and the contribution by (b) the stretching term, (c) the eddy flux term and (d) the tilting term, over time and height, within a box of 4° around the surface cyclone center. Similar to Fig. 5.33, but here for simulation H1812-hi.

observed extratropical re-intensifications, that occurs as a type B cyclogenesis, when the cyclone merges with a pre-existing upper-level trough.

5.2.5. Discussion

Sinlaku underwent ET in a rather unusual way. After tropical re-intensification and decay, Sinlaku moved parallel to the orography of Japan, which played a key role in the blocking of midlatitude air. The actual interaction with the baroclinic zone started when Sinlaku moved away from Japan's orography and the rapid development resembled a Shapiro-Keyser-like cyclogenesis. It was rather unexpected that Sinlaku behaved like this. According to the frontal types of Kitabatake (2008),

Sinlaku most resembled the cold-advection-type and was indeed transported zonally as a relatively weak cyclone by a straight jet stream. Nevertheless, the structural development of Sinlaku represented the Shapiro-Keyser-like development of the seclusion-occlusion-type. Thus the large-scale development of an ET system does not necessarily give an indication of the meso-scale structural behaviour of the cyclone.

A Shapiro-Keyser extratropical cyclone can exhibit a warm jet, cold jet and sting jet, and Sinlaku's wind field contained similar features. To the right of the track, in the warm sector away from the RMW, a warm jet like feature is found. It can therefore be argued that this part of the wind field behaved according to warm jet dynamics. Near the center a cold jet like feature and sting jet like feature are observed. The CLJ is a complicated composition of upward and downward motion, creating an unstable area below a tower of descent. The SDJ is relatively similar to what was found in the literature. Remarkable is that, in contrast to previous studies, the CLJ has higher wind speeds than the SDJ, and that the CLJ and SDJ are located at opposite sides of the center, whereas in literature, the sting jet is stronger and often located above the cold jet and at its leading edge. The difference may occur due to the rapid development of Sinlaku as an extratropical cyclone. Another explanation can be that the dynamics behind both features is different during ET, which is a topic of further investigation.

The vertical motion field, in particular the downward motion, played a key role in the structural changes of Sinlaku. The downward motion is caused by three mechanisms. In the first place, air parcels ahead of the warm front sink in the direct frontal circulation, enhanced by diabatic cooling below Sinlaku's precipitation field, while they move towards the cyclone center. Secondly, due to VWS, Sinlaku's vortex is tilted, which enhances a vertical motion dipole with downward motion left of the direction of tilt. Thirdly, frontolysis occurs west of Sinlaku's center and induces an indirect circulation with downward motion closest to the center. All three mechanisms are co-located and create a tower of descent, which lies over the area of strongest wind speeds. In previous studies, the downward motion of the sting jet was hypothesized to be caused by frontolysis or evaporative cooling as well (see Section 2.2.2). In this case study, the downward motion due to vortex tilting in VWS is added. The frontolysis, however, did not occur in the frontal fracture region, as expected, but rather at the downstream side of the translation direction. Over time the environmental VWS increased (from 14 m/s on 19/22 to 21.5 m/s on 20/06) and the vortex becomes more tilted including a turn of the tilt with height. The mechanisms of vertical motion decrease in intensity and are not co-located anymore. Subsequently, also the tower of descent decreases, both in magnitude and extent and the low-level wind speed weakened.

Although the entire cyclone decreases its intensity near the center, the intensity in terms of PV or relative vorticity over a larger area stays constant or even increases. This is due to the broadening of the cyclone. At upper levels, the jet stream is present, which advects high vorticity air away from Sinlaku. The vertical extent of the vortex thus decreases. But at lower levels, a positive PV anomaly is found below

the warm anomaly of the VWS-induced horizontal temperature dipole. At the same time, relative low-level vorticity that was created along the warm front is advected towards the cyclone center. The increase in PV and vorticity near the broadening cyclone causes a slower decay of the cyclone.

Despite the maintenance of the storm by PV and vorticity advection, Sinlaku still becomes weaker over time. Low-level subtropical air mixes with low-level midlatitude air, decreasing the amount of warm moist air near the center. A negative influence of the VWS-related downward motion in the midlatitudes is the advection of dry air near a level of 850 hPa. The dry air is advected into the warm front, making the front drier. Also, the early lifting and subsequent condensation of subtropical air along the cold front reduces the supply of warm moist air to the warm front. Due to a lower amount of moisture supply in the warm front, less specific humidity can condense and latent heating decreases. Consequently, the amount of precipitation and evaporative cooling decreases also. This weakens the frontal temperature gradient and the cross-frontal circulation. Additionally, less diabatic PV is created and advected toward the cyclone center. So, when the warm front decreased due to dry air inflow, also Sinlaku's intensity decreased.

5.3. Conclusions

The transformation stage of ET is characterised by the change of a tropical cyclone structure into an extratropical cyclone structure. The development has therefore characteristics of both tropical and extratropical cyclone dynamics, and is not yet investigated in much detail. Additionally, the use of high resolution simulations allows to identify and diagnose meso-scale features that have not been described in previous studies. By applying different diagnostic tools to the high resolution simulations, the development of structural changes for the case of Typhoon Sinlaku could be investigated. The research questions regarding dynamics can be answered and are given below:

What mechanisms contributed to the tropical re-intensification and decay of Sinlaku? Sinlaku could re-intensify in a warm moist area due to the blocking of midlatitude air by Japan's orography. South of the orography, a convergence of air streams caused a band of convection in a potentially unstable environment. Diabatic created PV in the convective band is cyclonically transported inwards and contracts, causing Sinlaku to intensify. Also the tilting of horizontal into vertical vorticity due to the ascent of the rainband near a tilted vortex structure, contributed to the intensification.

Decay occurred not only due to the movement over the mountains. Local orography was also favourable for the inflow of air that was diabatically cooled below Sinlaku's own precipitation field. Besides, orography caused a vertical wind shear in combination with rising motion that was unfavourable for the tilting of horizontal vorticity to positive vertical vorticity.

How did the structure of Sinlaku change during its ET?

The frontal structure of Sinlaku resembled a Shapiro-Keyser-like cyclone development, which occurred within a few hours, as if a circulation was superimposed on the baroclinic zone. The low-level wind field included features that were relatively similar to a warm jet, cold jet and sting jet, related to this type of cyclone development. Additional remarkable changes in the structure are the development of a stable area south of Sinlaku by sinking air that created a warm anomaly. Below the warm anomaly, a low-level positive PV anomaly is observed with a broadening low-level wind field around it.

What mechanisms govern the structural changes during the ET of Sinlaku?

Three mechanisms are identified that influence the downward motion of Sinlaku. (1) Environmental VWS tilted the vortex. The balanced response to the vortex tilt led to a temperature anomaly along with descent left of the tilt and ascent right of the tilt. (2) Frontogenesis, frontolysis and (3) diabatic descent by evaporative cooling of air parcels below Sinlaku's own warm frontal precipitation contributed to the asymmetric vertical motion field also. These three mechanisms were vertically aligned to form a tower of descent, below which one of the two maxima in low-level wind speeds was found.

A sting-jet-like feature also descended under the influence of these mechanisms and transported warm dry air downwards, resulting in the stable warm anomaly. At the location where the cyclonically advected downward motion was forced to rise again, the second maximum in low-level wind speed was found. Below the warm anomaly a field of low-level positive PV anomaly is found. Air parcels with a high PV and relative vorticity are advected from along the warm front towards the center, and cause a slower decay of the cyclone.

The dry air that is transported downward subsequently flows into the warm front and makes it more dry influencing the temperature gradient as less latent heat is released. The weakening of the warm front weakens all related processes also (diabatic sinking, cross-frontal circulation, vorticity advection) and thereby it decreases the cyclone intensity.

Additionally, an increase in vertical wind shear and vortex tilting causes a reduced QG forcing to vertical motion. The tower of descent becomes less intense, as does the low-level horizontal wind field. Eventually all processes become weaker and the cyclone decays.

What influence does orography have on the track and structural changes of Sinlaku?

During the tropical re-intensification phase, Sinlaku was protected from inflowing midlatitude air by Japan's orography, and therefore remained in a warm and moist environment. Subsequently, low-level air was channelled between the cyclone center and orography, which influenced the convergence zone that played a key role in the re-intensification. Shortly afterwards, the orography had a major role in the decay of the cyclone also, due to local inflow of cold air and tilting of negative vorticity. The track was, however, not clearly effected by the topography and Sinlaku's translation speed was so high that dry air from the land did not reach the circulation.

During ET, orography did play a key role in postponing the interaction of Sinlaku with the baroclinic zone, due to blocking of midlatitude air. Once Sinlaku passed

Japan and was over the open ocean again, cold dry air could penetrate equatorwards and interact with the cyclone. A minor influence was seen by channelling of cold midlatitude air at lower levels, before the actual interaction with the baroclinic zone started. Additionally, the orography and differential shear may have played a minor role in the development of strong wind speeds on a short time interval around 19/18. Sinlaku's track was dominated by the steering flow and no clear track deflection due to topography was observed.

6. Summary and outlook

The extratropical transition of tropical cyclones is a complex evolution, in which the structure of the cyclone changes from axi-symmetric to asymmetric in a baroclinic environment. The complexity of the structural changes makes it difficult for models to adequately forecast the development. At the same time, improving the forecast skill is important because the transitioning cyclone can provoke high impact weather either locally or, by an indirect impact, thousands of kilometers downstream. Therefore it is necessary to better understand the actual development of the structural changes and the sensitivities in modelling them. TY Sinlaku serves as a suitable case study to improve this knowledge. Sinlaku was one of the typhoons that was investigated during the T-PARC field campaign (2008). It had a rather unusual development during extratropical transition, in which the cyclone first tropically re-intensified after which the transformation stage started. Sinlaku's unexpected behaviour was reflected in forecasts that did not properly predict its development. The unusual ET and the difficulties in modelling it, together with the unique dataset for detailed analysis of structural development, as provided by T-PARC, made Sinlaku an interesting case study for the improvement of the dynamical understanding and model sensitivities during ET. Furthermore, Sinlaku moved close to Japan, and the influence of land on a developing ET system has not yet been investigated in detail.

Modelling ET

The challenge in modelling ET has different reasons. A review of literature is summarised in a schematic overview of the propagation of errors within a model for the case of ET (Fig. 2.16). Errors are initiated either in the initial setup or they develop due to incomplete representations of the model physics and dynamics. The sensitivity of the initial data and several model setups are therefore tested on Sinlaku. In the first place, the initial data was verified with observational data from the T-PARC field campaign. The structure of Sinlaku was already investigated by Foerster et al. (2014) and Quinting et al. (2014) at two specific time steps, 19/04 and 20/06. Here, these studies are complemented by the use of multiple kinds of observational data, for describing both the environment and Sinlaku's structure over a 2.5 day period during extratropical transition (18/12 to 21/00). Furthermore, the observational data is used to verify the quality of the analysis data and the model simulations. The environment in which Sinlaku is embedded is represented relatively well in the initial data. Sinlaku is located near a zonal upper-level jet, which is modified by Sinlaku's upper-level outflow, and to the north the baroclinic zone is present. The

moisture distribution is, however, less well represented in the initial data, where the boundary layer is too humid. The cyclone structure is not represented well at any of the investigated time steps, and Sinlaku is too weak and often located too close to Japan in the initial data.

After gaining insight into the quality of the initial data, simulation experiments are performed. Different model setups are used in which the initialisation time and resolution are changed. Corresponding to the resolution, also the convection parametrization of deep convection is switched off for the high resolution simulations. The initialisation time did not only influence the forecast lead time, but also the initial location of Sinlaku relative to Japan. When Sinlaku was initially close to land in a simulation, it interacted with orography during the spin-up time and its initially weak structure was not able to intensify. Nevertheless, a short forecast lead time resulted in a simulation that agrees very well with observations during the period of tropical re-intensification. For the ET period, however, none of the simulations with standard initial data represented the ET phase of Sinlaku adequately. The cyclone either remained too weak or even re-intensified as an extratropical cyclone.

The initial data has been modified in this study in order to improve the initial storm structure. Sinlaku's vortex is replaced by a more realistic version of the storm based on gridded observational data (SAMURAI data), by the use of piecewise PV inversion. Since the cyclone is sensitive to land in all resolutions, especially in the spin-up time, Sinlaku is also moved horizontally with respect to Japan's topography. At low horizontal resolutions, Sinlaku could still not properly develop near the terrain of Japan. In high resolutions, however, a better representation of orography gave a better typhoon-terrain interaction. Furthermore, simulations of Sinlaku benefited from the resolved convection and higher horizontal gradients that caused stronger wind speed in the center region. This resulted in a more realistic development of the storm after Sinlaku moved over the open ocean again and underwent its actual extratropical transition. In this case study the initialisation of the model played a key role in obtaining a proper simulation. High horizontal resolution simulations in combination with the improved cyclone structure in the initial data and the additional relocation away from land, resulted in a reliable simulation, in which the structural changes agree well with the observations.

Finally, two high-resolution simulations are selected for analysis of the structural changes; one simulation for the tropical intensification period and one simulation for the extratropical transition period. Both simulations are analysed with a range of diagnostic tools (trajectory analysis, vorticity budget analysis, QG-omega forcing, 2-D frontogenesis) in order to gain understanding into the mechanisms that determine structural changes during Sinlaku's ET.

Structural changes during ET

The complete transformation from a tropical into an extratropical cyclone has not yet been investigated in much detail. Previous studies either analysed a single time

of the ET period (e.g. Foerster et al., 2014; Quinting et al., 2014), or used a lower horizontal resolution simulation (e.g. Ritchie and Elsberry, 2001). In this study, TY Sinlaku is investigated during the entire period of re-intensification and decay, and the use of high resolution simulations allowed to identify meso-scale features that have not been analysed before. The focus here lies on mechanisms that are responsible for structural changes and the re-intensification and decay of the cyclone system. The analysis is divided into two periods: the tropical re-intensification period and the actual extratropical transition period.

Starting with the tropical re-intensification period, Sinlaku was present south of Japan and the orography blocked the inflow of midlatitude air from the north. Sinlaku was therefore located in a warm and moist area, with potential for re-intensification. Enhanced convection can be induced by two reasons. In the first place an area of convection was present at the downtilt left side, which is favourable for ascending motion, similar to what was found by Foerster et al. (2014). Secondly, the outer circulation of Sinlaku was channelled between the center and Japan's orography. Thereby the outer and inner circulation converged and caused a band of convection. PV is created diabatically in the lower levels of the convective area and it is transported inwards cyclonically, while new PV is created below the convection. The PV field contracts and causes Sinlaku to intensify. Additionally, the tilted vortex due to environmental vertical wind shear by the jet stream causes an internal vertical wind shear within the vortex, with associated horizontal vorticity. In combination with the ascent in the convergence area, the horizontal vorticity is tilted to become positive vertical vorticity near the cyclone center, which contributed to the intensification of Sinlaku. When Sinlaku moved over Japan, its intensity suddenly decreased due to the direct interaction with the terrain. Additional mechanisms for the decay are also related to orography. In the first place, the topography was locally favourable for the advection of cold air from the east. This air was diabatically cooled below Sinlaku's own precipitation field. Additionally, the orography caused a vertical wind shear that, in combination with orographic lifting, tilted horizontal vorticity to become negative vertical vorticity and thereby weakening the vortex.

The ET period is characterised by the transformation of a tropical cyclone structure into an extratropical cyclone structure. The development has therefore characteristics of both tropical and extratropical cyclone dynamics. But, before the actual transformation stage started, orography played a key role in postponing the interaction of Sinlaku with the baroclinic zone, by blocking of low-level midlatitude air. Once Sinlaku moved over the open ocean again, midlatitude air was free to move equatorwards. The frontal structure of Sinlaku developed in a similar manner to a Shapiro-Keyser cyclone, with the difference here that this evolution occurred within a few hours, instead of the more common 1-7 days. The quick development occurs because Sinlaku's circulation is already present, and almost superimposed on the baroclinic zone as soon Sinlaku moves away from Japan. Related to this type of cyclone are the warm jet, cold jet and sting jet like features, that were also found for Sinlaku. These areas of strong low-level wind are important for the direct impact of ET to life and property.

The vertical motion played a key role in the structural changes of Sinlaku. The downward motion is caused by three mechanisms. In the first place, air parcels cool diabatically below Sinlaku's precipitation field. Secondly, due to the influence of VWS and the tilting of the cyclone vortex, a dipole in vertical motion occurs, with downward motion left of the direction of tilt. The third mechanism is related to frontolysis at the downstream side of Sinlaku. These three mechanisms are co-located and are responsible for a tower of descent, which lies over the area of strongest low-level wind speeds. Air parcels that moved through the tower of descent turned cyclonically and sank adiabatically in the last hour before they arrived south of Sinlaku. Due to the adiabatic sinking, they created a warm anomaly. This warm stable area prevents convection and cloud formation, and is a key feature in the asymmetric structure during ET. Below the warm anomaly, a PV anomaly was present. A part of the PV anomaly was diabatically created along the warm front and advected to the center. The PV anomaly subsequently modified the cyclonic wind field and corresponded to a broader low-level circulation. Due to the advection of potential and relative vorticity and the broadening of the cyclone, the intensity in terms of vorticity stayed relatively constant within a large box around the storm, although the intensity near the center weakened.

Over time, the influence of the upper-level jet stream becomes stronger, which has different consequences. In the first place, vorticity is advected away from Sinlaku at upper levels, due to which the vertical extent of the vortex decreases. Secondly, the vertical wind shear increases to a magnitude in which the vortex is no longer resilient to the shear. Sinlaku's vortex becomes more tilted and includes a turn of the tilt with height. Consequently, the upper- and lower-level QG- ω forcing become weaker and are not co-located anymore.

In the meantime, midlatitude air interferes with the subtropical warm moist air supply in different ways. In the first place, low-level subtropical air mixes with low-level midlatitude air near the center of the storm, decreasing the amount of warm moist air near the center. Secondly, the dry air of the warm anomaly is advected into the warm front. Additionally, the lifting of subtropical air and subsequent condensation of specific humidity along the cold front causes a lower supply of warm moist air at the warm front. This weakens the warm front and its associated processes for vertical motion. In addition, as less latent heat is released, also the diabatic creation of PV and its advection into the cyclone decreases. Finally, the tower of descent decreases, both in magnitude and in vertical extent, and the low-level wind speeds weaken. So a decrease in moisture supply and an increase in vertical wind shear caused a decrease of Sinlaku's intensity. Eventually all processes become weaker and the cyclone decays.

Outlook

The challenges in modelling and the structural changes that were found in this thesis are based on only one case study. More case studies are needed to get a better and more general understanding of structural changes during ET, and to get insight

in similarities and differences in structural changes under different environmental conditions. Idealised modelling at a high horizontal resolution would give an impression of the structural changes under prescribed environmental conditions. This would give a better insight in general features of the transitioning cyclone. Additionally, measurement data is of importance in both verifying the model results and analysing detailed structural changes during ET, like Foerster et al. (2014) and Quinting et al. (2014) did. The measurement data that was obtained during the T-PARC field campaign was an excellent source for this goal. In future field campaigns, it would be of interest if research flights would gather data of the temporal development of the warm front and warm moist air supply, which played a key role in the structural changes. Furthermore, measurement data of the wind, temperature and moisture field near the cyclone, especially in and near the warm anomaly and the bent back warm front, would contribute to the understanding of the development of the stable air, the broadening wind field and the areas of strong low-level winds.

Regarding topography, this case study gives a first impression of the influence of land on ET. Further analysis is needed, because the influence of land highly influenced the quality of the simulations, and may thereby be a source of uncertainty in forecasting ET. It is suggested that the actual influence of land during ET would be investigated by experiments in which the orography of, for example, Japan is flattened or even replaced by an ocean surface. Idealised experiments similar to those conducted by e.g. Chan and Liang (2003), Wong and Chan (2006), Szeto and Chan (2010) and Li et al. (2014), where a vortex is present near a simplified version of Japan or even just a straight coastline, would be a start, and different setups of orography and vertical wind shear should be used. In this study, the influence of the ocean temperature is mostly neglected. Sinlaku moves over the relatively warm Kuroshio ocean current. Therefore it remained near a gradient of relatively warm and cool water which can have an impact on the development. Hurricane Sandy, for example, intensified when it was located over the Gulf stream (Galarneau-Jr. et al., 2013). The influence of this locally warm ocean water to the development of cyclones is topic of further research.

Idealised studies, however, do not cover the large variability of ET cases that occur in reality. Case studies on the influence of land would therefore complement the knowledge about this topic. Every year, several typhoons move near Japan. After Sinlaku in 2008, nine typhoons had a relatively similar course along the south coast or just over the main island of Japan. The majority of them made landfall over Japan, and their central pressure quickly increased (TY Melor (2009), TY Guchol (2012), TY Jelawat (2012), TY Malakas (2016)). TY Phanfone (2014), on the other hand, first showed a stable pressure development south of Shikoku, after which it also quickly decayed. A relatively stable pressure development during the path along the south coast of Japan was seen for TY Lupit (2009), TY Vongfong (2014) and TY Neoguri (2014). These examples can be used to investigate what the influence of the topography on the onset and development of ET was, in relation to the blocking of midlatitude air inflow while the intensity remained relatively stable. Another interesting case is the intensification of TY Roke (2011), south of Shikoku, at a

similar location to that where Sinlaku intensified. TY Olga (1970) intensified at this location also (Matano and Sekioka, 1971). This indicates the need for further research about why some typhoons intensify near Japan, and in particular near Shikoku, and others do not.

The structural changes of Sinlaku that are related to extratropical cyclone development, give promising new results, that need further investigation. The cold jet and sting jet like features and their development are partly similar to cases previously documented in literature, but differences were present as well. These features should be analysed for multiple storms, both in ET cases as in cyclones that develop in the midlatitudes, in order to distinguish general mechanisms that are present in the bulk of the cyclones. Since cold jets and sting jets are especially known from extratropical cyclones that cause damage in populated areas, this topic is of great relevance for the accurate prediction of high impact weather.

Appendices

A. Verification of the Best Track data

Best Track data will be verified by the use CTT, Quikscat and dropsonde data. The need for verification of the Best Track lies in the often unreliable quality of the Best Track during ET. Although the Best Track of Sinlaku is expected to be relatively good, because T-PARC measurements are included, it will nevertheless be verified, because the Best Track is used for comparison with modelled data throughout Chapter 4 and its quality should therefore be known.

Quikscat surface winds are available every 12 hours, at 9 UTC and 21 UTC. The surface center was not entirely captured at all times and also not always circular, but an indication of the surface center can be obtained from it. On 18/21 the center lies at 133.3E, 31.9N (Fig. 4.2c), which is 0.3° south of the Best Track.

During the re-intensification period just before 19 September, Sinlaku developed an eyewall again. The location of the eyewall gives additional information about the location of the storm. In infrared satellite data, a (broken) eyewall can be observed between 18/22:45 and 19/01:15 (Fig. 4.2b,c). On 19/00, Sinlaku is situated at 134.1° E, 32.5° N according to the Best Track, which fits with the location of the eye on 18/23:45. In the 850 hPa SAMURAI data wind field the core lies at 135.15° E, 32.9° N (Section 4.1.2, Fig. 4.9e). The measurement data used to produce SAMURAI data was obtained between 3 and 6 UTC and the interpolated Best Track location between 3 and 6 UTC corresponds to the SAMURAI data.

At 19/09 a suspected center lies around 137° E and 33° N - 33.5° N according to Quikscat data (Fig. 4.2d), which is again south of the Best Track (33.6° N at 19/09). 12 hours later, on 19/21 (Fig. 4.2e), the estimated surface circulation center equals the Best Track at 141° E, 34.6° N. Also the center at about 145.8 E, 35.2 N (Fig. 4.2f) agrees with the interpolated location of the Best Track on 20/09.

After 20/09, not many observations are available. On 21/00 The Falcon aircraft did not capture the storm, but remained west of it. Dropsondes from this flight reveal a sinking surface pressure when the airplane flew towards the suspected core region, and a rising pressure when flying away from it (not shown), reaching a minimum of 1003.36 hPa (Falcon-20/23:58). The Falcon reached a maximum longitude of 151.4 E and Sinlaku was indeed east of this point on 21/00 according to the Best Track.

Continuing with the pressure development, dropsonde data in or near the center are available for comparison at two specific time steps. On 19 September, the P3 aircraft flew through the eyewall and into the core region of the storm (Fig. 3.1). Dropsondes were launched in the core and the pressure at 0 m altitude of successive

Aircraft	time (dd/hh:mm)	pressure (hPa)
P3	19/03:57	977.38
P3	19/04:00	974.02
P3	19/04:03	987.26
P3	19/04:06	977.69
P3	19/04:09	980.56
C130	20/05:20	997.63
C130	20/05:27	985.15
C130	20/05:32	990.44
C130	20/05:35	992.25
C130	20/08:05	993.33
C130	20/08:09	988.19
C130	20/08:11	988.96
C130	20/08:15	991.90
C130	20/08:22	998.50

Table .1. – Pressure at 0 m altitude from dropsonde data, launched from the given aircraft at the given time. For details of data used see Section 3.1.1.

dropsondes is given in Table .1. A large horizontal pressure gradient of about 13 hPa within $\sim 0.22^\circ$ distance (dropsondes P3-19/04:00 and P3-19/04:03) is present near the core. Directly outside the core, pressure values quickly rise from below 980 hPa to over 990 hPa (not shown). The C130 aircraft flew nearby but not through the center. Its dropsonde pressure values at 0 m altitude do not reach below 993 hPa (not shown).

On 20 September, no eyewall was present anymore and the transitioning storm is asymmetric. A 'core'-region can therefore not be determined, but instead the circulation center is used. Both aircrafts flew near the circulation center, releasing multiple dropsondes (Fig. 3.1). The P3 aircraft dropsondes mainly registered > 1000 hPa at sea level, with a minimum of 995.08 hPa (P3-20/06:22). The P3 aircraft was therefore probably not near the cyclone center. The C130 aircraft possibly hit the center region twice. A strong pressure gradient is observed in consecutively released dropsondes around 5:30 UTC and 8:10 UTC, with minima of 985.15 hPa and 988.19 hPa respectively (Table .1).

Although calm wind speeds are expected in a TC core, the low level wind speeds of the dropsondes given in Table .1 were rather in the order of 20-40 m/s. Only dropsonde C130-20/08:11 had wind speeds < 5 m/s between 800 and 750 hPa, but > 50 m/s between 930 and 956 hPa (for C130-20/08:09, no wind data is available). It is therefore more likely that the C130 flew near the radius of strongest surface winds. Nevertheless, the pressure values and locations of dropsondes P3-19/04:00, C130-10/05:27 and C130-20/08:09 are plotted as a reference in Figure 4.1. These plotted dropsonde locations are not necessarily the storm center locations, but merely show where the relatively low pressures were measured.

In general the Best Track location of Sinlaku corresponds relatively well with ob-

servations, apart from a few locations where the storm in reality was located more south. The measured surface pressure of the dropsondes is in the order of 5 hPa lower than the Best Track surface pressure (Fig. 4.1) but the increasing trend between the two observation periods is similar. Model data, especially in case of 0.25° horizontal resolution, will not be able to capture the measured low pressures and large pressure gradient within the core region. The Best Track data is therefore suitable as a reference to verify model output.

B. Details to Sinlaku's evolution in CTT data

Tropical re-intensification starts with a convective burst, a sudden change to colder temperatures (here below $-60\text{ }^{\circ}\text{C}$) on a meso-scale in consecutive satellite images, occurring around 18/19:15 (Fig. .1a, shown by the red and dark green area). The convective burst develops within only two hours and turns cyclonically around the cyclone center from east to west within the next two hours (not shown). The burst disintegrates into multiple convective cells on 18/20:15 that continue to move cyclonically downstream around a newly formed eyewall (Fig. .1b) (Foerster et al., 2014). The eyewall is present for only a few hours. After 19/00, eyewall erosion starts (Fig. .1c), and on 19/03 the eyewall has disappeared (Fig. .1d).

On 20 September, the ET phase of Sinlaku is dominated by two convective bursts: first between 20/03:45 and 20/08:45 (Fig. .2a) and a second burst between 20/20 and 21/04 (Fig. .2b).

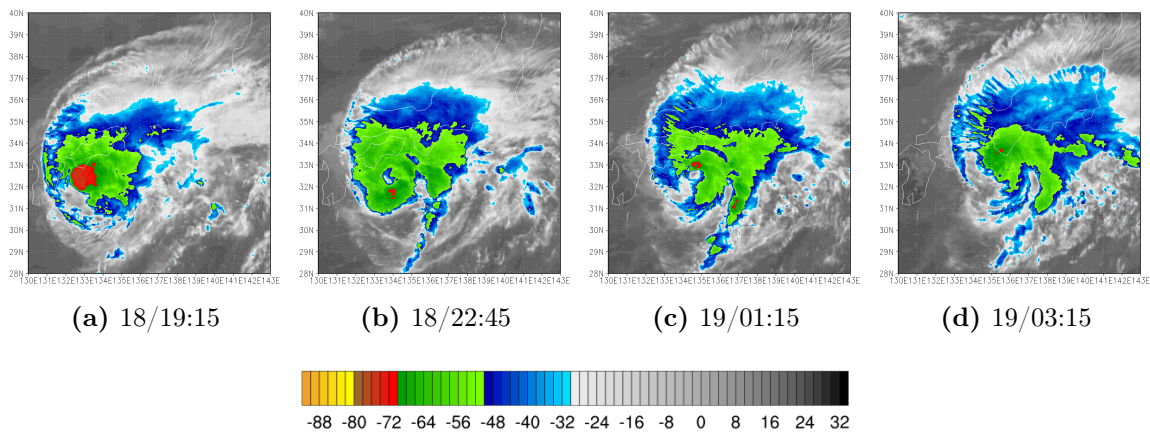


Figure .1. – MTSAT cloud top temperature ($^{\circ}\text{C}$) during the presence of an eyewall and during its erosion, around the time of Fig. 4.2c. For details of data used see Section 3.1.2.

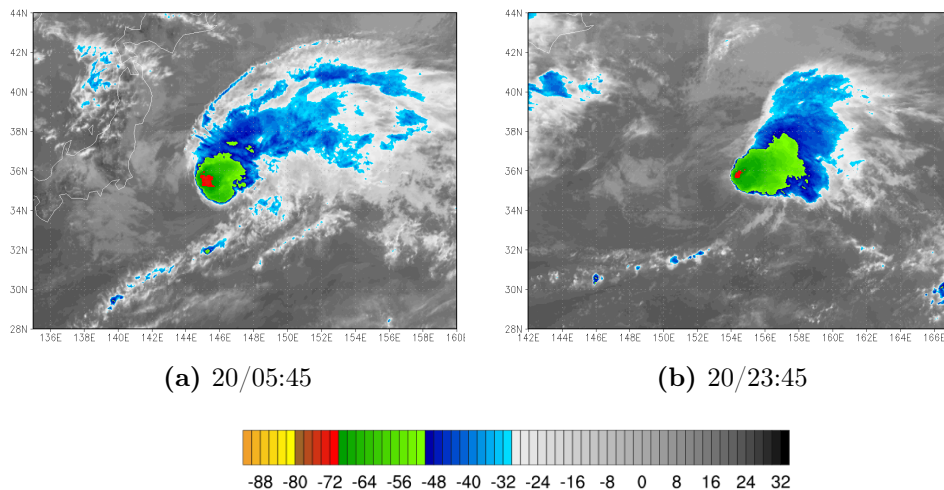


Figure .2. – MTSAT cloud top temperature ($^{\circ}\text{C}$) of two convective bursts during ET. For details of data used see Section 3.1.2.

C. Details to Sinlaku's evolution in standard COSMO simulations

The hindcasts of Section 4.2 are verified in more detail here, based on AMVs and LIDAR data.

Comparison to AMV data

The upper level development of the storm is analysed by the mean error between the simulations and the AMV wind velocity and direction (Fig. .3). A positive value in wind speed represents a stronger wind speed in the hindcast. Since the wind direction at 200 hPa is dominated by westerly winds (270°), a positive value in wind direction represents a more southwesterly wind component in the AMVs.

During tropical re-intensification (18/18 - 19/00) upper level wind speed was about 1 - 2 m/s too strong in all simulations (Figs. .3a,b,c). In comparison to an upper level flow in the order of 20 m/s to > 40 m/s (Fig. 4.5), this is an error of 3-10 %. The wind direction of the upper level outflow is captured relatively well with a direction that is in the order of 10° more westerly in the hindcasts (Figs. .3d). The mean error in wind direction is relatively similar for all resolutions, and therefore only shown for HiRes. After tropical re-intensification, all hindcasted storms are near to make landfall in Japan. Their intensity decreases at this point and so does the upper level outflow. This is reflected in the mean error of the wind speed which suddenly increases on 19/06 (Fig. .3 a,b,c).

The mean error in both wind speed and wind direction remains relatively high during the period that Sinlaku moves parallel to Japan's coastline. When Sinlaku's intensity (unexpectedly) increased on 20/00 and the storm moves over the open ocean again, the hindcasts also become more similar to the AMVs again. The signal from the two extratropically intensifying simulations (H1812-hi and H1818-hi) is expected to have a negative error in the wind direction, meaning that the simulations have a more southerly component in their strong outflow. They indeed have a strong outflow which is not seen in Fig. .3d because the tracks of these simulations are north of the best track and for the computation of the mean error the absolute location is used. For all hindcasts, the positive values of mean error suggest that the storm is too weak in all simulations. The outflow is not as strong as observed and the jet stream is therefore a rather strong westerly wind.

Comparison to LIDAR data

The environmental situation is also compared to LIDAR data. The correlation coefficients for wind speed, wind direction and specific humidity between the model output and the LIDAR data are given in Table .2. The correlation coefficients for LoRes, MiRes and HiRes are similar in magnitude and only small differences are

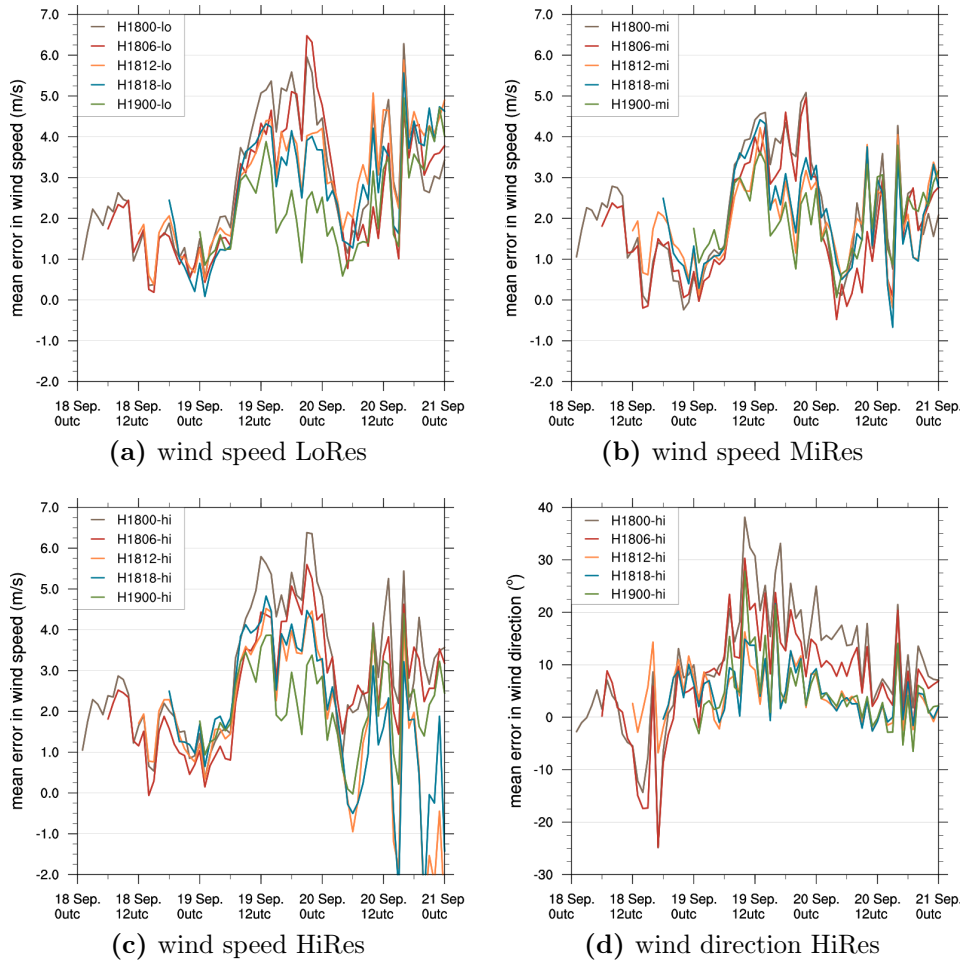


Figure 3. – Mean error of the wind speed at LoRes, MiRes, HiRes (a,b,c) and wind direction at HiRes (d) in hindcasts at 200 hPa compared to atmospheric motion vectors at 150–250 hPa. A box around the storm represents the outflow region (6°S, 10°N, 10°W, 15°E relative to the storm location). The available AMVs between 150 and 250 hPa are brought to a horizontal grid of 0.25° and are subtracted from the hourly output of the hindcasts at 200 hPa. For details of the AMV data see Section 3.1.2.

found. This suggests that the environment is not better represented in HiRes hindcasts than in LoRes hindcasts. More detailed analysis shows that the correlation coefficient for wind direction and wind speed in general becomes higher when the initialisation time of the hindcast lies closer to the time of measurement ($\sim 19/01 - 19/04$). This is as expected, since for a longer forecast lead time, the error growth is larger. For specific humidity the opposite is found. Correlation coefficients become lower when the initialisation time is closer to the measurement. This is caused by the initial data that was found to be too moist in the boundary layer (section 4.1.2). The model needs time to recover from the error in the initial data. An exception is seen for H1900-lo and H1900-mi. Dropsonde observations were already assimilated

	H1800-lo	H1806-lo	H1812-lo	H1818-lo	H1900-lo
Wind speed	0.964	0.964	0.975	0.977	0.986
Wind dir.	0.804	0.815	0.836	0.813	0.883
Spec.hum.	0.847	0.849	0.832	0.837	0.857

	H1800-mi	H1806-mi	H1812-mi	H1818-mi	H1900-mi
Wind speed	0.945	0.954	0.976	0.977	0.985
Wind dir.	0.806	0.818	0.835	0.792	0.870
Spec.hum.	0.845	0.837	0.836	0.835	0.857

	H1800-hi	H1806-hi	H1812-hi	H1818-hi	H1900-hi
Wind speed	0.962	0.966	0.979	0.974	0.985
Wind dir.	0.814	0.815	0.833	0.763	0.870
Spec.hum.	0.874	0.877	0.861	0.857	0.857

Table .2. – Correlation coefficient of the lidar data compared to the available simulations, for wind speed, wind direction and specific humidity. For details of the lidar data see Section 3.1.1.

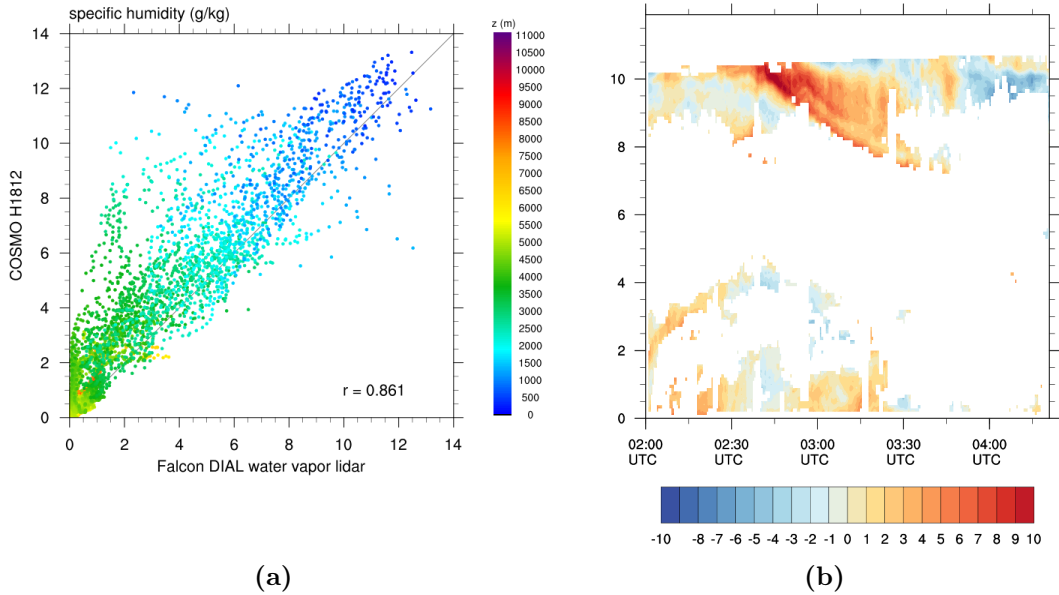


Figure .4. – (a) Correlation between lidar and simulation 18/12 at 2 km resolution for specific humidity. (b) Cross section with wind speed difference between lidar data and H1812-hi (lidar-H1812-hi). Similar to Fig. 4.6. For details of the lidar data see Section 3.1.1.

in the analysis data used here. Although the dropsonde assimilation did not entirely correct for the overrepresented amount of moist in the boundary layer, it did improve the data.

Despite the relatively high correlation coefficients for all simulations, two differences with the observations will be highlighted.

(1) All simulations are still too moist in the boundary layer and have moist features at about 2UTC and just before 4UTC (not shown), similar to the analysis data in Fig. 4.8. The boundary layer in the hindcasts therefore stays too moist also, in the first hours after initialisation. There is, however, an improvement compared to the analysis data. Fig. 4.4a for example shows the correlation of specific humidity between H1812-hi and the LIDAR data, and is less moist in the 1500 - 3500 m layer than the analysis data (Fig. 4.7).

(2) The wind speed has a relatively high correlation coefficient in all simulations (Table 4.2). Nevertheless, there are differences in the structure. The wind speed difference between H1812-hi and the LIDAR data is shown in Fig. 4.4b (see Fig. 4.6 for the actual wind speed structure). The jet core in the simulation is situated too much south (further in time) and is too weak, especially at the northern part (earlier in time, red colors in Fig. 4.4b). A different location of the jet structure would imply a slightly different TC-jet interaction.

D. Characteristics of the low level wind field at 19/18

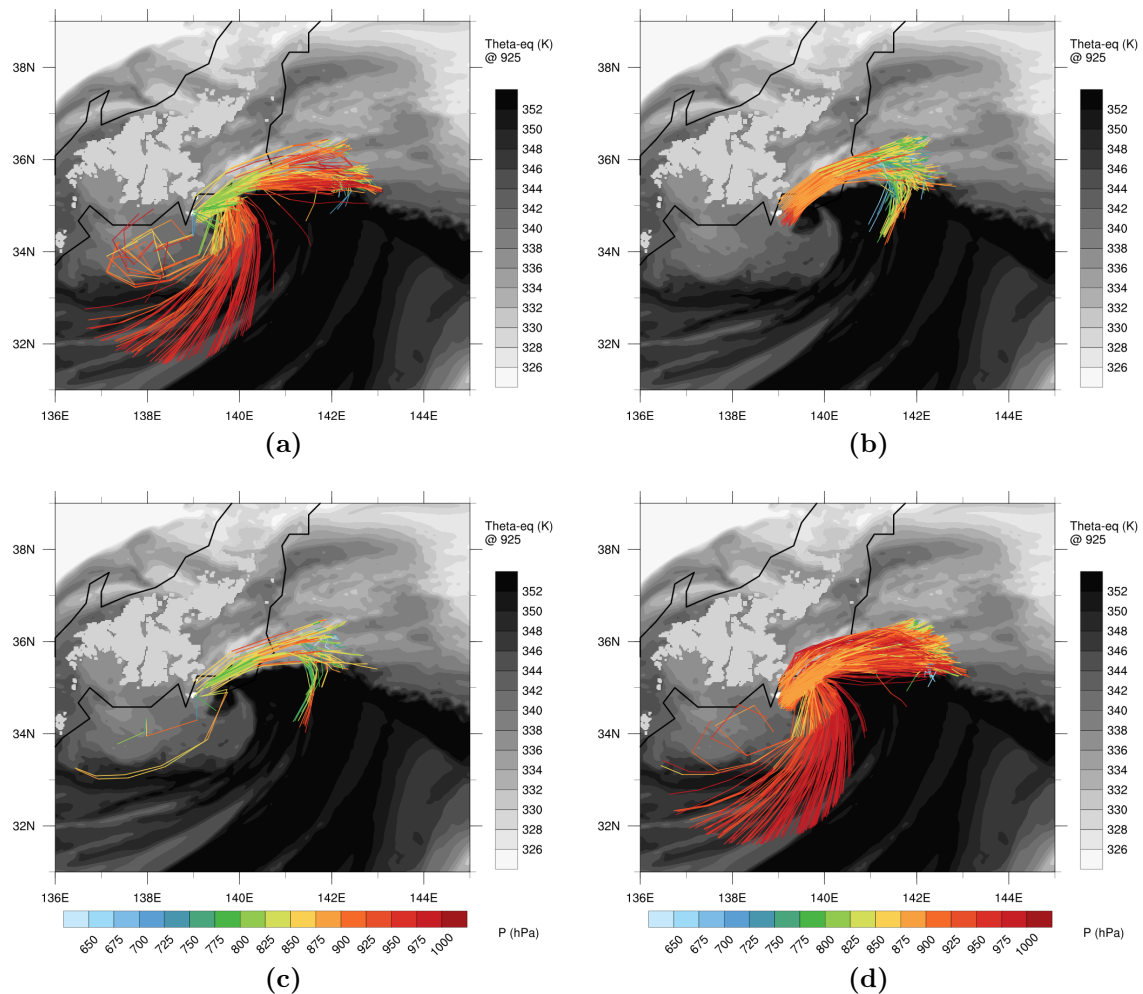


Figure .5. – 6h backward trajectories arriving at 19/18 at the west side of Sinlaku's center with $>40\text{m/s}$. The trajectories are divided in (a) rising, (b) sinking, (c) residing below 875 hPa and (d) residing above 875 hPa, based on their pressure level at $t=-3$ and $t=0$ relative to a boundary of 875 hPa.

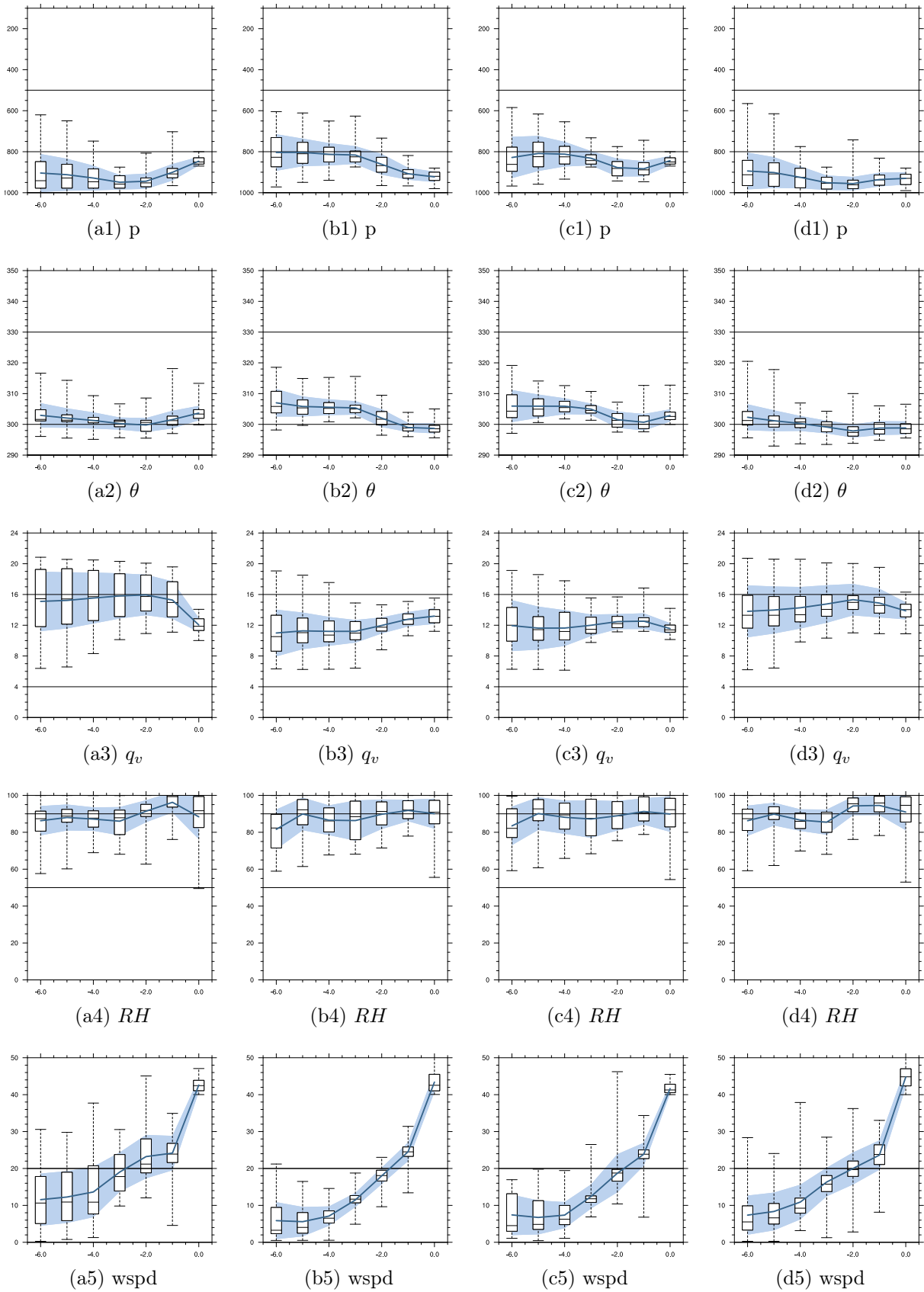


Figure .6. – Statistics corresponding to the trajectories of Fig. .5, with (a) rising, (b) sinking, (c) residing relatively high and (d) residing relatively low air parcels. For details of the statistic figures see Section 3.3.5.

List of abbreviations

19/00	19 September, 00 UTC
19/00:12	19 September, 00:12 UTC
AMV	atmospheric motion vector
CCB	cold conveyor belt
CJ	cold jet
CLJ	cold low-level jet
COSMO	consortium for small-scale modeling
CTT	cloud top temperature
DI	dry intrusion
DIAL	differential absorption Lidar
DWD	German weather service (Deutscher Wetterdienst)
DWL	Doppler wind Lidar
ECMWF	European center for medium-range weather forecast
ELDORA	electra doppler radar
ET	extratropical transition
JMA	Japan Meteorological Agency
LAGRANTO	lagrangian analysis tool
MTSAT	multifunctional transport satellite
NWP	numerical weather prediction
PANDOWAE	predictability and dynamics of weather systems in the Atlantic-European sector
PPI	piecewise PV inversion
PV	potential vorticity
QG	quasi-geostrophic
RMW	radius of maximum winds
SAMURAI	spline analysis at mesoscale utilizing radar and aircraft instrumentation
SDJ	sinking dry jet
SJ	sting jet
SST	sea surface temperature
TC	tropical cyclone
THORPEX	the observing system research and predictability experiment
T-PARC	THORPEX Pacific Asian regional campaign
TY	typhoon
VWS	vertical wind shear
WCB	warm conveyor belt
WJ	warm jet

Bibliography

- Agustí-Panareda, A. (2008). The contribution of ex-tropical cyclone Gert (1999) toward the weakening of a midlatitude cyclogenesis event. *Mon. Wea. Rev.*, 136:2091–2111.
- Agustí-Panareda, A., Gray, S. L., Craig, G. C., and Thorncroft, C. D. (2005). The extratropical transition of tropical cyclone Lili (1996) and its crucial contribution to a moderate extratropical development. *Mon. Wea. Rev.*, 133:1562–1573.
- Agustí-Panareda, A., Thorncroft, C. D., Craig, G. C., and Gray, S. L. (2004). The extratropical transition of hurricane Irene (1999): A potential-vorticity perspective. *Q. J. R. Meteorol. Soc.*, 130:1047–1074.
- Aiyyer, A. (2015). Recurving western north pacific tropical cyclones and midlatitude predictability. *Geophys. Res. Lett.*, 42:7799–7807.
- Anwender, D., Harr, P. A., and Jones, S. C. (2008). Predictability associated with the downstream impacts of the extratropical transition of tropical cyclones: Case studies. *Mon. Wea. Rev.*, 136:3226–3247.
- Archambault, H. M., Bosart, L. F., Keyser, D., and Cordeira, J. M. (2013). A climatological analysis of the extratropical flow response to recurving western north Pacific tropical cyclones. *Mon. Wea. Rev.*, 141:2325–2346.
- Atallah, E. H. and Bosart, L. F. (2003). The extratropical transition and precipitation distribution of hurricane Floyd (1999). *Mon. Wea. Rev.*, 131:1063–1081.
- Au-Yeung, A. Y. M. and Chan, J. C. L. (2010). The effect of a river delta and coastal roughness variation on a landfalling tropical cyclone. *J. Geophys. Res.*, 115, D19121:1–14.
- Bell, M. M., Montgomery, M. T., and Emanuel, K. A. (2012). Air–sea enthalpy and momentum exchange at major hurricane wind speeds observed during CBLAST. *J. Atmos. Sci.*, 69:3197–3222.
- Bjerknes, J. and Solberg, H. (1922). Life cycle of cyclones and the polar front theory of atmospheric circulation. *Geophys. Publ.*, 3, No. 1:1–18.
- Boettcher, M. and Wernli, H. (2011). Life cycle study of a diabatic rossby wave as a precursor to rapid cyclogenesis in the north atlantic—dynamics and forecast performance. *Mon. Wea. Rev.*, 139:1861–1878.
- Bolton, D. (1980). The computation of equivalent potential temperature. *Mon. Wea. Rev.*, 108:1046–1053.

- Bosart, L. F. and Dean, D. B. (1991). The Agnes rainstorm of June 1972: Surface feature evolution culminating in inland storm redevelopment. *Wea. Forecasting*, 6:515–537.
- Bretherton, F. P. (1966). Critical layer instability in baroclinic flows. *Q. J. R. Meteorol. Soc.*, 92:325–334.
- Browning, K. A. (2004). The sting at the end of the tail: Damaging winds associated with extratropical cyclones. *Q. J. R. Meteorol. Soc.*, 130:375–399.
- Browning, K. A., Vaughan, G., and Panagi, P. (1998). Analysis of an ex-tropical cyclone after its reintensification as a warm-core extratropical cyclone. *Q. J. R. Meteorol. Soc.*, 124:2329–2356.
- Carlson, T. N. (1980). Airflow through midlatitude cyclones and the comma cloud pattern. *Mon. Wea. Rev.*, 108:1498–1509.
- Chan, J. C. L. and Kepert, J. D. (2010). *Global Perspectives on Tropical Cyclones - From Science to Mitigation*, volume volume 4 of World Scientific Series on Asia-Pacific Weather and Climate. World Scientific Publishing Co. Pte. Ltd., Singapore, Hackensack, London.
- Chan, J. C. L., Ko, F. M. F., and Lei, Y. M. (2002). Relationship between potential vorticity tendency and tropical cyclone motion. *J. Atmos. Sci.*, 59:1317–1336.
- Chan, J. C. L. and Liang, X. (2003). Convective asymmetries associated with tropical cyclone landfall. part I: f-plane simulations. *J. Atmos. Sci.*, 60:1560–1576.
- Chang, S. W.-J. (1982). The orographic effects induced by an island mountain range on propagating tropical cyclones. *Mon. Wea. Rev.*, 110:1255–1270.
- Charney, J. (1955). The use of the primitive equation of motion in numerical prediction. *Tellus*, 7:22–26.
- Clark, P. A., Browning, K. A., and Wang, C. (2005). The sting at the end of the tail: Model diagnostics of fine-scale three-dimensional structure of the cloud head. *Q. J. R. Meteorol. Soc.*, 131:2263–2292.
- Clough, S. A., Davitt, C. S. A., and Thorpe, A. J. (1996). Attribution concepts applied to the omega equation. *Q. J. R. Meteorol. Soc.*, 122:1943–1962.
- Colle, B. A. (2003). Numerical simulations of the extratropical transition of Floyd (1999): Structural evolution and responsible mechanisms for the heavy rainfall over the northeast United States. *Mon. Wea. Rev.*, 131:2905–2926.
- Davis, C., Wang, W., Dudhia, J., and Torn, R. (2010). Does increased horizontal resolution improve hurricane wind forecasts? *Wea. Forecasting*, 25:1826–1841.
- Davis, C. A. (1992). Pieceflow potential vorticity inversion. *J. Atmos. Sci.*, 49(16):1397–1411.
- Davis, C. A. and Emanuel, K. A. (1991). Potential vorticity diagnostics of cyclogenesis. *Mon. Wea. Rev.*, 119:1929–1953.

- Davis, C. A. and Galarneau-Jr., T. J. (2009). The vertical structure of mesoscale convective vortices. *J. Atmos. Sci.*, 66:686–704.
- Davis, C. A., Jones, S. C., and Riemer, M. (2008). Hurricane vortex dynamics during atlantic extratropical transition. *J. Atmos. Sci.*, 65:714–736.
- Deveson, A. C. L., Browning, K. A., and Hewson, T. D. (2002). A classification of FASTEX cyclones using a height-attributable quasi-geostrophic vertical-motion diagnostic. *Q. J. R. Meteorol. Soc.*, 128:93–117.
- DiMego, G. J. and Bosart, L. F. (1982a). The transformation of tropical storm Agnes into an extratropical cyclone Part I: The observed fields and vertical motion computations. *Mon. Wea. Rev.*, 110:385–411.
- DiMego, G. J. and Bosart, L. F. (1982b). The transformation of tropical storm Agnes into an extratropical cyclone Part II: Moisture, vorticity and kinetic energy budgets. *Mon. Wea. Rev.*, 110:412–433.
- Doms, G., Förstner, J., Heise, E., Herzog, H.-J., Mironov, D., Raschendorfer, M., Reinhardt, T., Ritter, B., Schrodin, R., Schulz, J.-P., and Vogel, G. (2011). *A description of the nonhydrostatic regional COSMO-model. Part II: Physical parameterization*. Deutscher Wetterdienst, Offenbach, www.cosmo-model.org.
- Dvorak, V. F. (1975). Tropical cyclone intensity analysis and forecasting from satellite imagery. *Mon. Wea. Rev.*, 103:420–430.
- Ebuchi, N., Graber, H. C., and Caruso, M. J. (2002). Evaluation of wind vectors observed by QuikSCAT/SeaWinds using ocean buoy data. *J. Atmos. Oceanic Technol.*, 19:2049–2062.
- Emanuel, K. A. (1986). An air-sea interaction theory for tropical cyclones. part I: Steady-state maintenance. *J. Atmos. Sci.*, 43:585–604.
- Emanuel, K. A. (1991). The theory of hurricanes. *Annu. Rev. Fluid Mech.*, 23:179–196.
- Emanuel, K. A. (2003). Tropical cyclones. *Annu. Rev. Earth Planet. Sci.*, 31:75–104.
- Ertel, H. (1942). Ein neuer hydrodynamischer erhaltungssatz. *Meteorol. Z.*, 59:277–281.
- Evans, C. and Hart, R. E. (2008). Analysis of the wind field evolution associated with the extratropical transition of Bonnie (1998). *Mon. Wea. Rev.*, 136:2047–2065.
- Evans, C., Wood, K. M., Aberson, S. D., Archambault, H. M., Milrad, S. M., Bosart, L. F., Corbosiero, K. L., Davis, C. A., Pinto, J. D. D., Doyle, J., Fogarty, C., Galarneau-Jr., T. J., Grams, C. M., Griffin, K. S., Gyakum, J., Hart, R. E., Kitabatake, N., Lentink, H. S., McTaggart-Cowan, R., Perrie, W., Quinting, J. F. D., Reynolds, C. A., Riemer, M., Ritchie, E., Sun, Y., and Zhang, F. (2017). The extratropical transition of tropical cyclones. Part I: Cyclone evolution and direct impacts. *Mon. Wea. Rev.*, (in review).

- Evans, J. L., Arnott, J. M., and Chiaromonte, F. (2006). Evaluation of operational model cyclone structure forecasts during extratropical transition. *Mon. Wea. Rev.*, 134:3054–3072.
- Evans, J. L. and Hart, R. E. (2003). Objective indicators of the life cycle evolution of extratropical transition for atlantic tropical cyclones. *Mon. Wea. Rev.*, 131:909–925.
- Foerster, A. M., Bell, M. M., Harr, P. A., and Jones, S. C. (2014). Observations of the eyewall structure of Typhoon Sinlaku (2008) during the transformation stage of extratropical transition. *Mon. Wea. Rev.*, 142:3372–3391.
- Fogarty, C. T., Greatbatch, R. J., and Ritchie, H. (2006). The role of anomalously warm sea surface temperatures on the intensity of Hurricane Juan (2003) during its approach to Nova Scotia. *Mon. Wea. Rev.*, 134:1484–1504.
- Fogarty, C. T., Greatbatch, R. J., and Ritchie, H. (2007). The use of a vortex insertion technique to simulate the extratropical transition of hurricane Michael (2000). *Wea. Forecasting*, 22:480–500.
- Frank, W. M. and Ritchie, E. A. (1999). Effects of environmental flow upon tropical cyclone structure. *Mon. Wea. Rev.*, 127:2044–2061.
- Frank, W. M. and Ritchie, E. A. (2001). Effects of vertical wind shear on the intensity and structure of numerically simulated hurricanes. *Mon. Wea. Rev.*, 129:2249–2269.
- Frisius, T. (2004). Numerical simulation of tropical cyclogenesis with the Lokal-Modell. *COSMO Newsletter*, 4:189–196.
- Frisius, T. and Hasselbeck, T. (2009). The effect of latent cooling processes in tropical cyclone simulations. *Q. J. R. Meteorol. Soc.*, 135:1732–1749.
- Frisius, T., Hasselbeck, T., and Herbert, F. (2006). The effect of ice-phase microphysics on tropical cyclones simulated by the Lokalmodell. *COSMO Newsletter*, 6:236–241.
- Fujibe, F. and Kitabatake, N. (2007). Classification of surface wind fields of tropical cyclones at landfall on the japan main islands. *J. Meteor. Soc. Japan*, 85(6):747–765.
- Galarneau-Jr., T. J., Davis, C. A., and Shapiro, M. A. (2013). Intensification of hurricane Sandy (2012) through extratropical warm core seclusion. *Mon. Wea. Rev.*, 141:4296–4321.
- Grams, C. M. (2011). *Quantification of the downstream impact of extratropical transition for Typhoon Jangmi and other case studies*. PhD thesis, Karlsruhe Institute of Technology, Karlsruhe, Germany.
- Grams, C. M. and Blumer, S. R. (2015). European high-impact weather caused by the downstream response to the extratropical transition of north atlantic hurricane Katia (2011). *Geophys. Res. Lett.*, 42:8738–8748.

- Grams, C. M., Jones, S. C., and Davis, C. A. (2013a). The impact of typhoon Jangmi (2008) on the midlatitude flow. Part II: Downstream evolution. *Q. J. R. Meteorol. Soc.*, 139:2165–2180.
- Grams, C. M., Jones, S. C., Davis, C. A., Harr, P. A., and Weissmann, M. (2013b). The impact of typhoon Jangmi (2008) on the midlatitude flow. Part I: Upper-level ridgebuilding and modification of the jet. *Q. J. R. Meteorol. Soc.*, 139:2148–2164.
- Grams, C. M., Lang, S. T. K., and Keller, J. H. (2015). A quantitative assessment of the sensitivity of the downstream midlatitude flow response to extratropical transition of tropical cyclones. *Geophys. Res. Lett.*, 42:9521–9529.
- Gray, S. L., Dunning, C. M., Methven, J., Masato, G., and Chagnon, J. M. (2014). Systematic model forecast error in rossby wave structure. *Geophys. Res. Lett.*, 41:2979–2987.
- Gray, W. M. (1968). Global view of the origin of tropical disturbances and storms. *Mon. Wea. Rev.*, 96:669–699.
- Griffin, K. S. and Bosart, L. F. (2014). The extratropical transition of Tropical Cyclone Edisoana (1990). *Mon. Wea. Rev.*, 142:2772–2793.
- Harnisch, F., Weissmann, M., Cardinali, C., and Wirth, M. (2011). Experimental assimilation of DIAL water vapour observations in the ECMWF global model. *Q. J. R. Meteorol. Soc.*, 137:1532–1546.
- Harr, P. A., Anwender, D., and Jones, S. C. (2008). Predictability associated with the downstream impacts of the extratropical transition of tropical cyclones: Methodology and a case study of typhoon Nabi (2005). *Mon. Wea. Rev.*, 136:3205–3225.
- Harr, P. A. and Dea, J. M. (2009). Downstream development associated with the extratropical transition of tropical cyclones over the western north pacific. *Mon. Wea. Rev.*, 137:1295–1319.
- Harr, P. A. and Elsberry, R. L. (2000). Extratropical transition of tropical cyclones over the western north pacific. part i: Evolution of structural characteristics during the transition process. *Mon. Wea. Rev.*, 128:2613–2633.
- Harr, P. A., Elsberry, R. L., and Hogan, T. F. (2000). Extratropical transition of tropical cyclones over the western north pacific. part ii: The impact of midlatitude circulation characteristics. *Mon. Wea. Rev.*, 128:2634–2653.
- Harr, P. A., Sanabia, E. R., and Penny, A. B. (2010). Typhoon Sinlaku during T-PARC: sensitivity of the re-intensification and downstream development to the track following recurvature. In *29th Conference on Hurricanes and Tropical Meteorology*, American Meteorological Society, Boston, MA.
- Hart, R. E. and Evans, J. L. (2001). A climatology of the extratropical transition of atlantic tropical cyclones. *J. Climate*, 14:546–564.

- Hart, R. E., Evans, J. L., and Evans, C. (2006). Synoptic composites of the extratropical transition life cycle of North Atlantic tropical cyclones: Factors determining posttransition evolution. *Mon. Wea. Rev.*, 134:553–578.
- Haynes, P. H. and McIntyre, M. E. (1987). On the evolution of vorticity and potential vorticity in the presence of diabatic heating and friction or other forces. *J. Atmos. Sci.*, 44, No. 5:828–841.
- Hewson, T. D. and Neu, U. (2015). Cyclones, windstorms and the IMILAST project. *Tellus A*, 67, 27128:1–33.
- Hildebrand, P. H., Lee, W.-C., Walther, C. A., Frush, C., Randall, M., Loew, E., Neitzel, R., Parsons, R., Testud, J., Baudin, F., and LeCornec, A. (1996). The EL-DORA/ASTRAIA airborne Doppler weather radar: High-resolution observations from TOGA COARE. *Bull. Amer. Meteor. Soc.*, 77:213–232.
- Hock, T. F. and Franklin, J. L. (1999). The NCAR GPS dropwindsonde. *Bull. Amer. Meteor. Soc.*, 80:407–420.
- Hoskins, B. J., Draghici, I., and Davies, H. C. (1978). A new look at the ω -equation. *Q. J. R. Meteorol. Soc.*, 104:31–38.
- Hoskins, B. J., McIntyre, M. E., and Robertson, A. W. (1985). On the use and significance of isentropic potential vorticity maps. *Q. J. R. Meteorol. Soc.*, 111:877–946.
- Huang, Y.-H., Montgomery, M. T., and Wu, C.-C. (2012). Concentric eyewall formation in Typhoon Sinlaku (2008). part II: Axisymmetric dynamical processes. *Mon. Wea. Rev.*, 69:662–674.
- Huang, Y.-H., Wu, C.-C., and Wang, Y. (2011). The influence of island topography on typhoon track deflection. *Mon. Wea. Rev.*, 139:1708–1727.
- Jian, G.-J. and Wu, C.-C. (2008). A numerical study of the track deflection of supertyphoon haitang (2005) prior to its landfall in taiwan. *Mon. Wea. Rev.*, 136:598–615.
- Jones, S. C. (1995). The evolution of vortices in vertical shear. I: Initial barotropic vortices. *Q. J. R. Meteorol. Soc.*, 121:821–851.
- Jones, S. C., Harr, P. A., Abraham, J., Bosart, L. F., Bowyer, P. J., Evans, J. L., Hanley, D. E., Hanstrum, B. N., Hart, R. E., Lalaurette, F., Sinclair, M. R., Smith, R. K., and Thorncroft, C. (2003). The extratropical transition of tropical cyclones: Forecast challenges, current understanding, and future directions. *Wea. Forecasting*, 18:1052–1092.
- Jones, S. C., Velden, C. S., Aberson, S., Abraham, J., and Harr, P. A. (2004). Extratropical transition and THORPEX. reprints. In *26th Conference on Hurricanes and Tropical Meteorology, American Meteorological Society, Miami, FL*, pages 643–644.

- Joos, H. and Wernli, H. (2012). Influence of microphysical processes on the potential vorticity development in a warm conveyor belt: a case-study with the limited-area model COSMO. *Q. J. R. Meteorol. Soc.*, 138:407–418.
- Keller, J. H., Jones, S. C., Evans, J. L., and Harr, P. A. (2011). Characteristics of the tigre multimodel ensemble prediction system in representing forecast variability associated with extratropical transition. *Geophys. Res. Lett.*, 38, L12802:1–6.
- Keyser, D., Reeder, M. J., and Reed, R. J. (1988). A generalization of Petterssen’s frontogenesis function and its relation to the forcing of vertical motion. *Mon. Wea. Rev.*, 116:762–780.
- Kirk, J. R. (2007). A phase-plot method for diagnosing vorticity concentration mechanisms in mesoscale convective vortices. *Mon. Wea. Rev.*, 135:801–820.
- Kitabatake, N. (2008). Extratropical transition of tropical cyclones in the western North Pacific: Their frontal evolution. *Mon. Wea. Rev.*, 136:2066–2090.
- Kitabatake, N. and Fujibe, F. (2009). Relationship between surface wind fields and three-dimensional structures of tropical cyclones landfalling in the main islands of Japan. *J. Meteor. Soc. Japan*, 87(6):959–977.
- Klein, P. M., Harr, P. A., and Elsberry, R. L. (2000). Extratropical transition of western north Pacific tropical cyclones: an overview and conceptual model of the transformation stage. *Wea. Forecasting*, 15:373–396.
- Klein, P. M., Harr, P. A., and Elsberry, R. L. (2002). Extratropical transition of western north Pacific tropical cyclones: Midlatitude and tropical cyclone contributions to reintensification. *Mon. Wea. Rev.*, 130:2240–2259.
- Klemp, J. B. and Wilhelmson, R. B. (1978). The simulation of three-dimensional convective storm dynamics. *J. Atmos. Sci.*, 35:1070–1096.
- Komaromi, W. A., Majumdar, S. J., and Rappin, E. D. (2011). Diagnosing initial condition sensitivity of typhoon Sinlaku (2008) and hurricane Ike (2008). *Mon. Wea. Rev.*, 139:3224–3242.
- Kossin, J. P. and Velden, C. S. (2004). A pronounced bias in tropical cyclone minimum sea level pressure estimation based on the Dvorak Technique. *Mon. Wea. Rev.*, 132:165–173.
- Kuo, H.-C., Chang, C.-P., and Liu, C.-H. (2012). Convection and rapid filamentation in typhoon Sinlaku during TCS-08/T-PARC. *Mon. Wea. Rev.*, 140:2806–2817.
- Lackmann, G. (2011). *Midlatitude synoptic meteorology - dynamics, analysis, and forecasting*. American Meteorological Society, Boston, Massachusetts.
- Leroux, M.-D., Davidson, N. E., Ma, Y., and Kepert, J. D. (2013). Prediction and diagnosis of the motion and rapid intensification of typhoon Sinlaku during Tropical Cyclone Structure Experiment 2008 (TCS08). *Mon. Wea. Rev.*, 141:1413–1436.

- Li, Y., Cheung, K. K. W., and Chan, J. C. L. (2014). Numerical study on the development of asymmetric convection and vertical wind shear during tropical cyclone landfall. *Q. J. R. Meteorol. Soc.*, 140:1866–1877.
- Li, Y., Cheung, K. K. W., and Chan, J. C. L. (2015). Modelling the effects of land–sea contrast on tropical cyclone precipitation under environmental vertical wind shear. *Q. J. R. Meteorol. Soc.*, 141:396–412.
- Lin, Y.-L., Chen, S.-Y., and Hill, C. M. (2005). Control parameters for the influence of a mesoscale mountain range on cyclone track continuity and deflection. *J. Atmos. Sci.*, 62:1849–1866.
- Loridan, T., Scherer, E., Dixon, M., Bellone, E., and Khare, S. (2014). Cyclone wind field asymmetries during extratropical transition in the western north pacific. *J. Appl. Meteor. Climatol.*, 53:421–428.
- Ma, S., Ritchie, H., Gyakum, J., Abraham, J., Fogarty, C., and McTaggart-Cowan, R. (2003). A study of the extratropical reintensification of former Hurricane Earl using Canadian Meteorological Centre regional analyses and ensemble forecasts. *Mon. Wea. Rev.*, 131:1342–1359.
- Magnusson, L., Bidlot, J.-R., Lang, S. T. K., Thorpe, A., and Wedi, N. (2014). Evaluation of medium-range forecasts for hurricane Sandy. *Mon. Wea. Rev.*, 142:1962–1981.
- Martin, J. E. (2006). *Mid-latitude Atmospheric Dynamics - a first course*. John Wiley & Sons Ltd, The Atrium, Southern Gate, Chichester, England.
- Martínez-Alvarado, O., Baker, L. H., Gray, S. L., Methven, J., and Plant, R. S. (2014). Distinguishing the cold conveyor belt and sting jet airstreams in an intense extratropical cyclone. *Mon. Wea. Rev.*, 142:2571–2595.
- Mashiko, W. (2008). Formation mechanisms of a low-level jet during the passage of Typhoon Ma-on (2004) over the southern Kanto District. *J. Meteor. Soc. Japan*, 86(1):183–202.
- Matano, H. and Sekioka, M. (1971). Some aspects of extratropical transformation of a tropical cyclone. *J. Meteor. Soc. Japan*, 49:736–743.
- McTaggart-Cowan, R., Bosart, L. F., Gyakum, J. R., and Atallah, E. H. (2006). Hurricane Juan (2003). Part II: Forecasting and numerical simulation. *Mon. Wea. Rev.*, 134:1748–1771.
- McTaggart-Cowan, R., Gyakum, J. R., and Yau, M. K. (2001). Sensitivity testing of extratropical transitions using potential vorticity inversions to modify initial conditions: Hurricane Earl case study. *Mon. Wea. Rev.*, 129:1617–1636.
- McTaggart-Cowan, R., Gyakum, J. R., and Yau, M. K. (2004). The impact of tropical remnants on extratropical cyclogenesis: Case study of hurricanes Danielle and Earl (1998). *Mon. Wea. Rev.*, 132:1933–1951.

- Neiman, P. J., Shapiro, M. A., and Fedor, L. S. (1993). The life cycle of an extratropical marine cyclone. Part II: Mesoscale structure and diagnostics. *Mon. Wea. Rev.*, 121:2177–2199.
- Palmén, E. (1948). On the formation and structure of tropical hurricanes. *Geophysica*, 3:26–38.
- Pantillon, F., Chaboureau, J.-P., Lac, C., and Mascart, P. (2013). On the role of a rossby wave train during the extratropical transition of hurricane Helene (2006). *Q. J. R. Meteorol. Soc.*, 139:370–386.
- Petterssen, S. (1956). *Weather Analysis and Forecasting. Vol. 1, Motion and Motion Systems, 2d ed.* McGraw-Hill.
- Petterssen, S. and Smebye, S. J. (1971). On the development of extratropical cyclones. *Q. J. R. Meteorol. Soc.*, 97:457–482.
- Prater, B. E. and Evans, J. L. (2002). Sensitivity of modeled tropical cyclone track and structure of Hurricane Irene (1999) to the convective parameterization scheme. *Meteorol*, 80:103–115.
- Quinting, J. F. (2015). *The impact of tropical convection on the dynamics and predictability of midlatitude Rossby waves: a climatological study.* PhD thesis, Karlsruhe Institute of Technology, Karlsruhe, Germany.
- Quinting, J. F., Bell, M. M., Harr, P. A., and Jones, S. C. (2014). Structural characteristics of T-PARC Typhoon Sinlaku during its extratropical transition. *Mon. Wea. Rev.*, 142:1945–1961.
- Quinting, J. F. and Jones, S. C. (2016). On the impact of tropical cyclones on Rossby wave packets: A climatological perspective. *Mon. Wea. Rev.*, 144:2021–2048.
- Reasor, P. D., Montgomery, M. T., and Grasso, L. D. (2004). A new look at the problem of tropical cyclones in vertical shear flow: Vortex resiliency. *J. Atmos. Sci.*, 61:3–22.
- Reasor, P. D., Montgomery, M. T., Jr., F. D. M., and Gamache, J. F. (2000). Low-wavenumber structure and evolution of the hurricane inner core observed by airborne dual-doppler radar. *Mon. Wea. Rev.*, 128:1653–1680.
- Riemer, M. and Jones, S. C. (2010). The downstream impact of tropical cyclones on a developing baroclinic wave in idealized scenarios of extratropical transition. *Q. J. R. Meteorol. Soc.*, 136:617–637.
- Riemer, M. and Jones, S. C. (2014). Interaction of a tropical cyclone with a high-amplitude, midlatitude wave pattern: Waviness analysis, trough deformation and track bifurcation. *Q. J. R. Meteorol. Soc.*, 140:1362–1376.
- Riemer, M., Jones, S. C., and Davis, C. A. (2008). The impact of extratropical transition on the downstream flow: An idealized modelling study with a straight jet. *Q. J. R. Meteorol. Soc.*, 134:69–91.

- Riemer, M., Montgomery, M. T., and Nicholls, M. E. (2010). A new paradigm for intensity modification of tropical cyclones: thermodynamic impact of vertical wind shear on the inflow layer. *Atmos. Chem. Phys.*, 10:3163–3188.
- Riemer, M., Montgomery, M. T., and Nicholls, M. E. (2013). Further examination of the thermodynamic modification of the inflow layer of tropical cyclones by vertical wind shear. *Atmos. Chem. Phys.*, 13:327–346.
- Ritchie, E. A. and Elsberry, R. L. (2001). Simulations of the transformation stage of the extratropical transition of tropical cyclones. *Mon. Wea. Rev.*, 129:1462–1480.
- Ritchie, E. A. and Elsberry, R. L. (2007). Simulations of the extratropical transition of tropical cyclones: Phasing between the upper-level trough and tropical cyclones. *Mon. Wea. Rev.*, 135:862–876.
- Sanabia, E. R. (2010). *The re-intensification of Typhoon Sinlaku (2008)*. PhD thesis, Naval Postgraduate School, Monterey, CA.
- Schäfler, A. and Harnisch, F. (2015). Impact of the inflow moisture on the evolution of a warm conveyor belt. *Q. J. R. Meteorol. Soc.*, 141:299–310.
- Schättler, U., Doms, G., and Schraff, C. (2011). *A description of the nonhydrostatic regional COSMO-model. Part VII: User’s guide*. Deutscher Wetterdienst, Offenbach, www.cosmo-model.org.
- Scheck, L., Jones, S. C., and Juckes, M. (2011a). The resonant interaction of a tropical cyclone and a tropopause front in a barotropic model. part I: Zonally oriented front. *J. Atmos. Sci.*, 68:405–419.
- Scheck, L., Jones, S. C., and Juckes, M. (2011b). The resonant interaction of a tropical cyclone and a tropopause front in a barotropic model. part II: Frontal waves. *J. Atmos. Sci.*, 68:420–429.
- Schultz, D. M. (2001). Reexamining the cold conveyor belt. *Mon. Wea. Rev.*, 129:2205–2225.
- Schultz, D. M. and Sienkiewicz, J. M. (2013). Using frontogenesis to identify sting jets in extratropical cyclones. *Wea. Forecasting*, 28:603–613.
- Schwendike, J. (2010). *Convection in an African Easterly Wave over West Africa and the Eastern Atlantic: a Model Case Study of Hurricane Helene (2006) and its Interaction with the Saharan Air Layer*. PhD thesis, Karlsruhe Institute of Technology, Karlsruhe, Germany.
- Schwendike, J. and Jones, S. C. (2010). Convection in an african easterly wave over west africa and the eastern atlantic: A model case study of Helene (2006). *Q. J. R. Meteorol. Soc.*, 136:364–396.
- Shapiro, M. A. and Keyser, D. (1990). *Extratropical cyclones: The Erik Palmén Memorial Volume*, chapter 10: Fronts, jet streams and the tropopause, pages 167–191. Amer. Meteor. Soc.

- Shea, D. J. and Gray, W. M. (1973). The hurricane's inner core region. I. symmetric and asymmetric structure. *J. Atmos. Sci.*, 30:1544–1564.
- Sinclair, M. R. (1993). A diagnostic study of the extratropical precipitation resulting from Tropical Cyclone Bola. *Mon. Wea. Rev.*, 121:2690–2707.
- Sinclair, M. R. (2002). Extratropical transition of southwest pacific tropical cyclones. part i: Climatology and mean structure changes. *Mon. Wea. Rev.*, 130:590–609.
- Smart, D. J. and Browning, K. A. (2014). Attribution of strong winds to a cold conveyor belt and sting jet. *Q. J. R. Meteorol. Soc.*, 140:595–610.
- Sprenger, M. and Wernli, H. (2015). The LAGRANTO Lagrangian analysis tool - version 2.0. *Geosci. Model Dev.*, 8:2569–2586.
- Srock, A. F. and Bosart, L. F. (2009). Heavy precipitation associated with southern Appalachian cold-air damming and Carolina coastal frontogenesis in advance of weak landfalling tropical storm Marco (1990). *Mon. Wea. Rev.*, 137:2448–2470.
- Stappeler, J., Doms, G., Schättler, U., Bitzer, H. W., Gassmann, A., Damrath, U., and Gregoric, G. (2003). Meso-gamma scale forecasts using the nonhydrostatic model LM. *Meteorol.*, 82:75–96.
- Stoelinga, M. T. (1996). A potential vorticity-based study of the role of diabatic heating and friction in a numerically simulated baroclinic cyclone. *Mon. Wea. Rev.*, 124:849–874.
- Szeto, K. C. and Chan, J. C. L. (2010). Structural changes of a tropical cyclone during landfall: beta-plane simulations. *Adv. Atmos. Sci.*, 27 (5):1143–1150.
- Tang, C. K. and Chan, J. C. L. (2014). Idealized simulations of the effect of Taiwan and Philippines topographies on tropical cyclone tracks. *Q. J. R. Meteorol. Soc.*, 140:1578–1589.
- Thorncroft, C. and Jones, S. C. (2000). The extratropical transitions of Hurricanes Felix and Iris in 1995. *Mon. Wea. Rev.*, 128:947–972.
- Thorncroft, C. D., Hoskins, B. J., and McIntyre, M. E. (1993). Two paradigms of baroclinic-wave life-cycle behaviour. *Q. J. R. Meteorol. Soc.*, 119:17–55.
- Thorpe, A. J. (1986). Synoptic scale disturbances with circular symmetry. *Mon. Wea. Rev.*, 114:1384–1389.
- Thorpe, A. J. and Pedder, M. A. (1999). The semi-geostrophic diagnosis of vertical motion. II: Results for an idealized baroclinic wave life cycle. *Q. J. R. Meteorol. Soc.*, 125:1257–1276.
- Tiedtke, M. (1989). A comprehensive mass flux scheme for cumulus parameterization in large-scale models. *Mon. Wea. Rev.*, 117:1779–1800.
- Torn, R. D. (2010). Diagnosis of the downstream ridging associated with extratropical transition using short-term ensemble forecasts. *J. Atmos. Sci.*, 67:817–833.

- Torn, R. D. and Hakim, G. J. (2009). Initial condition sensitivity of western pacific extratropical transitions determined using ensemble-based sensitivity analysis. *Mon. Wea. Rev.*, 137:3388–3406.
- Torn, R. D., Whitaker, J. S., Pegion, P., Hamill, T. M., and Hakim, G. J. (2015). Diagnosis of the source of GFS medium-range track errors in Hurricane Sandy (2012). *Mon. Wea. Rev.*, 143:132–152.
- Uhlhorn, E. W., Klotz, B. W., Vukicevic, T., Reasor, P. D., and Rogers, R. F. (2014). Observed hurricane wind speed asymmetries and relationships to motion and environmental shear. *Mon. Wea. Rev.*, 142:1290–1311.
- Velden, C. S., Daniels, J., Stettner, D., Santek, D., Key, J., Dunion, J., Holmlund, K., Dengel, G., Bresky, W., and Menzel, P. (2005). Recent innovations in deriving tropospheric winds from meteorological satellites. *Bull. Amer. Meteor. Soc.*, 86 (2):205–223.
- Velden, C. S., Harper, B., Wells, F., Beven, J. L., Zehr, R., Olander, T., Mayfield, M., Guard, C., Lander, M., Edson, R., Avila, L., Burton, A., Turk, M., Kikuchi, A., Christian, A., Caroff, P., and McCrone, P. (2006). The Dvorak tropical cyclone intensity estimation technique: A satellite-based method that has endured for over 30 years. *Bull. Amer. Meteor. Soc.*, 87:1195–1210.
- Velden, C. S., Hayden, C. M., Nieman, S. J., Menzel, W. P., Wanzong, S., and Gerss, J. S. (1997). Upper-tropospheric winds derived from geostationary satellite water vapor observations. *Bull. Amer. Meteor. Soc.*, 78 (2):173–195.
- Wang, Y. and Holland, G. J. (1996). Tropical cyclone motion and evolution in vertical shear. *J. Atmos. Sci.*, 53:3313–3332.
- Weisman, M. L. and Davis, C. A. (1998). Mechanisms for the generation of mesoscale vortices within quasi-linear convective systems. *J. Atmos. Sci.*, 55:2603–2622.
- Weissmann, M., Busen, R., Dörnbrack, A., Rahm, S., and Reitebuch, O. (2005). Targeted observations with an airborne wind lidar. *J. Atmos. Oceanic Technol.*, 22:1706–1719.
- Weissmann, M., Harnisch, F., Wu, C.-C., Lin, P.-H., Ohta, Y., Yamashita, K., Kim, Y.-H., Jeon, E.-H., Nakazawa, T., and Aberson, S. (2011). The influence of assimilating dropsonde data on typhoon track and midlatitude forecasts. *Mon. Wea. Rev.*, 139:908–920.
- Weissmann, M., Langland, R. H., Cardinali, C., Pauley, P. M., and Rahm, S. (2012). Influence of airborne Doppler wind lidar profiles near Typhoon Sinlaku on ECMWF and NOGAPS forecasts. *Q. J. R. Meteorol. Soc.*, 138:118–130.
- Wernli, H. and Davies, H. C. (1997). A Lagrangian-based analysis of extratropical cyclones. I: The method and some applications. *Q. J. R. Meteorol. Soc.*, 123:467–489.
- Wong, M. L. M. and Chan, J. C. L. (2006). Tropical cyclone motion in response to land surface friction. *J. Atmos. Sci.*, 63:1324–1337.

- Wood, K. M. and Ritchie, E. A. (2014). A 40-year climatology of extratropical transition in the eastern North Pacific. *J. Climate*, 27:5999–6015.
- Wu, C.-C. (2001). Numerical simulation of typhoon gladys (1994) and its interaction with taiwan terrain using the gfdl hurricane model. *Mon. Wea. Rev.*, 129:1533–1549.
- Wu, C.-C., Chen, S.-G., Lin, S.-C., Yen, T.-H., and Chen, T.-C. (2013). Uncertainty and predictability of tropical cyclone rainfall based on ensemble simulations of typhoon Sinlaku (2008). *Mon. Wea. Rev.*, 141:3517–3538.
- Wu, C.-C., Chen, S.-G., Yang, C.-C., and Lin, P.-H. (2012a). Potential vorticity diagnosis of the factors affecting the track of typhoon Sinlaku (2008) and the impact from dropwindsonde data during t-parc. *Mon. Wea. Rev.*, 140:2670–2688.
- Wu, C.-C., Huang, Y.-H., and Lien, G.-Y. (2012b). Concentric eyewall formation in Typhoon Sinlaku (2008). part I: Assimilation of T-PARC data based on the Ensemble Kalman Filter (EnKF). *Mon. Wea. Rev.*, 140:506–527.
- Wu, C.-C., Li, T.-H., and Huang, Y.-H. (2015). Influence of mesoscale topography on tropical cyclone tracks: Further examination of the channeling effect. *J. Atmos. Sci.*, 72:3032–3050.
- Wu, L. and Wang, B. (2000). A potential vorticity tendency diagnostic approach for tropical cyclone motion. *Mon. Wea. Rev.*, 128:1899–1911.
- Wu, L. and Wang, B. (2001). Effects of convective heating on movement and vertical coupling of tropical cyclones: A numerical study. *J. Atmos. Sci.*, 58:3639–.
- Yeh, T.-C. and Elsberry, R. L. (1993). Interaction of typhoons with the Taiwan orography. Part I: Upstream track deflections. *Mon. Wea. Rev.*, 121:3193–3212.

Acknowledgements

I would like to thank my supervisor Prof. Sarah Jones for her advice and for enabling me to work on this interesting topic in the framework of PANDOWAE.

I would like to thank Prof. Corinna Hoose as well, for doing the proof reading and for her feedback on an earlier version of this dissertation.

I am very grateful to Dr. Christian Grams for introducing me to this topic in the first place and for supervising me afterwards. Dear Christian, you always took the time for motivating discussions and you were interested in my working progress. Furthermore, you believed that I could do it, which was an essential part in order to successfully finish this thesis. Thank you very much!

Without data and technical support it would not have been possible to analyze the development of Sinlaku. Therefore I would like to thank Julia Keller, Martin Weissmann and the ECMWF for providing the research analysis data that was used to initialize COSMO.

Concerning the measurement data, the United States Air Force (USAF), the Naval Research Laboratory (NRL) and the German Aerospace Center (DLR) are acknowledged for making their aircraft data during T-PARC available. GPS dropsonde data, LIDAR data and AMV data was provided by NCAR/EOL via the T-PARC support page, under sponsorship of the National Science Foundation. <http://data.eol.ucar.edu/>. The Japan Meteorological Agency (JMA) is acknowledged for providing high-resolution MTSAT CTT and Quikscat data via their T-PARC support page, together with Best Track data via www.digital-typhoon.org. Thanks goes in particular to Munehiko Yamaguchi (MRI-JMA) for help with the MTSAT and Quikscat data acquisition.

The analysis and measurement data were combined to obtain the SAMURAI data. Especially the 19 September SAMURAI data was an indispensable part in order to improve the storm structure in the initial data and to obtain a proper simulation of Sinlaku's ET. Many thanks go to Annette Foerster and Michael Bell for producing an adapted fully gridded version of the SAMURAI data for Sinlaku on early 19 September. Thanks also goes to Julian Quinting for providing his SAMURAI data for Sinlaku on early 20 September.

Simulations are performed with the numerical weather prediction model COSMO. I would like to thank Uli Blahak, Leonhard Gantner and Christian Barthlott, not only for helping me with the first steps of getting to know the model, but also for their support and valuable experience later on. COSMO simulations were conducted on

the high performance computing systems HP XC3000 and the InstitutsCluster II, with the help and maintenance of the Steinbuch Centre for Computing (SCC).

The resulting model data is analyzed with several tools. I would like to thank Christian Grams for technical help with the Piecewise PV Inversion tool, Julian Quinting for providing and assisting with the QG-omega tool and Gregor Pante, Michael Sprenger and Daniel Lüthi for their assistance with LAGRANTO and for applying its pre-processor p2s_lm to my large data files. Finally, visualizations and additional computations are performed with the use of NCAR Command Language (Version 6.3.0) [Software]. (2015). Boulder, Colorado: UCAR/NCAR/CISL/TDD.

This research was done in the framework of the Research Unit PANDOWAE (Forschergemeinschaft FOR896), funded by the German Research Foundation (Deutsche Forschungsgemeinschaft, DFG). It was an honor to be part of PANDOWAE and this study benefited from the several meetings we had. I learned much about different research topics, which made me look at my own topic from different perspectives, and I got introduced to various new tools and methods. I would like to thank Dr. Michael Riemer in particular for interesting discussions about ET. Additionally, I would like to thank my fellow PhD students in the project for the many inspiring and enjoyable Young Scientist Summer/Winter Schools: Luisa Röhrner, Lisa-Ann Quandt, Julian Quinting, Franziska Gierth, Gabriel Wolf, Paraskevi Giannakaki.

My time as a PhD student at the Institute of Meteorology and Climate Research as well as my experience with Germany wouldn't have been so successful or pleasant without good colleagues, from whom many of you became friends.

I would like to thank everyone from Campus South for the interesting and relaxing breaks, and Doris Stenschke, Friederike Schönbein and Gerhard Brückel for their administrative and technical support. A thanks also goes to the once from Campus North that I regularly met and to the "Süddeutsche Klimabüro" for trusting me with another job as soon as my PhD finance ran out.

Additionally, I would like to thank my working group: Lisa-Ann Quandt, Julian Quinting, Julia Keller, Leonhard Scheck, Susanna Hopsch and Aurelia Müller. Although the time with some of you was only short, I am still thankful that we got to know each other. To Lisa and Julian I would like to say "Thank you for your enthusiastic and motivating presence in the office, for enlightening discussions and for the help wherever needed. We made it!".

A good distraction from work which made me fit both physically and mentally were the many running, cycling, swimming and other sports activities in the lunch breaks and after work with the motivating company of e.g. Axel, Christian, Enrico, Florian, Heinz Jürgen, Julia, Julian, Katharina, Linda, Lisa, Luisa and Rik.

Furthermore an extra thanks goes to Luisa, Katharina, Julia, Eva and Elody for our many pleasant moments after work. Another pleasant distraction from work were the many visits from family and friends from the Netherlands. Thank you all for coming by and having a good time Robrecht, Anja, Esmée, Ringo, Hans, Pia, Bas, Jeannine, Marthe, Wessel, Jaap, Caat, Rens, Anouk, Derk, Kasia, Charlotte, Thijs,

Marie-Jette, Marco, Nanouk, Joost, Miriam, Arthur, Mark, Peter, Mayumi, Menno, Marije, Kirsten, Tim, Vincent, Lotte, Menno, Astrid, Eveline, Harm Jan, Nienke.

Furthermore I would like to thank my parents for believing in me, for seeing the positive side of things and having faith in that everything will be fine.

Finally, Rik, you are the best of all. You kept me standing, every time I almost drowned. You made me smile every time I lost confidence and you were there every time I needed some positive thoughts. We did it! Now you may give it a try and I will make sure that you keep on smiling!